

Reconstructing late Proterozoic magmatism, geomagnetic field behavior, and paleogeography: Insights from anorthosite xenoliths, large igneous provinces, and paleomagnetic records

by

Yiming Zhang

A dissertation submitted in partial satisfaction of the

requirements for the degree of

Doctor of Philosophy

in

Earth & Planetary Science

in the

Graduate Division

of the

University of California, Berkeley

Committee in charge:

Professor Nicholas L. Swanson-Hysell, Chair

Professor Bruce A. Buffett

Professor Seth Finnegan

Spring 2024

Reconstructing late Proterozoic magmatism, geomagnetic field behavior, and paleogeography: Insights from anorthosite xenoliths, large igneous provinces, and paleomagnetic records

Copyright 2024  
by  
Yiming Zhang

## Abstract

Reconstructing late Proterozoic magmatism, geomagnetic field behavior, and paleogeography: Insights from anorthosite xenoliths, large igneous provinces, and paleomagnetic records

by

Yiming Zhang

Doctor of Philosophy in Earth & Planetary Science

University of California, Berkeley

Professor Nicholas L. Swanson-Hysell, Chair

The Proterozoic Eon is a period of Earth's history that began 2.5 billion years ago and ended 539 million years ago. By this time, stable continents have appeared and began to amalgamate, the first abundant fossils of living organisms started to appear in the geologic records, and the atmospheric concentration of oxygen started to rise from nearly null. At the boundary between the Mesoproterozoic (1.7 to 1.0 billion-years ago) and Neoproterozoic Eras (1.0 to 0.54 billion-years ago), the majority of the global continents conjoined together and formed a supercontinent called Rodinia, which eventually broke up throughout the Neoproterozoic Era. In this dissertation, I use field observations and paleomagnetic data in the ancient North American craton, Laurentia, to study the magmatic and tectonic history at the time, and to investigate the geodynamic linkages between these lithospheric processes with deep-Earth evolution leading up to the assembly of Rodinia.

I use paleomagnetic data in combination with geochronologic data and geochemical data to investigate the magmatic characteristics of the late Mesoproterozoic Midcontinent Rift. I test a hypothesis that the voluminous Beaver River diabase was the feeder system for one of the largest lava flows known on Earth—the Greenstone Flow. I show that the diabase and the lava flow were emplaced synchronously and share chemical and petrological characteristics. With the diabase outcropping in Minnesota along the western shore of Lake Superior while the lava flow outcropping on Isle Royale and on the Keweenaw Peninsula, they together define an episode of rapid and voluminous mafic magmatism ca. 1092 Ma as Laurentia rapidly traveled from high latitudes toward the equator.

The large and well-preserved anorthosite xenoliths within the Beaver River diabase not only serve as evidence for wide magma conduits and vigorous magmatism at the time, but also provide an opportunity to directly reconstruct the strengths of Earth's surface magnetic field in the Mesoproterozoic. Previously, it was proposed that Earth did not have a solid inner

core until the Ediacaran Period, and the Proterozoic Eon witnessed a progressive decay of Earth's magnetic field strength due to the decrease in the vigor of fluid convection in the core. I developed paleointensity data from the Beaver River anorthosite xenoliths. Instead of showing weak geomagnetic field strengths as predicted by the hypothesis, the data reveal a strong geodynamo at the time. I argue that the high geomagnetic field intensities shown by the anorthosites indicate that there were strong power sources to the geodynamo in the late Mesoproterozoic. Whether or not such power source include compositional convection driven by a substantial solid inner core requires more paleomagnetic data, geodynamo modeling, and advances in material property characterization at Earth's core conditions.

While protracted magmatism occurred in the Midcontinent Rift region in the late Mesoproterozoic, mafic magmatism also occurred  $\sim$ 2000 km away in southwestern Laurentia. I report new paleomagnetic data paired with high-precision zircon U-Pb geochronology data from the Death Valley region of California and the Grand Canyon region of Arizona and investigate the temporal magmatic correlations between the the Midcontinent Rift and the southwestern Laurentia. I show that the rapid emplacement of thick mafic intrusions throughout a large extent in southwestern Laurentia define a large igneous province ca. 1098 Ma. The timing and scale of this episode of magmatism allows for a geodynamic linkage between it and the large igneous province associated with the Duluth Complex in the Midcontinent Rift, where a mantle plume first arrived and resulted in widespread magmatism in the southwest, before draining toward the Midcontinent Rift where it drove the emplacement of the Duluth Complex and associated volcanism.

Lastly, I report new paleomagnetic data from sedimentary rocks of the Jacobsville Formation in Michigan for constraining the global paleogeography in the earliest Neoproterozoic. Clastic sedimentary rocks are an important archive of Earth history. Detrital hematite-bearing red bed sedimentary rocks are particularly useful for providing crucial paleogeographic constraints. With the red siltstone and fine-grained sandstone facies of the Jacobsville Formation, I show that Laurentia's plate speed slowed down by an order of magnitude in the late Mesoproterozoic to early Neoproterozoic following the onset of the Grenvillian orogeny. I further hypothesize that the previous estimates of the ages of the paleomagnetic poles of the Grenville Loop need to be recalibrated and are likely much younger.

# Contents

<b>Contents</b>	i
<b>List of Figures</b>	iii
<b>List of Tables</b>	vi
<b>Preface</b>	vii
<b>Acknowledgements</b>	xi
<b>1 Introduction</b>	1
1.1 Late Mesoproterozoic magmatism in the Midcontinent Rift and the south-western Laurentia large igneous province . . . . .	2
1.2 Probing the evolution of Earth's interior via paleointensity observations . . . . .	8
1.3 Recovering deep-time paleointensity records from silicate-hosted Fe-oxides . . . . .	11
1.4 Using detrital remanent magnetization in hematite-bearing sedimentary rocks to reconstruct paleogeography . . . . .	13
1.5 Global paleogeography in the earliest Neoproterozoic: progress and future directions . . . . .	15
<b>2 Synchronous emplacement of the anorthosite xenolith-bearing Beaver River diabase and one of the largest lava flows on Earth</b>	19
2.1 Abstract . . . . .	19
2.2 Introduction . . . . .	20
2.3 Geologic Setting . . . . .	23
2.4 Methods and Results . . . . .	28
2.5 Discussion . . . . .	37
2.6 Conclusion . . . . .	45
2.7 Acknowledgments . . . . .	45
<b>3 High geomagnetic field intensity recorded by anorthosite xenoliths requires a strongly powered late Mesoproterozoic geodynamo</b>	46
3.1 Abstract . . . . .	46

3.2	Introduction . . . . .	47
3.3	Methods . . . . .	50
3.4	Results and Interpretations . . . . .	54
3.5	Discussion . . . . .	61
3.6	Acknowledgements . . . . .	65
<b>4</b>	<b>Paleomagnetism of the southwestern Laurentia large igneous province and Cardenas Basalt: pulsed magmatism during rapid late Mesoproterozoic plate motion</b>	<b>66</b>
4.1	Abstract . . . . .	66
4.2	Introduction . . . . .	67
4.3	Geological Background . . . . .	70
4.4	Methods . . . . .	76
4.5	Results and Interpretations . . . . .	79
4.6	Discussion . . . . .	83
4.7	Acknowledgments . . . . .	92
<b>5</b>	<b>Tracking Rodinia into the Neoproterozoic: new paleomagnetic constraints from the Jacobsville Formation</b>	<b>93</b>
5.1	Abstract . . . . .	93
5.2	Introduction . . . . .	94
5.3	Geologic setting . . . . .	96
5.4	Paleomagnetic results and interpretation . . . . .	101
5.5	Discussion . . . . .	108
5.6	Conclusion . . . . .	119
5.7	Acknowledgments . . . . .	120
	<b>Bibliography</b>	<b>121</b>
<b>A</b>	<b>Supporting Information for “Synchronous emplacement of the anorthosite xenolith-bearing Beaver River diabase and one of the largest lava flows on Earth”</b>	<b>161</b>
<b>B</b>	<b>Supporting Information for “High geomagnetic field intensity recorded by anorthosite xenoliths requires a strongly powered late Mesoproterozoic geodynamo”</b>	<b>171</b>
<b>C</b>	<b>Supporting Information for “Paleomagnetism of the southwestern Laurentia large igneous province and Cardenas Basalt: pulsed magmatism during rapid late Mesoproterozoic plate motion”</b>	<b>181</b>
<b>D</b>	<b>Supporting Information for “Tracking Rodinia into the Neoproterozoic: new paleomagnetic constraints from the Jacobsville Formation”</b>	<b>188</b>

# List of Figures

1.1	Overview of thesis study area and geochronology data . . . . .	3
1.2	The GAD hypothesis . . . . .	6
1.3	Schematic illustration of the IZZI paleointensity protocol . . . . .	10
1.4	The inclination shallowing problem in detrital remanent magnetization . . . . .	14
1.5	Summary paleomagnetic poles and associated paleogeography reconstruction for Laurentia and some of its conjugate continents through the late Mesoproterozoic to the early Neoproterozoic. . . . .	16
2.1	Simplified geologic map of the Midcontinent Rift and regional maps of the Beaver Bay Complex . . . . .	21
2.2	Field photographs and petrographic images of the Beaver River diabase and the anorthosite xenoliths . . . . .	24
2.3	Bar plot of ten of the world's most voluminous single mafic lava flows currently known. . . . .	25
2.4	$^{206}\text{Pb}/^{238}\text{U}$ zircon ages associated with the Beaver Bay Complex . . . . .	29
2.5	Cathodoluminescence (CL) image montage of the 15 zircons laser-ablated for trace element analysis from sample MS99033. . . . .	30
2.6	Rare earth element (REE) analyses for plagioclase crystals from anorthosite xenoliths and for 15 zircons from geochronology sample MS99033 . . . . .	31
2.7	Example orthogonal vector demagnetization diagrams for diabase and anorthosite specimens of the Beaver Bay Complex . . . . .	32
2.8	Summary equal area plots and paleomagnetic pole plots of the Beaver River diabase and anorthosite . . . . .	34
2.9	Thermal history model of the Beaver River diabase and its anorthosite xenoliths after emplacement at hypabyssal depths. . . . .	35
2.10	Zircon Pb and Dy diffusion modeling associated with sample MS99033 . . . . .	40
2.11	Box plots of geochemical analyses of olivine, pyroxene, and plagioclase in the Beaver River diabase (BRD) and Greenstone Flow (GSF). . . . .	42
2.12	Schematic illustration of the emplacement of the ca. 1096 Ma Duluth Complex, the ca. 1092 Ma Beaver Bay Complex, Greenstone Flow and associated anorthositic lithologies . . . . .	44
3.1	Simplified geologic map of the Lake Superior region . . . . .	48

3.2	Petrographic images and magnetic field maps of anorthosite samples from the Beaver Bay Complex and the Duluth Complex . . . . .	51
3.3	Example Arai plots of paleointensity experiment results from Beaver River diabase and anorthosite . . . . .	56
3.4	Summary paleointensity results from the Beaver River anorthosite xenoliths . .	57
3.5	Beaver River anorthosite xenoliths coercivity spectra and median destructive field (MDF) values associated with back-field demagnetization . . . . .	58
3.6	Compilation of geomagnetic virtual (axial) dipole moment estimates through Earth's history . . . . .	61
4.1	Overview of the inferred extent of the southwestern Laurentia large igneous province and compilation of high-precision zircon U-Pb geochronology data . . .	68
4.2	Simplified geologic maps of the Death Valley area and the Grand Canyon area .	71
4.3	Simplified regional stratigraphy in Death Valley and Grand Canyon . . . . .	73
4.4	Volcanostratigraphy of the Cardenas Basalt at Basalt Canyon, Lava Chuar Canyon, and Nankoweap Canyon . . . . .	75
4.5	Field photos of Cardenas Basalt . . . . .	77
4.6	Example orthogonal vector diagrams of specimen thermal demagnetization results of diabase intrusions in the Death Valley region and the Grand Canyon region .	81
4.7	Equal area diagrams for the site level directional results from the Death Valley region and the Grand Canyon region . . . . .	83
4.8	Pole positions of the Death Valley mafic sills, mafic intrusions in the Unkar Group, and the Cardenas Basalt . . . . .	85
4.9	Compilation of paleomagnetic data from central Arizona mafic sills . . . . .	87
5.1	Overview map of the Midcontinent Rift and the geologic map of the Jacobsville Formation and associated units . . . . .	95
5.2	Lithostratigraphy and magnetostratigraphy for studied sections of the Jacobsville Formation . . . . .	98
5.3	Field photos of the Jacobsville Formation. . . . .	99
5.4	Jacobsville Formation intraclast conglomerate test . . . . .	103
5.5	Jacobsville Formation fold test . . . . .	105
5.6	Summary figures for paleomagnetic results from the Jacobsville Formation . . .	107
5.7	Jacobsville Formation inclination shallowing correction . . . . .	111
5.8	Jacobsville Formation paleomagnetic pole position in context of the Keweenawan Track and the Grenville Loop . . . . .	116
5.9	Paleogeographic position of Laurentia through the late Mesoproterozoic to early Neoproterozoic . . . . .	118
A.1	Image of individual zircons used for ID-TIMS U-Pb geochronology from sample MS99033 . . . . .	163

A.2	U-Pb concordia plots for the new zircon dates from anorthosite xenoliths AX16, geochronology sample MS99033 . . . . .	164
A.3	Backscattered electron (BSE) images of anorthosite xenoliths. . . . .	166
A.4	Tilt correction analyses for the Beaver River diabase and anorthosite paleomagnetic data . . . . .	167
B.1	Beaver River anorthosite and diabase paleointensity estimates based on the Bi-CEP method . . . . .	172
B.2	Beaver River diabase and anorthosite low-temperature magnetic property measurement results . . . . .	173
B.3	Beaver River anorthosite cooling rate correction for paleointensity estimates . .	174
B.4	Plot of thermal remanent magnetization acquisition experiment results . . . .	175
B.5	Comparison between Beaver River anorthosite paleointensity results and compilation of the Cenozoic database . . . . .	176
B.6	Example coercivity spectra of anorthosite and diabase specimens . . . . .	177
C.1	Major element geochemical data of the Cardenas Basalt and diabase intrusions in the Unkar Group . . . . .	183
C.2	Paleomagnetic data of Cardenas Basalt lava flow site CB4 . . . . .	184
C.3	Paleomagnetic data of Cardenas Basalt lava flow site CB11 and the interflow sandstone site CBS1 below CB11 . . . . .	185
C.4	Death Valley diabase sill paleomagnetic tilt test . . . . .	186
C.5	Cardenas Basalt VGPs Fisher distribution test . . . . .	187
C.6	Trace element geochemistry data of the Cardenas Basalt and the Hance sill . .	187
D.1	Petrographic images of the fine-grained sandstone facies of the Jacobsville Formation . . . . .	188
D.2	Representative orthogonal vector diagrams of demagnetization experiments for specimens from different stratigraphic sections of the Jacobsville Formation . . .	189
D.3	Jacobsville Formation present day local field component . . . . .	191
D.4	Paleomagnetic fold test at the Snake Creek tributary of the Jacobsville Formation	192
D.5	Paleomagnetic reversal test of the Jacobsville detrital remanent magnetization .	193
D.6	Jacobsville Formation chemical remanent magnetization . . . . .	194
D.7	Jacobsville detrital remanence pole position in context of Laurentia's paleomagnetic poles during the Appalachian orogeny (ca. 460-260 Ma) . . . . .	195
D.8	Monte Carlo simulations of apparent polar wander rates implied by paleomagnetic and geochronologic data between the Nonesuch Formation and the Jacobsville Formation . . . . .	196

# List of Tables

2.1	Summary of new site level paleomagnetic data for the Beaver River diabase and anorthosite xenoliths . . . . .	36
4.1	Site-level paleomagnetic data from mafic sills in Death Valley, Cardenas Basalt, and mafic intrusions in the Unkar Group . . . . .	80
5.1	Kent mean paleomagnetic pole for the Jacobsville Formation . . . . .	110
A.1	Summary of anorthosite xenolith dimensions and their approximate distance from the closest diabase site. . . . .	162
B.1	Specimen paleointensity results that passed our selection . . . . .	178
B.2	Summary statistics for the $Q_{PI}$ quality criteria of Biggin and Paterson (2014) .	179
B.3	Summary paleointensity result statistics at site-level, region-level, and overall arithmetic mean . . . . .	180
C.1	Compilation of paleomagnetic data developed from mafic sills in central Arizona by Harlan (1993) and Donadini et al. (2011) . . . . .	182
D.1	Compilation of Laurentian paleomagnetic poles . . . . .	190

# Preface

The material within the chapters 2, 3, and 4 of this dissertation are from previously published articles. Chapter 5 has been submitted for publication and is in revision as of April 2024. The following text identifies these articles, and provides brief summaries of each chapter.

## **Chapter 2 - Synchronous emplacement of the anorthosite xenolith-bearing Beaver River diabase and one of the largest lava flows on Earth**

Zhang, Y., Swanson-Hysell, N.L., Schmitz, M.D., Miller Jr., J.D., and Avery, M.S., (2021), Synchronous emplacement of the anorthosite xenolith-bearing Beaver River diabase and one of the largest lava flows on Earth. *Geochemistry, Geophysics, Geosystems*. doi: [10.1029/2021GC009909](https://doi.org/10.1029/2021GC009909)

While magmatic activity within the 1.1 Ga North American Midcontinent Rift was protracted, it was punctuated by rapid pulses of voluminous events. One of these pulses is the massive *ca.* 1096 Ma Duluth Complex while another is the *ca.* 1092 Ma Beaver Bay Complex. A remarkable aspect of the Midcontinent Rift compared to most large igneous provinces is the extensive exposure both of extrusive lava flows and intrusive suites. Typically, in a large igneous province one sees either the continental flood basalts (with the intrusions still in the subsurface) or the intrusions (with the extrusive flows having been eroded away). The exposure of both intrusive and extrusive units provides opportunities to more fully characterize the magmatic system and establish linkages. In this study, I developed paleomagnetic directional data from anorthosite xenoliths and their diabase host of the Beaver Bay Complex, and collaborated with Professor Mark Schmitz and Professor Jim Miller to use paleomagnetic data, geochronology data, and geochemistry data to establish such an intrusive-extrusive connection. We show evidence that the anorthosite-bearing Beaver River diabase outcropping in northeastern Minnesota acted as a feeder system for the Greenstone Flow — one of the largest single mafic lava flows on Earth.

The Beaver River diabase contains abundant anorthosite xenoliths liberated from a lower crustal cumulate. These xenoliths can exceed 150 meters which illuminates the large magma transfer enabled by wide conduits as magma transited to the near-surface and erupted into the rift basin. Thermal history modeling, U-Pb geochronology and paleomagnetic data from

these anorthosite xenoliths give insights into their origin and history. Overall, we highlight that the rapid emplacement of the intrusive Beaver River diabase, anorthosite xenoliths therein, and the extrusive Greenstone Flow together punctuate an episode of rapid and voluminous magmatic activity *ca.* 1092 Ma during Midcontinent Rift development.

Data and code used in this article are available on GitHub at [https://github.com/Swanson-Hysell-Group/2021\\_AX\\_BD](https://github.com/Swanson-Hysell-Group/2021_AX_BD) and on Zenodo at <https://zenodo.org/records/5394529>.

### **Chapter 3 - High geomagnetic field intensity recorded by anorthosite xenoliths requires a strongly powered late Mesoproterozoic geodynamo**

Zhang, Y., Swanson-Hysell, N.L., Avery, M.S., Fu, R.R., (2022), High geomagnetic field intensity recorded by anorthosite xenoliths requires a strongly powered late Mesoproterozoic geodynamo. PNAS. doi: 10.1073/pnas.2202875119

Acquiring high-fidelity observational records of ancient magnetic field intensity from the remanent magnetization of rocks is crucial for constraining the long-term evolution of Earth's core. However, robust estimates of ancient field strengths are often difficult to recover due to alteration or non-ideal rock magnetic behavior. In this contribution, I developed high-quality paleointensity data with the best site-level standard deviation of  $0.04 \mu\text{T}$  from well-preserved anorthosite xenoliths of the Beaver River diabase which were rapidly emplaced within the *ca.* 1.1 Ga North America Midcontinent Rift. The primary interpretation for the high paleointensity values gains strong support for there being a strongly powered geodynamo during the late Mesoproterozoic. These observations agree with previous results from Midcontinent Rift volcanic rocks and support that such a strong field could have lasted at least 14 Myr. Together, paleointensity records from the Midcontinent Rift are inconsistent with there being a progressive monotonic decay of Earth's dynamo strength through the Proterozoic Eon. Our updated paleointensity data compilation show multiple observed paleointensity transitions from weak to strong in the Phanerozoic and the Proterozoic. Given that these records cannot all be the minimum prior to the beginning of inner core nucleation, they instead could indicate that processes such as plate tectonics could have modulated the core-mantle heat flow pattern in the Proterozoic with resulting fluctuation in field strength. Regardless of when the initiation of inner core nucleation occurred, the observation of large variability in paleointensity in the Precambrian may present challenges in detecting the increase in surface geomagnetic field strength that could have occurred at the onset of inner core crystallization.

Data and code used in this article are available on GitHub at [https://github.com/Swanson-Hysell-Group/AX\\_BD\\_PINT](https://github.com/Swanson-Hysell-Group/AX_BD_PINT) and on Zenodo at <https://doi.org/10.5281/zenodo.6658064>.

## **Chapter 4 - Paleomagnetism of the southwest Laurentia large igneous province and Cardenas Basalt: pulsed magmatism during rapid late Mesoproterozoic plate motion**

Mohr, M.T., Schmitz, M.D., Swanson-Hysell, N.L., Karlstrom, K.E., Macdonald, F.A., Holland, M.E., Zhang, Y., Anderson, N. (2024). High-Precision U-Pb geochronology links magmatism in the SW Laurentia Large Igneous Province and Midcontinent Rift. *Geology*. doi: 10.1130/g51786.1

Zhang, Y., Anderson, N., Mohr, M.T., Schmitz, M.D., Macdonald, F.A., Nelson, L.L., Thurston, O.G. Guenthner, W.R., Karlstrom, K.E., Swanson-Hysell, N.L. (in review). Widespread mafic magmatism across Laurentia in the late Mesoproterozoic: new paleomagnetic data from southwestern Laurentia. Submitted to JGR: Solid Earth.

High-precision geochronology data show that the emplacement of the ca. 1096 Ma voluminous mafic Duluth Complex and associated ~ 8 km thick lava flows of the North Shore Volcanic Group occurred within 500 Kyr—consistent with these units being a large igneous province. In Mohr et al. (2024), we use high-precision geochronology data from the southwestern part of the ancient North American craton, Laurentia, to show that there was a ca. 1098 Ma pulse of large-igneous-province style mafic magmatism featuring the emplacement of thick mafic sills across at least eastern California and central Arizona. Geochronology data from that work further show that the Cardenas Basalt lava flows which previously were thought to be surface expressions of the ca. 1098 Ma mafic sills, are actually ca. 1082 Ma in age. This indicates that they occurred during a distinct magmatic episode in the Grand Canyon. In this study, I develop new paleomagnetic data from mafic sills in Death Valley along with undergraduate mentee Nick Anderson, and I developed new paleomagnetic data from mafic intrusions and the Cardenas Basalt in the Grand Canyon. These new data help better delineate the extent of the ca. 1098 Ma southwestern Laurentia large igneous province.

Prior to this work, late Mesoproterozoic global paleogeography reconstructions largely depend on data from the Midcontinent Rift. New paleomagnetic data from this study provide independent support for there being a large latitudinal change in Laurentia's paleogeographic position at the time due to rapid plate tectonic motion. The new paleomagnetic pole from the Cardenas Basalt help further improve Laurentia's apparent polar wander path in the late Mesoproterozoic.

Data and code used in this study are available on GitHub at [https://github.com/Swanson-Hysell-Group/2024\\_SWLLIP](https://github.com/Swanson-Hysell-Group/2024_SWLLIP) and on Zenodo at <https://doi.org/10.5281/zenodo>.

## Chapter 5 - Tracking Rodinia into the Neoproterozoic: new paleomagnetic constraints from the Jacobsville Formation

Zhang, Y., Hodgin, E.B., Mohr, M.T., Alemu, T.B., Pierce, J., Fuentes, A.J., Swanson-Hysell, N.L. (2024). Tracking Rodinia into the Neoproterozoic: new paleomagnetic constraints from the Jacobsville Formation. *Tectonics*. doi: 10.1029/2023TC007866

The assembly of the supercontinent Rodinia in the late Proterozoic is a pivotal event in the history of global tectonics. However, there has been a lack of well-dated paleomagnetic poles for its central piece, Laurentia, for 300 Myr between the onset of the assembly ca. 1070 Ma and the initial break up of the supercontinent ca. 770 Ma. In this study, I develop high-quality paleomagnetic data from the Jacobsville Formation and pair them with previously developed state-of-the-art geochronology results to constrain cratonic North America's paleogeographic position ca. 990 Ma. High-resolution thermal demagnetization experiments on the siltstone and fine-grained sandstone facies of the Jacobsville Formation resulted in successful isolation of the primary detrital magnetization from the secondary overprints. The primary interpretation for the detrital paleomagnetic pole gains support from both an intraformational conglomerate test and a fold test.

Using the statistical method that we developed in the study of Pierce et al. (2022), we were able to quantitatively represent the uncertainties associated with the inclination shallowing issue in the Jacobsville paleomagnetic records. Our new high-quality paleomagnetic pole shows Laurentia's plate motion to have slowed down significantly following a previous period of rapid plate tectonic motion in the late Mesoproterozoic. Such slowdown in plate motion is coincident with continent-continent collision along Laurentia's margin associated with the Grenvillian orogeny. This result ties in with the geodynamics of the orogeny and supercontinent assembly. The new pole adds a reliable constraint in the early Neoproterozoic that will be at the heart of future efforts to reconstruct the paleogeography of Rodinia.

Data and code used in this study are available on GitHub at <https://github.com/Swanson-Hysell-Group/Jacobsville> and on Zenodo at <https://doi.org/10.5281/zenodo>.

## Acknowledgments

I thank my parents for supporting my study abroad in the past eight years. It is a privilege to be able to experience both the oriental and occidental lives, and to find my own identity through studying and traveling.

I thank my Ph.D. advisor, Nicholas Swanson-Hysell for admitting me as a student. I always look up to him as a role model in academia and life. His adept field geology skills, broad scientific interests and rigorous science ethics constantly challenged me to be a better scholar. I thank Nick for providing many field work opportunities around the globe in the past five years. I especially appreciate that Nick kept his office door open and allowed numerous walk-in discussions. I am also grateful for the company in the field and lab from Nick's family. I have always enjoyed my time in the field together with Sarah, Maddy, and Wilma.

I thank Scott Bogue and Margi Rusmore, my research advisors at Occidental College for their encouragement and support throughout this journey of graduate study. I treasure our meetings at Santa Cruz and Los Angeles in the past five years.

I thank my qualification exam committee, including Professor Ben Gilbert, Professor Harriet Lau, and Professor Fernando Perez for providing guidance in the first two years of Ph.D. I thank Professor Bruce Buffett and Professor Seth Finnegan for being on my thesis committee and helping me improve this dissertation.

I thank my advisors for the courses where I taught as a graduate student instructor. I learned a lot about Berkeley local bedrock geology by teaching EPS 101 Field Geology and Digital Mapping with Nick and Professor Matt Gleeson. The special 2020 COVID edition of video shooting the field geology class with Nick will be a life-long memory. I thank Daniel Stolper for his guidance during the EPS 50 course in Spring 2021. Engaging with undergraduate students through EPS 50 lab sessions helped me stay positive and enthusiastic while the world was in a lockdown.

I thank John Grimsich for providing me with hands-on experiences on many excellent instruments hosted at Berkeley EPS. I am grateful for the countless hours that John spent teaching me to make professional petrographic thin sections, tuning and using scanning electron microscopes, using the X-ray diffraction machine, and crafting custom-build research equipment. I also treasure our occasional geology hikes in the Bay Area.

I am grateful to the organizations whose funding enabled the research during my graduate course. The funding sources include:

- University of California, Berkeley
  - Hearts to Humanity Eternal Graduate Research Grant
  - Cheveron-Xenel Gateway Fellowship, Berkeley International House
  - UC Berkeley student conference travel grant

- Institute for Rock magnetism
  - US visiting student fellowship
- Institute on Lake Superior Geology
  - ILSG Student Research Fund
- Geological Society of America
  - 2022 GSA Graduate Student Research Grant
  - 2023 AGeS3-Grad Geochronology Award
- National Science Foundation
  - 2023 AGeS3-Grad Geochronology Award
  - NSF Tectonics CAREER grant EAR-1847277 (awarded to Nick Swanson-Hysell)
  - NSF Frontier Research in Earth Science (FRES) grant EAR-1925990 (awarded to Nick Swanson-Hysell)

I thank the earth, for being such a beautiful cosmic palimpsest.

# Chapter 1

## Introduction

The major tool I use throughout this dissertation is magnetism. While the ongoing evolution of electromagnetism continues to shape our future, the study of paleomagnetism harnesses the same theoretical framework to delve into the past, by scrutinizing minuscule magnetic minerals embedded within rocks. Just as a compass needle tends to align with Earth's predominantly dipolar magnetic field, the microscopic compasses in rocks—magnetic minerals such as iron-titanium oxides tend to align with Earth's field during cooling through critical temperatures or settling through water columns. These minerals, abundantly present in igneous, sedimentary, and metamorphic rocks, serve as microscopic guides into our planet's history.

In this dissertation, I apply paleomagnetism to reconstruct late Proterozoic magmatism, geomagnetic field behavior, and paleogeography. In chapter 2, I develop paleomagnetic directional data and pair them with geochemical, geochronological, and petrographic data to study the characteristics of mafic magmatism associated with the emplacement of the 1.1 billion-year-old anorthosite xenolith-bearing Beaver River diabase and the extrusive Greenstone lava flow. In chapter 3, I develop paleointensity data from anorthosite xenoliths of the Beaver River diabase to gain insight into the strength of the geodynamo at the time. In chapter 4, I develop paleomagnetic directional data from 1.1 billion-year-old mafic intrusions and lava flows in the Death Valley and the Grand Canyon to interrogate the extent of the southwestern Laurentia large igneous province and its temporal-magmatic relationship with the Midcontinent Rift. In chapter 5, I develop paleomagnetic directional data from the Neoproterozoic Jacobsville Formation to constrain global paleogeography during the assembly of the supercontinent Rodinia.

## 1.1 Late Mesoproterozoic magmatism in the Midcontinent Rift and the southwestern Laurentia large igneous province

The ancient North American craton, Laurentia, first formed in the Paleoproterozoic Era when a series of collisional orogenies culminating the Trans-Hudson orogeny led to the amalgamation of Archean provinces (Hoffman, 1988; Whitmeyer, 2007). The craton continued to grow through the rest of the Paleoproterozoic and into the Mesoproterozoic via accretionary orogenesis along its margin. In the latest Mesoproterozoic (ca. 1109 to 1083 Ma), the large intracontinental Midcontinent Rift (Fig. 1.1), which was co-located with a large igneous province (LIP) (Swanson-Hysell et al., 2021b) led to extension within the Archean Superior province and adjacent Paleoproterozoic provinces to the south (Cannon, 1992). Magmatic activities punctuated by rapid and voluminous emplacement of extrusive and intrusive rocks in the rift led to the emplacement of a thick succession of volcanic rocks and associated mafic intrusions in Laurentia's interior. Syn- to post-rift thermal subsidence led to deposition of clastic sedimentary rocks on top of the igneous rocks.

The Midcontinent Rift eventually failed to split the continent into two. Far-field compressional forces associated with the onset and development of the Grenvillian orogeny along the eastern margin of Laurentia led to cessation and subsequent inversion of the rift (Cannon et al., 1993; Swanson-Hysell et al., 2019b). In the southern Lake Superior region, Midcontinent Rift volcanic and sedimentary rocks were uplifted along with Paleoproterozoic and Archean lithologies via thrust faults, forming the crustal-scale Montreal River monocline (Cannon et al., 1993). The resultant topography led to erosion that was followed by the deposition of the early Neoproterozoic Jacobsville Formation (Hamblin, 1958; Kalliokoski, 1982; Hodgin et al., 2022), which overlies an angular unconformity that developed on lithologies that were exhumed through this earlier episode of contractional deformation associated with Grenvillian orogenesis.

The intracontinental nature of the rift and its cessation led to a large amount of rift rocks being preserved in the interior of Laurentia far from continental margins. Rocks in the rift subsequently experienced mild burial and metamorphism history. Thermochronology data from the uplifted basement rocks and the intrusive rocks in the Lake Superior region show that the area has had mild thermal history since ca. 1050 Ma (Cannon et al., 1993; Härtel et al., 2023).  $^{10}\text{Be}$  data show that some surface bedrock exposures have only recently been near the surface due to Pleistocene glacial and recent fluvial erosion (e.g. Ullman et al., 2015).

The well-preserved Midcontinent Rift rocks provide a wealth of opportunities for characterizing the magmatic history of Laurentia at the time. Geochronology and geochemistry data have been used to group magmatic activities in the rift into four stages based on interpreted changes in relative magmatic volume and the nature of magmatism: early (~1109–1104 Ma), latent (~1104–1098 Ma), main (~1098–1090 Ma) and late (~1090–1083 Ma) (Vervoort et al., 2007; Heaman et al., 2007; Miller and Nicholson, 2013). In recent

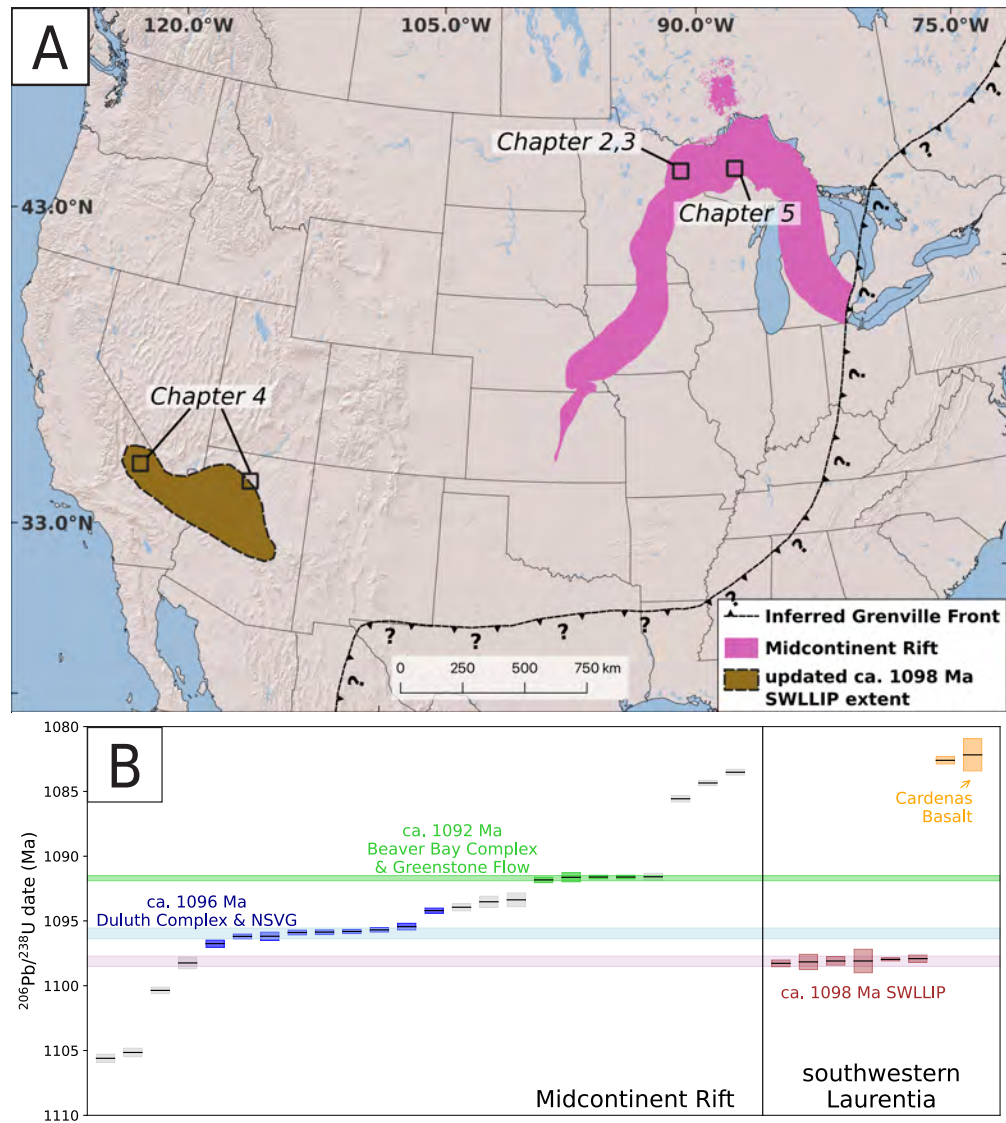


**Figure 1.1:** (A) Simplified map of North America showing the extent of the 1.1 Ga Midcontinent Rift (purple) and the inferred extent of the southwestern Laurentia large igneous province (SWLLIP) based on available high-precision geochronology data. The inset boxes show the areas of study of the dissertation chapters. Inferred trace of the Grenville Front is shown as dashed thrust fault line with question marks and ticks on the hanging wall. (B) Compilation of chemical abrasion-isotope dilution-thermal ionization mass spectrometry (CA-ID-TIMS) zircon U-Pb geochronology data from the Midcontinent Rift and southwestern Laurentia. Data are from Fairchild et al. (2017); Swanson-Hysell et al. (2014b, 2019b); Mohr et al. (2024). The colored zones represent the estimated duration of the pulsed and voluminous magmatic events in Laurentia ca. 1.1 Ga.

decades, the development of the chemical abrasion-isotope dilution-thermal ionization mass spectroscopy (CA-ID-TIMS) enabled high-precision determination of zircon U-Pb ages in

deep time. In the Midcontinent Rift, these data have been combined with high-quality paleomagnetic data from the extrusive and intrusive rocks. The data show that Laurentia experienced rapid plate tectonic motion with a speed that reached up to  $\sim$ 30 cm/yr during the development of the Midcontinent Rift (Swanson-Hysell et al., 2019b; Rose et al., 2022). These data also show distinct rapid and voluminous episodes of magmatism in the rift during the overall protracted period of magmatic activities that lasted  $\sim$ 25 Myr (Swanson-Hysell et al., 2019b, 2021b; Zhang et al., 2021). In particular, a large igneous province, consisting of the massive mafic intrusions of the Duluth Complex and associated  $\sim$ 8 km thick extrusive lava flows of the North Shore Volcanic Group, formed within 500 Kyr ca. 1096 Ma (Swanson-Hysell et al., 2021b). Stratigraphically above the Duluth Complex, the ca. 1092 Ma mafic Beaver Bay Complex represents another rapid and voluminous pulse of magmatism. It features the emplacement of the hypabyssal intrusions of the Beaver River diabase that has wide magma conduits containing large anorthosite xenoliths that can be as much as 300 meters wide. Unlike the Duluth Complex and the North Shore Volcanic Group, whose magmatic linkage is supported by the exposed stratigraphic relationships and geochronologic data, there is no volcanic rocks that overlie conformably on top of the Beaver River diabase. Previously, on the basis of geochemical data and petrographic observations, a hypothesis was put forward that the Greenstone Flow of the Portage Lake Volcanics that outcrop in the upper Keweenaw Peninsula in Michigan could be the surface expression of the Beaver River diabase (Doyle, 2016). In chapter 2, I test this hypothesis by using paleomagnetic and geochronologic data to investigate the synchronicity of the emplacement of the intrusive and extrusive rocks (Fig. 1.1). The data support that the Beaver River diabase was the feeder system for the  $\sim$ 400 meters thick Greenstone Flow which ranks one of the largest lava flows known on Earth. In chapter 3, I utilize the exceptionally well-preserved anorthosite xenoliths hosted in the Beaver River diabase to shed new light on the strength of Earth's geodynamo in the late Mesoproterozoic.

While rapid and voluminous mafic magmatism occurred in the Midcontinent Rift, CA-ID-TIMS zircon U-Pb geochronologic data and paleomagnetic data show that distinct episodes of mafic magmatism occurred in southwestern Laurentia ca. 1098 Ma and ca. 1082 Ma (Fig. 1.1; Mohr et al., 2024). During a period of  $<0.25$  Myr ca. 1098 Ma, thick diabase sills and dikes intruded into the crystalline basement rocks and Mesoproterozoic sedimentary rocks in southwestern Laurentia. The Mesoproterozoic sedimentary successions that contain these intrusions include the Crystal Spring Formation in the Death Valley, Unkar Group sedimentary rocks in the Grand Canyon, and the Apache Group sedimentary rocks in central Arizona (Bright et al., 2014). The tempo and extent of the ca. 1098 Ma episode of mafic magmatism (Mohr et al., 2024), together with their juvenile geochemical signatures (Hammond and Wooden, 1990; Bright et al., 2014) are interpreted to be consistent with them being driven by an upwelling mantle plume. That the emplacement of the voluminous intrusions in the southwest occurred 2 Myr prior to the Duluth Complex led Mohr et al. (2024) to invoke a model where a mantle plume first arrived ca. 1098 Ma in southwestern Laurentia and laterally advected toward the thinned crust of the Midcontinent Rift. That study posits that the arrival of the plume material in the rift postdates the latent magmatic

stage ( $\sim$ 1104–1098 Ma) and led to a replenishment of mafic magma and heat supply in the rift, which eventually drove the emplacement of the ca. 1096 Ma Duluth Complex and the associated lava flows of the North Shore Volcanic Group. In chapter 4, I update the extent of the southwestern Laurentia large igneous province by developing new paleomagnetic data that are paired with new high-precision geochronology data from Mohr et al. (2024) and by developing additional paleomagnetic data from undated mafic units.

As the Grenvillian orogeny commenced along Laurentia’s eastern margin, Laurentia’s plate speed slowed down and magmatism in Laurentia waned (Swanson-Hysell et al., 2019b). The orogenesis also led to the assembly of the supercontinent Rodinia (Swanson-Hysell et al., 2023). However, there is lack of well-dated paleomagnetic data from Laurentia for constraining global paleogeography between the end of the Mesoproterozoic and the late Tonian (ca. 1050 Ma and ca. 775 Ma; Swanson-Hysell et al., 2023; Eyster et al., 2019). With new geochronologic data that constrain the depositional age of the Jacobsville Formation to be ca. 990 Ma (Hodgin et al., 2022), in chapter 5, I develop new paleomagnetic data from the Jacobsville Formation in a detailed stratigraphic context and provide a first robust anchor for global paleogeography in the earliest Neoproterozoic.

## The GAD hypothesis in the late Proterozoic

Earth’s magnetic field today is dominated by the dipole component (Alken et al., 2021). It is the working hypothesis that the time-averaged Earth’s surface magnetic field approximates a geocentric axial dipole (GAD)—one consistent with being produced by a single magnetic dipole at the center of the Earth and aligned with the rotation axis that grants power to paleomagnetic interpretations (Fig. 1.2). In the GAD model, an observation of an inclination of magnetization ( $I$ ) uniquely corresponds to a latitude value ( $\lambda$ ) (Fig. 1.2). This relationship is expressed in the “dipole equation”

$$\tan(I) = 2\tan(\lambda)$$

The GAD hypothesis also empowers paleomagnetic field intensity observations in that there is a correlation between an observed field strength at a latitude and the axial dipole moment (Fig. 1.2), which is expressed as

$$H = \frac{M\sqrt{1 + 3\cos^2\theta}}{r^3}$$

Where  $H$  is the observed magnetic field intensity,  $M$  is the magnetic moment of Earth,  $\theta$  is colatitude where  $\theta = 90 - \lambda$ , and  $r$  is Earth’s radius.

Effective ways of testing the robustness of the GAD hypothesis through time include comparing observed latitudinal dependence of paleomagnetic inclination data and intensity data with those predicted by the dipole equations. In addition, the symmetry of paleomagnetic reversals also provides insights into the dipolarity of the field. A geomagnetic field with a

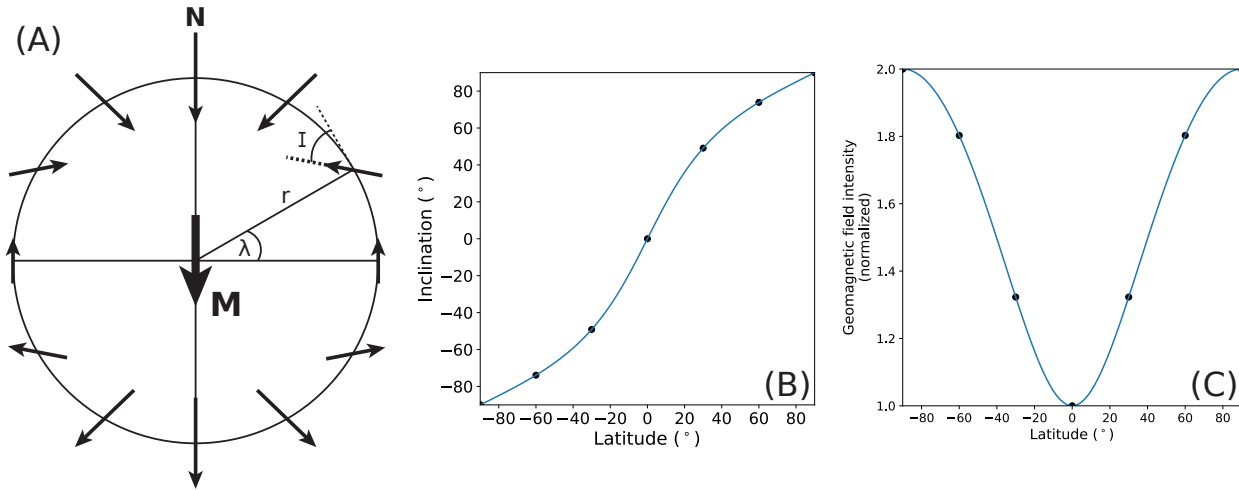


**Figure 1.2:** (A) Geocentric axial dipole model. Magnetic dipole  $M$  is placed at the center of the Earth and aligned with the spin axis; the geographic latitude is  $\lambda$ ; the mean Earth radius is  $r$ ; the magnetic field directions and relative intensities at Earth's surface produced by the geocentric axial dipole are schematically shown by the arrows; inclination,  $I$ , is shown for one location;  $N$  is the geographic north pole. Modified after McElhinny (1973). (B) Correlation between magnetic field inclination and latitude of a dipolar magnetic field. (C) Correlation between latitude and normalized magnetic field intensity produced by a dipolar magnetic field. The intensities are normalized by the field at the equator.

non-dipolar component that does not reverse and a reversing dipolar component with minor contributions would have asymmetric reversals (e.g. Pesonen and Nevanlinna, 1981; Pesonen and Halls, 1983). It has been demonstrated that the GAD hypothesis is robust for the past 10,000 years on the basis of global compilations of archeological sites and sediments (e.g. McElhinny et al., 1996). For the past 5 million years, compilations of paleomagnetic data are best described with a GAD-dominated field with minor persistent contributions from non-dipole components (1-5 %; Tauxe, 2005; Valet and Herrero-Bervera, 2011). Statistical analyses of compilations of the relatively abundant paleomagnetic directional and intensity data further back in time show that Earth's magnetic field has been compatible with being GAD-dominated throughout the Phanerozoic (Evans, 1976; Lhuillier et al., 2023). The use of paleomagnetic data under the GAD assumption lies at the core of reconstructing past plate tectonic configurations (Creer et al., 1954; Irving, 1977; Besse and Courtillot, 2002; Torsvik et al., 2012). The GAD model gains support in the Phanerozoic in that the reconstructed plate motions are smooth with rates typically  $<20$  cm/y (Torsvik et al., 2012). Such results are independently verified by marine magnetic anomalies and hotspot tracks since the mid-Mesozoic (Doubrovine et al., 2012; Müller et al., 1993).

However, some Precambrian paleomagnetic observations challenge the uniformitarianism of a dipolar geomagnetic field through deeper time. There is increasing evidence that suggest Earth's magnetic field in the Ediacaran may not be GAD-dominated. Anomalously rapid changes in paleomagnetic field directions have been found in Ediacaran rocks from a variety

of localities (e.g. Abrajevitch and Van der Voo, 2010; Meert, 2014; Halls et al., 2015). Magnetostратigraphy data developed by Kodama (2021) show the Ediacaran Johnnie Formation records anomalously frequent reversals ( $\sim 13$  per Myr). A series of low paleointensity values have been obtained primarily using single silicate crystals (i.e. dominantly monomineralic crystal aggregates) from Ediacaran rocks (Bono et al., 2019; Thallner et al., 2021a,b). These data have led to a hypothesis that Earth's magnetic field was not GAD-dominated in the Ediacaran Period. Some have posited that the very low paleointensity observations in the Ediacaran indicate a time when the strength of the geodynamo reached its minimum prior to a recovery brought by the onset of inner core nucleation (e.g. Bono et al., 2019). Today, the characteristics of the geodynamo in the Ediacaran remain enigmatic, and the mechanism for the anomalous directional and intensity data remains debated (Domeier et al., 2023).

In the Proterozoic, it had also been previously hypothesized that non-dipole components dominated the geomagnetic field (e.g. Pesonen and Nevanlinna, 1981; Sears, 2022). Prior to the development of high-precision geochronology data that are paired with detailed paleomagnetic data within a volcanostratigraphic context in the Midcontinent Rift became available, the apparent asymmetry in paleomagnetic field reversal records in the Midcontinent Rift rocks led the literature (e.g. Halls and Pesonen, 1982; Pesonen and Nevanlinna, 1981) to interpret there being a significant non-GAD field component in the late Mesoproterozoic. However, high-resolution paleomagnetic data that span three geomagnetic field reversals in a stratigraphic context show each reversal was symmetric (Swanson-Hysell et al., 2009). Since that work, more data and sophisticated statistical analyses have further clarified that the paleomagnetic pole progression recorded by rocks of the Midcontinent Rift most likely represent a period of rapid plate tectonic motion of Laurentia (Swanson-Hysell et al., 2019b; Rose et al., 2022). Nonuniformitarian events such as there being significant non-GAD geomagnetic field components or significant and rapid true polar wander event need not be invoked in the late Mesoproterozoic.

Additional statistical analyses also show that the late Proterozoic geomagnetic field is consistent with being dipole-dominated. Tauxe and Kodama (2009) show that the shape of the distribution of the paleomagnetic directional data recorded by lava flows of the North Shore Volcanic Group in the Midcontinent Rift is consistent with that of a dipole-dominated field model for the past 5 million years (model TK03 of Tauxe and Kent, 2004). My collaborative work with Pierce et al. (2022) also show that correcting the inclination shallowing of syn-rift hematite-bearing sedimentary rocks of the Cut Face Creek Sandstone based on the geomagnetic field model of TK03 results in a mean direction that agrees with that recorded by the volcanic rocks that bracket the sedimentary rocks. These analyses support the interpretation that the geomagnetic field ca. 1.1 Ga was consistent with being dipole-dominated and had a secular variation pattern similar to that of recent geologic times. In addition, the analyses of Gong et al. (2023) show that the available paleomagnetic directional observations across Laurentia in the Proterozoic can be better fit with a dipole than a quadrupole configuration. Overall, the increasingly rich paleomagnetic directional and intensity data in the Proterozoic have been adding further support for there being a GAD-dominated geomagnetic field throughout much of the Proterozoic Eon (Veikkolainen et al., 2014a; Salminen et al.,

2017; Veikkolainen and Pesonen, 2021).

With confidence in the GAD-dominated field in the Mesoproterozoic, we can utilize paleomagnetic directional data to explore temporal associations between rock units. In chapter 3 I develop new paleomagnetic data from the ca. 1092 Ma Beaver River diabase and compare their pole position to that of the Greenstone Flow of the Portage Lake Volcanics. The agreement between the pole positions between the extrusive and intrusive rocks indicate a close temporal linkage and support a magmatic linkage between the two units. In chapter 4, I develop new paleomagnetic data from mafic intrusive and extrusive rocks in southwestern Laurentia and investigate the extent of the southwestern large igneous province as well as its temporal and magmatic relationship with the Duluth Complex. These new data add to the existing paleomagnetic database for Laurentia for the reconstruction of the Keweenawan Track—the late Mesoproterozoic apparent polar wander path which is central to the global paleogeographic reconstruction leading up to the assembly of the Rodinia supercontinent.

## 1.2 Probing the evolution of Earth’s interior via paleointensity observations

Earth’s magnetic field is powered by convective flow of liquid iron-alloy in Earth’s outer core. At present day, the geodynamo is collectively driven by heat flow across the core-mantle boundary and from the crystallization of the solid inner core from the liquid outer core which provides latent heat and compositional buoyancy due to the exclusion of light elements (Buffett, 2000). The global entropy balance for the convective core that relates the Ohmic dissipation to thermal and compositional convection show that the compositional convection is more efficient in maintaining the current energy dissipation (Labrosse, 2003; Landeau et al., 2022). A question thus arises regarding whether Earth has had an inner core since the beginning of its formation, and if not, when did the inner core begin to nucleate. Theoretical calculations show large uncertainties associated with the predicted timing of the inner core nucleation (e.g. Buffett, 2003; Pozzo et al., 2012; Nimmo and Schubert, 2015) due to the lack of constraints including the thermal conductivity of the core (Gubbins et al., 2004; Konôpková et al., 2016; Ohta et al., 2016). Such uncertainties remain until further constraints on the core composition and agreements on experimental results of thermal conductivity values of iron-alloy at Earth’s core conditions become available in the literature.

Paleomagnetic observations provide a unique tool that can provide constraints on the thermal evolution of Earth’s core. Based on paleomagnetic directional and intensity data, we know that an active dynamo has existed since ca. 3.5 Ga (Selkin et al., 2007; Biggin et al., 2011; Tarduno et al., 2014; Brenner et al., 2020, 2022) and probably earlier (Tarduno et al., 2015). Some theory and modeling predict that the nucleation of the inner core should produce a notable increase in the efficiency of convection in the outer core such that a notable increase in the surface geomagnetic field intensity may be reflected in the paleomagnetic intensity records (e.g. Labrosse, 2003; Aubert et al., 2009; Driscoll, 2016; Landeau et al.,

2022).

Absolute paleointensity experiments are used to reconstruct records of past absolute geomagnetic field intensity from thermoremanent magnetizations based on the linear dependence of acquired intensity of thermal remanence on the external magnetic field strength. Based on the single domain thermal remanence magnetization blocking theory of Néel (1955), the following equation for the acquisition of thermal remanence magnetization (TRM) of a population of identical single-domain ferromagnetic grains when cooling in a constant magnetic field ( $H$ ) from the blocking temperature ( $T_B$ ) to ambient temperature ( $T_0$ ) can be deduced:

$$TRM[T_0] = N[T_B]vj_s[T_0]\tanh\left(\frac{vj_s[T_B]H}{kT_B}\right)$$

where  $[T_0]$ ,  $[T_B]$  denote the temperature of the temperature-dependent parameters,  $N[T_B]$  represents the number of single-domain grains per unit volume with blocking temperature  $T_B$ ,  $v$  is the volume of the single domain grains,  $j_s$  is the saturation magnetization, and  $k$  is the Boltzmann constant. This equation assumes the grains block in the remanence magnetization sharply when cooling through the blocking temperature  $T_B$ . Typically the term  $\frac{vj_s[T_B]H}{kT_B}$  which measures the degree of alignment of the grains at the blocking temperature has a value  $<< 1$ . Therefore, equation 1.2 becomes

$$TRM[T_0] = AH$$

where  $A$  is a generalized proportionality constant. A rock sample that acquires a thermal remanent magnetization that follows this linear relationship with the magnetic field in which it cools would thus have a proportionality constant  $A$  which depicts both  $TRM_{paleo} = AH_{paleo}$  and  $TRM_{lab} = AH_{lab}$ , where  $H_{paleo}$  represents the ancient field and  $H_{lab}$  represents the lab field. Therefore, the paleointensity can be obtained by eliminating the proportionality constant,  $A$ , and

$$H_{paleo} = \frac{TRM_{paleo}}{TRM_{lab}} \times H_{lab}$$

With this theoretical basis, Thellier (1959) developed the experimental protocol known as the Thellier double-heating paleointensity method that features step-wise removal of the natural thermal remanence magnetization ( $TRM_{paleo}$ ) and imposition of new partial thermal remanence ( $TRM_{lab}$ ) in a known lab field through heating and cooling. This technique is based upon Thellier's laws, which state that partial thermal remanence (pTRM) must be additive, independent (partial remanence acquired between distinct temperature steps is distinct from one another) and reciprocal (the unblocking temperature is the same as the blocking temperature). The resultant comparison between a sample's capability of acquiring a TRM in the lab and its acquired TRM in nature can then be illustrated on the paleointensity plot first introduced by Arai (1963) (Fig. 1.3). In an ideal experiment with ideal magnetic recorders, the relationship between natural remanence lost and pTRM gained is linear, and the slope of the best-fit line to the data is proportional to the intensity of the ancient field (Fig. 1.3). Using this slope, and multiplying by the known lab field, one can calculate an

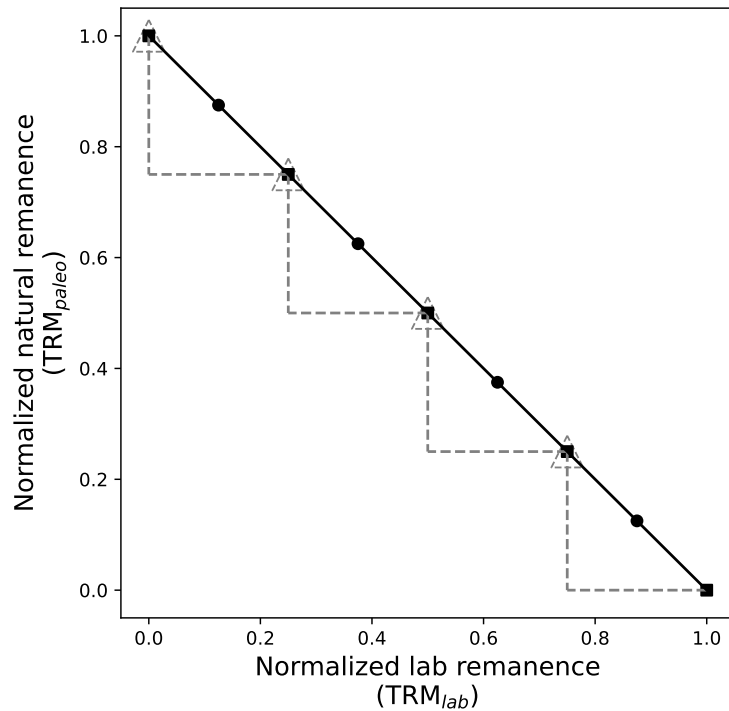


**Figure 1.3:** Schematic Thellier paleointensity diagram showing an ideal experimental results using the “in field-zero field-zero field-in field” paleointensity protocol developed by Yu et al. (2004). The squares and circles represent in field or zero field steps. Grey dashed lines and triangles illustrate the pTRM check steps where a repeat TRM acquisition step is performed to test for changes in a specimen’s ability to acquire TRM at blocking temperatures below the temperature of the check.

estimate of the ancient magnetic field strength. The Thellier method has subsequently been improved such that sample behaviors that diverge from being ideal single-domain described in the theory above can be better detected (e.g. Coe, 1967; Riisager and Riisager, 2001; Yu, 2003; Yu et al., 2004; Yu and Tauxe, 2006). Today, the “in field-zero field-zero field-in field” (IZZI) Thellier paleointensity protocol combined with result filtering based on a series of statistical selection criteria is one of the most robust and widely used heating-based absolute paleointensity methods (Yu et al., 2004).

With the GAD assumption, Earth’s (virtual) axial dipole moment can be calculated given known paleointensity and paleolatitude of a locality at a time. There are compilations of absolute paleointensity data that show Earth’s axial dipole moment through history (e.g. Veikkolainen et al., 2014b; Bono et al., 2022b). Based on a selected compilation, Bono et al. (2019) interpreted that the existing Precambrian paleointensity database shows a monotonic decay of the geomagnetic dipole moment throughout the Proterozoic. Together with their new data developed from silicate crystals of the ca. 565 Ma Sept-Îles mafic intrusions with the Thellier–Coe paleointensity method which were interpreted to show near-zero values, Bono et al. (2019) hypothesized that a geodynamo primarily driven by waning thermal

convection might have persisted through the Proterozoic until the nucleation of the inner core, which they interpreted to have happened in the Ediacaran. Bono et al. (2019) further argued that their results are consistent with modeling results using an approach combining dynamo simulations and theoretical scaling relationships that predicted that progressive decay of the field’s dipole moment would be followed by a rapid increase in geomagnetic field intensity soon after the onset of inner core nucleation such that a minimum in dipole moment would occur just before inner core nucleation (Driscoll, 2016).

However, the geodynamo evolution model put forward by Bono et al. (2019) was based on a sparse Precambrian paleointensity database and is challenged by more recent observations. Low paleointensity values similar to those in the Ediacaran have been observed in the Mesoproterozoic (Lloyd et al., 2021b; Shcherbakova et al., 2022, 2023), the Neoproterozoic (Lloyd et al., 2021a), the early-Cambrian (Lloyd et al., 2022), and the Paleozoic (Shcherbakova et al., 2021). These new data challenge the uniqueness of the Ediacaran weak geodynamo. In chapter 3, I develop new paleointensity data from the ca. 1092 Ma anorthosite xenoliths of the Beaver River diabase. The paleomagnetic directional data I developed in chapter 1 establish that the anorthosite xenoliths are stable remanence recorders that acquired remanence during cooling in the host diabase. I then used the “IZZI” Thellier paleointensity protocol (Yu et al., 2004) to develop absolute paleointensity data from the same xenoliths and calculated the axial dipole moment of Earth’s magnetic field. My data together with previous observations from rocks of the Midcontinent Rift show high paleointensity values ca. 1.1 Ga. Some of the xenoliths unequivocally show exceptionally high paleointensity values. Those high values require there being a strong dynamo in the late Mesoproterozoic, which does not fit in the interpreted Proterozoic monotonic decay trend hypothesized by Bono et al. (2019).

Overall, the high paleointensity values of the Beaver River anorthosite xenoliths necessitate a strong late Mesoproterozoic geodynamo. The enriching paleomagnetic database for the Precambrian is revealing a more complex history of Earth’s magnetic field than previously thought. The observational data from paleomagnetism are now stirring renewed interests in better understanding the core’s material properties in deep-Earth conditions and in understanding the dynamic connections between the mantle and the core.

### 1.3 Recovering deep-time paleointensity records from silicate-hosted Fe-oxides

Successful recovery of deep-time paleomagnetic records is dependent on rocks maintaining primary magnetic remanence through time and having stable behaviors during paleointensity experiments. Rocks contain assemblages of fine-grained ferromagnetic particles with various remanence stability that are dispersed within a matrix of diamagnetic and paramagnetic minerals. Not all ferromagnetic particles can maintain a magnetic memory through deep time. The characteristic time through which a ferromagnetic grain is capable of maintaining a

magnetization before spontaneous relaxation is a function of temperature, external magnetic field, composition, size, and shape (Néel, 1955; Nagy et al., 2017). Theoretical derivations show that single-domain particles with a narrow size range are stable magnetic remanence carriers (Butler and Banerjee, 1975; Butler, 1992). Based on the single domain theory of Néel (1955), ensembles of magnetite grains with sizes ranging from a few tens of nanometers to beyond one micron, and hematite grains with sizes up to  $15\text{ }\mu\text{m}$  can maintain a stable magnetization for billions of years. Recent advances in micromagnetic modeling and fine-scale magnetic imaging show that in geologic samples, stable ferromagnetic particles are likely to be more often in vortex states which can behave similarly to the single domain state (Nagy et al., 2017; Tauxe et al., 2020; Cortés-Ortuño et al., 2022).

Other ferromagnetic particles in rocks include multidomain grains (i.e. particles with multiple magnetic domains) and grains with complex vortex states which have more complex magnetic behaviors (Williams et al., 2010). While some of them may be capable of maintaining primary paleomagnetic directional records through deep time, others are more prone to having their magnetizations overwritten by heating or prolonged immersion in Earth's magnetic field postdating the acquisition of the primary remanence. Results of such processes typically manifest in rock samples as superposition of secondary remanence components on top of variably preserved primary remanence.

While isolation of primary paleomagnetic directional data from secondary overprints is possible via step-wise thermal demagnetization experiments and vector subtractions, the existence of multidomain and complex vortex state grains complicate the determination of paleointensity records as their remanence acquisition and removal behaviors deviate from the Thellier laws. In addition, alteration of rocks in nature and in the lab can also complicate paleomagnetic records by changing the magnetic mineralogy. This includes destruction of original minerals and formation of new magnetic minerals associated with chemical alteration during heating in the lab. Such mineralogical alterations are detrimental to paleointensity experiments, since the acquired remanence during the in-field steps in the lab would be held by grains distinct from those that record the natural remanence. Due to such complexities, recovering deep time paleointensity records is usually more difficult than recovering paleomagnetic directional records.

It has been found that well-behaved ferromagnetic grains enshrouded by silicate mineral hosts can be well-protected from alteration and be faithful paleointensity recorders (Cottrell and Tarduno, 1999, 2000; Tarduno and Cottrell, 2005; Tarduno et al., 2006; Cottrell et al., 2008; Selkin et al., 2000, 2007, 2008). In particular, titanomagnetite grains hosted in plagioclase crystals are intriguing targets. Petrography, electron microscopy, and microprobe data have shown that minor amount (<1% by weight) of iron commonly exist in plagioclase crystals which can be present as fine-scale magnetite needles (Selkin et al., 2000; Feinberg et al., 2005, 2006; Wenk et al., 2011; Bian et al., 2021). Rock magnetic analyses show that many of the rocks have ferromagnetic mineral assemblages dominated by single-domain-like behaviors with stable remanence carrying abilities. In addition, the alteration of the plagioclase does not readily result in the formation of secondary iron oxides in contrast with Fe-silicate minerals such as olivine and pyroxene.

In chapter 3, I develop new paleointensity data using the anorthosite xenoliths of the Beaver River diabase in the Midcontinent Rift to characterize Earth's magnetic field ca. 1092 Ma. Electron microscopy images show that plagioclase crystals within these anorthosite xenoliths can enclose small pyroxene crystals which have fine-scale exsolved titanomagnetite grains. These observations correspond to rock magnetic data that a number of the xenoliths typically have a dominant population of stable single-domain-like particles. The failed intracontinental rift nature of the Midcontinent Rift results in the anorthosite xenoliths being distant from subsequent tectonic events along Laurentian margins such that the lithology and magnetization of the anorthosite xenoliths have been minimally altered following initial formation.

## 1.4 Using detrital remanent magnetization in hematite-bearing sedimentary rocks to reconstruct paleogeography

Sedimentary rocks are important archives of Earth history. Paleomagnetic data developed from sedimentary rocks provide major contributions to global paleogeography reconstructions (e.g. Torsvik et al., 2012; Domeier et al., 2012; Vaes et al., 2023). While igneous rocks acquire thermal remanent magnetizations during cooling through blocking temperatures of ferromagnetic minerals (Néel, 1955), sedimentary rocks acquire detrital remanent magnetizations as a result of preferential alignment of detrital ferromagnetic particles with the local magnetic field during deposition. In the Midcontinent Rift, clastic sedimentary rocks of the Oronto Group deposited during post-rift thermal subsidence following the bulk of rift magmatic activity provide paleomagnetic poles that extend the Keweenawan Track to ca. 1070 Ma (Henry et al., 1977; Slotnick et al., 2023).

However, the accuracy of paleomagnetic directions recorded by the detrital remanent magnetization of sedimentary rocks has long been recognized as problematic due to the issue of inclination shallowing (e.g. King, 1955; Kodama, 2012; Tauxe and Kent, 1984; Van Andel and Hospers, 1966). The rotation of ferromagnetic grains during deposition and compaction toward the bedding plane can result in the acquisition of a detrital remanence that is biased shallow relative to the local geomagnetic field in which it was acquired (Fig. 1.4; Tauxe, 2005). Such inclination shallowing effect can be described as

$$\tan(I_o) = f \tan(I_f)$$

where  $I_o$  represents the observed inclination of the specimen magnetization and  $I_f$  represents the inclination of the field in which the magnetization was acquired. If uncorrected, shallower inclinations obtained from sedimentary rocks can potentially result in erroneously low estimates of paleolatitudes, biasing the interpreted past positions of continents and hindering plate reconstructions.

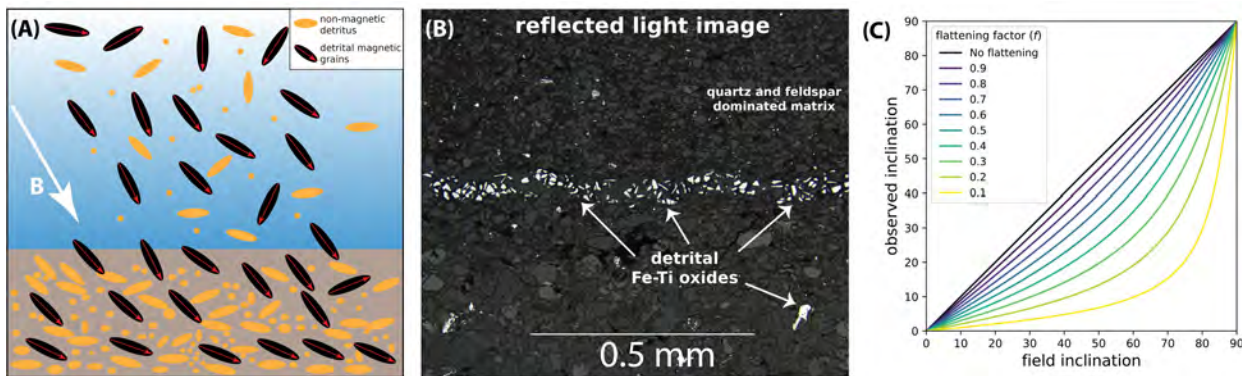


**Figure 1.4:** (A) Schematic illustration of detrital remanence magnetization acquisition process. The existence of Earth's magnetic field  $B$  biases the orientation of the detrital ferromagnetic particles such that they would be preferentially aligned with the local field direction during settling. The apparently rotated detrital ferromagnetic grains in the deposited sedimentary layers represent inclination shallowing due to rotation of the grains toward the bedding plane. Modified after Tauxe (1993). (B) Reflected petrographic image showing detrital Fe-Ti oxides with bright colors in a matrix dominated by quartz and feldspar grains. (C) The relationship between the inclination of the local magnetic field compared to the observed inclination in sedimentary rock records that experienced various degrees of inclination shallowing is shown. A value of 1.0 corresponds to no flattening while a value of 0.0 means the magnetizations are completely flattened. Modified after Pierce et al. (2022).

Experimental methods such as magnetic fabric analyses (e.g. Kodama and Davi, 1995; Bilardello and Kodama, 2010a,b,c) as well as statistical approaches (e.g. Tauxe and Kent, 2004) have been developed for correcting inclination shallowing in sedimentary records. However, there had been limited efforts in reporting uncertainties associated with the amount of shallowing, let alone propagating such uncertainties into sedimentary paleomagnetic poles for paleogeographic reconstructions. We developed a new method for quantifying uncertainties associated with inclination shallowing by using a spherical bivariate Kent distribution to represent uncertainties associated with paleomagnetic mean pole position through collaboration with an undergraduate honors thesis project in the UC Berkeley Earth and Planetary Science Department which is published as Pierce et al. (2022). This method has had successful applications in paleogeography reconstructions (Slotznick et al., 2023; Vaes et al., 2023; Zhang et al., 2024).

In chapter 5, I develop new paleomagnetic data from the hematite-bearing sedimentary rocks of the Jacobsville Formation which overlies unconformably on top of rocks of the Mid-continent Rift. Hodgin et al. (2022) developed geochronology data that constrain the timing of deposition of the Jacobsville Formation to be associated with compressional deformation of the Grenvillian orogenesis ca. 990 Ma. I used Kent mean statistics to represent the pole position and associated uncertainty. That pole is the first well-dated constraint from Laurentia's interior for the global paleogeography in the earliest Neoproterozoic. In that chapter, I show that the data from the Jacobsville Formation together with the Keweenawan Track support a tectonic model where Laurentia traveled rapidly equatorward in the latest Mesoproterozoic

and significantly slowed down following the onset of collisional Grenvillian orogenesis.

## 1.5 Global paleogeography in the earliest Neoproterozoic: progress and future directions

The evolution of the configuration of ancient continents is foundational to our knowledge of global tectonics, geodynamics, and climate through Earth history. We know that in the late Proterozoic, ancient continents conjoined together to form the supercontinent Rodinia (e.g. Li et al., 2008; Swanson-Hysell, 2021; Evans, 2021). The position of Laurentia is particularly crucial given its central location in the supercontinent. The Keweenawan Track of Laurentia has become a central record for reconstructing the assembly of Rodinia (Evans, 2021). The Keweenawan Track records rapid equatorward motion associated with the closure of the Unimos Ocean basin between Laurentia and conjugate continents leading up to the collisional Grenvillian orogeny (Fig. 1.5). The Grenvillian orogeny initiated ca. 1090 Ma with granulite-facies metamorphism of the Ottawan Stage of the orogeny occurring ca. 1050 Ma. The protracted collisional orogenesis continued through the 1010 to 980 Ma Rigolet Stage (Rivers, 2008, 2012; Swanson-Hysell et al., 2023). This later stage of the orogeny led to the formation of the Grenville Front, as contractional deformation propagated further into Laurentia.

Rocks of the Grenville orogen experienced granulite facies metamorphism with peak metamorphic temperatures up to 950°C (e.g. Shinevar et al., 2021; Metzger et al., 2021). The heating exceeds the Curie temperature of magnetite (580°C) and Néel temperature of hematite (690°C). As a result, the remanent magnetization that the rocks acquired during initial formation was entirely erased by heating during peak metamorphism, and subsequently overwritten during cooling associated with exhumation (McWilliams and Dunlop, 1975). Therefore, these rocks have the potential to provide additional insights into the global paleogeography following Grenville peak metamorphism. Previously, a large amount of paleomagnetic data have been developed from rocks of the Grenville orogen. The paleomagnetic poles cluster in a distinct position that is south to the end of the Keweenawan Track and also south to the ca. 990 Ma Jacobsville Formation pole (Fig. 1.5).

However, it has been challenging to precisely determine the age of the Grenville poles. Constraining the timing of remanence acquisition in the Grenville orogen requires constraining the cooling history of the orogen. Pioneering work that pairs thermochronology with paleomagnetic data recognized the long duration of cooling within the orogen and the necessity of determining cooling curves to assign ages to paleomagnetic poles (Berger et al., 1979). This work has subsequently been built upon through the development of additional  $^{40}\text{Ar}/^{39}\text{Ar}$  and U-Pb thermochronology data (e.g. Mezger et al., 1991; Warnock et al., 2000) and the use of estimated cooling curves interpreted from such data to assign ages of paleomagnetic poles (e.g. Warnock et al., 2000; Brown and McEnroe, 2012). As a result, high latitude Grenville Loop poles from the Haliburton intrusions in Ontario and the Adirondack Highlands have been assigned ages ranging between 1015-960 Ma. Albeit that these age

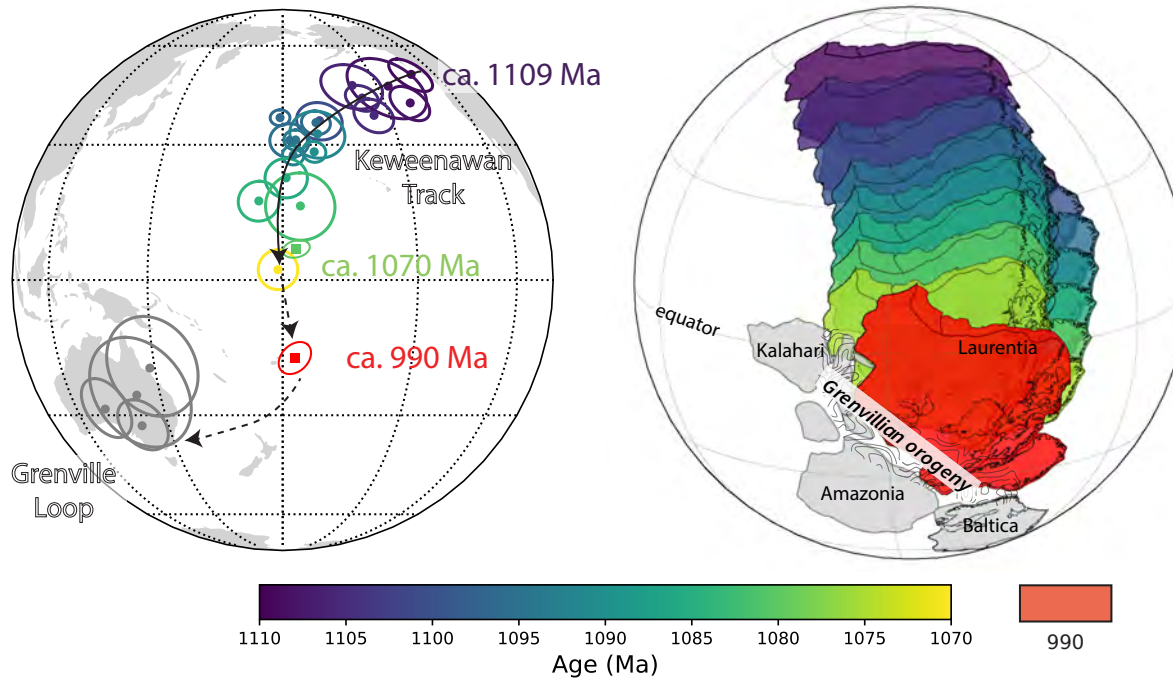


**Figure 1.5:** Summary paleomagnetic data and paleogeography reconstruction for Laurentia through the late Mesoproterozoic to the early Neoproterozoic. Left panel shows a compilation of paleomagnetic poles that constructs the ca. 1109-1070 Ma Keweenawan Track, the ca. 990 Ma Jacobsville Formation pole, and representative paleomagnetic poles developed from rocks of the Grenville orogen. Right panel shows the progression of Laurentia’s plate tectonic motion through the Keweenawan Track and a snapshot of paleogeography reconstruction ca. 990 Ma. Positions of Laurentia and the conjugate continents along Laurentia’s present-day eastern margin where the Grenvillian orogenesis occurred are reconstructed based on the Jacobsville pole and previously published paleomagnetic and geologic constraints. The details of the data compilation and reconstructions are presented in chapter 4.

assignments to Grenville Loop poles are based on rough estimates of the timing of magnetic remanence acquisition along simplified interpolation of cooling history paths with no uncertainty evaluations, they have been incorporated into curated paleomagnetic database for paleogeography reconstructions (e.g. Weil et al., 2003; Evans et al., 2021).

The now well-dated ca. 990 Ma configuration of Laurentia based on the paleomagnetic pole position of the Jacobsville Formation challenges previous configurations based on the Grenville poles (Fig. 1.5). In chapter 5, robust field tests constrain the Jacobsville pole to be a primary detrital remanent magnetization. We consider it to be a reliable representation of the position of Laurentia ca. 990 Ma. That the ages assigned to the Grenville Loop poles are both the same and bracketing the age of the Jacobsville pole presents a conundrum given the very different positions they imply for Laurentia and associated continents in Rodinia. However, it is not feasible to invoke a model where Laurentia and the Grenville Province were separated at the time of Jacobsville Formation deposition, since geochronology data show

that the Jacobsville Formation was deposited in a synorogenic basin as the Grenville Front developed and propagated into the interior of Laurentia during the last pulse of Grenvillian contractional deformation. Alternatively, I hypothesize that the Grenville poles must be a representation of Laurentia's paleogeographic position, but the question is at what time?

In previous Grenville paleomagnetic literature, the lack of reporting uncertainties associated with pole age assignments is partly due to the lack of using quantitative methods to represent uncertainties in the thermal history paths based on the thermochronology data. The fact that measurement-level data and specimen-specific details such as grain sizes are not available for the historic thermochronology literature makes it difficult to reproduce or improve those estimated ages for remanence acquisition. Additional uncertainty that was not fully taken into account in the previous literature comes from the cooling-rate dependence of magnetic remanence acquisition. In some contributions that have assigned ages to Grenville paleomagnetic poles, the Curie temperature of magnetite ( $580^{\circ}\text{C}$ ) was used as the temperature with which to assign pole ages from an interpreted cooling curve. While the Curie temperature is certainly relevant, as above it the mineral is paramagnetic rather than ferromagnetic, blocking temperatures for an assemblage of grains will be below the Curie temperature. For a population of magnetite grains in the single-domain state, acquisition of magnetization occurs as a rock cools through temperatures where the thermal fluctuation energy is no longer sufficient to reset the magnetization of the population of particles to align with the ambient field on a given timescale (the relaxation time). For rapidly cooled rocks such as lava flows, the cooling rate during emplacement and that during demagnetization in the lab are similar and the observed unblocking temperatures in the lab are close to the natural blocking temperatures during remanence acquisition. In contrast to a rapidly cooled lava, magnetite-bearing rocks in the Grenville orogen acquired remanence during protracted cooling after peak metamorphism leading to a several orders of magnitude difference between the natural cooling rate and lab cooling rate. This slow cooling leads to an expression of the cooling rate dependence where the temperatures at which a magnetization is acquired are lower than the temperatures at which it is removed in the lab (Pullaiah and Irving, 1975; Halgedahl et al., 1980; Dodson and McClelland-Brown, 1980). Estimating the age of remanence acquisition in conjunction with cooling trajectories necessitates developing a framework that implements these relationships. These considerations further highlight the importance of precisely determining the unblocking temperatures of magnetite-held remanence associated with a paleomagnetic direction, instead of picking single temperature values.

In the future, I am interested in testing a hypothesis that the poles from the Grenville orogen are younger than currently interpreted. Instead of the poles having remanence that was acquired while the Grenvillian orogeny was still ongoing (as is the case of the interpretation of the Haliburton pole; Warnock et al., 2000), the magnetic remanence could instead have been acquired during exhumation well after the ca. 980 Ma cessation of contractional deformation. In this scenario, the migration of Rodinia to the higher latitude position represented by the Grenville Loop poles would have occurred further into the Neoproterozoic (Fig. 1.5). Testing this hypothesis is of central importance to Neoproterozoic paleogeogra-

phy as the ages associated with those Grenville Loop poles are crucial for constraining the motion of Laurentia and the configuration between Laurentia and hypothesized conjugate continents at this time. For example, in the case of Baltica's position, it has been argued through comparison between paleomagnetic poles from the Grenville orogen and Sveconorwegian orogen that there were multiple oscillatory true polar wander rotations in the early Neoproterozoic (Evans et al., 2015; Gong et al., 2018). This interpretation is reliant on the assigned ages of the poles in both orogens. I plan to approach this question by developing high-precision U-Pb thermochronology data and new high-resolution paleomagnetic data. I will quantitatively construct thermal history paths and evaluate their associated uncertainties using U-Pb apatite system as a thermochronometer which have closure temperatures similar to the blocking temperatures of titanomagnetite in Grenville rocks. I will pair these results with new high-resolution thermal demagnetization data such that the natural blocking temperature of the Grenville rocks can be better constrained based on the unblocking spectra obtained in the lab, taking the cooling-rate effect into consideration.

Overall, I hope this thesis dissertation is a descent showcase of the power of paleomagnetism for reconstructing magmatism, geomagnetic field behavior, and paleogeography in deep time. I look forward to continuing to develop more paleomagnetic data to tell Earth history stories while integrating interdisciplinary approaches to overcome challenges along the way.

## Chapter 2

# Synchronous emplacement of the anorthosite xenolith-bearing Beaver River diabase and one of the largest lava flows on Earth

### 2.1 Abstract

New geochronologic and paleomagnetic data from the North American Midcontinent Rift (MCR) reveal the synchronous emplacement of the Beaver River diabase, the anorthosite xenoliths within it, and the Greenstone Flow — one of the largest lava flows on Earth. A U-Pb zircon date of  $1091.83 \pm 0.21$  Ma ( $2\sigma$ ) from one of the anorthosite xenoliths is consistent with the anorthosite cumulate forming as part of the Midcontinent Rift and provides a maximum age constraint for the Beaver River diabase. Paired with the minimum age constraint of a cross-cutting Silver Bay intrusion ( $1091.61 \pm 0.14$  Ma;  $2\sigma$ ) these data tightly bracket the age of the Beaver River diabase to be  $1091.7 \pm 0.2$  Ma (95% CI), coeval with the eruption of the Greenstone Flow ( $1091.59 \pm 0.27$  Ma;  $2\sigma$ ) — which is further supported by indistinguishable tilt-corrected paleomagnetic pole positions. Geochronological, paleomagnetic, mineralogical, and geochemical data are consistent with a hypothesis that the Beaver River diabase was the feeder system for the Greenstone Flow. The large areal extent of the intrusives and large estimated volume of the volcanics suggest that they represent a

---

This chapter is published as a peer-reviewed manuscript: Zhang, Y., Swanson-Hysell, N.L., Schmitz, M.D., Miller Jr., J.D., and Avery, M.S., (2021), Synchronous emplacement of the anorthosite xenolith-bearing Beaver River diabase and one of the largest lava flows on Earth. *Geochemistry, Geophysics, Geosystems*. doi: <https://doi.org/10.1029/2021GC009909>.

rapid and voluminous ca. 1092 Ma magmatic pulse near the end of the main stage of MCR magmatism.

## 2.2 Introduction

The North American Midcontinent Rift (MCR) is a ca. 1.1 Ga large igneous province for which there is excellent exposure of both the intrusive and extrusive components in the Lake Superior region (Fig. 2.1). An exceptional feature within the Midcontinent Rift is the occurrence of large anorthosite xenoliths within a diabase sill and dike network known as the Beaver River diabase that outcrops in northeastern Minnesota, USA, as part of the Beaver Bay Complex (Fig. 2.1). The anorthosite xenoliths range in size from centimeter-scale megacrysts to meter-scale, decimeter-scale and even >150 meter-scale blocks (Fig. 2.2; Morrison et al., 1983; Grout and Schwartz, 1939). A particularly large anorthosite xenolith is exposed at Carlton Peak in the eastern Beaver Bay Complex with minimum dimensions of 180 × 240 meters (Fig. 2.1, 2.2; Boerboom et al., 2006). In the southern Beaver Bay Complex, a large anorthosite xenolith near Corundum Point has dimensions of 180 × 230 meters while one exposed at Split Rock Point has dimensions of 180 × 260 meters (Boerboom, 2004). To be able to accommodate such large xenoliths during magma ascent, the Beaver River diabase conduits must have been of at least the width of the anorthosite short axis diameters. Such wide conduits in these near-surface intrusions suggest high magma flux rates and make it likely that the magma extruded to the surface — feeding voluminous lava flows.

Miller and Chandler (1997) emphasized the composite nature of the Beaver River diabase network and Silver Bay intrusions (Fig. 2.1), which are locally marked by abrupt transitions to progressively more evolved lithologies. Furthermore, Miller and Chandler (1997) documented geochronologic, geochemical and structural evidence to support the notion that the diabase network may have served as principal feeder conduits to lava flows including parts of the Portage Lake Volcanics on the Keweenaw Peninsula and Isle Royale of Michigan (Fig. 2.1). To more directly test this inferred intrusive-extrusive correlation, Doyle (2016) compared the mineralogical, textural, and geochemical attributes and the composite lithologic nature of the Beaver River diabase against those of the Greenstone Flow, the largest lava flow within the Midcontinent Rift and one of the largest lava flows on Earth (Fig. 2.3). Doyle (2016) documented remarkable similarities in petrography, mineral chemistry, whole rock geochemistry, and interpreted lithologic zonation between the Beaver River diabase intrusions in northern Minnesota and the Greenstone Flow on both Isle Royale and Keweenaw Peninsula. Based on the interpreted feeder system being in northern Minnesota, Doyle (2016) estimated the full areal extent of the Greenstone Flow to be ~20000 km<sup>2</sup> and its volume to be between 2000 and 6000 km<sup>3</sup> (Fig. 2.3).

A comagmatic relationship between the Beaver River diabase and the Greenstone Flow is consistent with the similar  $^{207}\text{Pb}/^{206}\text{Pb}$  dates developed from a granophyric ferrogabbro within the Beaver Bay Complex ( $1095.8 \pm 1.2$  Ma; Paces and Miller, 1993) and the Green-

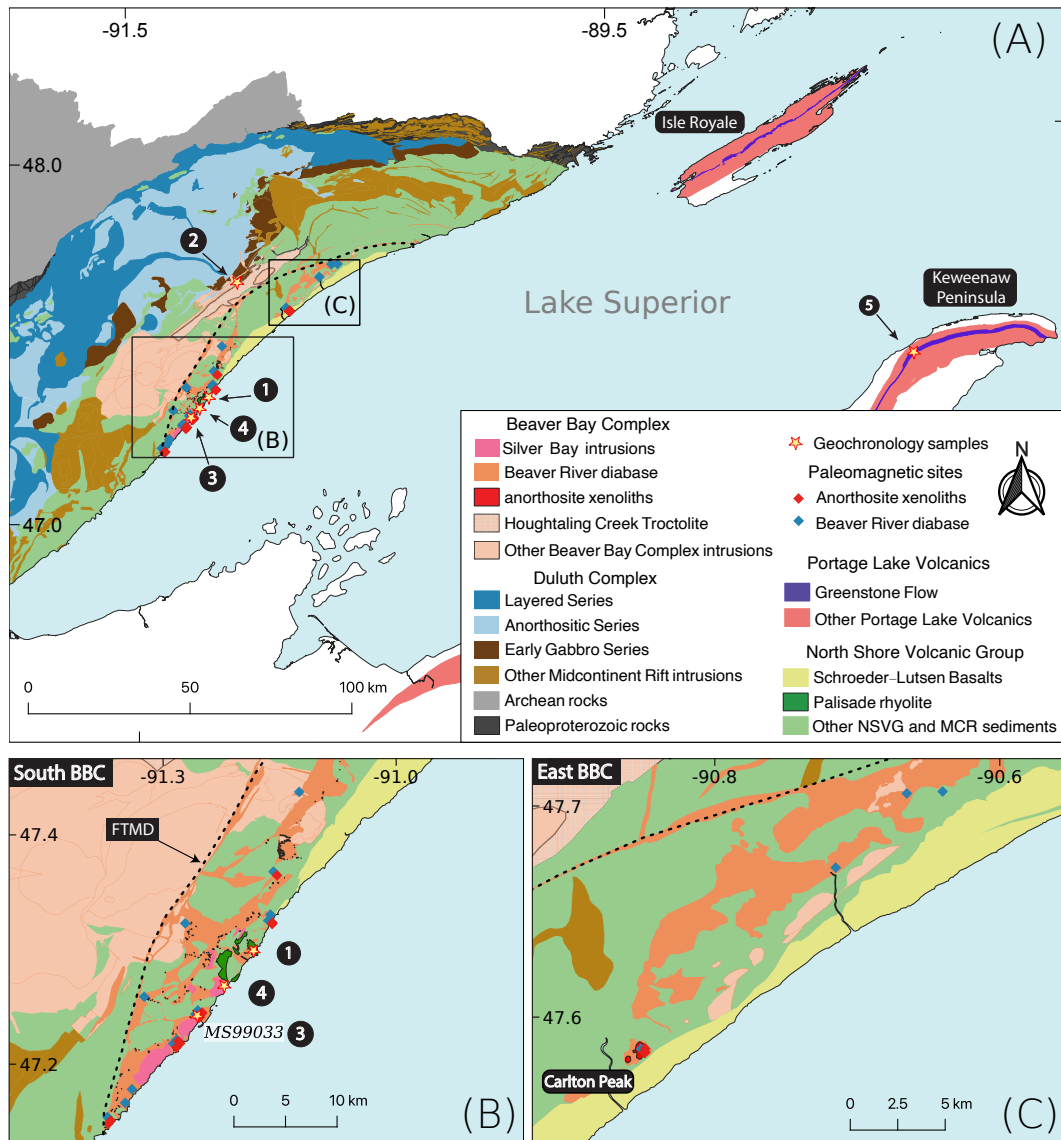


**Figure 2.1:** (A) Geologic map of exposures of Midcontinent Rift volcanics and intrusives in the western Lake Superior region. The Greenstone Flow (purple) of the Portage Lake Volcanics (red) outcrops throughout the Keweenaw Peninsula and Isle Royale. (B) Regional map of paleomagnetic and geochronologic sites in the southern Beaver Bay Complex (south BBC). Note that paleomagnetic site AX16 and geochronology sample MS99033 are from the same anorthosite xenolith. The geochronology sample numbers in (A) and (B) correspond to those in Fig. 2.4. (C) Regional map of paleomagnetic sites in the eastern Beaver Bay Complex (east BBC). The xenolith at Carlton Peak is >100 meters in diameter. The younger Schroeder-Lutsen basalt of the North Shore Volcanic Group (NSVG) is lying unconformably atop the Beaver River diabase and other NSVG units. The nomenclature of the “southern” and “eastern” Beaver Bay Complex follows Miller and Chandler (1997). FTMD - Finland tectonomagmatic discontinuity, traced out by the dashed black line. Bedrock geology is from Miller et al. (2001) and Jirsa et al. (2011).

stone Flow ( $1094.0 \pm 1.5$  Ma; Davis and Paces, 1990). The relatively large uncertainties provided by the existing  $^{207}\text{Pb}/^{206}\text{Pb}$  geochronology provide less precise estimates of the temporal relationships between these rapid events than is possible with modern methods. Modern-day U-Pb geochronology techniques for chemical abrasion isotope dilution-thermal ionization mass spectrometry (CA-ID-TIMS) allow high-precision  $^{206}\text{Pb}/^{238}\text{U}$  dates to be developed from chemically abraded zircon crystals (Mattinson, 2005). Studies utilizing these methods on Midcontinent Rift volcanic and intrusive rocks have shown that the analytical uncertainties on weighted mean  $^{206}\text{Pb}/^{238}\text{U}$  dates of multiple chemically abraded single zircons can be  $\sim 200$  kyr, an order of magnitude smaller than previous dates that are based exclusively on the  $^{207}\text{Pb}/^{206}\text{Pb}$  system (Fairchild et al., 2017; Swanson-Hysell et al., 2019b, 2021b). These  $^{206}\text{Pb}/^{238}\text{U}$  dates are also considered to be more accurate than systematically older  $^{207}\text{Pb}/^{206}\text{Pb}$  dates (Schoene et al., 2006). Such  $^{206}\text{Pb}/^{238}\text{U}$  dates indicate that the massive Layered Series and Anorthositic Series rocks of the Duluth Complex were emplaced in  $\sim 500$  kyr ca. 1096 Ma (Swanson-Hysell et al., 2021b).

In this work, we use a new  $^{206}\text{Pb}/^{238}\text{U}$  zircon date for an anorthosite xenolith hosted within the Beaver River diabase, in conjunction with  $^{206}\text{Pb}/^{238}\text{U}$  dates from a Silver Bay intrusion and the Greenstone Flow (Fig. 2.1; Fairchild et al., 2017), to evaluate the timing of emplacement of the Beaver River diabase, and the hypothesized intrusive-extrusive correlation between the Beaver River diabase and the Greenstone Flow.

Paleomagnetic data can also provide chronological constraints on rock units. Laurentia experienced a period of rapid latitudinal plate motion during rift development (Swanson-Hysell et al., 2009). A synthesized apparent polar wander path (APWP) based on the Mid-continent Rift volcanic rocks indicates that motion exceeded 20 cm/yr (Swanson-Hysell et al., 2019b), faster than the maximum speed of India of  $\sim 17$  cm/yr during the Cenozoic (van Hinsbergen et al., 2011). This motion resulted in significant differences in pole positions recorded by Midcontinent Rift rocks that were emplaced a few million years apart (Swanson-Hysell et al., 2019b). In this study, we present paleomagnetic data from the anorthosite xenoliths and the host Beaver River diabase. Data from the xenoliths give equivalent directions to the host diabase (Figs. 2.7, 2.8), indicating that they were heated above the Curie temperature of magnetite and acquired a thermal remanent magnetization when they cooled within the diabase. This thermal history is consistent with thermal diffusion modeling of the xenoliths (Fig. 2.9). The paleomagnetic data can be compared to data from the Greenstone Flow to further test the hypothesis that they are synchronous. The resulting paleomagnetic pole positions can also be compared to the synthesized Laurentia APWP to obtain chronological constraints (Fig. 2.8).

Here, by integrating the geochronologic and paleomagnetic perspectives with previous lithologic and geochemical analyses (Miller and Chandler, 1997; Doyle, 2016), we show that these data are consistent with the Beaver River diabase network acting as the feeder system for the Greenstone Flow of the Portage lake Volcanics. Alternatively, they could both be the distinct manifestations of magmatism from a similar source. Regardless, their shared geochemical signatures and the inference of giant magma conduits that transported large anorthosite xenoliths characterize a period of ca. 1092 Ma voluminous magmatic activity

(based on  $^{206}\text{Pb}/^{238}\text{U}$  zircon dates; Fig. 2.1).

## 2.3 Geologic Setting

### Beaver Bay Complex and Related Rocks of NE Minnesota

The North American Midcontinent Rift (MCR) is a failed intracontinental rift where protracted magmatic activity lasted from ca. 1109 Ma to ca. 1084 Ma (Swanson-Hysell et al., 2019b). Midcontinent Rift rocks extensively outcrop in today's Lake Superior region, with the total extent traceable by arcuate magnetic and gravity anomalies that extend to the southwest to Kansas, and to the southeast, to southern Michigan (Hinze and Chandler, 2020). Previous studies have divided magmatic activity in the rift into four stages based on interpreted changes in relative magmatic volume and the nature of magmatism: early (~1109–1104 Ma), latent (~1104–1098 Ma), main (~1098–1090 Ma) and late (~1090–1083 Ma) (Vervoort et al., 2007; Heaman et al., 2007; Miller and Nicholson, 2013). In northeastern Minnesota, the Early Gabbro Series and the Felsic Series rocks of the Duluth Complex and reversed-polarity lavas of the lower North Shore Volcanic Group were emplaced during the early stage. The more voluminous Duluth Complex Layered Series and the plagioclase-rich Anorthositic Series, together with an associated ~8 km thick extrusive volcanic sequences of the North Shore Volcanic Group (NSVG), were rapidly emplaced about 10 myr later at ca. 1096 Ma during the main stage (Paces and Miller, 1993; Swanson-Hysell et al., 2021b).

The Beaver Bay Complex, which sits stratigraphically above the Duluth Complex, is another intrusive complex that resulted from main stage magmatism. The exposed area of the Beaver Bay Complex is  $\sim 1000 \text{ km}^2$  where it has been mapped along the northwestern shore of Lake Superior in northeastern Minnesota (Fig. 2.1). The Beaver Bay Complex is a multi-phase, composite intrusive complex that intrudes parts of the NSVG (Fig. 2.1; Miller and Chandler, 1997; Swanson-Hysell et al., 2021b). Distinct from the deep plutonic intrusions of the Duluth Complex, the majority of the Beaver Bay Complex is formed of hypabyssal intrusions that were emplaced as dikes and sills at shallow depths (Miller and Chandler, 1997). Most of the Beaver Bay Complex intrusions are dioritic to gabbroic in composition (Miller and Chandler, 1997). The main lithology of the Beaver River diabase dikes and sills network within the Beaver Bay Complex is an ophitic olivine gabbro (Fig. 2.2), but in wider areas of dikes and the upper parts of thick sills, this rock type can abruptly transition into intergranular olivine oxide gabbro, then into subprismatic (and commonly foliated) ferrogabbro, and finally into granophyric monzodiorite. The more evolved and later emplaced components of the Beaver River diabase network are commonly distinguished as the Silver Bay intrusions in the southern Beaver Bay Complex (Fig. 2.1). Overall being intermediate in composition, the Silver Bay intrusions lithologies range from ophitic olivine gabbro to ferrogranite (Shank, 1989). Field mapping by Miller et al. (1994) found intrusive relationships between the Silver Bay intrusions and the Beaver River diabase. Angular inclusions of the host Beaver River diabase within marginal zones of the Silver Bay intrusions

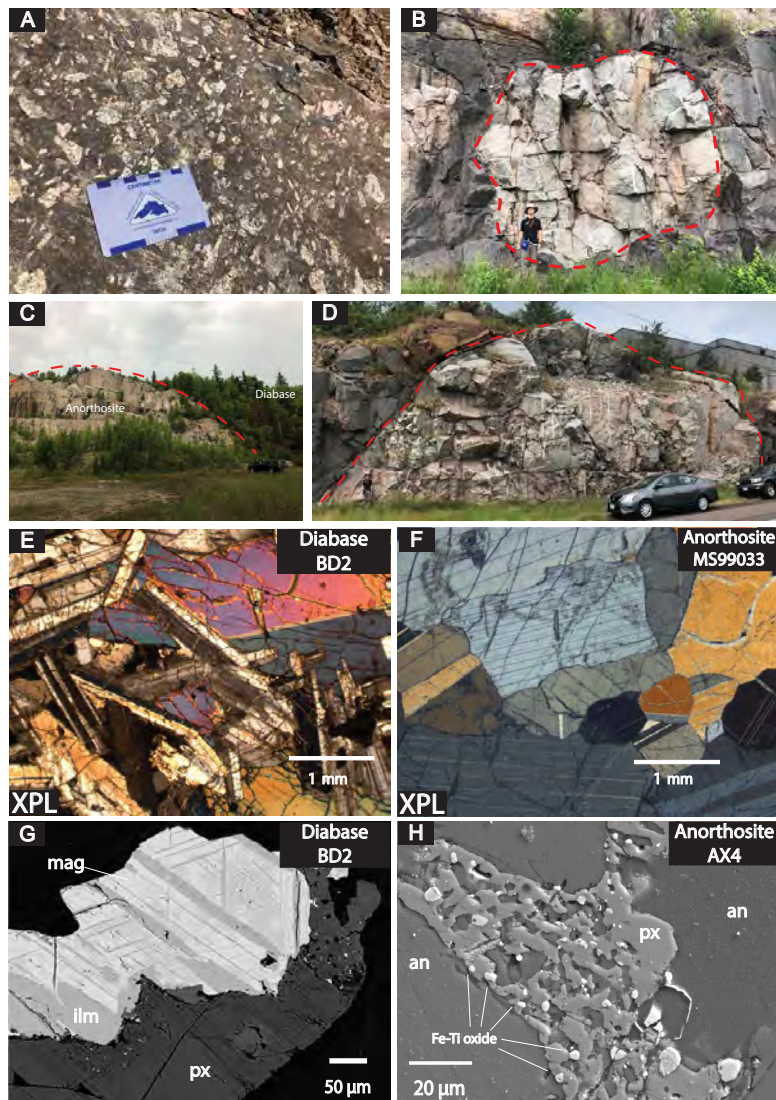


**Figure 2.2:** Field photographs and petrographic images of the Beaver River diabase and the anorthositic xenoliths within it. (A) Centimeter-sized plagioclase megacrysts in the diabase. (B) Rounded anorthositic xenolith with a diameter of  $\sim 7$  meters fully enclosed within the diabase. (C) Exposure of a giant Carlton Peak anorthositic xenolith with a diameter  $>100$  m. (D) 27.5 m diameter anorthositic xenolith sampled as paleomagnetic site AX16 and geochronology sample MS99033. (E) Cross polarized (XPL) image of the subophitic texture of diabase at site BD2 (pyroxene partially enclosing plagioclase). (F) XPL image of anorthositic geochronology sample MS99033. Plagioclase crystals exhibit both granoblastic texture and interlocking lath fabrics. (G) Backscattered electron (BSE) image of a large Fe-Ti oxide with titanomagnetite-ilmenite lamellae in Beaver River diabase site BD2. (H) BSE image of micron-sized Fe-Ti oxides exsolved from pyroxene between plagioclase crystals in anorthositic xenolith site AX4. an-plagioclase with  $\sim 70\%$  anorthite; ilm-ilmenite; mag-magnetite; px-pyroxene.

led Miller and Chandler (1997) to interpret that the Silver Bay intrusions intruded after the diabase crystallized.

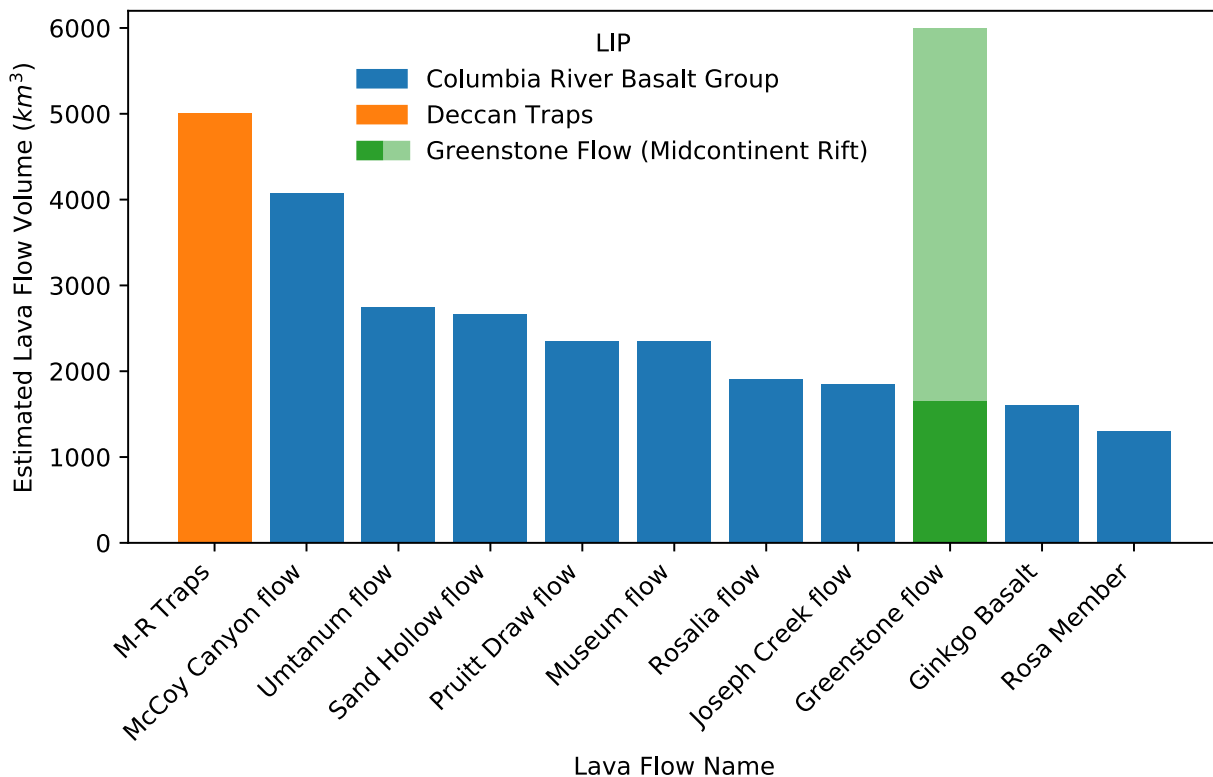


**Figure 2.3:** Bar plot of ten of the world's most voluminous single mafic lava flows currently known. With an estimated minimum volume of  $\sim 1650 \text{ km}^3$  and likely volume as high as  $\sim 6000 \text{ km}^3$ , the Greenstone Flow from the 1.1 Ga Midcontinent Rift stands amongst the giant lava flows from the Deccan Traps and Columbia River basalts. M-R Traps = Mahabaleshwar–Rajahmundry lava flow in the Deccan Traps. Volume estimates from Self et al. (2008), Bryan et al. (2010), Longo (1984), and Doyle (2016).

One distinctive feature of the Beaver River diabase is its inclusions of anorthosite xenoliths. In the southern part of the Beaver Bay Complex, the Beaver River diabase occurs as dikes and sills, typically including anorthosites with various sizes ranging from centimeters to over 150 meters (Figs. 2.1, 2.2; Grout and Schwartz, 1939; Morrison et al., 1983). The diabase in this region intrudes the Palisade rhyolite of the North Shore Volcanic Group (Fig. 2.1), which has a  $^{206}\text{Pb}/^{238}\text{U}$  date of  $1093.94 \pm 0.28 \text{ Ma}$  ( $2\sigma$  analytical uncertainty is presented for CA-ID-TIMS dates throughout this work; Swanson-Hysell et al. (2019b)). The Beaver River diabase is locally intruded by the Silver Bay intrusions (Fig. 2.1). An aplite unit within the granophyre zone of one of these Silver Bay intrusions has a  $^{206}\text{Pb}/^{238}\text{U}$  date of  $1091.61 \pm 0.14 \text{ Ma}$  (Swanson-Hysell et al., 2019b). Another arcuate, sill-like diabase body mapped as the Beaver River diabase outcrops along the eastern part of the complex (Fig. 2.1; Miller and Chandler, 1997). The diabase composition there is similar to that

in the south and it also contains large anorthosite xenoliths with dimensions that exceed 100 meters at Carlton Peak (Fig. 2.1). The Beaver River diabase in the northern part of the complex, near the Houghtaling Creek area, typically forms narrow, near-vertical dikes instead of sheets in the southern and eastern regions (Fig. 2.1; Miller et al., 1994). The diabase in this region only locally contains xenoliths of anorthosite.

Hundreds of anorthosite xenoliths have been recognized and mapped within the Beaver River diabase (Fig. 2.1). Many hill tops in the Beaver Bay Complex, such as Carlton Peak and Britton Peak, are large anorthosite blocks (which lead Lawson (1893) to erroneously conclude that they were relict Archean topography). Later work established the anorthosite blocks as xenoliths, which are now extensively documented through geologic mapping of the region (Fig. 2.1; Miller et al., 2001; Miller, 1988; Miller and Boerboom, 1989; Boerboom, 2004; Boerboom and Green, 2006; Boerboom et al., 2006, 2007) and outcrop-scale exposures (Fig. 2.2). In the field, the anorthosites typically appear as subrounded to rounded, light-colored, translucent blocks that are in sharp contact with the hosting diabase (Fig. 2.2). They also occur as exposures whose contact with the diabase is covered (Fig. 2.2). Grout and Schwartz (1939) suggested that the rounded anorthosites are the result of abrasion during transportation as they were entrained by the diabase (i.e. physical weathering within a magmatic system). While the Beaver River diabase is chilled against the North Shore Volcanic Group lithologies that it intrudes, the diabase is not chilled against the margin of the anorthosite xenoliths (Morrison et al., 1983; Miller and Chandler, 1997). The lack of chilled contacts is consistent with the anorthosite being at elevated temperatures and cooling at the same time as the diabase magma (Fig. 2.9).

The anorthosite xenoliths are dominantly monomineralic plagioclase that has an average anorthite content of  $\sim$ 70% (Morrison et al., 1983; Doyle, 2016). Interstitial pyroxene and olivine are present in minor concentrations in the xenoliths. Within the Carlton Peak anorthosite xenolith, up to 10 cm oikocrysts of olivine and pyroxene can occur. Nevertheless, the overall olivine content in the anorthosites is low. Interstitial titanomagnetite-ilmenite intergrowths that exceed  $100\ \mu\text{m}$  can be found with microscopy and  $<20\ \mu\text{m}$  Fe-Ti oxide grains can be detected with scanning electron microscopy (Fig. 2.2). Based on textural differences Morrison et al. (1983) divided the anorthosite xenoliths into four groups: one group which typically have well-developed granoblastic texture characterized by equigranular plagioclase crystals; another group which have interlocking, lath-shaped plagioclase crystals; an intermediate group which can have both granoblastic texture and interlocking plagioclase laths; and a brecciated group that have brittle deformation textures superposed on pre-existing textures.

## Portage Lake Volcanics and the Greenstone Flow

The Portage Lake Volcanics (PLV) is a  $\sim$ 5 km thick, normally magnetized, dominantly olivine basalt to andesite volcanic succession that outcrops in northern Michigan (particularly along the Keweenaw Peninsula) as well as on Isle Royale (Fig. 2.1; Huber, 1973; Cannon and Nicholson, 2001; Green, 1982). The Greenstone Flow of the Portage Lake Volcanic Group

has been recognized as one of the largest lava flows on earth (Figs. 2.1, 2.3). It outcrops as the main ridge along the Keweenaw Peninsula and Isle Royale (Fig. 2.1). The flow can be correlated between the two outcrop regions on the basis of geochemical, petrographic, and paleomagnetic similarity of the flow itself and the flows above and below (Longo, 1984). In both outcrop regions, the Greenstone Flow is underlain by conglomerate and overlain by pyroclastic breccia (Lane, 1911; Huber, 1973). On the Keweenaw Peninsula, the Greenstone Flow is exposed over 90 km with a range of thickness from ~100 meters to a maximum thickness of over 450 meters, dipping to the northwest (Fig. 2.1; White, 1960). On Isle Royale, the Greenstone Flow has a range of thickness from ~30 meters to a maximum thickness of about 250 meters, dipping toward the southeast (Fig. 2.1; Huber, 1973). More recently, Doyle (2016) estimated that the total aerial extent of the Greenstone Flow could be up to ~20000 km<sup>2</sup> by connecting it to the region of the Beaver Bay Complex. Taking thickness range of 100 to 300 meters, Doyle (2016) estimated a total volume of 2000 to 6000 km<sup>3</sup>. This volume range makes the Greenstone Flow one of the largest, if not the largest, single mafic lava flows on Earth (Fig. 2.3).

According to the mineralogical and textural attributes, the Greenstone Flow can be divided into four zones from bottom to top — a lower ophitic zone, a “pegmatoid” or heterolithic zone, an upper ophitic zone, and an amygdaloidal zone (Cornwall, 1951). The heterolithic zone contains lenses to layers of coarse-grained granophyric gabbro that are referred to in the literature as “pegmatoid.” Zircon crystallized in these layers have enabled the heterolithic zone to be targeted for U-Pb geochronology (Davis and Paces, 1990; Swanson-Hysell et al., 2019b). A <sup>206</sup>Pb/<sup>238</sup>U zircon date of 1091.59 ± 0.27 Ma for the Greenstone Flow was developed from a sample from this zone in Swanson-Hysell et al. (2019b). The Greenstone Flow is typically interpreted to represent emplacement of a single body of magma that then underwent in situ differentiation (Huber, 1973; Davis and Paces, 1990). Doyle (2016) favored a distinct model in which the Greenstone Flow is a composite unit, which they interpret to be indicated by lithologic zonation of ophitic basalt forming the upper and lower zones and an interior zone composed of prismatic ferrogabbro to granophyric monzodiorite. They envision emplacement of the Greenstone Flow started with voluminous eruption of olivine tholeiitic magma, forming the ophitic zones which, while still crystallizing, further inflated due to subsequent injection of a more evolved basaltic magma to form intergranular gabbro in the heterolithic zone. They considered this progression to be more consistent with observed abrupt lithologic changes from the ophitic zone to the heterolithic zone over centimeter to meter scales, inclusion relationships between evolved and ophitic Greenstone Flow lithologies, and remnant blocks of initially crystallized ophitic basalt interlayered with evolved lithologies within the heterolithic zone which contains the pegmatoids. In both the Doyle (2016) model of multiple magma injections and the earlier models of in situ differentiation, it is the migration of the most evolved and volatile-rich melts within the interior of the flow in the final stages of flow crystallization that led to the formation of some aplite dikes and the coarsest segregations containing granophyre. Both models also invoke a single basaltic parental magma with distinction of where differentiation occurred in fractionally crystallizing an evolving magma chamber or solely within a single, very thick

flow.

## 2.4 Methods and Results

### Zircon Geochronology and Geochemistry

A sample of an anorthosite xenolith within the Beaver River diabase was collected for U-Pb geochronology along Hwy 61 across from the Silver Bay taconite plant (MS99033; 91.26358°W 47.28888°N; Fig. 2.1). This sample comes from the same xenolith sampled for paleomagnetic study as site AX16 which has an exposed diameter of 27.5 meters (Fig. 2.2). Thin sections were made from the geochronology sample as well as multiple paleomagnetic cores. As is shown in Fig. 2.2F, plagioclase in this anorthosite xenolith have both equigranular crystals displaying a granoblastic texture and lath-shaped crystals displaying an interlocking texture. The occurrence of both textures is consistent with an interpretation that this anorthosite xenolith formed under elevated temperatures and experienced heating after initial crystallization.

Zircons were separated from a kilogram of the anorthosite using common mineral separation methods (Supporting Information). The separated zircons were subhedral to anhedral crystals (z1-z4) and platy fragments (z5-z8). The subhedral to anhedral crystals are consistent with intercumulus crystallization within an adcumulate with platy fragments also being a common zircon morphology within anorthosites (e.g. sample AS3 of the Duluth Complex anorthositic series; Schmitz et al. (2003)). Eight chemically abraded zircons were analyzed by isotope dilution-thermal ionization mass spectrometry (ID-TIMS) in the Boise State Isotope Geology Laboratory using EARTHTIME tracer solutions (Condon et al., 2015). Both zircon morphologies yield indistinguishable dates. Using six of these single grain dates (and excluding two due to interpreted Pb-loss) results in a weighted mean  $^{206}\text{Pb}/^{238}\text{U}$  date of  $1091.83 \pm 0.21/0.37/1.15$  Ma (analytical/ analytical+tracer/ analytical+tracer+decay uncertainty; Fig. 2.4).

This date provides a tight constraint on the age of the Beaver River diabase. Previously, the maximum age constraint for the Beaver River diabase came from the relationship that it cross-cuts the Palisade rhyolite of the North Shore Volcanic Group which has a  $^{206}\text{Pb}/^{238}\text{U}$  date of  $1093.94 \pm 0.28$  Ma (Swanson-Hysell et al., 2019b). With this new date, we know the crystallization age of the diabase to have been near-synchronous or younger than the date from the anorthosite xenolith. The Silver Bay intrusions, from which an aplite has a  $^{206}\text{Pb}/^{238}\text{U}$  date of  $1091.61 \pm 0.14$  Ma, (Fairchild et al., 2017), cross-cut the Beaver River diabase. These dates constrain the diabase to have been emplaced between  $1091.83 \pm 0.21$  and  $1091.61 \pm 0.14$  Ma (Fig. 2.4). Assuming a uniform probability of diabase emplacement between the anorthosite and aplite dates and their normal distributed uncertainties, a 95% confidence interval on the age of the diabase can be estimated by Monte Carlo simulation. This analysis gives an age for the diabase of  $1091.7 \pm 0.2$  Ma (95% CI).

An additional 15 zircons were characterized using cathodoluminescence (CL) imaging

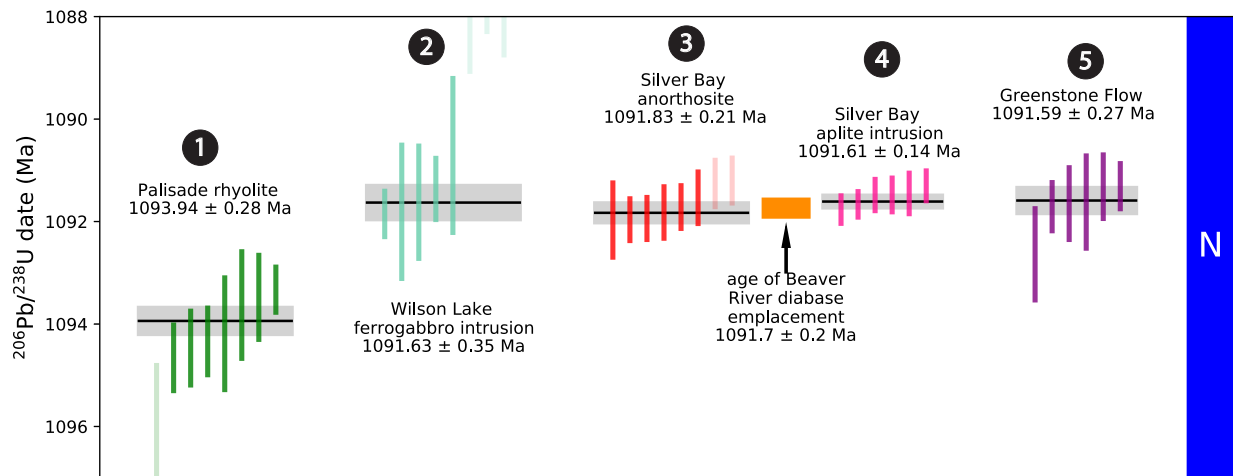


**Figure 2.4:** New  $^{206}\text{Pb}/^{238}\text{U}$  zircon date of the anorthositic xenolith (dark orange) plotted in context of previously published  $^{206}\text{Pb}/^{238}\text{U}$  zircon dates from the North Shore Volcanic Group (NSVG) and other Beaver Bay Complex intrusions (Swanson-Hysell et al., 2019b, 2021b). These high-precision dates are consistent with field observations that the Beaver River diabase crosscuts the Palisade rhyolite (dark green) and is cut by the Silver Bay intrusions (pink). The estimated age of the Beaver River diabase from these constraints is shown by an orange box representing the 95% confidence interval. Each vertical bar corresponds to one  $^{206}\text{Pb}/^{238}\text{U}$  date from a single zircon crystal. The translucent bars represent zircons with interpreted Pb loss and are therefore not included in the weighted mean age calculations. Horizontal lines and gray boxes represent weighted mean  $^{206}\text{Pb}/^{238}\text{U}$  dates and their analytical uncertainty. The numbers of each geochronology sample correspond to those in Fig. 2.1 where locations of these samples are shown.

and laser ablation-inductively coupled plasma mass spectrometry (LA-ICPMS), with methods and instrumentation described in the Supporting Information. CL images reveal internal planar zones of variable brightness, often with darker interior zones and brighter outer zones (Fig. 2.5). All crystals exhibit sharp, micron-scale transitions between zones, and LA-ICPMS analyses quantify CL brightness as correlated with rare earth elements (REE) content. REE patterns in zircons exhibit a significant chondrite-normalized negative Eu anomaly (Fig. 2.6). The Ti-in-zircon thermometer gives a range of estimated zircon crystallization temperatures from 998°C to 860°C with a mean of ~950°C (Ferry and Watson, 2007; Supporting Information). Decreasing temperatures are correlated with deepening of the negative Eu anomaly and increasing incompatible trace element (e.g. Hf, Th) incorporation into zircon. These data are consistent with a model of magmatic zircon crystallizing from cooling and fractionating interstitial residual melt within the cumulate plagioclase framework.

## Paleomagnetism

We collected paleomagnetic cores that are 2.5 cm in diameter along the southern and eastern Beaver Bay Complex with a particular focus on acquiring paired sites of anorthositic xenoliths and their local diabase hosts. Sample cores were collected using a hand-held gasoline-powered

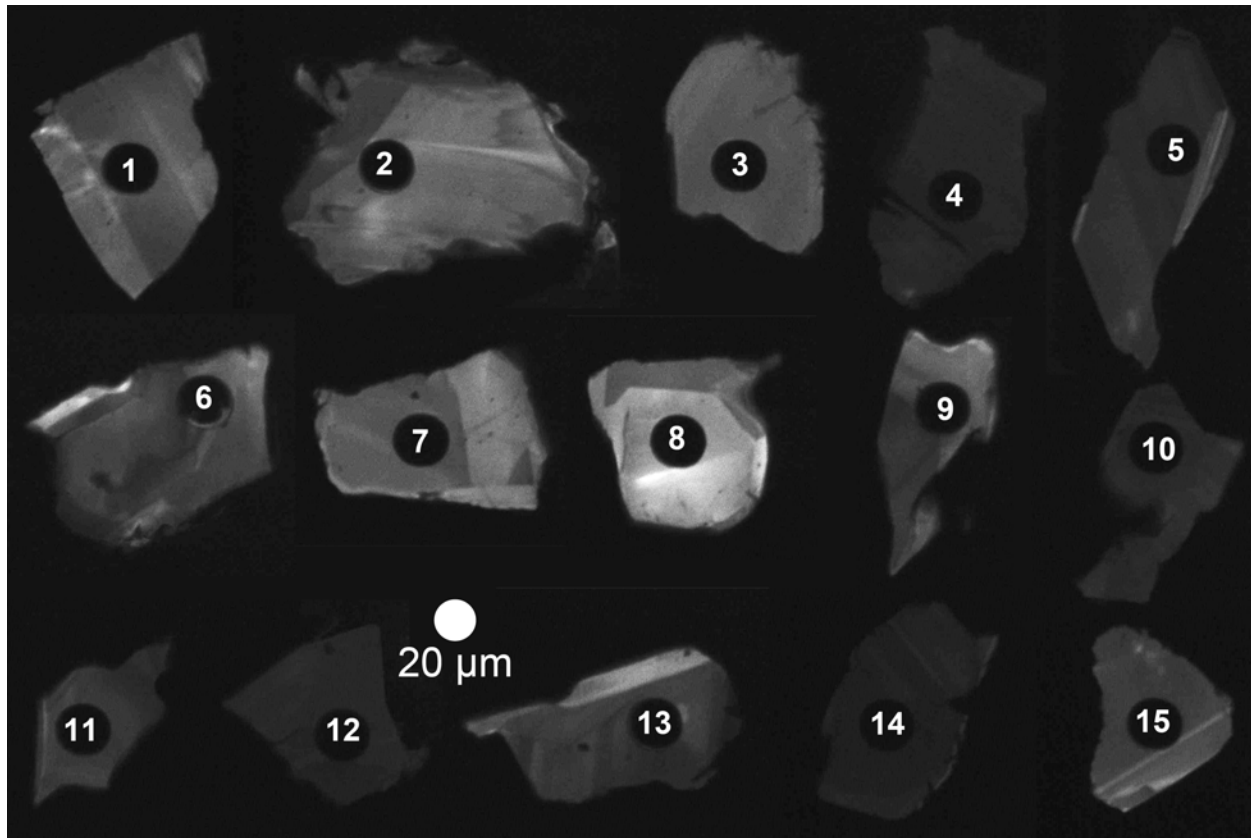


**Figure 2.5:** Cathodoluminescence (CL) image montage of the 15 zircons laser-ablated for trace element analysis from sample MS99033. There are sharp boundaries between zones of differing CL response within many of the zircons attributable to variable REE concentrations. For example, the bright zoning in grain 15 has a thickness of  $\sim 2 \mu\text{m}$ . Note that grain 1 (corresponding to spot 1) has a platy morphology, while the rest of the grains are subhedral to anhedral.

drill and were oriented using a magnetic compass as well as a sun compass when possible. Sun compass orientations were preferentially used for determining the sample azimuth. Typically, 7-10 cores were collected for each anorthosite xenolith and their diabase hosts. A total of 17 diabase and 22 anorthosite sites were sampled (Table 2.1). A table that summarizes the measured dimensions of each anorthosite xenolith sampled and the distance between each anorthosite paleomagnetic site and closest diabase host site is provided in the Supporting Information.

Samples underwent step-wise demagnetization and analyses in the magnetically-shielded room at the UC Berkeley Paleomagnetism Lab. 7 sites from the Beaver River diabase underwent alternating field (AF) demagnetization with peak fields from 1 mT to 130 mT. An ASC TD-48SC thermal demagnetizer was used to demagnetize 10 diabase sites and all 22 anorthosite sites in a step-wise manner, with reduced step increments between 540°C and 585°C. The typical magnetic field inside the shielded room is <500 nT and the field

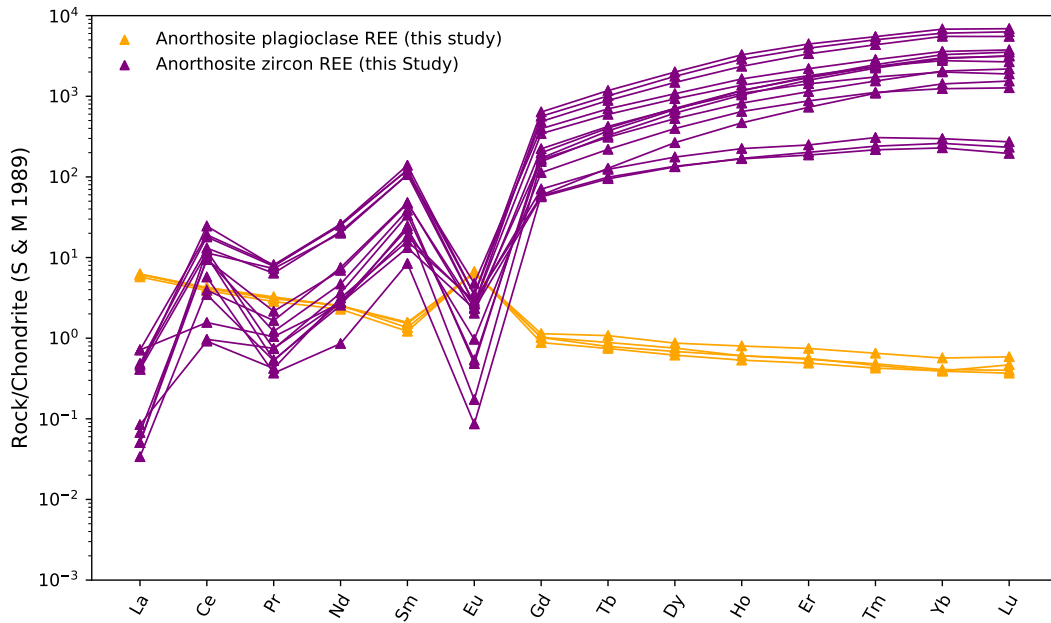


**Figure 2.6:** Rare earth element (REE) analyses for plagioclase crystals from anorthosite xenoliths and for 15 zircons from geochronology sample MS99033 (anorthosite xenolith site AX16) developed by inductively coupled plasma mass spectrometry. All data are chondrite-normalized (Sun and McDonough, 1989).

inside the thermal demagnetizer chamber is  $<10$  nT. The quartz glass sample rod of the UC Berkeley system is typically measured at  $5 \times 10^{-12}$  Am $^2$ . All remanence measurements were made on a 2G Enterprises DC-SQUID superconducting rock magnetometer equipped with inline AF coils and an automated sample changer system. The PmagPy software package was used to implement least-square fits to specimen demagnetization data (Tauxe et al., 2016). Measurement level data are available within the MagIC database (<https://earthref.org/MagIC/doi/10.1029/2021GC009909>)

For both the diabase and anorthosite demagnetization, principal component analyses show that an origin trending characteristic remanent magnetization (ChRM) can be isolated after the removal of a minimal secondary component during the first few low coercivity ( $<10$  mT) or low temperature ( $<200^\circ\text{C}$ ) demagnetization steps (Fig. 2.7). The ChRMs typically unblock through thermal demagnetization steps from  $\sim 500^\circ\text{C}$  to  $\sim 580^\circ\text{C}$ , consistent with the component being held by low-titanium titanomagnetite. We interpret this component as a primary remanent magnetization acquired during the emplacement and cooling of the Beaver River diabase.

The site mean paleomagnetic directions are shown in Table 2.1. We present both AF and thermal demagnetization results for the Beaver River diabase as both methods are effective

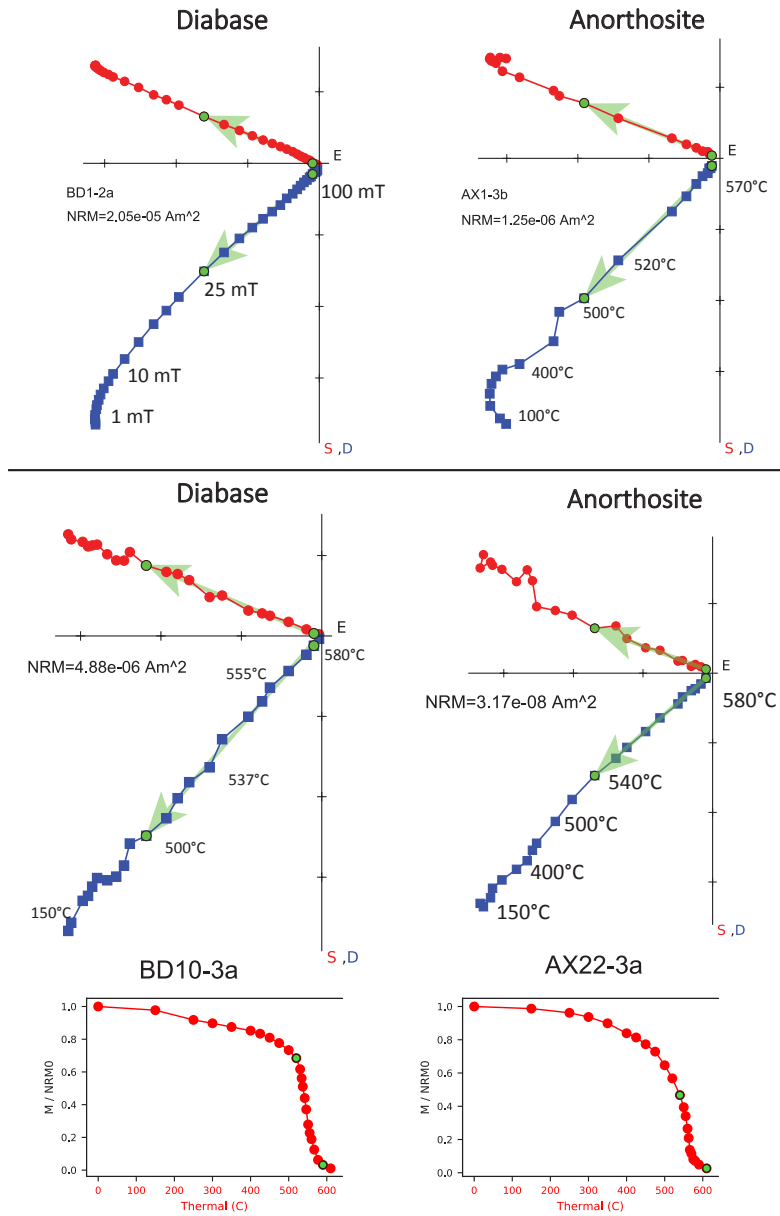


**Figure 2.7:** Example orthogonal vector demagnetization diagrams for diabase and anorthosite specimens. Anorthosite site AX1 is a xenolith within the diabase sampled as BD1. Similarly, AX22 is from a xenolith within the BD10 diabase. Both AF and thermal demagnetization show dominantly univectoral decay of characteristic remanent magnetizations (ChRM) toward the origin after removal of minimal secondary components. The data show very similar ChRM directions between the paired diabase and anorthosite xenolith sites. Representative magnetization intensity versus thermal demagnetization step plots are paired with orthogonal vector plots for specimen BD10-3a and AX22-3a.

in removing the secondary components and isolating the coherent and univectoral ChRM. Based on specimen and site level demagnetization behavior and the proximity between paired paleomagnetic sites of the anorthosite xenoliths and the diabase, we grouped the anorthosite xenoliths and their diabase hosts into individual cooling units and calculated a paleomagnetic pole position from the mean of the cooling unit virtual geomagnetic poles (Fig. 2.8).

Tilt-correcting the paleomagnetic directions to paleohorizontal is necessary for developing accurate paleomagnetic poles from the diabase and the anorthosite xenoliths to be compared to the Keweenawan Track apparent polar wander path (APWP; Fig. 2.8; Swanson-Hysell et al., 2019b). For intrusive igneous rocks, tilt corrections can be difficult to constrain due to the lack of a clear paleohorizontal reference. Many paleomagnetic studies of Midcontinent Rift intrusive rocks in the Lake Superior region did not apply tilt corrections to their data (e.g. Beck and Lindsley, 1969; Beck, 1970; Books et al., 1966). However, we can determine the structural orientation of the Beaver River diabase using the abundant igneous fabric orientations measured on the diabase as well as bedding orientations measured from adjacent volcanic units (Boerboom, 2004; Boerboom and Green, 2006; Boerboom et al., 2006, 2007; Miller et al., 2001). We compile the igneous layering measurements from the Beaver River diabase and the volcanic bedding orientations from the Schroeder-Lutsen basalt which is overlying the Beaver Bay Complex (Fig. 2.1). Despite the uncertainties associated with using igneous fabrics orientations as paleohorizontal references, the mean tilt orientations of the fabrics of the Beaver River diabase and the volcanic bedding orientations of the Schroeder-Lutsen basalt are similar (diabase overall dip direction - dip: 128.5 - 10.2; basalt dip direction - dip: 142.2 - 13.6). We combine the structural measurements from the Beaver River diabase and the Schroeder-Lutsen basalt and derived two sets of tilt corrections for the paleomagnetic directions of the diabase and anorthosite (dip direction - dip in the southern Beaver Bay complex: 128.7 - 12.9; in the eastern Beaver Bay Complex: 145.6-13.1, Supporting Information). The advantage of using the structural orientations from the Schroeder-Lutsen basalt is that the arcuate shape of the Beaver River diabase intrusions is nicely captured by the variation of lava dip directions while the dip angles of the basalt and diabase are very similar (Fig. 2.1).

The tilt-corrected ChRMs in both lithologies are west-northwest and down, yielding good specimen-level and site-level consistency (Figs. 2.7 and 2.8). Close directional similarities between each anorthosite xenolith and their host diabase are supported by 9 out of a total of 17 diabase-anorthosite paleomagnetic site pairs passing a common mean test (McFadden and McElhinny, 1990). The overall mean directions between the two lithologies are indistinguishable as they also pass a common mean test (Fig. 2.8, McFadden and McElhinny, 1990). For the anorthosite sites that do not pass a common mean test with their diabase hosts, they nevertheless have coherent specimen-level directions that are close to their host diabase directions (Fig. 2.8). We also plot the tilt-corrected mean pole of sites from both lithologies (diabase: 32.5°N, 189.5°E, N = 15, A95 = 6.3°, k = 37.4; anorthosite: 30.9°N, 190.8°E, N = 17, A95: 5.2°, k = 48.5; Table. 2.1) in context of a previously synthesized APWP from the volcanics of the Midcontinent Rift (Swanson-Hysell et al., 2019b) and show the poles to lie near the expected 1090 Ma and 1095 Ma pole positions (Fig. 2.8). The mean

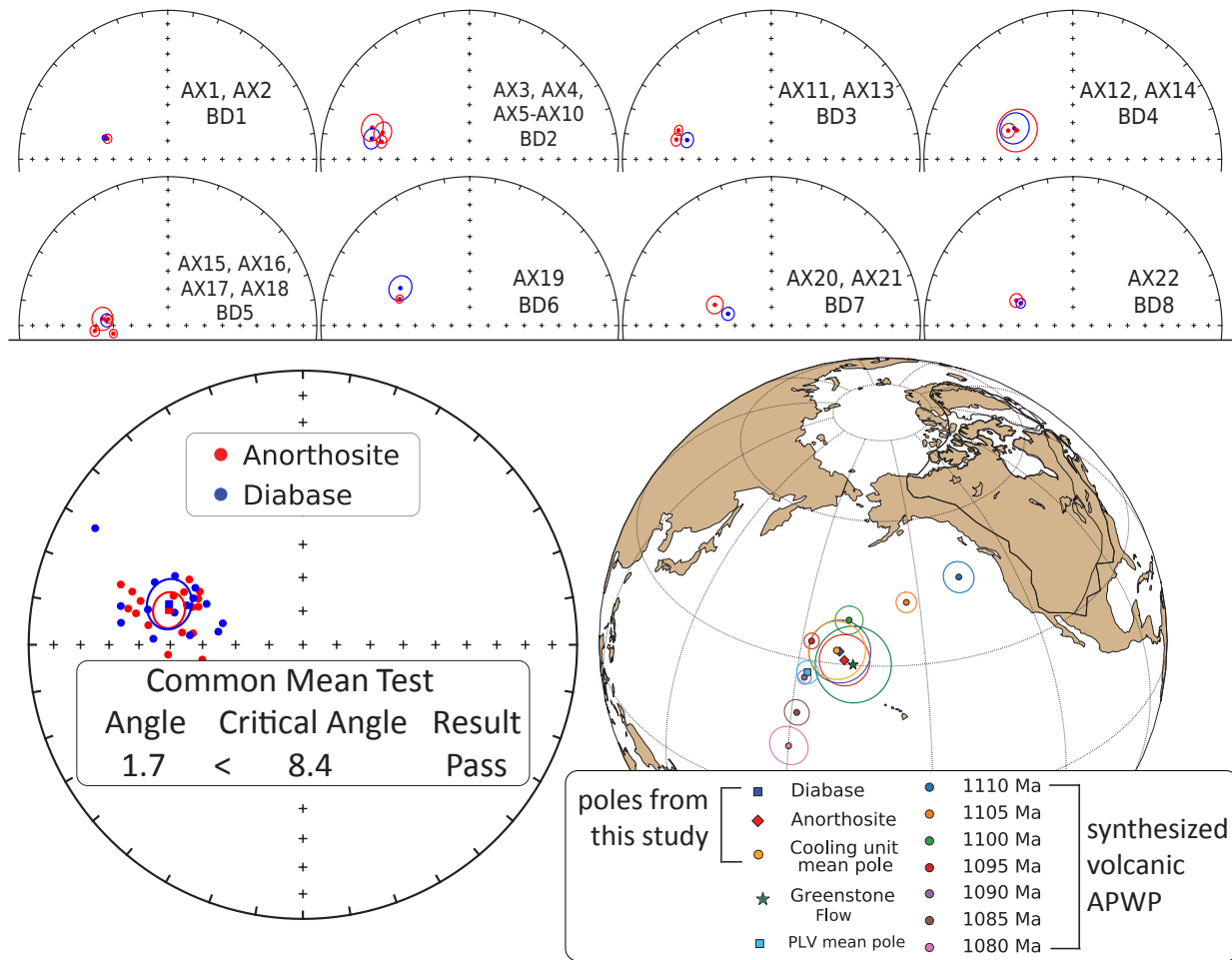


**Figure 2.8:** Top: Equal area plots of paleomagnetic directions from the anorthosite xenoliths and their local diabase hosts. AX: anorthosite xenolith site; BD: Beaver River diabase site. Bottom: Site mean paleomagnetic directions from the Beaver River diabase and anorthosite xenoliths are plotted on equal area plots. The anorthosite and diabase sites share a common mean as summarized by the results of the McFadden and McElhinny (1990) common mean test. Mean paleomagnetic pole positions of all diabase sites, all anorthosite sites, as well as a grand mean pole developed by grouping the anorthosite and diabase sites into individual cooling units are plotted against a synthesized Laurentia APWP based on poles from Midcontinent Rift volcanics and sedimentary rocks (Swanson-Hysell et al., 2019b). The paleomagnetic poles from the diabase and anorthosite are indistinguishable with the Greenstone Flow pole developed by Foucher (2018), but they all are distinct from the Portage Lake Volcanics mean pole (Swanson-Hysell et al., 2019b). All directions shown are tilt corrected.

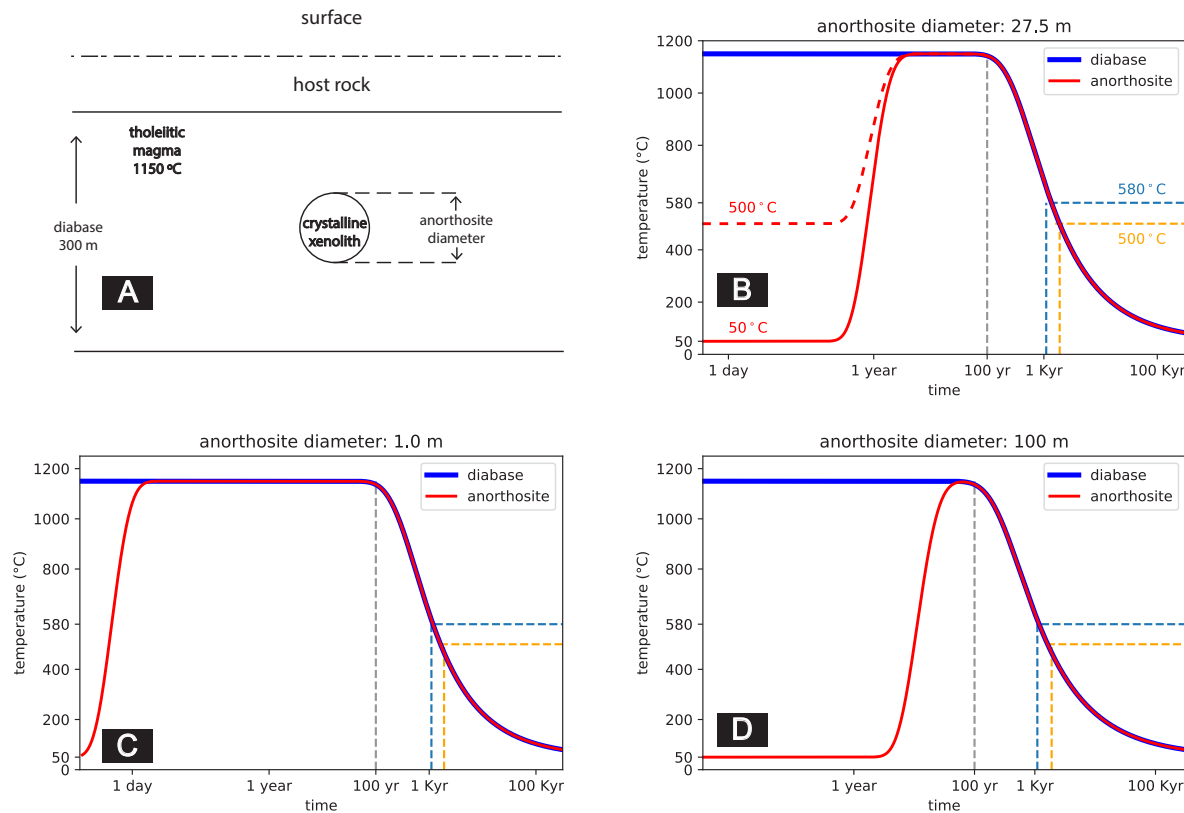


**Figure 2.9:** Thermal history model of the Beaver River diabase and its anorthositic xenoliths after emplacement at hypabyssal depths. (A) Schematic diagram for the thermal model considering cool anorthositic xenoliths as crystalline spheres residing in the middle of a diabase sill. Together they are hosted by cool country rocks at shallow depths. (B) Specific model for anorthositic AX16 (diameter of 27.5 meters) within its diabase sill host which is estimated to be 323 meters thick. (C) Thermal history model considering an anorthositic xenolith 1 meter in diameter residing in a 300 meter diabase sill. (D) Thermal history model considering an anorthositic xenolith 100 meter in diameter residing in a 300 meter diabase sill. These models show that anorthositic xenoliths were heated up to the diabase melt temperature after the emplacement, regardless of size. The time elapsed between magnetite blocking temperatures ( $580^{\circ}\text{C}$  and  $500^{\circ}\text{C}$ ) during cooling is on the scale of a thousand years.

pole position of the interpreted cooling units ( $32.7^{\circ}\text{N}$ ,  $188.8^{\circ}\text{E}$ ,  $N = 15$ ,  $A95 = 5.9^{\circ}$ ,  $k = 41$ ) lies close to the mean pole position derived from the ca. 1092 Ma Portage Lake Volcanics (Fig. 2.8), consistent with the coeval magmatic activity between the Beaver River diabase and the Portage Lake Volcanics. If it is included in future Laurentia APWP compilations, it is this cooling unit mean pole paired with the estimated diabase emplacement age of  $1091.7 \pm 0.2$  Ma that should be used.

**Table 2.1:** Summary of new site level paleomagnetic data for the Beaver River diabase and anorthosite xenoliths. n/N: number of samples/sites analyzed and included in the site/grand mean;  $dec_{is}$  &  $inc_{is}$ : in situ mean declination and inclination for the site;  $dec_{tc}$  &  $inc_{tc}$ : tilt-corrected mean declination and inclination for the site; k: Fisher precision parameter; R: resultant vector length;  $\alpha 95$ : 95% confidence limit in degrees; VGP lat—latitude of the virtual geomagnetic pole for the site; VGP lon—longitude of the virtual geomagnetic pole for the site. Full measurement level data are available within the MagIC database. <https://earthref.org/MagIC/doi/10.1029/2021GC009909>.

site	lat	lon	n/N	$dec_{is}$	$inc_{is}$	$dec_{tc}$	$inc_{tc}$	k	$\alpha 95$	VGP lat <sub>is</sub>	VGP lon <sub>is</sub>	VGP lat <sub>tc</sub>	VGP lon <sub>tc</sub>
AX1	47.2	-91.4	8.0	293.3	42.6	288.8	54.9	536.0	2.4	33.4	180.0	37.1	193.2
AX2	47.2	-91.4	9.0	282.0	31.3	277.2	42.6	145.0	4.3	20.4	181.8	22.6	191.1
AX3	47.6	-90.9	10.0	290.4	28.2	285.1	38.6	69.0	5.9	24.7	174.5	25.9	183.7
AX4	47.6	-90.9	7.0	291.9	20.0	288.3	30.7	91.0	6.4	22.3	169.8	24.4	177.2
AX5-10	47.6	-90.9	14.0	286.2	29.1	280.7	38.1	269.5	2.5	22.3	178.1	22.7	186.5
AX11	47.4	-91.2	8.0	284.9	23.5	281.7	35.2	305.0	3.2	19.1	176.3	22.0	184.1
AX12	47.3	-91.3	6.0	299.9	42.5	297.3	55.2	36.0	11.3	37.8	175.1	43.0	188.4
AX13	47.4	-91.2	9.0	289.8	23.0	287.3	35.1	434.0	2.5	22.2	172.4	25.7	180.0
AX14	47.3	-91.3	7.0	296.9	38.2	293.9	50.8	256.0	3.8	33.7	174.5	38.2	186.1
AX15	47.3	-91.3	8.0	282.9	42.3	275.8	53.5	86.0	6.0	26.2	187.2	27.9	199.8
AX16	47.3	-91.3	8.0	273.7	39.1	265.8	49.2	396.0	2.8	18.5	191.6	19.0	202.9
AX17	47.3	-91.3	8.0	273.6	49.8	261.6	59.6	647.0	2.2	24.3	198.3	23.7	213.5
AX18	47.3	-91.3	9.0	283.8	45.5	276.0	56.9	535.0	2.2	28.5	188.7	30.2	202.8
AX19	47.3	-91.3	8.0	293.9	35.8	290.7	48.2	695.0	2.1	30.5	175.4	34.6	186.0
AX20	47.3	-91.3	5.0	294.5	44.3	290.0	56.7	271.0	4.7	35.1	180.4	39.0	194.5
AX21	47.3	-91.3	8.0	301.7	37.7	299.9	50.5	803.0	2.0	36.7	170.4	42.1	181.7
AX22	47.4	-91.2	9.0	297.2	43.1	293.8	55.7	208.0	3.6	36.3	177.6	41.0	191.1
Anorthosite mean			17.0	289.3	36.5	284.5	48.2	55.0	4.9	28.0	179.6	30.9	190.8
BD1	47.2	-91.4	15.0	293.1	40.9	288.8	53.2	623.0	1.5	32.4	179.0	36.1	191.6
BD2	47.6	-90.9	8.0	286.6	22.7	282.0	32.6	122.0	5.0	19.9	175.0	21.0	182.8
BD3	47.4	-91.2	8.0	286.6	29.8	282.8	41.6	212.0	3.8	22.9	177.9	25.8	186.9
BD4	47.3	-91.3	8.0	300.2	40.7	297.9	53.4	47.0	8.2	37.1	173.6	42.3	186.0
BD5	47.3	-91.3	8.0	282.7	44.8	274.8	56.0	271.0	3.4	27.4	188.9	28.9	202.6
BD6	47.3	-91.3	9.0	300.0	33.2	298.3	46.0	64.0	6.5	33.4	169.2	38.6	178.9
BD7	47.3	-91.3	7.0	292.4	53.1	285.0	65.3	305.0	3.5	38.5	189.2	41.3	208.3
BD8	47.2	-91.4	10.0	287.9	52.8	278.8	64.5	300.0	2.8	35.3	191.8	37.1	209.9
BD9	47.2	-91.3	7.0	278.2	33.8	272.3	44.6	55.0	8.2	19.0	185.7	20.4	195.6
BD10	47.4	-91.2	10.0	297.0	46.2	293.0	58.7	341.0	2.6	37.8	180.0	42.2	195.1
BD11	47.4	-91.3	8.0	296.4	41.7	293.0	54.2	429.0	2.7	35.1	177.1	39.5	189.9
BD12	47.3	-91.3	8.0	288.8	38.1	284.1	50.1	141.0	4.7	28.1	180.4	31.3	191.8
BD13	47.5	-91.1	8.0	280.4	22.4	276.9	33.6	341.0	3.0	15.6	179.2	18.0	186.7
BD15	47.7	-90.6	8.0	300.1	2.3	299.3	14.2	119.0	5.1	20.6	156.9	24.8	161.7
BD17	47.4	-91.2	8.0	295.1	28.5	292.9	41.0	550.0	2.4	28.0	170.8	32.3	179.3
Diabase mean			15.0	291.0	35.7	286.9	47.7	51.6	5.0	29.0	178.2	32.5	189.5

## Thermal history model

The consistency of the paleomagnetic directions between the anorthosite xenoliths and the host diabase indicate that the anorthosites were heated above the Curie temperature of low-titanium titanomagnetite ( $\sim 580^\circ\text{C}$ ) within the Beaver River diabase. To determine whether this thermal history is consistent with the geometry of the units and to gain more insight into the emplacement history of the xenoliths, we developed a cooling model. In this model, the anorthosite xenoliths are considered to be solid spheres with an initial cool temperature embedded in a uniform sheet of diabase magma (Delaney, 1987; Unsworth and Duarte, 1979). The modeled thermal histories for various sizes of anorthosite xenoliths are shown in Fig. 2.9. In one end member case, the initial temperature of the anorthosites is assumed to be  $50^\circ\text{C}$ . While this temperature is unrealistically low given that the anorthosites likely have a deep crustal source, thermal modeling shows that even a 100-meter anorthosite xenolith with such low initial temperature would have been heated to the temperature of the tholeiitic magma ( $1150^\circ\text{C}$ ) within the sill. This temperature is well above the Curie temperature of magnetite. Anorthosite xenoliths with an assumed initial temperature of  $500^\circ\text{C}$  will equilibrate with the magma temperature on a similar, but slightly shorter, timescale. Therefore, the model predicts that the remanent magnetizations of the anorthosites will be reset during emplacement within the diabase sills, regardless of their initial temperatures. Model parameters set to match the xenolith AX16, from which a U-Pb date was developed in this study, leads to a model where the 27.5 m xenolith would have stayed at the magma temperature for about 100 years after sill emplacement (Fig. 2.9). This duration estimate is a minimum as it does not consider heating associated with melt in the lower crust or during ascent prior to emplacement although this was likely rapid. The xenolith would have then cooled through the Curie temperature of magnetite ( $580^\circ$ ) after  $\sim 1$  kyr and acquired its magnetization as it cooled through magnetite blocking temperatures (down to  $\sim 500^\circ$ , Fig 2.7).

## 2.5 Discussion

### Origin and Age of the Anorthosite Xenoliths

There have been divergent interpretations regarding the age and magma source of the anorthosite xenoliths in the Beaver River diabase (Fig. 2.1). Grout and Schwartz (1939) recognized the xenolithic nature of the anorthosites and suggested that the massive intrusion of the older anorthositic gabbro within the Duluth Complex may have supplied anorthosite fragments that were later entrained by the Beaver River diabase emplacement. Morrison et al. (1983), on the other hand, argued that the xenoliths were sourced from Paleoproterozoic or Archean lower crust that were liberated and contaminated by Midcontinent Rift magmas based on Sm and Nd isotopic data. They interpreted a Sm-Nd model age of 1.9 Ga from one of the xenoliths as providing a minimum crystallization age for the anorthosites though they acknowledged that these constraints are not definitive with respect to the age.

In contrast to this Archean to Paleoproterozoic model, Miller and Chandler (1997) favored a scenario where the anorthosite crystallized as part of Midcontinent Rift magmatism. They cited work by Kushiro (1980) who showed that the changing density contrast between labradoritic to bytownitic plagioclase and tholeiitic magma at different crustal pressures would promote flotation of plagioclase in deep ( $>20$  km) crustal magma chambers and the creation of anorthosite cumulates in the lower crust. This mechanism of plagioclase flotation likely created massive anorthosite cumulates in the roof zones of subcrustal magma chambers during MCR magmatism. Miller and Weiblen (1990) speculated that plagioclase-phyric magmas tapped from these deep chambers fed shallow ( $\sim 5$  km) subvolcanic intrusions of the Duluth Complex, thereby creating the troctolitic anorthosites and gabbroic anorthosites of the Anorthositic Series. Miller and Chandler (1997) suggested that the nearly pure anorthosite xenoliths occurring in the younger and more hypabyssal diabase intrusions of the Beaver Bay Complex were harvested from these phase-segregated intrusions in the lower crust. They further argued that the isotopic data of Morrison et al. (1983) can be explained by anorthosite-forming MCR magmas having been contaminated by older crust rather than the anorthosites being older lower crust that was contaminated by MCR magmas.

Our new geochronology documents that the anorthosite xenoliths were liberated from depth and were emplaced within the shallow intrusions of the Beaver River diabase at  $1091.7 \pm 0.2$  Ma (95% CI). This timing of emplacement is constrained by the Beaver River diabase postdating the new  $^{206}\text{Pb}/^{238}\text{U}$  zircon date of  $1091.83 \pm 0.21$  Ma for the AX16 xenolith and being older than the cross-cutting  $1091.61 \pm 0.14$  Ma Silver Bay intrusives.

The most straight-forward interpretation of the anorthosite  $1091.83 \pm 0.21$  Ma U-Pb zircon dates is that they record crystallization of the anorthosite cumulates during Beaver Bay Complex magmatism just before the time of Beaver River diabase emplacement. The significant negative Eu anomaly in the zircons within the anorthosite constrains them to have crystallized from a magma that had experienced significant plagioclase extraction (Fig. 2.6; Rubatto, 2002; Schaltegger et al., 1999). This result indicates that the zircons were comagmatic with their host anorthosite plagioclase. The Ti-in-zircon temperature estimates indicate that they crystallized from temperatures of  $\sim 998$  to  $860^\circ\text{C}$  (Supporting Information; Ferry and Watson, 2007). In addition, zircons that have lower Ti-in-zircon temperatures have lower Eu abundance, but enrichment of incompatible elements such as Hf and Th (Supporting Information). This systematic pattern of elemental concentration variation is consistent with the zircons crystallizing from residual melts on a cooling path that increased incorporation of incompatible trace elements and deepened the Eu anomaly with decreasing temperature and melt fraction. Scanning electron microscopy on two undated anorthosite xenoliths with plagioclase laths displaying interlocking textures shows zircon crystals with subhedral to anhedral shapes within the mineral assemblage that is interstitial to the plagioclase (Supporting Information). Cathodoluminescence (CL) images show internal zoning in zircons which can be attributed to variations in REE, particularly Dy elemental concentrations, during zircon crystallization (Fig. 2.5; Remond et al. (1992)). These data confirm that the zircons formed from residual melt within the interstitial spaces of the plagioclase cumulate and are inconsistent with a later metamorphic origin.

This scenario requires that there were large lower crustal magma chambers in which flotation of plagioclase resulted in cumulate formation during ca. 1092 Ma Beaver Bay Complex magmatism and contrasts with the model of Miller and Chandler (1997) for an older origin of the anorthosite during the ca. 1096 Ma Duluth Complex magmatism. Zircon U-Pb dates nearly always record crystallization age as the temperatures necessary for significant diffusive Pb loss exceed typical liquidus temperatures of zircon-bearing rocks. However, the anorthosites are a rather unique case given that the melting point of anhydrous plagioclase with an average composition of the Beaver River anorthosite (~70% anorthite; Morrison et al., 1983; Doyle, 2016) is quite high at ~1400°C. Thermal modeling indicates that the xenoliths would have equilibrated to the temperature of the olivine tholeiitic magma (~1100 to 1200°C) and remained at that temperature for more than 100 years in the diabase sill interior (Fig. 2.9). While these temperatures would not have melted the plagioclase or zircon, they are high enough to consider the possibility of Pb diffusion out of zircon. Could diffusive resetting of the zircon in the anorthosite cumulates xenoliths allow their crystallization at ca. 1096 Ma in the deep crust, but the closure of U-Pb zircon chronometer upon emplacement and cooling at ca. 1091.8 Ma?

The magnitude of Pb diffusion is dependent on the time spent at such a temperature. Using the diffusion parameters of Cherniak and Watson (2001), a sustained temperature of 1200°C for ~10 thousand years is required for diffusive loss of ~90% of Pb from a ~120  $\mu\text{m}$  diameter zircon. In this case, zircons that crystallized at 1096 Ma and then lost >90% of their Pb at 1091.6 Ma could give apparent U-Pb dates of 1091.8 Ma that are reproducible at the measurement resolution (Fig. 2.10). However, CL imagery reveals sharp boundaries between zones of differing CL response (Fig. 2.5) on the scale of ~2  $\mu\text{m}$ . Such CL zoning patterns are dominantly attributed to concentration variations in the rare earth element Dy (Remond et al., 1992). A time-temperature history that results in 90% Pb diffusion out of a 120  $\mu\text{m}$  diameter zircon would also cause Dy re-equilibration throughout a zircon, leaving no clear zonation (Fig. 2.10; Cherniak et al., 1997). Therefore, a scenario where the zircons first crystallized during Duluth Complex magmatism and subsequently lost more than 90% of Pb is exceedingly difficult to reconcile with the preservation of such thin, sharp zones. In fact, preservation of REE zoning in these zircons limits heating at the emplacement temperatures of the Beaver River diabase to a duration more consistent with our modeled duration of ~100 years of heating prior to cooling to the temperatures that preserve such zonation (Fig. 2.9, 2.10). It is therefore most probable that the Beaver River diabase anorthosite xenoliths are entrained cumulate enclaves that formed at the time of Beaver Bay Complex magmatism.

## A comagmatic relationship between the Beaver River diabase and the Greenstone Flow

Given the existence of many anorthosite xenoliths whose short-axis diameters often reach tens of meters and can be as wide as 180 meters (Fig. 2.1; Boerboom, 2004; Boerboom et al., 2006), the Beaver River diabase magma conduits must have been at least this wide during

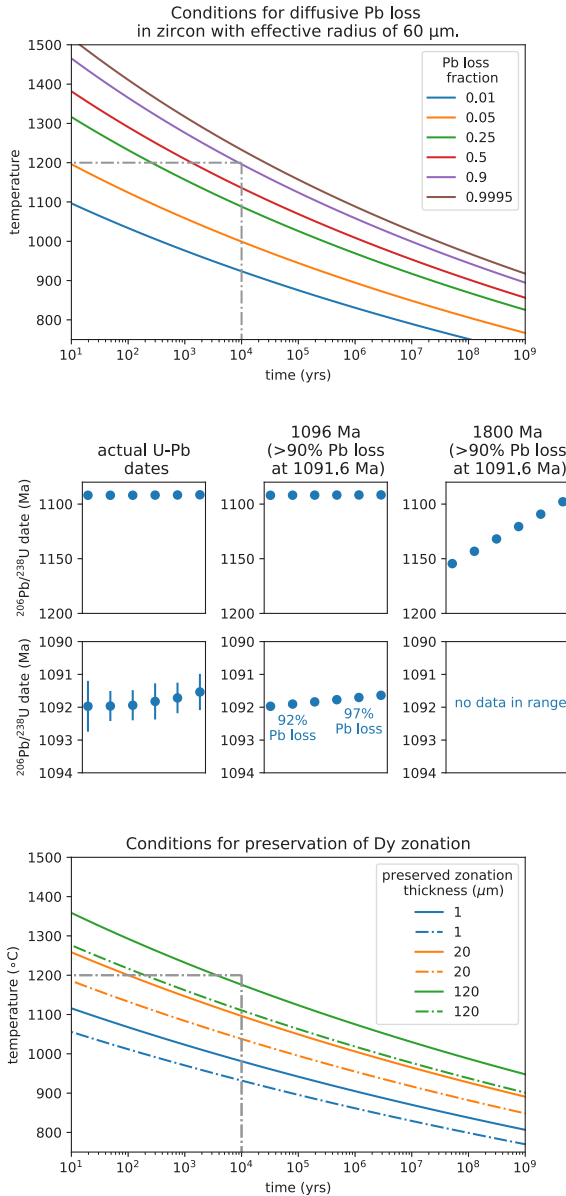


**Figure 2.10:** Top: Conditions for diffusive Pb loss in crystalline zircon for zircons of effective radii of 60 µm. Curves represent time-temperature conditions under which zircon will lose the indicated fraction of total Pb. Middle: Modeled zircon Pb loss scenarios with initial crystallization ages of 1091.8 Ma, 1096 Ma, and 1800 Ma with varying degrees of Pb loss at 1091.6 Ma compared to the actual U-Pb dates. Bottom: Conditions for preservation of Dy zoning in zircon. Curves represent time-temperature conditions under which different zoning thicknesses would be preserved in zircon. For conditions above the upper solid curves in each group, well-defined zoning will be lost at a given thickness. For conditions above the dashdot lines, zones will be partially lost but will retain initial composition in zone center. Pb diffusion and Dy zoning models follow Cherniak and Watson (2001) and Cherniak et al. (1997).

magma ascent. It would be consistent with such wide conduits extending to hypabyssal depths for magma that flowed through these conduits to have vented to the surface.

The high volume of the extrusive Greenstone Flow of the Portage Lake Volcanics lead to a potential match for this large feeder system. Doyle (2016) proposed a comagmatic link between the Beaver River diabase and the Greenstone Flow. Doyle (2016) discovered that both the intrusive Beaver River diabase and the Greenstone Flow have indistinguishable primary compositions that followed similar differentiation patterns. Doyle (2016) also highlighted the shared petrographic textures between the ophitic Beaver River diabase and the ophitic Greenstone Flow, which features the plagioclase laths clustering together and joining along their long crystallographic axes. The forsterite content of the olivines and enstatite content of the pyroxenes in the Beaver River diabase together with the Silver Bay intrusions, and the Greenstone Flow have overlapping compositions consistent with the same magma source (Fig. 2.11). The composition of the plagioclase within the units further strengthens this interpretation. Although there are no known multi-crystalline anorthosite xenoliths in the Greenstone Flow, plagioclase megacrysts occur in the lava flow. Analyses of the anorthite content from plagioclase megacrysts show very similar values between the Beaver River diabase and the Greenstone Flow basalt (Fig. 2.11; Doyle, 2016). In both units, the plagioclase cores are more enriched in anorthite than the rim and the groundmass. These data provide evidence that the core of the plagioclase megacrysts in the Greenstone Flow derived from a similar source with those in the Beaver River diabase and that the rims are later overgrowths. These mineralogical similarities are consistent with the interpretation that the Beaver River diabase and the Greenstone Flow have the same magma source.

The synchronicity between the Beaver River diabase and the Greenstone Flow inferred from comparable lithologies and geochemistry can be further evaluated using the paleomagnetic pole positions and radioisotopic dates from both units (Fig. 2.8, 2.4). The heat diffusion model of the cooling history of the anorthosite xenoliths within the diabase suggests that the time it takes to cool the diabase and anorthosite from low-titanium titanomagnetite Curie temperature ( $\sim 580^\circ\text{C}$ ) to their blocking temperatures ( $\sim 500^\circ\text{C}$ ) is on the time scale of a few thousand years (Fig. 2.9). This time scale is close to the typical  $10^4$  years which is considered to be sufficient for averaging out secular variations of the geomagnetic field. Fig. 2.8 shows the site mean paleomagnetic pole positions from all diabase and anorthosite sites in this study against the previously synthesized Laurentia APWP developed using an Euler pole inversion to chronostratigraphically constrained volcanic poles in present-day coordinates (Swanson-Hysell et al., 2019b). The site-mean pole positions of the diabase and anorthosite overlap within uncertainty ellipses and the mean pole positions fall between the 1095 Ma and 1090 Ma pole path positions (Fig. 2.8), consistent with the geochronology results (Fig. 2.4). Further, the mean paleomagnetic pole position derived from the Greenstone Flow share a common mean with those of the Beaver River diabase and the anorthosite xenoliths, but these poles do not share a common mean with the mean pole derived from the Portage Lake Volcanics (Fig. 2.8; Swanson-Hysell et al., 2019b). This result suggests that the timescale over which the Beaver River diabase and the Greenstone Flow acquired their magnetization may be too short to fully average out secular variation. In this case,

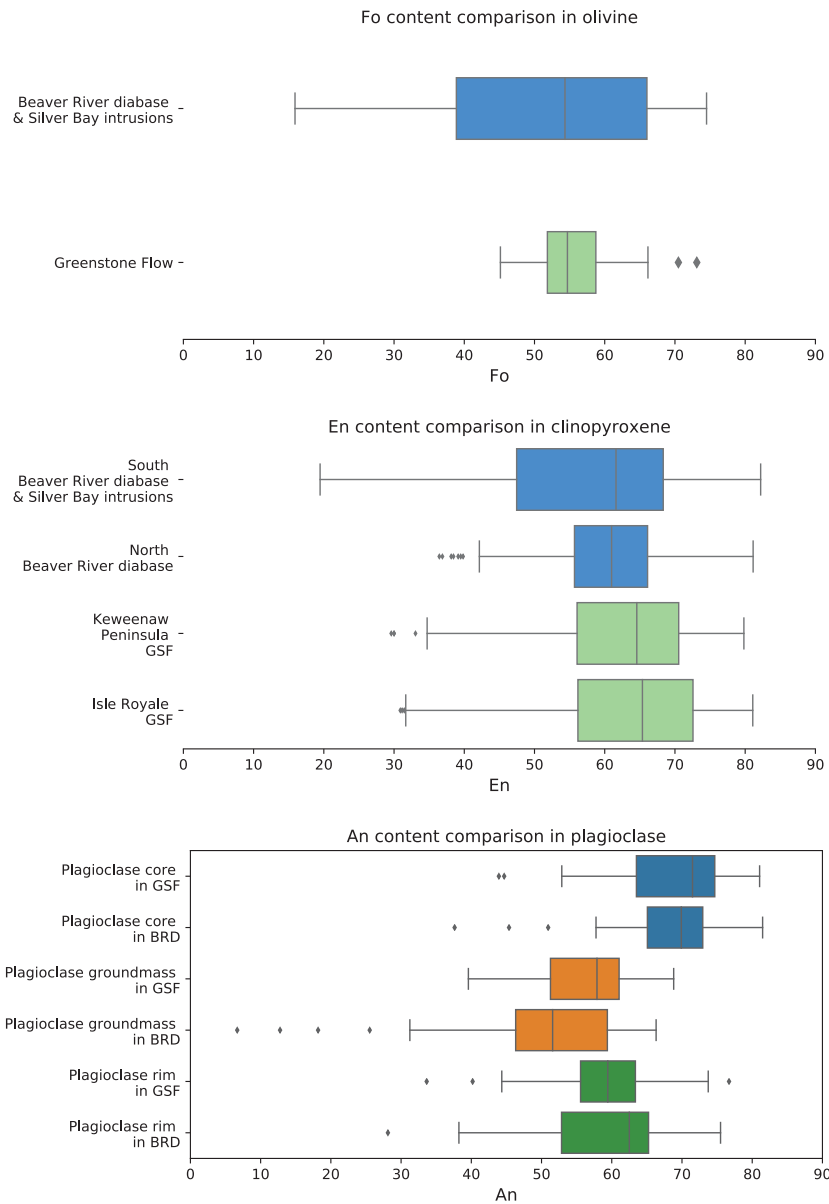


**Figure 2.11:** Box plots of geochemical analyses of olivine, pyroxene, and plagioclase in the Beaver River diabase (BRD) and Greenstone Flow (GSF). The forsterite content in olivine crystals and the enstatite content in clinopyroxene crystals are very similar in the Beaver River diabase and the Greenstone Flow. The anorthite concentrations in the core, groundmass, and rim of the plagioclase megacrysts within the Beaver River diabase and the Greenstone Flow share very similar patterns and the distributions are nearly identical. The box encloses the middle 50% of the data ranges (i.e., the interquartile range), and the notch represents the median values. The whiskers extend to the 2.5th and 97.5th percentile values. Fo-forsterite; En-enstatite; An-anorthite. Data from Doyle (2016).

the overlapping pole positions between the Beaver River diabase and the Greenstone Flow strengthens their temporal correlation even more (Fig. 2.8).

The U-Pb dates are consistent with a comagmatic relationship as they reveal indistinguishable ages for the Beaver River diabase and the Greenstone Flow. The age of the Beaver River diabase is constrained to be between the  $^{206}\text{Pb}/^{238}\text{U}$  dates of  $1091.83 \pm 0.21$  Ma and  $1091.61 \pm 0.14$  Ma (Fig. 2.4) giving an age estimate of  $1091.7 \pm 0.2$  Ma (95% CI). This age is indistinguishable with the  $^{206}\text{Pb}/^{238}\text{U}$  date of  $1091.59 \pm 0.27$  Ma for the Greenstone Flow (Fig. 2.4).

The Portage Lake Volcanics, including the Greenstone Flow, are interpreted to have erupted into the main central graben of the Midcontinent Rift during an interval of significant subsidence (Fig. 2.12; Miller and Chandler, 1997; Cannon and Hinze, 1992). In contrast to the thick accumulation in the Portage Lake Volcanics, the Beaver Bay Complex has an erosional (and slightly angular) unconformity atop it that is then covered by the younger Schroeder-Lutsen basalt (Fig. 2.1; Miller et al. (2001)). This relationship suggests that the Beaver River diabase was emplaced into a rift flank highland that experienced uplift during the active development of the central graben (Swanson-Hysell et al., 2019b). Eruptions fed through the Beaver River diabase network would have emerged from the rift flank and flowed from the highland into main rift basin (Fig. 2.12).

The proposed intrusive-extrusive connection between the Beaver River diabase and the Greenstone Flow would imply that the Greenstone Flow extended for more than 250 km from northeastern Minnesota to the northern end of Isle Royale where the flow is  $\sim 100$  m thick and to the northeastern end of the Keweenaw Peninsula, where the flow is  $\sim 400$  m thick (Fig. 2.1). With this length, the full volume of the Greenstone Flow reaches  $\sim 6000$  km $^3$  (Doyle, 2016), rivaling the largest known lava flows on Earth (Fig. 2.3). Such lengths were achieved for multiple high volume flows within the Columbia River basalts (Reidel et al., 2013) and are modest compared to the Rajahmundry Trap lavas of the Deccan Traps which traveled  $\sim 1000$  km (Self et al., 2008). One potential challenge for a flow having traveled from the Beaver River diabase to the Portage Lake Volcanics is that a reconstruction of present-day rift basin isopachs from seismic data indicates that there is a deep bowl-shaped volcanics-filled basin offshore of Minnesota and the Beaver Bay Complex (Stewart et al., 2018). While this basin has a thicker accumulation of volcanics than surrounding regions, it is unclear whether it was a topographic barrier. If it was, it could have prevented lavas from present-day northern Minnesota from reaching the portion of the basin now exposed on the Keweenaw Peninsula. Therefore, it is also possible that the indistinguishable ages and similar geochemistry between the Beaver River diabase and the Greenstone Flow are the result of them having been derived from a contemporaneous deep magmatic source without being connected on the surface.

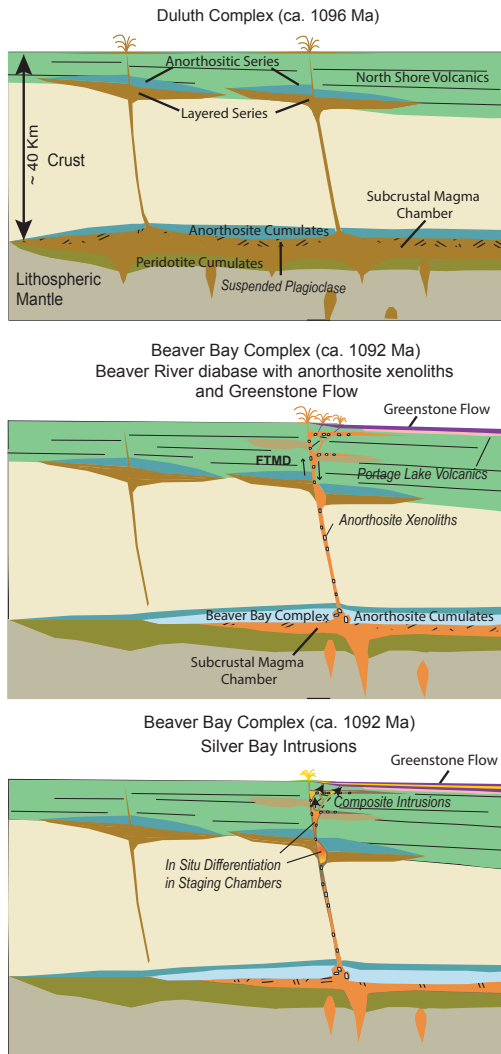


**Figure 2.12:** Schematic illustration of the emplacement of the ca. 1096 Ma Duluth Complex, the ca. 1092 Ma Beaver Bay Complex, Greenstone Flow and associated anorthositic lithologies. Top: Duluth Complex Anorthositic Series formed by subhorizontal emplacement of plagioclase crystal mushes generated by plagioclase flotation in subcrustal magma chambers. The Layered Series formed by emplacement of crystal-poor mafic magmas beneath the Anorthositic Series and variable differentiation by in situ fractional crystallization. Middle: Development of a deep crustal magma chamber that formed anorthositic cumulates and intrusion of the anorthositic xenolith-bearing Beaver River diabase of the Beaver Bay Complex along a major crustal fault (FTMD-Finland Tectonomagmatic Discontinuity) and its massive eruption at surface that could have formed the Greenstone Flow. Bottom: Emplacement of the Beaver River diabase and the Greenstone Flow. The Silver Bay intrusion may have added to the composite composition of both units, through magma differentiation in deeper staging chambers. The erosional unconformity between the Schroeder-Lutsen basalt and the Beaver River diabase suggest the diabase was emplaced into an uplifted rift flank highland which would have led to flank eruptions into the main Midcontinent Rift basin.

## 2.6 Conclusion

There was voluminous emplacement of magma into the shallow subsurface and eruption into the Midcontinent Rift basin ca. 1091.7 Ma at the end of the main stage of Midcontinent Rift volcanism. The anorthosite xenoliths within the Beaver River diabase and their U-Pb geochronology, whose interpretation is informed by REE patterns, indicate that there was a contemporaneous deep crustal magmatic system in which flotation of plagioclase formed anorthosite cumulates. The large dimension of the anorthosite xenoliths require that conduits feeding magma to the surface had widths that exceeded 150 meters. These conduits would have delivered a high volume of magma into the rift basin. The high-precision U-Pb dates, together with paleomagnetic and geochemical data, are consistent with the hypothesis that the Beaver River diabase was the feeder system of the Greenstone Flow although they could have been disconnected at the surface and both be emblematic of this high-volume pulse of magmatism..

## 2.7 Acknowledgments

Project research was supported by NSF CAREER grant EAR-1847277 to Nicholas L. Swanson-Hysell and an Institute on Lake Superior Geology Student Research Fund grant to Yiming Zhang. Permits for fieldwork and sampling from the Minnesota Department of Natural Resources are gratefully acknowledged. The authors thank James Pierce and Blake Hodgin for assistance in the field. The authors thank Stephen Self for providing constructive comments regarding mafic lava flow volumes. We thank John Grimsich and Tim Teague at UC Berkeley EPS department for their help with petrographic sample preparation and analyses. We thank U.S. Geological Survey reviewer Jonathan Hagstrum and journal reviewers Bernie Housen and William Rose for their constructive comments on the manuscript.

# Chapter 3

## High geomagnetic field intensity recorded by anorthosite xenoliths requires a strongly powered late Mesoproterozoic geodynamo

### 3.1 Abstract

Obtaining estimates of Earth's magnetic field strength in deep time is complicated by non-ideal rock magnetic behavior in many igneous rocks. In this study, we target anorthosite xenoliths that cooled and acquired their magnetization within ca. 1092 Ma shallowly emplaced diabase intrusions of the North American Midcontinent Rift. In contrast to the diabase which fails to provide reliable paleointensity estimates, the anorthosite xenoliths are unusually high-fidelity recorders yielding high-quality, single-slope paleointensity results that are consistent at specimen and site levels. An average value of  $\sim 83$  ZAm $^2$  for the virtual dipole moment from the anorthosite xenoliths, with the highest site-level values up to  $\sim 129$  ZAm $^2$ , is higher than that of the dipole component of Earth's magnetic field today and rival the highest values in the paleointensity database. Such high intensities recorded by the anorthosite xenoliths require the existence of a strongly powered geodynamo at the time. Together with previous paleointensity data from other Midcontinent Rift rocks, these results indicate that a dynamo with strong power sources persisted for more than 14 million years ca. 1.1 Ga. These data are inconsistent with there being a progressive monotonic decay of Earth's dynamo strength through the Proterozoic Eon and could challenge the hypothesis

---

This chapter is published as a peer-reviewed manuscript: Zhang, Y., Swanson-Hysell, N.L., Avery, M.S., Fu, R.R., (2022), High geomagnetic field intensity recorded by anorthosite xenoliths requires a strongly powered late Mesoproterozoic geodynamo. PNAS. doi: <https://doi.org/10.1073/pnas.2202875119>.

of a young inner core. The multiple observed paleointensity transitions from weak to strong in the Paleozoic and the Proterozoic present challenges in identifying the onset of inner core nucleation based on paleointensity records alone.

## 3.2 Introduction

Earth's magnetic field is the result of convective flow of liquid iron-alloy in Earth's outer core. At present day, the geodynamo is collectively powered by heat flow across the core-mantle boundary (CMB) and from the crystallization of the solid inner core from the liquid outer core which provides latent heat and compositional buoyancy due to the exclusion of light elements (Buffett, 2000). However, while paleomagnetic studies have found that a dynamo field has existed since at least 3.4 billion years ago (Selkin et al., 2007; Biggin et al., 2011; Tarduno et al., 2014; Brenner et al., 2020), Earth's inner core likely crystallized more recently. Estimates of the timing of the initial crystallization of Earth's inner core are interconnected with estimates for the core's thermal conductivity. Higher conductivity values imply faster cooling rates to maintain the geomagnetic field, which in turn imply that the threshold for the crystallization of the inner core happened more recently (Davies et al., 2015). While some estimated thermal conductivity values are consistent with an inner core age  $>3$  Ga (Gubbins et al., 2004; Konôpková et al., 2016), other estimates have implied higher thermal conductivity values and an age for the inner core that is less than 1.5 Ga (Pozzo et al., 2012; de Koker et al., 2012; Gomi et al., 2013; Zhang et al., 2020; Frost et al., 2022), with some suggesting even younger ages ( $<700$  Ma; Labrosse, 2015; Ohta et al., 2016; Pozzo et al., 2022). The possibility of late inner core nucleation has motivated proposals of novel power sources to sustain the geomagnetic field through early Earth history including precipitation of light-element minerals such as MgO (Badro et al., 2016; O'Rourke et al., 2016; O'Rourke and Stevenson, 2016) and SiO<sub>2</sub> (Mittal et al., 2020) at the core-mantle boundary. Given that estimates for the core's thermal conductivity continue to be debated, it is crucial to use observational records as an independent constraint on the thermal evolution of Earth's core and mantle.

Paleomagnetic records from ancient rocks are one of the few types of observational data that have the potential to provide constraints on the thermal evolution of Earth's core. Evidence for a persistent magnetic field through the Proterozoic, for example, likely necessitates the existence of plate tectonics that sustained core-mantle boundary heat flow (Swanson-Hysell, 2021). However, strikingly low estimates of geomagnetic field strengths have been obtained ca. 565 Ma during the Ediacaran Period (Bono et al., 2019; Shcherbakova et al., 2019; Thallner et al., 2021a) and ca. 370 Ma during the Devonian Period (Shcherbakova et al., 2017, 2021; Hawkins et al., 2021), potentially indicating unusual periods of core dynamo activity at those times. The Ediacaran data have been interpreted to indicate that there was a progressively decaying field up to that time that was soon followed by initial crystallization of the inner core (Bono et al., 2019). Sparse paleointensity data in the Proterozoic Era (2500 to 539 Ma) and the reality of high variability in Phanerozoic Era records

(539 to 0 Ma) necessitate additional data to evaluate interpreted trends.

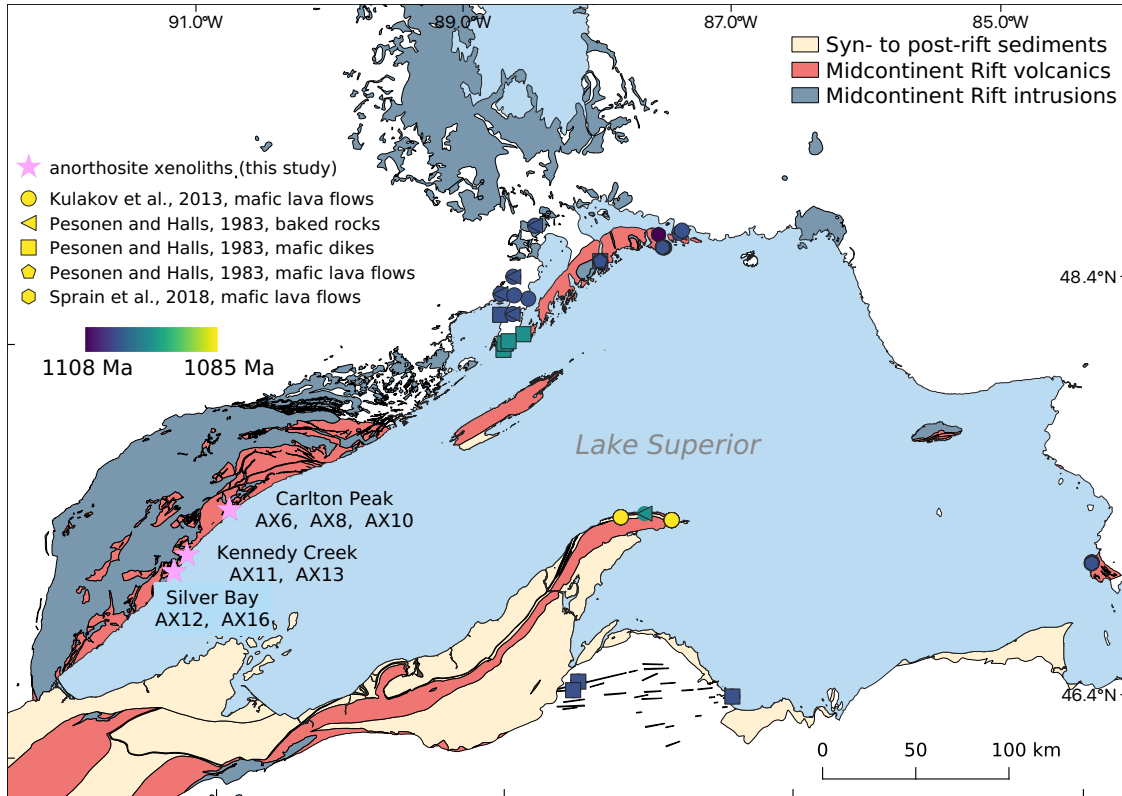


**Figure 3.1:** Simplified geologic map of the Lake Superior region showing the distribution of rocks associated with the late Mesoproterozoic Midcontinent Rift. Purple stars mark sites with paleointensity results that passed the selection criteria from this study. Paleomagnetic sites from Pesonen and Halls, 1983 are categorized by lithology. All sites from refs. Pesonen and Halls, 1983; Kulakov et al., 2013a; Sprain et al., 2018 are color-coded by their ages.

Determinations of the absolute value of ancient geomagnetic field strength rely on igneous rocks that acquire thermal remanent magnetizations as they cool. These magnetizations need to be unmodified by subsequent heating or chemical alteration in order to maintain the record of the ancient geomagnetic field from the time of cooling. Intracontinental magmatic events are an important target for determination of ancient paleointensity as they can be well-preserved within continental interiors. This interior position results in them typically being distant from tectonic events along continental margins that can drive alteration through heat and fluid flow. However, intraplate magmatism associated with large igneous provinces is typically of geologically short duration with the bulk of magmatic products emplaced within 1 Myr or less (Kasbohm et al., 2021). The Midcontinent Rift (Fig. 3.1) is an exception as it is a large igneous province where magmatism lasted  $\sim$ 25 Myr from ca. 1109 Ma to 1084 Ma during which there were pulsed intervals of more rapid magmatic activity (Swanson-Hysell et al., 2021b). Additionally, extension ceased in the Midcontinent Rift prior

to lithospheric separation, preserving volcanic, intrusive, and sedimentary rocks of the rift within the continental interior far from the continental margin and subsequent orogenesis. As a result, rocks of the rift have unusually simple paleomagnetic behavior for their greater than one billion-year-old age and paleomagnetic data from rift rocks form a central record of Mesoproterozoic paleogeography (Swanson-Hysell, 2021). The duration of magmatic activity within the Midcontinent Rift is longer than the entire 20.4 Myr long Neogene Period such that it provides an extended well-preserved window into the intensity of Earth's magnetic field in the late Mesoproterozoic.

Despite the excellent preservation of the rocks, non-ideal paleointensity behaviors have posed challenges for the interpretation of many previous paleointensity results from the Midcontinent Rift (Pesonen and Halls, 1983; Kulakov et al., 2013a; Sprain et al., 2018). The most trusted type of paleointensity estimate is that obtained through experiments in which the primary natural remanent magnetization (NRM) is progressively replaced by a laboratory magnetization that is imparted in a known field with internal consistency checks (such as in IZZI-style Thellier experiments; Yu et al., 2004). In such Thellier paleointensity experiments, one typical departure from ideal behavior due to the presence of nonuniformly magnetized grains (with either multidomain (Dunlop and Özdemir, 2001) or vortex states (Tauxe et al., 2020)) is sagging or double-slopes as visualized in Arai plots that show thermal remanent magnetization (TRM) acquired versus NRM lost. For such data, distinct paleointensity estimates may be calculated depending on the interpreter's choice of slope. Typically, such non-ideal behavior would result in a higher paleointensity estimate from the steeper-sloped low-temperature portion of the experiment and a lower paleointensity estimate from the high-temperature portion. For example, in data from the Midcontinent Rift, Pesonen and Halls (1983) used the low-temperature slope as the best representation of the past magnetic field strength (likely overestimating the field strength) whereas Kulakov et al. (2013a) used the high-temperature slope (likely underestimating the field strength). Such non-ideal results were rejected by Sprain et al. (2018) who applied stricter paleointensity selection criteria, but as a result had few accepted sites.

In this study, we target the high-purity anorthosite xenoliths of the Beaver River diabase in the Midcontinent Rift. While magmatic activity within the Midcontinent Rift was protracted, there were intervals of particularly rapid volcanism and voluminous emplacement of intrusions (Swanson-Hysell et al., 2021b). The ca. 1092 Ma Beaver Bay Complex in northern Minnesota punctuates one such period of magmatism during the main stage of Midcontinent Rift activity. The magma that formed the  $1091.7 \pm 0.2$  Ma Beaver River diabase dikes and sills of the Beaver Bay Complex transported numerous anorthosite xenoliths that have short-axis diameters up to 180 meters via wide conduits (Boerboom, 2004; Boerboom et al., 2006). These anorthosite xenoliths are plagioclase cumulates that formed comagmatically with the host diabase in the lower crust—an interpretation confirmed by U-Pb zircon geochronology (Zhang et al., 2021). They are attractive targets for paleomagnetic study as plagioclase crystals can protect magnetic inclusions from alteration. In addition, the alteration of the plagioclase crystals does not readily result in the formation of secondary iron oxides in contrast with Fe-silicate minerals such as olivine and pyrox-

ene. The anorthosite xenoliths targeted in this study were brought to the near surface in magma that formed hypabyssal (shallowly emplaced) intrusions of the Beaver River diabase (Zhang et al., 2021). They would have been heated to tholeiitic magma temperature ( $\sim 1100^{\circ}\text{C}$ ) which is below the melting point of the xenolith plagioclase (70% anorthite), but well above the Curie temperature of magnetite (Zhang et al., 2021). Fe-Ti oxides within the plagioclase likely exsolved above magnetite Curie temperature (Bian et al., 2021) and subsequently cooled and acquired thermal remanent magnetizations in conjunction with the host diabase at a paleolatitude of  $22 \pm 2^{\circ}$  (calculated from the paleomagnetic pole of the coeval Portage Lake Volcanics; Swanson-Hysell et al., 2019b). Paleointensity experiments on the anorthosite xenoliths have a high success rate, yielding consistent specimen- and site-level paleointensity results. The anorthosite xenoliths show low anisotropy of thermal remanent magnetization acquisition and can acquire TRM linearly within the range of relevant field strengths. Magnetic imaging shows that the anorthosite specimens have dominant magnetic carriers within and interstitial to plagioclase crystals without strong preferred orientations. Thermal modeling results and paleomagnetic directional data show that the anorthosite xenoliths acquired thermal remanent magnetizations while cooling with the Beaver River diabase (Zhang et al., 2021). Step-wise thermal demagnetization data show the anorthosite xenoliths to have dominantly single-component magnetizations that often unblock sharply within temperature ranges between  $500^{\circ}\text{C}$  and  $580^{\circ}\text{C}$ , consistent with remanence being held by low-titanium titanomagnetite (Zhang et al., 2021).

### 3.3 Methods

#### Sample collection and paleomagnetic directions

We collected paleomagnetic cores that are 2.5 cm in diameter along the southern and eastern Beaver Bay Complex with a particular focus on acquiring paired sites of anorthosite xenoliths and their local diabase hosts during summer field seasons in 2019 and 2020. Sample cores were collected using a hand-held gasoline-powered drill and were oriented using a magnetic compass as well as a sun compass when possible. Sun compass orientations were preferentially used for determining the sample azimuth. Sister specimens underwent step-wise alternating field (AF) or thermal demagnetization at the UC Berkeley Paleomagnetism Lab to isolate paleomagnetic directions (data presented in Zhang et al., 2021). Based on the anorthosite thermal demagnetization results, we selected sites whose unblocking temperature ranges are narrow and near  $580^{\circ}\text{C}$  for paleointensity experiments. Beaver River diabase sites with minimal secondary remanence were also selected for paleointensity experiments.

#### Paleointensity experiment

A total of 86 specimens from 14 anorthosite xenoliths and a total of 69 specimens from 7 diabase sites underwent paleointensity experiments that followed the step-wise double-heating

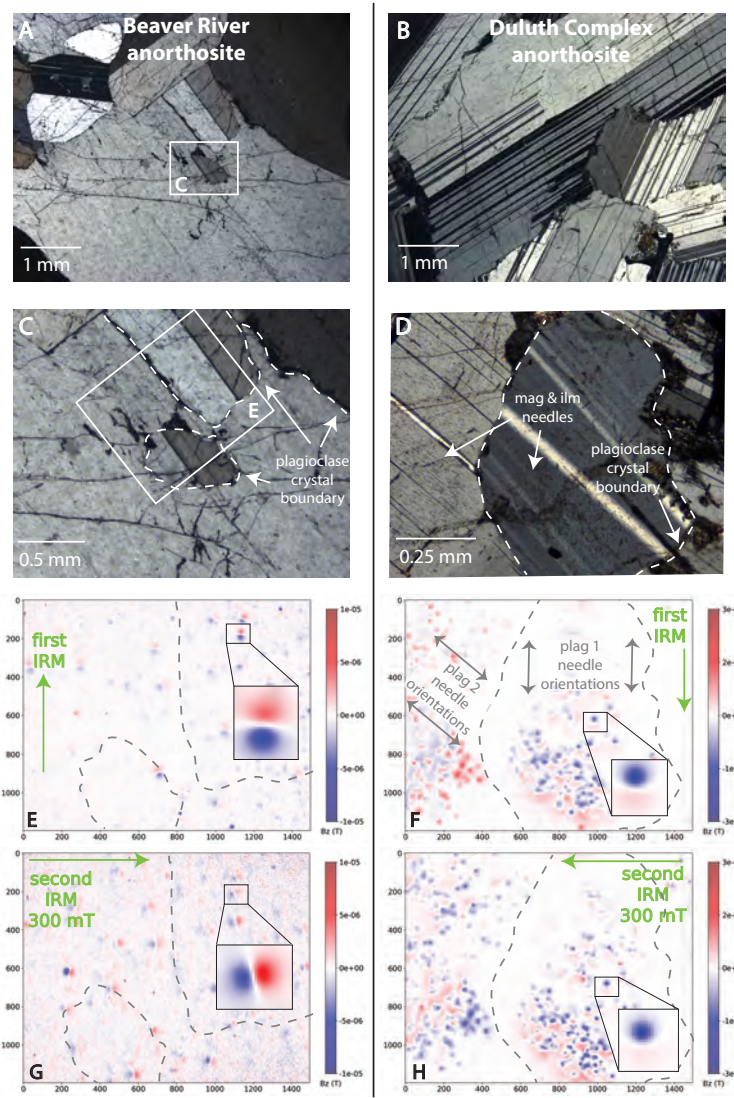


**Figure 3.2:** Thin section petrographic images (A,B,C,D) and magnetic maps (E,F,G,H) of an anorthosite sample from the Beaver River anorthosite xenolith in the Silver Bay region from which paleomagnetic site AX16 and geochronology sample MS99033 were collected (left column; Zhang et al., 2021) and from a distinct anorthosite within the Duluth Complex Anorthositic Series (right column). The Duluth Complex anorthosites were not targeted for paleointensity experiments in this study given complexities associated with more pronounced fabrics. Cross-polarized petrographic images of the Beaver River anorthosite (A,C) reveal plagioclase with a granoblastic texture of crystals that are largely free of large opaque inclusions. In contrast, plagioclase crystals in the Duluth Complex anorthosite have euhedral, interlocking crystals with an igneous foliation (B) and the plagioclase crystals contain abundant Fe-Ti oxide needles that have preferred orientations that are often parallel with the [001] axis of the plagioclase. Maps of the vertical component of magnetic field ( $B_z$ ) developed with a quantum diamond microscope (QDM) show relatively weak magnetic sources within plagioclase crystals in the Beaver River anorthosite (in E) relative to the strongly magnetic large oxide needles within Duluth Complex plagioclase (in F). The  $B_z$  color scale is an order of magnitude greater in the Duluth Complex anorthosite maps (F, H) than the maps for the Beaver River anorthosite (E, G). Panels (E) to (G) and (F) to (H) show experiments performed on both samples where we apply a first field along the y-axis of the field of view and then apply a second field of 300 mT orthogonal to the first field direction. The remanent magnetizations acquired by both anorthosites were mapped after the application of each field. The magnetic images show that remanent magnetizations of Beaver River anorthosite (i.e. the individual dipoles visible with paired red  $+B_z$  and blue  $-B_z$  lobes) align well with the first applied field direction (E) and then rotated to align with the second applied field direction indicating minimal anisotropic behavior (G). In contrast, the remanent magnetizations carried by the magnetic needles in plagioclase 1 of the Duluth anorthosite xenolith align well with the first applied field but those in plagioclase 2 acquired an oblique remanence direction with respect to the field direction (F). After the application of an orthogonal 300 mT external field, magnetization of those needles in plagioclase 1 did not change direction due to strong shape anisotropy whereas the magnetization of needles in plagioclase 2 flipped, but with the acquired remanence remaining oblique to the field direction (H). Insets in (E) to (H) show example dipole directions (fit using the algorithm of Lima and Weiss, 2016) in response to the application of orthogonal IRMs. The directional changes of the Beaver River anorthosite xenolith sources indicate a lower magnetic anisotropy compared to the relative lack of change for the Duluth Complex anorthosite xenolith sources. The unit of the axes in the QDM maps are in  $\mu\text{m}$ .

Thellier method (Thellier, 1959) using the IZZI protocol (Yu et al., 2004) with heating steps up to 585 °C. Partial thermal remanent magnetization (pTRM) checks were performed systematically throughout the experiment to test whether there was significant mineralogical alteration due to heating and were assessed using the SCAT parameter of Shaar and Tauxe, 2013. On top of the IZZI-Thellier experiment protocol, we also performed a comparative study where we added an extra step of 20 mT alternating field (AF) cleaning on some of the specimens after each in-field step. The purpose was to study whether the AF cleaning could help improve experiment success rate by removing the remanence component carried by materials such as multi-domain (MD) grains that contribute to non-ideal paleointensity behaviors. The results were similar when this step was applied without an observed change in experimental success rate. All remanence measurements were made on a 2G Enterprises DC-SQUID superconducting rock magnetometer equipped with an automated sample changer system at the UC Berkeley Paleomagnetism laboratory. The magnetometer is housed inside a three-layer magnetostatic shield that maintains background fields of less than 500 nT. Heating steps were performed using an ASC TD-48SC thermal demagnetizer with a controlled field coil that allows for a magnetic field to be generated in the oven in conjunction with a DC power supply. The thermal demagnetizer was degaussed with an alternating field in the axial orientation following each in-field step such that residual fields within the oven were <10 nT during zero-field steps. Samples were placed in the same location within the thermal demagnetizer for each heating step and were maintained in the same orientation with regard to the applied field. During each heating step, the oven remained at peak temperatures for 20 min to make sure each specimen reached the target temperature. An applied laboratory field of 30  $\mu$ T was used for all in-field steps. All heating steps were performed in air. The temperature increments for the experiments were chosen to isolate magnetizations held by (titano)magnetite informed by the previous demagnetization data, with smaller increments performed close to  $\sim$ 580°C.

## Paleointensity result selection

The following criteria were used as quality filters on the paleointensity results: (1) a maximum angular deviation (MAD; Kirschvink, 1980) of <10°; (2) scatter parameter ( $\beta$ ; Coe et al., 1978) values of <15%; (3) a deviation angle (DANG; Tauxe and Staudigel, 2004) of <5°; (4) fraction of remanence fitted for paleointensity estimate (FRAC; Shaar and Tauxe, 2013) >0.6; (5) scatter statistic (SCAT; Shaar and Tauxe, 2013) = TRUE; (6) a maximum magnetic moment difference between adjacent zero-field steps (GAP-Max; Shaar and Tauxe, 2013) < 0.25; (7) number of pTRM checks > 2; (8) and number of measurements used for paleointensity determination  $\geq$  4. MAD measures the scatter about the best-fit line through the natural remanent magnetization (NRM) steps in the selected interval for which the intensity is defined. DANG, the deviation angle, is the angle between the best-fit direction that is free floating and the direction between the center of mass of the data and the origin of the vector component diagram (Tauxe and Staudigel, 2004). Both MAD and DANG assess the directional variation of the NRM, with MAD measuring the scatter in

the NRM directions and DANG assessing whether the component is trending toward the origin of the Zijderveld plot.  $\beta$  is the “scatter” parameter of Coe et al. (1978) and is the ratio of the standard error of the slope of the best-fit line of the selected NRM and pTRM points on an NRM/TRM plot to the absolute value of the slope. FRAC is the fraction of the NRM that is used in the best-fit line (Shaar and Tauxe, 2013). The FRAC value was chosen to preferentially select samples with dominantly single-slope NRM/TRM plots. GAP-Max is the maximum gap between two points on the NRM/TRM plot determined by vector arithmetic. SCAT is a Boolean operator which uses the error on the best-fit slope of the selected data on the NRM/TRM plot to determine if the data are overly scattered. The parameter is used to assess pTRM checks in addition to assessing the degree to which IZZI steps are zigzagged.  $\beta$ , FRAC, GAP-Max and SCAT are all statistics to assess the behavior of NRM/TRM plots. See the Standard Paleointensity Definitions (Paterson et al., 2014; <https://earthref.org/PmagPy/SPD/home.html>) for more details. Data analysis was conducted using Thellier GUI (Shaar and Tauxe, 2013) within the PmagPy software package (Tauxe et al., 2016).

## Rock magnetic experiments

We conducted rock magnetic experiments to characterize the magnetic mineralogy and gain insights into the paleointensity results of the anorthosite and diabase. Back-field curves were measured at room temperature using a Micromag Princeton Measurements vibrating sample magnetometer (VSM) and a Lake Shore 8600 series VSM at the Institute for Rock Magnetism. Specimen median destructive fields (MDF) were calculated based on the back-field experiments. The calculated coercivity spectra were subsequently decomposed into one or more components using skew-normal distributions following the method of Maxbauer et al., 2016 examples of which are shown in Fig. 3.5. We also used a magnetic property measurement system (MPMS) at the Institute for Rock Magnetism to aid the identification of magnetic minerals. In the field-cooled (FC) experiments, specimen magnetizations were measured upon warming following the specimen having cooled in an applied field of 2.5 T from 300 to 10 K. In the zero-field-cooled (ZFC) experiment, a low-temperature saturation isothermal remanence (LTSIRM) of 2.5 T was applied at 10 K after the specimen cooled in a (near-)zero field. In the room-temperature saturation isothermal remanence (RTSIRM) experiment, the sample was pulsed with a 2.5 T field at room temperature ( $\sim$ 300 K) and then cooled to 10 K and warmed back to room temperature in a (near-)zero field. The magnetic moment transitions at critical temperatures shown through MPMS experiments were used to identify magnetic minerals such as magnetite within specimens (Feinberg et al., 2015).

To further identify the magnetic carriers within the Beaver River anorthosite xenoliths and compare them with the anorthosites of the Duluth Complex Anorthositic Series rocks, we used the quantum diamond microscope (QDM) at the UC Berkeley Paleomagnetism laboratory to image a thin section of sample MS99033 from anorthosite xenolith AX16 (which yielded a  $^{206}\text{Pb}/^{238}\text{U}$  zircon date of  $1091.83 \pm 0.21$  Ma; Zhang et al., 2021), and a

thin section of a Duluth Complex anorthosite (Fig. 3.2). We use the QDM to image the magnetic field over the polished thin section surfaces with a sample-sensor distance of  $\sim 5 \mu\text{m}$  in projective magnetic microscopy (PMM) mode with a spatial resolution of  $4.7 \mu\text{m}$  per pixel and an instantaneous  $0.9 \text{ mT}$  bias field that is canceled during the course of measurement (Glenn et al., 2017).

## 3.4 Results and Interpretations

### Petrography and magnetic imaging of anorthosite xenoliths

The dominantly monomineralic anorthosite xenoliths within the Beaver River diabase often have granoblastic texture characterized by equigranular crystals with weakly developed petrofabrics (Fig. 3.2A). Plagioclase crystals within coarse-grained intrusions often contain abundant elongate Fe-Ti oxide inclusions that are visible with optical microscopy (Feinberg et al., 2006; Wenk et al., 2011; Ageeva et al., 2016). The Beaver River anorthosite xenoliths lack such large ( $10\text{s of } \mu\text{m}$ ) oxide inclusions such that the oxides are not visible within the plagioclase crystals using optical microscopy (Fig. 3.2C). Magnetic imaging using a quantum diamond microscope (QDM), however, shows that there are magnetic remanence carriers within the plagioclase crystals (Fig. 3.2E, G). The sources of these magnetic remanence carriers are likely to be Fe-Ti oxides that exsolved within plagioclase crystals above the Curie temperature of magnetite (Zhang et al., 2021; Bian et al., 2021). To highlight these distinctive aspects of the Beaver River anorthosite xenoliths, we present petrographic and magnetic imaging data from the Beaver River anorthosite as well as an anorthosite sample from the Duluth Complex Anorthositic Series—an older intrusive complex within the Mid-continent Rift that was not targeted for paleointensity experiments in this study (Fig. 3.2). In contrast to the Beaver River anorthosite, the plagioclase crystals of this Duluth Complex anorthosite sample has a pronounced igneous foliation (Fig. 3.2B). In addition, there are abundant Fe-Ti oxide needles within the Duluth Complex plagioclase grains that are typically aligned with the [001] axes of the crystals (Fig. 3.2D). Magnetic imaging confirms that these needles have magnetic moments oriented along their long axes (Fig. 3.2F, H). As a result of this shape anisotropy, remanent magnetizations are acquired at angles highly oblique to applied fields (Fig. 3.2F). In an experiment where a second orthogonal field was applied, the first isothermal remanent magnetizations (IRM) of a set of magnetite needles within a plagioclase grain either fail to rotate or flip by  $180^\circ$ . When they flip, they remain in a direction that is oblique to the applied field direction dictated by shape anisotropy (Fig. 3.2F, H). These experiments enable novel visualization of the grain-scale magnetic anisotropy of elongated exsolved (titano)magnetite inclusions within plagioclase grains that leads to magnetic anisotropy observed at the bulk sample scale (Selkin et al., 2000; Feinberg et al., 2006). In contrast, the remanent magnetizations of the ferromagnetic grains imaged in the Beaver River anorthosite xenoliths, targeted for paleointensity in this study, align with the applied field directions indicating minimal remanence anisotropy (Fig. 3.2E, G). The

relative lack of petrofabrics and minimal grain-scale magnetic anisotropy make the Beaver River anorthosite xenoliths a particularly compelling target for paleointensity experiments.

## Paleointensity

Following IZZI-style paleointensity experiments (Yu et al., 2004), 40 from a total of 86 anorthosite specimens and 0 out of a total of 69 diabase specimens passed our paleointensity result selection criteria (see Materials and Methods section). Seven anorthosite sites and no diabase sites have specimen results that pass these selection criteria. Example NRM/TRM (Arai) plots are shown in Figure 3.3. Summary specimen absolute paleointensity estimates and site-level mean paleointensity values are plotted in Figure 3.4 (and provided in Table B.1) where each site represents an individual anorthosite xenolith. The paleointensity quality index ( $Q_{PI}$ ; Biggin and Paterson, 2014) for the anorthosite xenolith sites are all 5 or 6 (Table B.2). The cooling rate-corrected absolute paleointensity estimates from the anorthosite xenoliths have a mean of  $38.86 \pm 12.10 \mu\text{T}$ . The site-mean virtual dipole moment is  $\sim 83 \text{ ZAm}^2 (10^{21} \text{ Am}^2)$  ca. 1092 Ma. All measurement-level paleointensity experiment data are available within the MagIC database (<https://doi.org/10.7288/V4/MAGIC/19462>).

Typical paleointensity experimental data of the anorthosite specimens have straight, single-slope NRM/TRM plots and the accepted fractions of temperature steps span over the origin-trending, primary remanence components (Fig. 3.3). We accept specimen- and site-level absolute paleointensity results from those anorthosite xenoliths that pass the selection criteria. Other anorthosite xenoliths and diabase specimens failed the selection criteria largely because of double-slope or sagging behavior (fail FRAC selection; see Materials and Methods section), poor pTRM checks, and zigzagging behaviors occasionally superimposed on top of sagging behavior (fail SCAT, DANG selection; see Materials and Methods section; Fig. 3.3). A 20 mT alternating field treatment after in-field heating steps was applied to some specimens, but this treatment did not result in significant changes in the experimental results for the anorthosite xenolith or diabase specimens (Fig. 3.4).

In addition to estimating paleointensity values by introducing a set of selection criteria to filter our experiment results, we applied an independent statistical method from Cych et al. (2021) to all experimental data regardless of their NRM/TRM plot statistics to make a bias-corrected estimation of paleointensity (BiCEP). This Bayesian probabilistic method is based on the assumption that paleointensity estimates from specimens that come from a same cooling unit are distributed around a true paleointensity value with the various deflections being expressed as the curvature parameter of the NRM/TRM plot (Paterson, 2011). The posterior paleointensity distributions from these sites with high-quality specimen-level data are in agreement with the site-level averages developed using the selection criteria approach (Fig. 3.4; Fig. B.1). Overall, the high-quality results from the anorthosite xenoliths of the Beaver River diabase indicate that the anorthosite xenoliths record a high geomagnetic field ca. 1092 Ma.

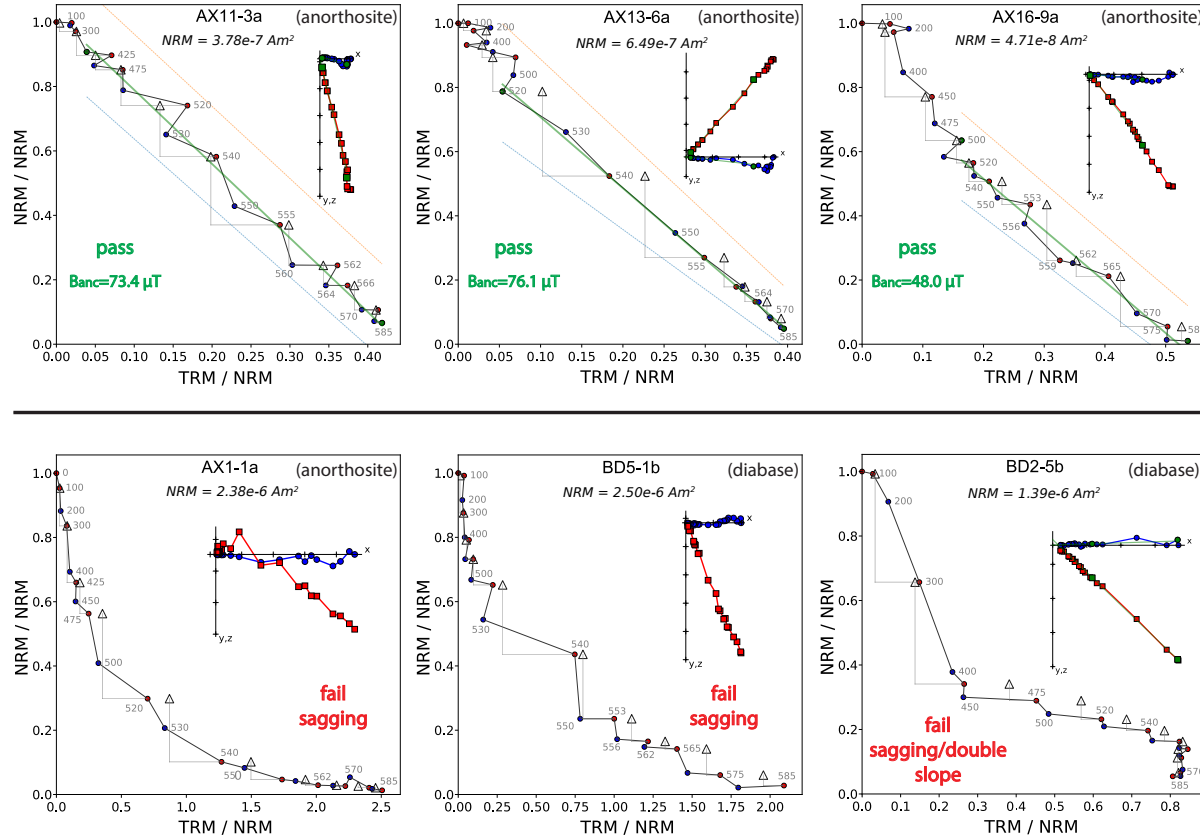


**Figure 3.3:** Example results of paleointensity experiments are displayed on Arai plots and zero-field heating results are shown as inset orthogonal plots (Zijderveld plots) for anorthosite and diabase specimens. Green squares and lines in Arai plots and green squares in orthogonal plots show the range of data points used for fitting. Red (blue) circles indicate zero-field/in-field (in-field/zero-field) steps ‘ZI’(‘IZ’). Triangles mark partial thermal remanent magnetization (pTRM) checks. Blue and red squares in the Zijderveld plots are X–Y and X–Z projections, respectively, of the NRMs in specimen coordinates. Dashed red and blue lines show bounding regions associated with the SCAT statistic (Shaar and Tauxe, 2013). Plots on the top row show successful specimen paleointensity results with straight, single-slope behaviors that pass our selection criteria. The green lines represent fits for the dominant single-slope component that passes the acceptance criteria and gives an estimate of the ancient field strength ( $B_{anc}$ ). The plots for anorthosite specimens AX1-1a and diabase BD5-1b on the bottom row show non-ideal sagging behaviour that fails our acceptance criteria. Specimen BD2-5a is an example where the data appear linear with distinct slopes in the low and high temperature ranges such that it could pass less restrictive selection criteria, particularly if a narrower temperature range was used for the experiment. Data analysis and visualization was conducted using PmagPy (Tauxe et al., 2016).

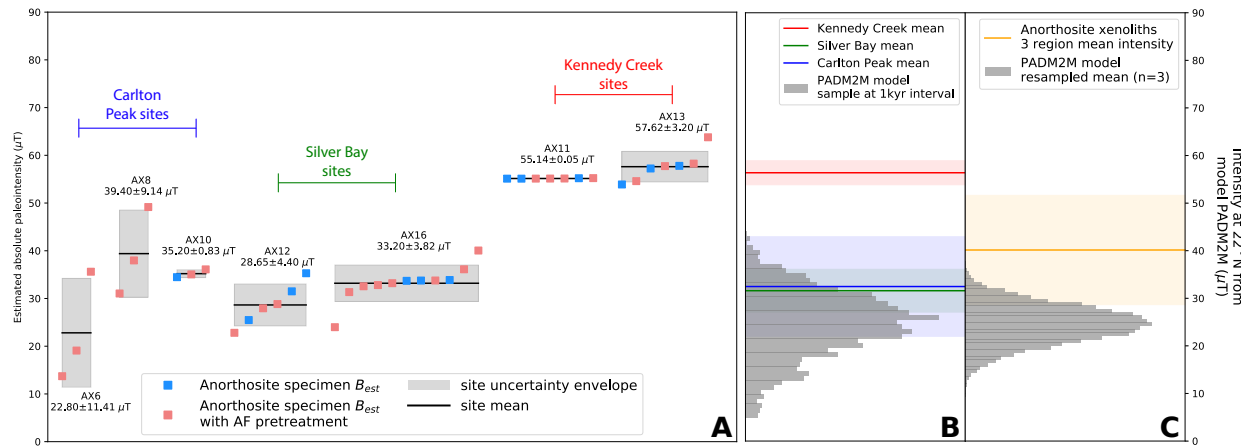


**Figure 3.4:** (A) Summary plot of individual specimen absolute paleointensity results (square symbols) and their averages and standard deviations at site level (black bars with grey one standard deviation uncertainty envelopes) where each ‘AX’ site is an individual anorthosite xenolith within the Beaver River diabase. All results are corrected for cooling rate bias with a factor of 0.75. The sites with successful experiments come from 3 regions (Carlton Peak, Silver Bay, Kennedy Creek) which would have cooled at distinct times yielding similar estimates within each region with differences between regions. (B) Regional means calculated from the specimen-level data are compared to the distribution of intensities calculated from a paleomagnetic axial dipole moment model for the past 2 million years (PADM2M; Ziegler et al., 2011) at the latitude corresponding to the paleolatitude of study region (22°N). (C) The mean of the 3 regional means is compared to means calculated from 3 random values drawn from the PADM2M model (Ziegler et al., 2011). The distribution represents a total of 10,000 iterations of taking 3 random draws and calculating the mean. These comparisons highlight that these anorthosites’ paleointensity values are strong in relation to the geomagnetic field over the past 2 million years. All shaded regions in (B) and (C) represent one standard deviation uncertainties.

## Rock magnetism

### Coercivity

Additional rock magnetic data indicate that those anorthosite specimens which pass the paleointensity selection criteria contain dominant magnetic remanence carriers with magnetic properties similar to stoichiometric, non-interacting, single domain magnetite, whereas anorthosite samples that failed the paleointensity result selection along with all diabase samples have more pronounced populations of non-ideal carriers. Magnetic property measurement system (MPMS) data show that both the diabase and anorthosite contain (titanio)magnetite as evidenced by the presence of the Verwey transition (Fig. B.2; Verwey, 1939; Feinberg et al., 2015). Anorthosite specimens from sites that yield successful paleointensity results have Verwey transition temperatures near 120 K as expected for stoichiometric magnetite with minimal Ti contents (Özdemir et al., 1993). However, diabase and anorthosite specimens that did not pass our paleointensity selection typically have Verwey transitions that are suppressed toward lower temperatures (Fig. B.2), indicating that their magnetic

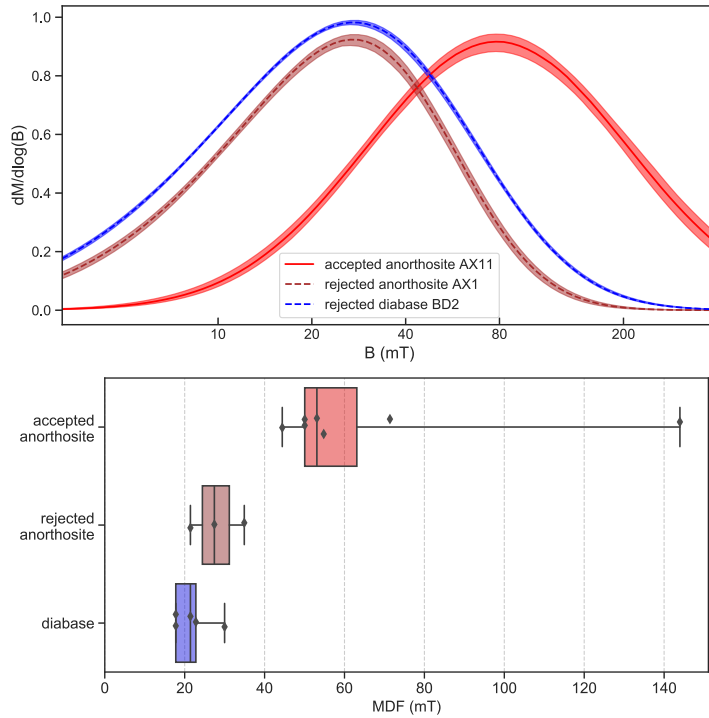


**Figure 3.5:** Top: Example coercivity spectra of anorthosite and diabase chips from sites that pass or fail our paleointensity selection criteria. Bottom: Box plots of median destructive field (MDF) values associated with back-field demagnetization for all anorthosite and diabase specimens with single-component coercivity unmixing results. Bars in the boxes show median values and the whiskers show the minimum and the maximum value of the datasets. Both plots show that anorthosite specimens that pass paleointensity selection criteria have higher coercivities consistent with a higher portion of single-domain-like magnetite grains than the other anorthosite specimens and the diabase.

grains either have relatively higher Ti content or have been partially oxidized (Özdemir et al., 1993). Another difference is that samples which pass paleointensity selection have distinctly higher average median destructive field values than other anorthosite and diabase specimens (Fig. 3.5). Single-component fits for coercivity spectra (Maxbauer et al., 2016) show that anorthosites having successful paleointensity results can contain magnetic grain populations that have higher coercivities. For these successful samples, median destructive (MDF) field values associated with back-field demagnetization experiments range from 44 to 144 mT with a median of 53 mT (Fig. 3.5). In contrast, other anorthosite and diabase specimens tend to have lower peak coercivities (MDF range of 18-35 mT with a median of 22 mT; Fig. 3.5). This result is consistent with an interpretation that magnetic grain populations with more multidomain-like behavior are responsible for the non-ideal paleointensity behaviors during experiments of such specimens (Xu and Dunlop, 2004).

### Bulk TRM anisotropy

Significant remanence anisotropy has been documented to exist within certain anorthositic rocks that formed in layered intrusive complexes (Selkin et al., 2000; Feinberg et al., 2006). Strong remanence anisotropy associated with the igneous foliation developed within anorthosite from the Stillwater Complex has been shown to cause significant overestimation or underestimation of paleointensity values depending on the relative orientations between the fabrics and an applied magnetic field (Selkin et al., 2000). To assess whether our paleointensity estimates are biased by bulk remanence anisotropy, we calculated the gamma statistic, which is the angular difference between the last pTRM step of paleointensity experiment and the applied field direction. The results show that the anorthosite specimens used in our paleointensity experiment have low gamma values ranging from  $0.9^\circ$  to  $11.9^\circ$ , with a median value of  $4.2^\circ$  (Table B.1). Because these anorthosite specimens were oriented at various directions with respect to the outcrops, the angles between the applied lab field direction during paleointensity experiments with respect to any fabrics within the anorthosite specimens are expected to cover a wide range of angles. These gamma values of the anorthosite xenolith bulk specimens are similar to those of the Midcontinent Rift volcanics studied by Sprain et al. (2018). Therefore, the bulk Beaver River anorthosite xenoliths do not have significant remanence anisotropy. Paleodirectional data from our anorthosite xenoliths indicate that they have minimal remanence anisotropy as their site mean directions closely match those of the Beaver River diabase hosts without deviating due to a fabric (Zhang et al., 2021). These bulk results are consistent with the data from the grain-scale magnetic anisotropy experiments that also show minimal remanence anisotropy (Fig. 3.2E, G).

### Considering secular variation and cooling rate

To best characterize the geomagnetic axial dipole field intensity during a certain time period, a paleointensity dataset should cover a sufficient amount of time such that paleosecular variations of the geomagnetic field are averaged. Thermal modeling results from Zhang et al., 2021 indicate that the Beaver River anorthosite xenoliths were heated to tholeiitic magma temperature ( $\sim 1100^\circ\text{C}$ )—lower than the melting temperature of the anorthosite plagioclase (given its composition of 70% anorthite; Morrison et al., 1983; Doyle, 2016) and acquired thermal remanent magnetization during cooling with their diabase host on a time scale of a few thousand years, partially averaging secular variation within single sites. Another consequence of the anorthosite xenoliths having slowly cooled in the interior of thick diabase intrusions is that slow cooling rates can bias paleointensity estimates toward higher values (Halgedahl et al., 1980). Large differences in cooling rates between acquisition of an NRM in nature versus a TRM in the lab can result in overestimated paleointensities for single domain grains (Dodson and McClelland-Brown, 1980; Halgedahl et al., 1980; Nagy et al., 2021). From the thermal history model of Zhang et al. (2021), we can estimate the duration over which the diabase and anorthosite cooled from the Curie temperature of magnetite ( $\sim 580^\circ\text{C}$ ) to the time when they blocked in the majority of their characteristic natural

remanence magnetization ( $\sim 500^\circ\text{C}$ ; Fig. 3.3; Zhang et al., 2021). We find the cooling time to  $\sim 500^\circ\text{C}$  to be  $\sim 1.5$  kyr, which corresponds to a cooling rate of  $\sim 1.7 \times 10^{-9} \text{ }^\circ\text{C s}^{-1}$ . In contrast, the lab cooling rate is much faster through the same temperature interval with an estimated cooling rate of  $\sim 1.3 \times 10^{-1} \text{ }^\circ\text{C s}^{-1}$ . The significant cooling rate difference leads to a predicted  $\sim 33\%$  overestimate of true ancient field following the model of Halgedahl et al. (1980) (Fig. B.3). This estimate on cooling rate effect is similar to the value of  $\sim 30\%$  overestimate derived from the model of Nagy et al. (2021). We therefore correct our paleointensity results by a factor of 0.75. Remanence held by vortex state (pseudo-single domain) and multidomain grains is not as biased by cooling rate (Biggin et al., 2013). The potential for some remanence to be held by these grains, as suggested by slightly zigzagging Arai plots (Fig. 3.3), could mean that this factor is an over-correction and true paleointensity values could be slightly higher than those reported here. The cooling rate-corrected specimen paleointensity estimates together with specimen- and site-level means are shown in Fig. 3.4.

Anorthosite xenoliths have paleointensity results that are consistent within small regions, but vary between regions. Anorthosite AX12 ( $28.65 \pm 4.40 \mu\text{T}$ ) and AX16 ( $33.20 \pm 3.82 \mu\text{T}$ ) in the Silver Bay area were emplaced  $\sim 450$  meters apart and have indistinguishable paleointensity estimates (Figs. 3.1 and 3.4).  $\sim 10$  km to the north, anorthosite xenoliths AX11 ( $55.14 \pm 0.05 \mu\text{T}$ ) and AX13 ( $57.62 \pm 3.20 \mu\text{T}$ ) in the Kennedy Creek area were also emplaced closely ( $\sim 125$  meters apart) and yield similar values to one another, but distinct paleointensity estimates from those of AX12 and AX16 (Figs. 3.1 and 3.4).  $\sim 30$  km further to the north in the Carlton Peak region, AX6 ( $22.80 \pm 11.41 \mu\text{T}$ ), AX8 ( $39.40 \pm 9.14 \mu\text{T}$ ), and AX10 ( $35.20 \pm 0.83 \mu\text{T}$ ) are anorthosite xenoliths within 10 meters of one another and also yield similar paleointensity estimates albeit with relatively large uncertainties (Fig. 3.4). The anorthosites of the three distinct regions captured three different intervals of geomagnetic field intensities during the emplacement and cooling of the Beaver River diabase sills ca. 1092 Ma. To contextualize the high paleointensity values, we plot the regional mean values (Table B.3) based on specimen-level paleointensity results together with calculated paleointensity values at  $22^\circ\text{N}$  latitude based on the PADM2M model of the time-varying geomagnetic field over the past 2 million years (Ziegler et al., 2011) in Figure 3.4B. The locality-mean values of these three regions are plotted in Figure 3.4C (and reported in Table B.3) where we also present the distribution of means calculated from 3 random values taken from the PADM2M model for a total of 10000 iterations. In addition, we perform the same comparison with the existing paleointensity data for the Cenozoic Era (the last 66 million years) from the PINT database (filtered by  $Q_{PI} \geq 3$ ; Fig. B.5) given that the observational dataset could record more geomagnetic field excursions or regional high flux patches. The anorthosite xenoliths three region-mean intensity is higher than all values from the resample results of the PADM2M model, and rival the top 3% values of the resample averages from the Cenozoic data (Fig. B.5). This comparison supports that the anorthosite xenoliths record an exceptionally strong geomagnetic field ca. 1092 Ma.

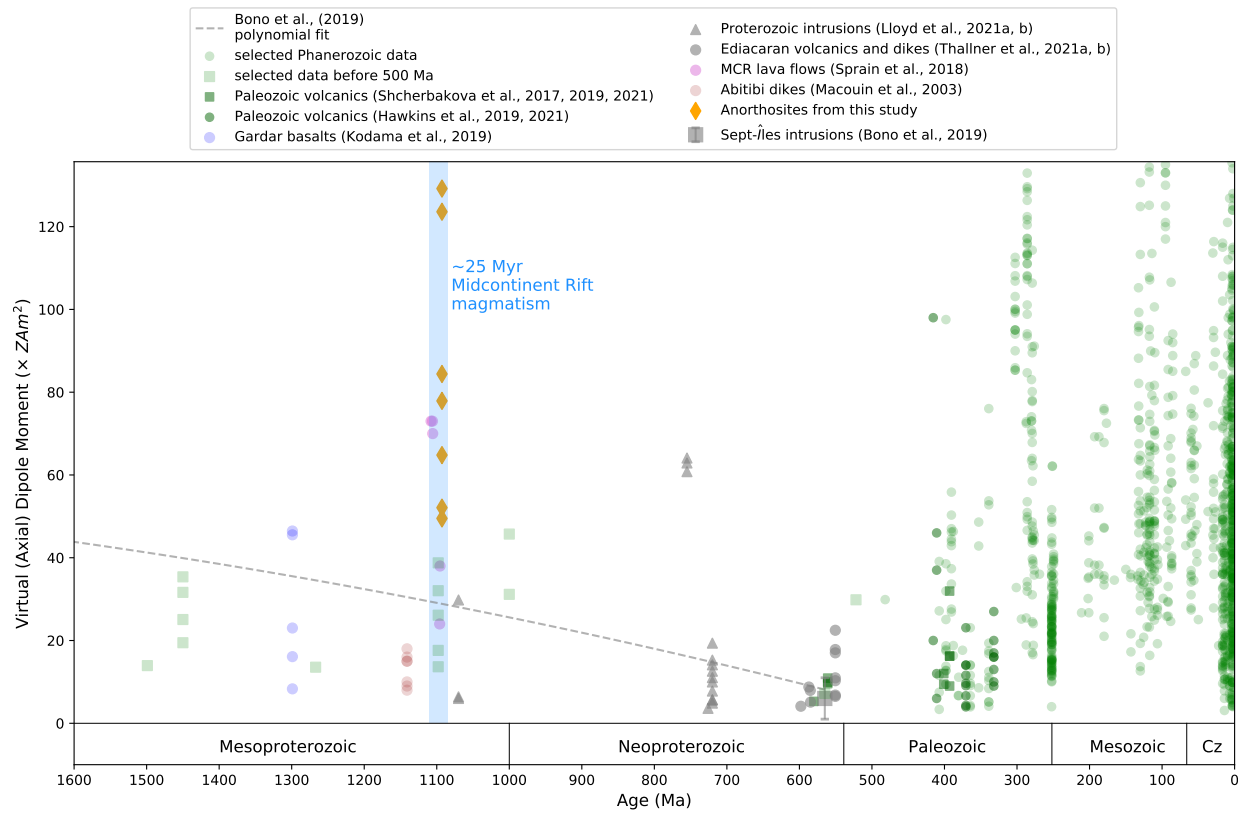


**Figure 3.6:** Compilation of calculated virtual (axial) dipole moment values from the PINT database (PINT v8.0.0; <http://www.pintdb.org/>; Bono et al., 2022a), including all Phanerozoic VDM and VADM records with  $Q_{PI}$  values  $>3$  and additional Neoproterozoic data from refs. Lloyd et al. (2021a,b); Thallner et al. (2021a,b). Paleointensity estimates from refs. Pesonen and Halls (1983) and Kulakov et al. (2013a) are not included in the compilation due to the specimen-level double-slope behavior as discussed in the text. Overall, the anorthosite xenoliths from this study record a high Mesoproterozoic field exceeding the value projected by the second order polynomial curve from Bono et al. (2019) which is based on an interpretation of there being a monotonic decay of the geodynamo through the Proterozoic. The highest site-mean virtual dipole moment of the anorthosites would rank in the top 2% of those in the database for the Cenozoic Era (the last 66 million years) when there was unequivocally a crystallizing inner core. The y-axis maximum is set at the 99th percentile of the compiled Cenozoic paleointensity data.

### 3.5 Discussion

The crystallization of the solid inner core is an important event in the long-term evolution of Earth's core and in sustaining the geodynamo (Buffett, 2000). The age of the inner core in thermal evolution models relies on estimates for the thermal conductivity of iron alloys at the temperatures and pressures of the core (Ohta and Hirose, 2021). Prior to studies of the last 10 years, an accepted value of  $\sim 30 \text{ W m}^{-1} \text{ K}^{-1}$  for this thermal conductivity constrained the timing of inner core nucleation to be during the first half of Earth's history

(Stacey and Loper, 2007; Konôpková et al., 2016). Subsequently, experimental data and *ab initio* simulations were interpreted to imply higher thermal conductivity values (Pozzo et al., 2012; Ohta et al., 2016) which in turn implied a younger age for the inner core (<700 Ma; Labrosse, 2015). However, other experimental studies continue to indicate lower thermal conductivity values consistent with prior estimates (Konôpková et al., 2016; Hsieh et al., 2020) with no consensus yet emerging (Williams, 2018; Ohta and Hirose, 2021). These experiments are challenging to conduct and interpret given complexities such as constraining the sample thickness under high pressure and temperature conditions, the validity of applying the Wiedemann-Franz law to extrapolate thermal conductivity values based on electrical resistivity measurements (Ohta et al., 2016), and propagating uncertainties from free parameters used in finite element modeling of direct thermal conduction experiments (Konôpková et al., 2016). Further experiments and theory are needed to explain these contrasting results which at present leave open very different trajectories for Earth’s thermal evolution. As a result, the age of the inner core is relatively unconstrained from a theoretical perspective.

The other data type that can provide insight into the long-term history of the core’s thermal regime and geodynamo is paleomagnetic data—both paleodirectional data that indicate the presence of a geomagnetic field and paleointensity data that constrain the field’s strength. Inner core nucleation would have increased the power to the geodynamo which has the potential to manifest as an increase in Earth’s surface field (Davies et al., 2021). An approach combining dynamo simulations and theoretical scaling relationships has predicted that progressive decay of the field’s dipole moment would be followed by a rapid increase in geomagnetic field intensity soon after the onset of inner core nucleation such that a minimum in dipole moment would occur just before inner core nucleation (Davies et al., 2021). Other scenarios are possible, however, such as the model-based prediction that while power increases associated with inner core nucleation strengthen Earth’s internal magnetic field, that the dynamo becomes more deeply seated in the core diminishes the increase in magnetic field strength at Earth’s surface (Aubert et al., 2009; Landeau et al., 2017). Such a scenario where the dynamo shifts to a greater depth associated with inner core nucleation led Aubert et al., 2009 to conclude that the increase in power to the dynamo would be difficult to detect with paleointensity data. Ultimately, further observational paleomagnetic records are key as they hold the potential for testing different model predictions and identifying transitions in ancient field strength (Biggin et al., 2015; Bono et al., 2019).

It has been proposed that Proterozoic paleointensity data are consistent with a progressive monotonic decay leading to a minimum ca. 565 Ma in the Ediacaran Period (Fig. 3.6; Bono et al., 2019). This interpretation was motivated by paleointensity estimates developed from the ca. 565 Ma Sept-Îles layered mafic intrusive complex of  $\sim 7 \text{ ZAm}^2$  that are among the lowest values in the paleointensity database (Fig. 3.6; Bono et al., 2019). A decay in the lead-up to this time was argued to be consistent with an absence of an inner core and a dynamo to which progressively less power was available through secular cooling (Bono et al., 2019; Davies et al., 2021). This timing of inner core formation would favor a high core thermal conductivity (e.g. Ohta et al., 2016). Paleomagnetic directional excursions (Halls et al., 2015), other weak paleointensity estimates (Thallner et al., 2021a), and frequent

polarity reversals (Kodama, 2021) in rocks of similar age are interpreted to be consistent with numerical simulations (Driscoll, 2016) associated with a weak dipole field.

The high paleointensity estimates from the 1.1 billion-year-old Midcontinent Rift rocks challenge the hypothesized monotonic decay of the geomagnetic field strength throughout the Proterozoic Era (Fig. 3.6). The well-preserved ca. 1092 Ma anorthosite xenoliths of the Beaver River diabase record a strong geomagnetic field in the late Mesoproterozoic that exceeds the modern-day field strength for which crystallization of the inner core is a power source (Figs. 3.4 and 3.6). Together with previous records obtained from the ca. 1106 Ma Osler Volcanics of the Midcontinent Rift (Sprain et al., 2018), these data indicate that appreciable power to Earth’s dynamo persisted through at least 14 Myr during the late Mesoproterozoic to maintain a strong surface field (Fig. 3.6). In addition to these high geomagnetic fields recorded by Midcontinent Rift rocks, the ca. 755 Ma Mundine Well dikes (Lloyd et al., 2021b) also require a stronger geomagnetic field in the Neoproterozoic than would be predicted by a progressive Proterozoic decline. Taken together, these results call into question whether the progressively decaying polynomial fit implemented by Bono et al. (2019) is an accurate representation for the evolution of the Proterozoic geomagnetic field (Fig. 3.6).

The hypothesis that a weak Ediacaran geomagnetic field is a telltale sign of the lack of an inner core with core nucleation following shortly thereafter may predict that it is the most significant weak to strong field transition in the paleointensity record. However, Fig. 3.6 shows that transitions from low to high field intensities occurred before, during, and after the Ediacaran Period. In the Ediacaran record developed to date, there is a two-fold increase in Earth’s virtual dipole moment when comparing estimates from the ca. 565 Ma Sept-Îles intrusions (Bono et al., 2019) to those from ca. 550 Ma volcanics of the Skinner Cove Formation (Fig. 3.6; Thallner et al., 2021b). In the late Mesoproterozoic, there is at least a six-fold increase within a period of  $\sim$ 35 Myr from a low average virtual dipole moment of  $\sim$ 13 ZAm<sup>2</sup> recorded by the ca. 1140 Ma Abitibi dikes which yielded straight Arai plots (Macouin et al., 2003), to a high moment of  $\sim$ 70 ZAm<sup>2</sup> recorded by the ca. 1106 Ma Osler Volcanics, with even stronger values from ca. 1092 Ma by Beaver River anorthosite xenoliths that record virtual dipole moments up to  $\sim$ 129 ZAm<sup>2</sup>. While the ca. 1140 Abitibi dikes’ paleointensity estimates are not as low as those of the ca. 565 Ma Sept-Îles intrusions, this virtual dipole moment increase in the Mesoproterozoic from the ca. 1140 Ma data to the ca. 1100 Ma data is the largest yet documented in the Precambrian on a 10s of millions of years timescale (Fig. 3.6). The tempo and scale of this field intensity transition could match with model-based predictions associated with the onset of inner core nucleation (Davies et al., 2021). This ca. 1.1 Ga timing would be broadly consistent with the ca. 1.3 Ga onset proposed by Biggin et al. (2015) albeit later given the exclusion of previous overestimated paleointensity values from the ca. 1.3 Ga Gardar basalts that are superseded by data in Kodama et al. (2019). However, a model prediction of sustained strong field values following inner core nucleation is challenged by data from the ca. 1070 Ma Bangemann Sills which include a sill with a low virtual dipole moment of  $\sim$ 6.4 ZAm<sup>2</sup> (Fig. 3.6; Lloyd et al., 2021b). Following the Ediacaran, there are also low paleointensity estimates from

Devonian rocks such as the ca. 370 Ma dikes and lavas of the Siberian Viluy Traps that give virtual dipole moment estimates of 4.3 to 14.9 ZAm<sup>2</sup> (Fig. 3.6; Hawkins et al., 2019). These low values as well as data from the ca. 414 Ma Strathmore lava flows (Hawkins et al., 2021), the ca. 410–380 Ma lava flows of Siberia and the Kola Peninsula (Shcherbakova et al., 2017), the ca. 408–393 Ma Buribay volcanics (Shcherbakova et al., 2021) and the ca. 332 Ma Kinghorn volcanics (Hawkins et al., 2021) have led to the proposal of this interval being the “Mid-Paleozoic Dipole Low” (Hawkins et al., 2021). This “Mid-Paleozoic Dipole Low” is followed by high paleointensity values such that there is a six-fold increase from virtual dipole moments of  $\sim$ 16 ZAm<sup>2</sup> ca. 332 Ma to  $\sim$ 99 ZAm<sup>2</sup> ca. 308 Ma in the late Carboniferous (Fig. 3.6; Hawkins et al., 2021).

Given that the multiple records of a weak field in the Proterozoic and Paleozoic cannot all be the minimum prior to the singular event of the onset of inner core nucleation, what processes could lead to a weak dipole at Earth’s surface even in the presence of a crystallizing inner core? Numerical models have shown that the dipole moment is sensitive to both the magnitude and spatial pattern of heat flow across the core-mantle boundary when there are strong available power sources to the geodynamo (Olson, 2007; Olson et al., 2010). In such models, relatively low total heat flux across the core-mantle boundary can prevent the axial dipole from reversing whereas a high heat flux through the boundary can result in an increase in reversal frequency and decrease in dipole intensity. The “Mid-Paleozoic Dipole Low” has been hypothesized to be the result of such elevated core-mantle boundary heat flux conditions at a time when there was also available power from a crystallizing inner core (Hawkins et al., 2019), thereby also explaining the observed low paleointensities which include values as weak as those of the ca. 565 Ma Sept-Îles intrusions (Fig. 3.6; Bono et al., 2019). Mantle convection can modulate core mantle boundary heat flow through changes in the structure of the deep mantle associated with upwelling plumes (Larson and Olson, 1991; Courtillot and Olson, 2007) and subducted slabs (Tan et al., 2002; Biggin et al., 2012; Hounslow et al., 2018). Strong evidence for differential plate tectonic motion extends back to ca. 2.2 Ga in the Paleoproterozoic (Mitchell et al., 2014; Swanson-Hysell et al., 2021a) and potentially back to ca. 3.2 Ga in the Archean (Brenner et al., 2020). Plate tectonic modulations of core mantle boundary heat flow are therefore expected throughout the Proterozoic. Such changes may explain large variability in Proterozoic paleointensity values similar to those seen in the Phanerozoic (Lloyd et al., 2021a) and may challenge our ability to detect the increase in surface geomagnetic field strength predicted to have happened at the onset of inner core crystallization.

Overall, the high-fidelity paleointensity recorders of the Beaver River anorthosite xenoliths in the well-preserved Midcontinent Rift record strong field strengths 1.1 billion years ago. The highest site-level value of the virtual dipole moment would rank in the top 2% of those in the database for the Cenozoic Era when there was unequivocally a crystallizing inner core. These high surface field strengths necessitate that appreciable power was provided to the late Mesoproterozoic geodynamo.

### 3.6 Acknowledgements

Project research was supported by NSF CAREER grant EAR-1847277 to N.L.S.-H., an Institute on Lake Superior Geology Student Research Fund grant to Y.Z., and an Institute for Rock Magnetism Visiting Student Fellowship to Y.Z. The Institute for Rock Magnetism is supported by the Instrumentation and Facilities program of the NSF Earth Science Division. Permits for fieldwork and sampling from the Minnesota Department of Natural Resources are gratefully acknowledged. We thank James Pierce and Blake Hodgin for their assistance in the field. We thank Jim Miller for providing us with the Duluth Complex anorthosite thin section. We thank Dario Bilardello, Peat Solheid, Mike Jackson, Josh Feinberg, and Bruce Moskowitz for their tremendous help with instrument operation, data interpretations, and research guidance at the IRM. Conversations with Bruce Buffett and Zachary Geballe informed our perspectives on the geodynamic and mineral physics literature. We thank Jon Hagstrum at USGS and two anonymous reviewers for their helpful comments on the manuscript.

## Chapter 4

# Paleomagnetism of the southwestern Laurentia large igneous province and Cardenas Basalt: pulsed magmatism during rapid late Mesoproterozoic plate motion

### 4.1 Abstract

Mafic intrusions, lava flows, and felsic plutons in southwestern Laurentia have been hypothesized to be associated with the emplacement of a late Mesoproterozoic large igneous province. Improved geochronologic data resolve distinct episodes of mafic magmatism in the region. The ca. 1098 main pulse of southwestern Laurentia large igneous province (SWLLIP) magmatism is recorded by mafic intrusions across eastern California to central Arizona. A younger episode of volcanism resulted in eruptions that formed the ca. 1082 Ma Cardenas Basalt—the uppermost unit of the Unkar Group in the Grand Canyon. Using the interpretation that the mafic intrusions within the Unkar Group were feeders to the lavas, a paleomagnetic pole was developed by combining data from the intrusions and the lavas. With the updated geochronological constraints, we develop new paleomagnetic data from mafic sills in the SWLLIP. Overlapping poles between the Death Valley sills and rocks of similar age in the Midcontinent Rift is inconsistent with large-scale Cenozoic vertical axis

---

Zhang, Y., Anderson, N., Mohr, M.T., Schmitz, M.D., Macdonald, F.A., Nelson, L.L., Thurston, O.G. Guenthner, W.R., Karlstrom, K.E., Swanson-Hysell, N.L. (2024). Paleomagnetism of the southwestern Laurentia large igneous province and Cardenas Basalt: pulsed magmatism during rapid late Mesoproterozoic plate motion. Submitted to JGR: Solid Earth.

rotations in Death Valley. We also develop a new paleomagnetic pole from the ca. 1082 Ma Cardenas Basalt (pole longitude=183.9°E, pole latitude=15.9°N, A<sub>95</sub>=7.4°, N=18). The new paleomagnetic data are consistent with the pole path developed from time-equivalent rocks of the Midcontinent Rift, supporting interpretations that changing pole positions are the result of rapid equatorward motion. These data add to the record of Laurentia's rapid motion from ca. 1110 to 1080 Ma that culminated in collisional Grenvillian orogenesis and the assembly of Rodinia.

## 4.2 Introduction

The ancient North American craton (Laurentia) has a rich record of Stenian (late Mesoproterozoic) mafic magmatism. In the Midcontinent Rift of the Lake Superior region, punctuated episodes of voluminous intrusions and associated volcanism have been dated between 1109-1084 Ma with high-precision geochronology (Figure 4.1). Paleomagnetic data from these well-preserved and well-dated rift-related rocks within the Midcontinent Rift make up the majority of the Stenian database of paleomagnetic poles for Laurentia (Evans et al., 2021). These data provide central constraints on global paleogeography during the assembly of supercontinent Rodinia (Swanson-Hysell, 2021; Evans, 2021).

In southwestern Laurentia, widespread Stenian magmatism led to the emplacement of mafic intrusions and lava flows as well as felsic plutons (Figure 4.1A; Wrucke, 1966; Shride, 1967; Hendricks, 1972; Howard, 1991; Bright et al., 2014). Based on petrologic and geochemical data (e.g. Wrucke, 1966; Wrucke and Shride, 1972; Hammond, 1986), it was previously suggested that the mafic intrusions in the region were contemporaneous. However, in comparison to the Midcontinent Rift where extensive high-precision zircon U-Pb geochronology data have been developed (typically with analytical uncertainties <1 Myr; e.g. Swanson-Hysell et al., 2019b), most ages from rocks associated with the Stenian southwestern Laurentia magmatism have been relatively imprecise (e.g. as compiled and developed in Bright et al. (2014)). The broadly overlapping ages, albeit with large uncertainties, of rocks that outcrop in California, Arizona, New Mexico, and Mexico led Bright et al. (2014) to hypothesize that they could be grouped as the southwestern Laurentia large igneous province (SWLLIP). Bright et al. (2014) further suggested that a temporal overlap of magmatism in the SWLLIP and in the Midcontinent Rift was the result of a geodynamic linkage. However, the available geochronology data from the SWLLIP at the time was not precise enough to test this relationship with the distinct magmatic intervals within the Midcontinent Rift.

Due to sparse geochronology data, temporal relationships between units in southwestern Laurentia are mostly inferred. In the Grand Canyon, it has been hypothesized that thick mafic sills and dikes that intrude Unkar Group sedimentary rocks are feeder systems for the Cardenas Basalt lava flows which are the uppermost unit of the Unkar Group (e.g. Hammond and Wooden, 1990; Timmons et al., 2005). This hypothesis is based on the spatial proximity and trace and major element concentration similarities of lava flows and nearby intrusions (Larson et al., 1994). No direct field evidence exists for feeder relations. Hendricks (1989)

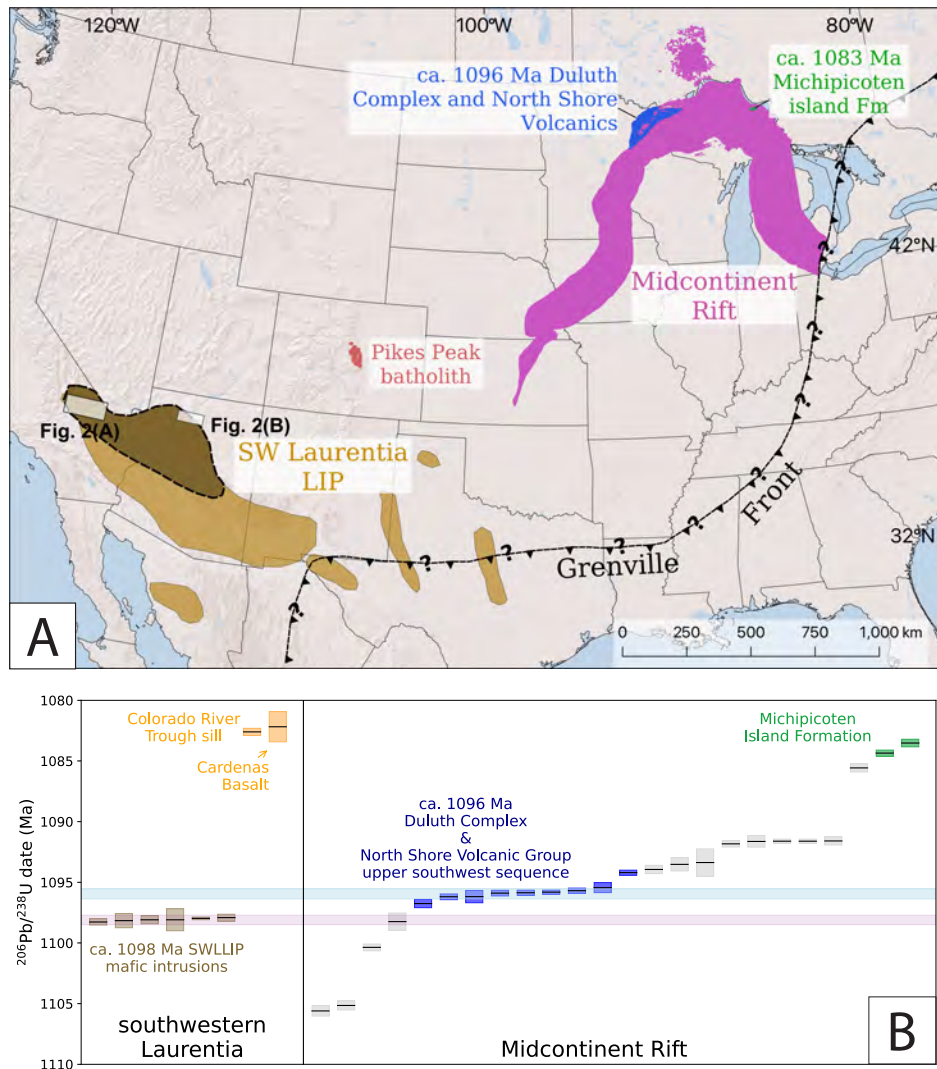


**Figure 4.1:** (A) Map of North America showing the inferred extent of the southwestern Laurentia large igneous province (SWLLIP) modified from Bright et al. (2014) in light brown color, a more strict version of the inferred extent of the SWLLIP based on encircling sills dated to be ca. 1098 Ma through the high-precision geochronology data of Mohr et al. (2024) in dark brown, together with the Pikes Peak batholith (Green, 1992), and the inferred extent of the Midcontinent Rift. The inferred trace of the Grenville Front is modified from Rivers (2015). The inset boxes show the extent of maps in Figure 4.2. (B) Summary of high-precision zircon U-Pb geochronology data from southwestern Laurentia (Mohr et al., 2024) and from the Midcontinent Rift, highlighting the Duluth Complex and the associated North Shore Volcanic Group (Swanson-Hysell et al., 2019b, 2021b), the Michipicoten Island Formation (Fairchild et al., 2017). The  $1082.6 \pm 0.3$  Ma Colorado River Trough sill is located in the Dead Mountains in southeastern California. Each black bar represents a  $^{206}\text{Pb}/^{238}\text{U}$  zircon weighted mean age. The colored shaded regions associated with the black bars represent uncertainties of the mean ages at 95% confidence level calculated with a Student's-T multiplier.

considered the sills and flows to be from the same parent magma, but did discuss a possible interpretation that the more differentiated flows erupted later than the emplacement of the sills. Applying the assumption that the extrusive and intrusive rocks were coeval, Weil et al. (2003) developed a paleomagnetic pole by grouping data derived from thirteen mafic intrusions and three Cardenas Basalt lava flows in the Grand Canyon. Similar directions had previously been developed for two Cardenas lava flows by Elston and Scott (1973). Weil et al. (2003) assigned an age of  $1090.6 \pm 4.5$  Ma ( $2\sigma$ ) to their pole based on an  $^{40}\text{Ar}$ - $^{39}\text{Ar}$  age they developed from biotite interpreted to have formed within the host Unkar sedimentary rocks during the intrusion of a mafic sill.

Paleomagnetic data have also been developed from SWLLIP mafic sills that intrude Apache Group sedimentary rocks in central Arizona (Helsley and Spall, 1972; Donadini et al., 2011). These studies interpreted sills with normal-polarity paleomagnetic directional data as coeval. Donadini et al. (2011) developed a mean pole from some normal-polarity sills and considered the age of the pole to be that of a baddeleyite U-Pb age of  $1088 \pm 11$  Ma ( $2\sigma$ ; age from one sill later published by Bright et al. (2014)). Although Harlan (1993) also obtained paleomagnetic samples of mafic sills in the same region with clearer distinction between individual cooling units, that the normal paleomagnetic pole of Donadini et al. (2011) was reported with paired radiometric age assignment led it to be the pole that is included in recent curated paleogeographic compilations (e.g. Evans et al., 2021). Other sills in the region record reversed directions with steeper inclinations relative to the normal polarity directions (Harlan, 1993; Donadini et al., 2011). In the field guide of Donadini et al. (2012), an age of  $1119 \pm 10$  Ma (weighted mean of  $^{207}\text{Pb}/^{206}\text{Pb}$  date of 2 baddeleyite grains) and a age of  $1111.6 \pm 8.9$  Ma (concordia intercept age of a combination of baddeleyite and zircon dates) were reported for sills of reversed polarity—these geochronology data remain unpublished. Both the steep reversed directions and the geochronological data are consistent with these sills being emplaced during an interval of reversed polarity prior to or during ca. 1109 to 1105 Ma early-stage Midcontinent Rift magmatism (Vervoort et al., 2007; Swanson-Hysell et al., 2019b).

More recently, Mohr et al. (2024) developed chemical abrasion-isotope dilution-thermal ionization mass spectrometry (CA-ID-TIMS) high-precision U-Pb geochronology data from zircon separated from differentiated zones in thick mafic sills in southwestern Laurentia and from zircon separated by bulk dissolution methods (applying the approach of Oliveira et al. (2022)) from a thick lava flow within the Cardenas Basalt (Figure 4.4). Three sills in Death Valley were dated at  $1097.91 \pm 0.29$  Ma,  $1098.27 \pm 0.27$  Ma, and  $1098.09 \pm 0.91$  Ma, two sills in western Grand Canyon at  $1098.16 \pm 0.59$  and  $1098.09 \pm 0.34$  Ma, and one sill in central Arizona at  $1097.97 \pm 0.12$  Ma (all ages are presented with analytical uncertainties at 95% confidence which is calculated including a Student's-T multiplier; Mohr et al., 2024). These ages agree with each other within uncertainty (Figure 4.1B) and suggest that the mafic intrusions across the region were rapidly emplaced in  $\sim 0.25$  Myr (Mohr et al., 2024). The data indicate an episode of LIP-style mafic magmatism ca. 1098 Ma in southwestern Laurentia that postdates the early plateau stage of volcanism in the Midcontinent Rift and predates the emplacement of the ca. 1096 Ma Duluth Complex and thick main stage rift

volcanics (Fig. 4.1). The data are consistent with a model where a plume head arrived ca. 1098 Ma under southwestern Laurentia leading to generation of melt and the emplacement of thick mafic intrusions. This plume could have then spread along the base of the lithosphere toward the Midcontinent Rift where it facilitated the reinvigoration of magmatism associated with the emplacement of the Duluth Complex and the North Shore Volcanic Group (Mohr et al., 2024). In addition, Mohr et al. (2024) developed a new zircon U-Pb age of  $1082.18 \pm 1.25$  Ma (95% confidence) from a Cardenas Basalt lava flow. That age indicates that the eruption of the lavas postdated the widespread ca. 1098 Ma mafic intrusions by  $\sim 16$  Myr (Figure 4.1B). Given the rapid apparent polar wander shown by the ca. 1109-1080 Ma Keweenawan Track (Swanson-Hysell et al., 2019b), the  $\sim 16$  Myr age difference between the Cardenas Basalt and thick mafic sills predict that they should record distinct paleomagnetic pole positions separated by a large angular distance. With the new chronological insights in hand, we develop new paleomagnetic data from the dated mafic sills and additional undated Mesoproterozoic intrusions in Death Valley and the Grand Canyon. We also develop new paleomagnetic data from lava flows of the Cardenas Basalt within the Grand Canyon with an increased number of sites as well as volcanostratigraphic context.

## 4.3 Geological Background

### Mafic intrusions in the Crystal Spring Formation, Death Valley

Rocks in the Death Valley region record the geological evolution of the southwestern margin of Laurentia since ca. 1.8 Ga in the Paleoproterozoic Era (Tapani Rämö and Calzia, 1998; Figure 4.2A, 4.3). The basement rocks include Paleoproterozoic para- and orthogneiss (Wasserburg et al., 1959; Barth et al., 2000; Strickland et al., 2013) and early Mesoproterozoic porphyritic quartz monzonite (Labotka et al., 1980). The Pahrump Group is a 1.5 to 4 km thick mixed carbonate and siliciclastic succession that unconformably overlies these basement lithologies (Figure 4.3; Wright et al., 1974; Macdonald et al., 2013). Formations of the Pahrump Group include the Mesoproterozoic Crystal Spring Formation, the Tonian Horse Thief Springs Formation, the Tonian Beck Spring Dolomite, and the Cryogenian Kingston Peak Formation (Macdonald et al., 2013; Mahon et al., 2014b). A  $>300$  Myr unconformity separates the Crystal Spring Formation, which contains mafic sills, and the overlying Horse Thief Springs Formation, which contains  $<775.4 \pm 0.7$  Ma detrital zircon (Mahon et al., 2014b; Dehler et al., 2023; Figure 4.3) and does not contain the sills. The region experienced Permian-Triassic contraction and magmatism (Snow et al., 1991; Stevens et al., 1997) followed by the Mesozoic Cordilleran orogeny (Burchfiel et al., 1992, 1970; Snow et al., 1991). Neogene felsic and mafic magmatism (Figure 4.2), high-angle normal faults, basement detachment faults, as well as transform faults associated with extensional tectonism are widespread in the region (Wright et al., 1974; Snow, 2000; Calzia and Rämö, 2000; Wrucke et al., 2007; Renik and Christie-Blick, 2013).

Tilting of crustal blocks related to Neogene extension in Death Valley resulted in the

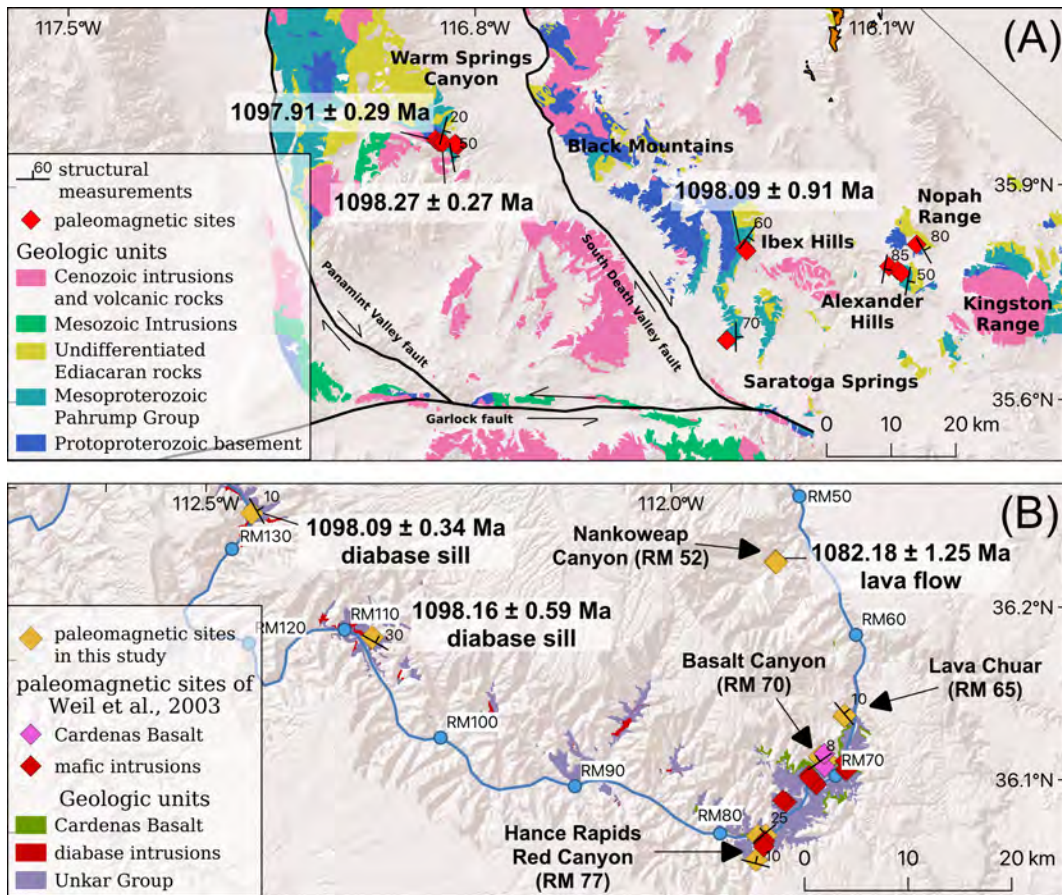


**Figure 4.2:** (A) Simplified geologic map of southern Death Valley, CA, (with units modified from Workman et al. (2003) and Wrucke et al. (2007)) showing the location of mafic sills that were sampled for paleomagnetism in this study and geochronology in Mohr et al. (2024). The Mesozoic and Cenozoic intrusions that occur in close proximity to the sills have the potential to have resulted in variable degrees of alteration and magnetic overprints. The sills typically were emplaced parallel to host sedimentary beds in the Crystal Spring Formation, but also intrude older crystalline lithologies. In the field, we collected multiple orientation measurements for sills from contact planes or adjacent sedimentary beds. An average orientation was calculated for each sill and was used to tilt-correct the paleomagnetic data. The representative orientations summarized on the map show that different regions are variably tilted. (B) Simplified geologic map of the Grand Canyon with units modified from Billingsley (2000) and Billingsley and Wellmeyer (2003) showing sedimentary rocks of the Unkar Group, mafic sills and dikes that intruded the sedimentary rocks, and the Cardenas Basalt that is the uppermost unit within the Unkar Group (Fig. 4.3). ‘RM’ stands for river mile using the widely adopted nomenclature of tracking distance through Grand Canyon. Bedding orientations at Nankoweap Canyon were collected from lava flow tops and the bedding of the overlying Nankoweap Formation which have very similar orientations; orientations at Lava Chuar Canyon were collected from the lava flow tops; orientations at Basalt Canyon were collected from lava flow tops, interflow sedimentary rocks, and the Dox Formation stratigraphically below the Cardenas Basalt. These bedding measurements were used for tilt-correcting paleomagnetic data. All geochronology data shown are U-Pb zircon ages from Mohr et al. (2024).

exposure of numerous sills and dikes that intrude the basement rocks and the Crystal Spring Formation. The thickness of the mafic sills ranges from <1 meter to over a hundred meters (Wright and Troxel, 1968; Hammond, 1983). Chilled margins with the Crystal Spring Formation have a finer grain size than the interiors. Olivine, pyroxene and plagioclase are typically altered within the sills (Hammond, 1983). Based on petrological analyses, Hammond (1983) interpreted that the alteration dominantly happened during mafic emplacement. Talc deposits up to 30 m thick are developed along contacts between the mafic and the dolomitic lithofacies of the Crystal Spring Formation (Wright and Troxel, 1968). Mining of talc within these contact metamorphosed zones has resulted in striking white scars in the regional landscape next to some of the sills.

Heaman and Grotzinger (1992) developed U-Pb TIMS dates from baddeleyite separated from pegmatitic zones within two mafic sills that outcrop in the southern Ibex Hills near Saratoga Spring in Death Valley National Park and in the Kingston Range (Figure 4.2A). Due to Pb loss in baddeleyite, the resultant dates are discordant, with interpreted concordia upper intercept ages of  $1069 \pm 3$  Ma and  $1087 \pm 3$  Ma ( $2\sigma$ ). The sill from Saratoga Spring yielded a lower intercept age of ca. 65 Ma which Heaman and Grotzinger (1992) interpreted to be related to growths of younger zircon rims around older baddeleyite crystals. In addition, Wasserburg et al. (1964) obtained a ca. 235 Ma K-Ar age from a Mesoproterozoic mafic sill in the Crystal Spring Formation that outcrops in Warm Spring Canyon. Although the baddeleyite lower intercept age and the K-Ar age are roughly constrained, these ages are consistent with the mafic sills having been affected by Mesozoic and Cenozoic metamorphism (Snow and Wernicke, 1989; Snow, 2000). Recently, Mohr et al. (2024) extracted zircons from granophyric segregations within two mafic sills from Warm Spring Canyon and one from the central Ibex Range (Figure 4.2A). High-precision CA-ID-TIMS zircon U-Pb geochronology yielded indistinguishable  $^{206}\text{Pb}/^{238}\text{U}$  ages of  $1097.91 \pm 0.29$  Ma,  $1098.27 \pm 0.27$  Ma, and  $1098.09 \pm 0.91$  Ma from the three individual sills (95% confidence; Figure 4.1B, 4.2A, 4.3).

## Mafic intrusions in the Unkar Group

The Grand Canyon Supergroup is divided into the Mesoproterozoic Unkar Group and the Neoproterozoic Chuar Group (Gundy, 1951; Elston, 1989; Dehler et al., 2017). The ~2 km-thick Unkar Group contains the Bass Formation, Hakatai Shale, Shinumo Quartzite, Dox Formation, and Cardenas Basalt (Figure 4.3; Beus et al., 1974; Elston, 1989). It is interpreted that the Unkar Group dominantly records shallow marine and fluvial depositional environments (Elston, 1989; Sears, 1990; Hendricks, 1989; Timmons et al., 2005). Siliciclastic deposition continued during eruption of the Cardenas Basalt resulting in interflow siltstone and sandstones—often with mudcracks and current ripples respectively (Fig. 4.4). Unkar Group strata typically dip at ~ $10^\circ$  to the northeast (Figure 4.2) toward normal faults that dip ~ $60^\circ$  to the southwest (Sears, 1973; Timmons et al., 2012). Intraformational faults and large thickness changes in sedimentary units across faults indicate that the Unkar Group was deposited in an extensional tectonic setting (Sears, 1990; Karlstrom and Humphreys, 1998; Timmons et al., 2001).

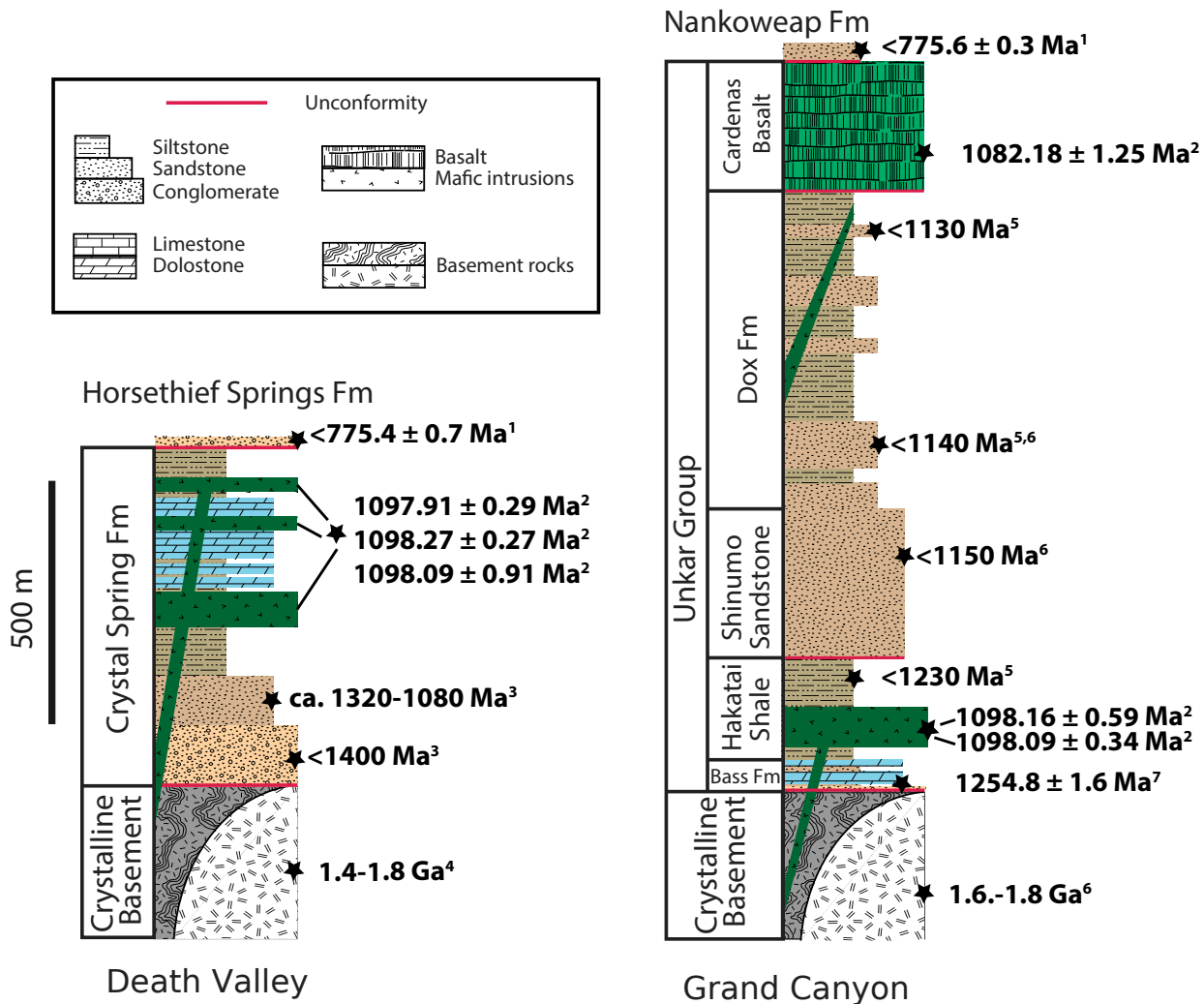


**Figure 4.3:** Simplified regional Mesoproterozoic stratigraphy in context of older basement rocks and younger Neoproterozoic sedimentary rocks and compiled geochronology in Death Valley and Grand Canyon. Red lines are unconformities. Black stars are existing radioisotopic age constraints. <sup>1</sup> CA-ID-TIMS U-Pb detrital zircon dates (Dehler et al., 2023); <sup>2</sup> CA-ID-TIMS U-Pb zircon dates (Mohr et al., 2024); <sup>3</sup> LA-MC-ICPMS U-Pb detrital zircon dates (Mahon et al., 2014a); <sup>4</sup> muscovite, biotite, and potassium feldspar  $^{40}\text{K}$ - $^{40}\text{Ar}$  and  $^{87}\text{Rb}$ - $^{87}\text{Sr}$  dates (Lanphere, 1964), biotite, muscovite, and hornblende  $^{40}\text{Ar}$ - $^{39}\text{Ar}$  dates (Labotka et al., 1985), and SHRIMP U-Pb zircon and monazite dates (Barth et al., 2001, 2009); <sup>5</sup> Compiled and new detrital zircon and detrital muscovite data (Mulder et al., 2017); <sup>6</sup> detrital zircon and detrital muscovite dates (Timmons et al., 2005); <sup>7</sup> TIMS U-Pb zircon dates from an ash layer (Timmons et al., 2005).

Numerous mafic sills and dikes intrude the Unkar Group, but not the overlying Chuar Group (Figures 4.2B and 4.3; Elston, 1989). Sills typically intrude the Bass Formation and the Hakatai Shale of the lower Unkar Group (Hendricks, 1989) whereas mafic dikes have been mapped to crosscut the Shinumo Sandstone and the Dox Formation of the upper

Unkar Group (Timmons et al., 2012). Typical dike plane orientations are subparallel to NW-trending faults in the Unkar Group (Huntoon et al., 1996; Timmons et al., 2012). The sills typically range in thickness between 20 to over 100 meters and are alkali-olivine basalt in composition (Hendricks, 1989; Larson et al., 1994; Figure C.1). Given their spatial proximity and stratigraphic relationship, it had been commonly inferred that all mafic intrusions in the Unkar Group are feeders to the Cardenas Basalt (e.g. Huntoon et al., 1996; Timmons et al., 2012), though no direct feeder relationships have been observed.

The interior of the thick mafic sills are medium- to coarse-grained with subophitic to ophitic texture characterized by plagioclase and olivine grains being enclosed by poikilitic pyroxenes (Hendricks, 1989). The intrusions are fine-grained at their margins where they are chilled against the Unkar sedimentary rocks. Some of the sill interiors contain zircon-bearing segregations (Mohr et al., 2024), which were dated with high-precision CA-ID-TIMS  $^{206}\text{Pb}/^{238}\text{U}$  at  $1098.16 \pm 0.59$  Ma at Hotauta Canyon (river mile [RM] 107) and  $1098.09 \pm 0.34$  Ma at Stone Creek (RM 132) (Figure 4.1B, 4.2B;  $2\sigma$  uncertainties).

## Cardenas Basalt

The Cardenas Basalt at the top of the Unkar Group exclusively outcrops in eastern Grand Canyon (Figure 4.2). The most complete section of the Cardenas Basalt outcrops at the Basalt Canyon area where  $\sim 315$  meters of lava flows and associated interflow sedimentary rocks are preserved up to the unconformity between the volcanics and the overlying Nankoweap Formation (Figure 4.2B, 4.4; Lucchitta and Hendricks, 1983; Hendricks, 1989). Cardenas Basalt also outcrops with variable thicknesses at localities including Lava Chuar Canyon and Nankoweap Canyon (Figure 4.2B, 4.4). The lava flows are typically trachy-basaltic andesite in composition, overall having higher  $\text{SiO}_2$  values than the mafic intrusions in the Unkar Group (Figure C.1; Hendricks, 1989; Larson et al., 1994).

Previous studies constructed volcanostratigraphic sections of the Cardenas Basalt at Basalt Cliffs, Ochoa Point, Basalt Canyon, and Lava Chuar Canyon (Lucchitta and Hendricks, 1983; Hendricks, 1989). In particular, Hendricks (1989) developed a stratigraphic section at Basalt Canyon with detailed petrologic and lithologic descriptions. In this study, we investigated three sections at Basalt Canyon, Lava Chuar Canyon, and Nankoweap Canyon (Figure 4.2). We measured volcanostratigraphic sections with a particular focus on determining individual lava flows that represent distinct cooling units such that paleomagnetic samples collected from a single lava flow are considered to capture the same snapshot of the geomagnetic field as they cooled (i.e. a paleomagnetic site; Fig. 4.4). Flow boundaries can be delineated by progressive changes in vesiculation and by highly vesiculated flow tops and/or interflow clastic sedimentary rocks (Figure 4.4, 4.5E). Interflow sedimentary rocks between lava flows are common (Figure 4.4).

At Basalt Canyon, flows in the initial 95 meters are subophitic to ophitic in texture and heavily weathered with a greenish color (Figure 4.5B). These flows form slopes characterized by small weathered basalt fragments that often are dislodged pyroxene oikocrysts. Walking on steep slopes mantled by these oikocrysts is like walking on ball bearings. Walcott (1883)

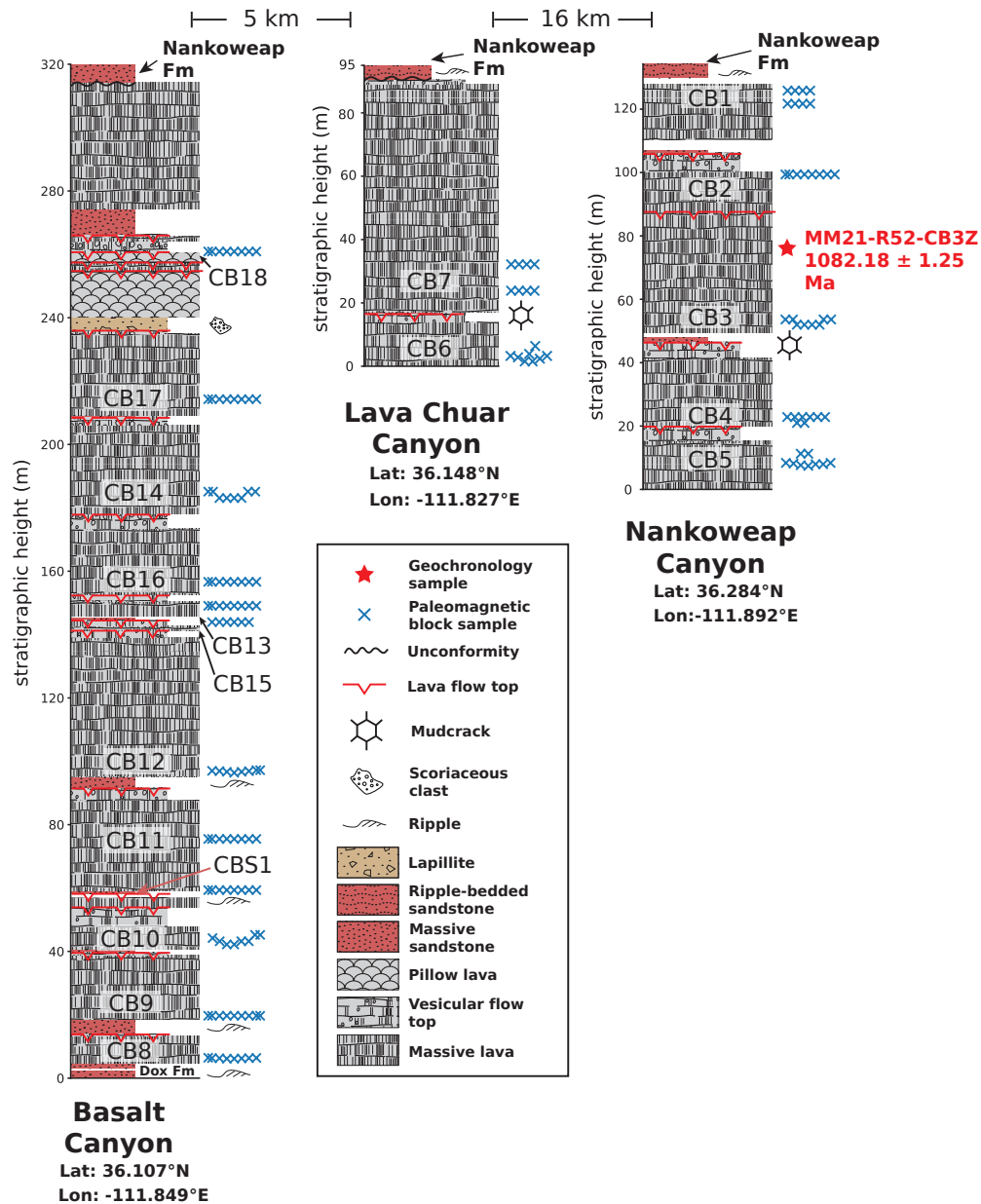


**Figure 4.4:** Volcanostratigraphy of the Cardenas Basalt at Basalt Canyon, Lava Chuar Canyon, and Nankoweap Canyon measured in this study. Section locations are shown in Figure 4.2B. Stratigraphic locations of the collected paleomagnetic samples and the geochronology sample dated by Mohr et al. (2024) are shown. The interflow sandstones and vesicular lava flow tops distinguish individual lava flows such that paleomagnetic samples from each lava flow constitute a site (labeled as ‘CB’ with distinct numbers). The latitude and longitude values correspond to the base of the stratigraphic sections.

and Lucchitta (1979) noted that those flows experienced spilitic alteration, interpreted as the result of subaqueous eruptions in a tidal flat or deltaic environment. The claim has also been made that there are pillows in these lower flows (Stevenson and Beus, 1982; Hendricks et al., 1974). However, our field observations, as well as those of Larson et al. (1994) and Elston and Scott (1976), did not find evidence of pillow lava indicative of subaqueous eruptions in these flows—note that spheroidal weathering can often be misidentified as pillows. While spheroidal weathering, granular grus piles, and ophitic textures on the weathered exposures are common, the features in these basal ophitic flows, including the presence of an observed pahoehoe flow top and basal pipe vesicles, are consistent with them being subaerially erupted sheet flows (Figure 4.5B). Aropy flow top consistent with pahoehoe lava flows was also reported in Hendricks (1989). The upper 200 meters of Cardenas Basalt flows consist of more competent, cliff-forming lava flows that are finer-grained than the lower sequence. A 4-meter-thick volcaniclastic layer containing cobble- to boulder-sized scoriaceous volcanic clasts surrounded by tan-colored, fine-grained matrix occurs at stratigraphic height of  $\sim$ 240 m (Figure 4.4, 4.5D). Lucchitta and Hendricks (1983) named this unit the lapillite member of the Cardenas Basalt and interpreted that it likely formed as pyroclastic debris deposited by lahars. Pillow lavas typically 0.8 to 1 m wide with horizons of volcaniclastic materials consistent with subaqueous eruption are found near the top of the section, above the lapillite layer (Figure 4.5F).

Shorter sections of Cardenas Basalt flows are exposed in Nankoweap Canyon (RM 52) and Lava Chuar Canyon (RM 65) (Figure 4.2B, 4.4). Due to the less complete exposures at these two localities, the volcanostratigraphic correlations between the three localities cannot be unequivocally drawn. However, large lateral variability of individual lava flow thicknesses has been reported (Lucchitta and Hendricks, 1983), indicating that lava flows likely pinch out laterally between the localities. Our stratigraphic sections at the three localities also show variable lava flow thicknesses directly below the Nankoweap Formation (Figure 4.4) although this could reflect variability in erosional truncation. We treat the sampled lava flows sampled at different localities as distinct cooling units in this study with each being an individual paleomagnetic site (Figure 4.4). The Mohr et al. (2024) geochronology sample for the Cardenas Basalts comes from the interior of a 57 m thick lava flow at Nankoweap Canyon (Figure 4.5A; CB3). Four zircon microlites yielded a weighted mean  $^{206}\text{Pb}/^{238}\text{U}$  ages of  $1082.18 \pm 1.25$  Ma (95% confidence; Figure 4.1B).

## 4.4 Methods

A total of 123 samples from 15 individual mafic sills were collected from the Death Valley region (Fig. 4.2A). Core samples were collected with a gasoline-powered drill outside of Death Valley National Park and block samples were collected from sills inside the park. In the Grand Canyon, a total of 184 block samples were collected from 18 individual Cardenas Basalt lava flows, 1 baked interflow sedimentary bed, and 5 mafic intrusions within the Unkar Group. When sampling, we preferentially targeted the finer-grained margins of flows

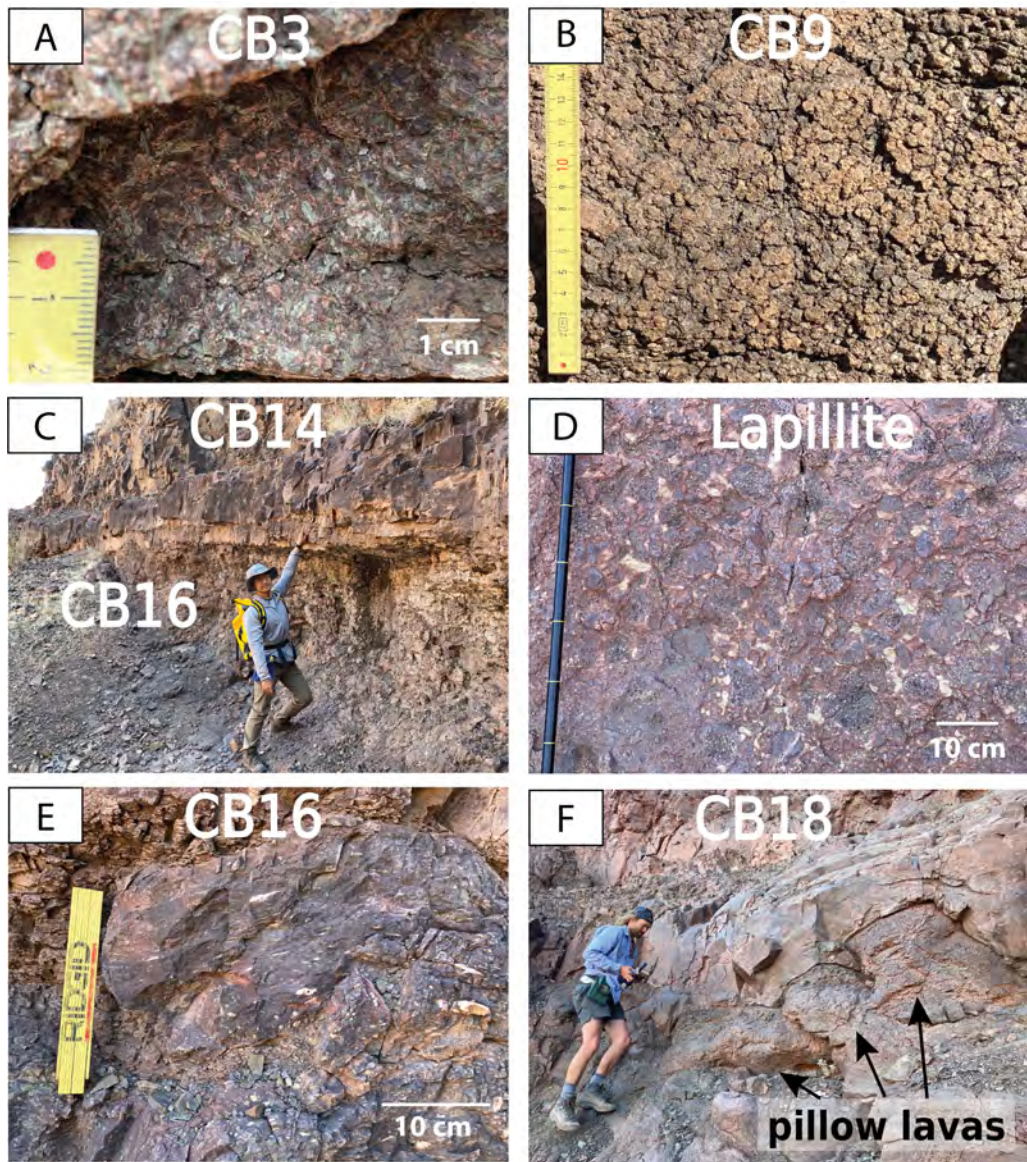


**Figure 4.5:** Field photos of Cardenas Basalt. The site names correspond to those shown in the stratigraphic section in Figure 4.4. (A) Coarse-grained interior of the 57 m thick CB3 lava flow at Nankoweap Canyon from which zircon were extracted and dated by Mohr et al. (2024). (B) Ophitic texture in the interior of flow CB9 at Basalt Canyon. Individual oikocrysts reach diameters of 9 mm. (C) Contact between two individual lava flows CB14 and CB16 (meter level 178 in Fig. 4.4). The massive flow bottom of the upper flow is more resistant to weathering than the recessive vesiculated flow top of the underlying flow. (D) The volcaniclastic marker bed containing scoriaceous volcanic clasts surrounded by tan-colored, very fine-grained matrix at 236 to 240 m in the Basalt Canyon section. (E) Amygdaloidal flow top of CB16. Elongate amygdules indicate that vesicles were stretched during flow. (F) Pillow lavas near the top of the exposed stratigraphy at Basalt Canyon (within interval from meter level 240 to 257; Fig. 4.4).

and intrusions over the coarser-grained interiors. Typically, 6-9 samples were collected at each site. Both magnetic compass and sun compass were used when orienting the drill cores and block samples in the field. Sun compass orientations were preferentially used when available. In the lab, standard paleomagnetic cores were drilled from the block samples and then oriented relative to the oriented surfaces.

The locations of the paleomagnetic sites are shown in Figure 4.2 and Table 4.1, and the stratigraphic positions of block samples collected from the Cardenas Basalt are shown in Figure 4.4. In western Grand Canyon, we sampled the  $1098.16 \pm 0.59$  Ma sill in Hotauta Canyon as UI4 (RM 107) and the  $1098.09 \pm 0.34$  Ma Stone Creek Canyon sill as UI5 (RM 132). In the eastern canyon, we sampled the Hance dike north to the Hance Rapids (UI2; RM 77) and the Hance sill south to the rapids (UI3). Another undated mafic sill was sampled at Red Canyon (RM 77) which is south of the river at Hance Rapids along the tributary stream channel of Red Canyon (UI1; Figure 4.2B). In Death Valley, within Warm Spring Canyon, we sampled the  $1097.91 \pm 0.29$  Ma sill as CS1 and the  $1098.27 \pm 0.27$  Ma sill as CS4, and in Ibex Hills, we sampled the  $1098.09 \pm 0.91$  Ma sill as CS7. Other undated sills are labeled in Figure (4.2) and locations for all sites are available in the archived data repository (<https://zenodo.org/doi/10.5281/zenodo.10625967>).

A suite of specimens from sills in the Crystal Spring Formation underwent step-wise thermal demagnetization up to  $680^{\circ}\text{C}$ . An additional suite of sister specimens from some samples also underwent thermal demagnetization with an added step of a liquid nitrogen bath following the measurement of natural remanent magnetization. This demagnetization step can preferentially remove overprint magnetization held by multidomain titanomagnetite grains and potentially improve the resolution of the characteristic component. All specimens from the Cardenas Basalt and the mafic intrusions within the Unkar Group underwent step-wise thermal demagnetization up to  $580^{\circ}\text{C}$  with some samples continuing up to  $680^{\circ}\text{C}$ . The thermal demagnetization protocol had increasingly higher resolution approaching the Curie temperature of magnetite ( $\sim 580^{\circ}\text{C}$ ) and Néel temperature of hematite ( $\sim 680^{\circ}\text{C}$ ).

All demagnetization experiments were carried out in the magnetically shielded room at the UC Berkeley Paleomagnetism Lab. The typical magnetic field inside the shielded room is  $<500$  nT. An ASC TD-48SC thermal demagnetizer with  $<10$  nT field inside the chamber was used for the demagnetization steps. All remanence measurements were made on a 2G Enterprises DC-SQUID superconducting rock magnetometer. The PmagPy software package (Tauxe et al., 2016) was used to implement least-square fits (Kirschvink, 1980) to specimen demagnetization data.

In the Death Valley region, multiple bedding orientations were measured along contacts between the sills and the host sedimentary rocks and along bedding of sedimentary rocks near the sills, and the averages of these measurements were used to tilt-correct paleomagnetic directions of each sill. In the Grand Canyon, the contact planes between the Hance sill and the adjacent sedimentary layers are poorly exposed. We collected bedding measurements from the nearby exposures of the Bass Formation for tilt correction. We also collected orientations from the Hance sill columnar joint planes—planes that are typically vertical prior to tilting. The best-fit plane orthogonal to the columnar joint planes has an orientation

similar to the mean bedding plane of the Bass Formation. Bedding orientations of the host Hakatai Shale were used to tilt-correct the Hance dike paleomagnetic data. Bedding orientations were taken on the Cardenas Basalt flow tops and on interflow sediments for tilt correction. All bedding orientation data are available in the archived data repository (<https://zenodo.org/doi/10.5281/zenodo.10625967>).

## 4.5 Results and Interpretations

Eight out of the 15 mafic sills from the Death Valley area yielded stable, consistent, and interpretable paleomagnetic directional data. All sites including 5 mafic sills, 18 lava flows, and 1 interflow sedimentary bed sampled in the Grand Canyon yielded well-grouped, consistent paleomagnetic directions. The site-level paleomagnetic statistics are summarized in Table 4.1. Data to the individual measurement level are available in the MagIC database (<https://doi.org/10.7288/V4/MAGIC/20009>).

### Death Valley mafic sills

Thermal demagnetization results on specimens with stable and consistent remanence from the Death Valley sills show that the specimens typically have an overprint component (Figure 4.6). That component can be removed by heating up to  $\sim 500^{\circ}\text{C}$ , although it is largely removed after heating to  $100^{\circ}\text{C}$ . The liquid nitrogen demagnetization step (77 K) was also efficient in removing this component. Following the removal of the secondary component, an origin-trending component was resolved through the progressive thermal demagnetization steps up to the Curie temperature of magnetite (i.e.  $\sim 580^{\circ}\text{C}$ ; Figure 4.6).

In geographic coordinates, the site level low-temperature component directions of the Death Valley sills lie very close to the direction of the present-day geomagnetic field direction in Death Valley (Figure 4.6). The low unblocking temperature and the directions of this component are consistent with it being a geologically recent viscous remanence overprint (Moskowitz et al., 1998; Muxworthy and McClelland, 2000). On the other hand, the origin-trending component in the sills removed at higher temperatures is directed to the northwest with steep downward inclinations after tilt correction (Figure 4.6). Eight sills yielded consistent results within site and well-grouped mean directions amongst sites. The other sills failed to yield resolvable characteristic directions or consistent results within sites. Figure 4.8A shows the virtual geomagnetic poles (VGP) and the mean pole position (pole longitude= $176.6^{\circ}$ , pole latitude= $44.9^{\circ}$ ,  $n=8$ ,  $A_{95}=11.8^{\circ}$ ; no rotation correction) calculated from the tilt-corrected sills in Death Valley.

### Intrusions in the Unkar Group and the Cardenas Basalt

The two dated ca. 1098 Ma sills in eastern Grand Canyon (UI4 and UI5) and three intrusions near Hance Rapids and in Red Canyon (UI1, UI2, and UI3; Figure 4.2B) all yielded

site	study region	geologic type	site (°N)	latitude (°E)	site (°N)	longitude	n	dec <sub>gc</sub>	inc <sub>gc</sub>	dec <sub>tc</sub>	inc <sub>tc</sub>	k	α95 (°)	vgp lat (°N)	vgp lon (°E)
CS1*	Death Valley	sill	35.9688	-116.9190	8	303.0	50.0	292.8	73.3	175	4.2	41.7	203.7		
CS2	Death Valley	sill	35.9651	-116.9130	7	290.2	43.2	206.3	65.3	27	11.9	42.5	187.7		
CS6	Death Valley	sill	35.9618	-116.8829	8	275.5	-4.7	281.3	48.4	45	8.3	25.2	172.3		
CS7*	Death Valley	sill	35.8154	-116.3886	2	318.0	-8.0	331.1	42.4	167	19.5	62.7	137.2		
CS8	Death Valley	sill	35.8114	-116.3854	9	305.2	5.2	297.1	58.7	78	5.9	41.1	177.8		
CS9	Death Valley	sill	35.8112	-116.3855	5	316.0	-2.0	317.5	52.6	39	12.3	55.1	161.9		
CS12	Death Valley	sill	35.7789	-116.1206	8	284.7	2.3	301.6	63.3	30	10.2	45.5	184.3		
CS13	Death Valley	sill	35.8187	-116.0938	3	269.0	-13.7	293.6	51.2	150	10.1	35.8	170.3		
CB1	Grand Canyon	lava flow	36.2839	-111.8919	8	249.3	52.9	270.3	51.1	200	3.9	18.4	184.5		
CB2	Grand Canyon	lava flow	36.2836	-111.8919	8	276.3	56.5	283.3	78.7	329	3.1	38.2	220.8		
CB3*	Grand Canyon	lava flow	36.2833	-111.8928	7	261.3	58.7	249.3	52.9	56	8.1	5.1	196.5		
CB4	Grand Canyon	lava flow	36.2831	-111.8928	7	248.6	35.0	261.3	58.7	37.1	10.0	16.9	196.9		
CB5	Grand Canyon	lava flow	36.2825	-111.8914	9	241.6	45.7	276.3	56.5	71	6.2	25.3	186.8		
CB6	Grand Canyon	lava flow	36.1458	-111.8275	8	270.3	51.1	252.7	47.0	88	5.9	3.8	190.7		
CB7	Grand Canyon	lava flow	36.1464	-111.8269	8	283.3	78.7	269.9	42.5	106	5.4	14.1	178.5		
CB8	Grand Canyon	lava flow	36.1072	-111.8486	8	271.9	53.0	272.7	38.5	132	4.8	14.7	174.5		
CB9	Grand Canyon	lava flow	36.1073	-111.8493	8	264.6	37.4	283.6	27.3	96	5.7	19.3	162.3		
CB10	Grand Canyon	lava flow	36.1075	-111.8489	7	264.0	32.3	273.9	38.0	88	6.5	15.4	173.6		
CB11	Grand Canyon	lava flow:	36.1082	-111.8489	13	278.1	28.4	268.3	69.5	93.2	4.3	27.2	206.5		
CBS1	Grand Canyon	lava flow	36.1100	-111.8531	8	265.9	37.1	268.8	42.0	193	4.0	13.1	178.8		
CB12	Grand Canyon	lava flow	36.1101	-111.8542	7	259.9	40.0	267.0	6.1	107	5.9	-0.6	162.4		
CB13	Grand Canyon	lava flow	36.1108	-111.8553	7	266.0	4.6	259.4	52.9	514	2.7	11.6	191.3		
CB14	Grand Canyon	lava flow	36.1103	-111.8533	6	247.4	49.1	263.3	45.7	89	7.1	10.7	184.1		
CB15	Grand Canyon	lava flow	36.1100	-111.8547	7	253.6	42.8	266.2	17.5	63	7.7	2.2	167.6		
CB16	Grand Canyon	lava flow	36.1114	-111.8533	8	263.2	15.7	264.8	49.3	233	3.5	13.5	185.9		
CB17	Grand Canyon	lava flow	36.1117	-111.8558	7	253.6	46.5	285.6	52.3	98	6.1	30.2	178.9		
CB18	Grand Canyon	lava flow	36.0247	-111.9300	8	243.9	66.1	269.1	23.9	216	3.8	6.6	168.7		
U11	Grand Canyon	dike	36.0456	-111.9183	8	263.9	19.3	264.0	10.0	75	6.5	-1.9	165.7		
U12	Grand Canyon	dike	36.0458	-111.9267	8	258.1	20.4	264.1	25.6	139	4.7	3.2	172.4		
U13	Grand Canyon	sill	36.2353	-112.3294	7	264.0	14.3	314.1	51.6	54	8.3	52.2	165.4		
U14*	Grand Canyon	sill	36.3483	-112.4525	8	278.2	49.2	295.6	49.3	76	6.4	36.8	170.8		

**Table 4.1:** Site-level paleomagnetic data from mafic sills in Death Valley, Cardenas Basalt, and mafic intrusions in the Unkar Group. dec<sub>gc</sub> and inc<sub>gc</sub> are site mean declination and inclination in geographic coordinates. dec<sub>tc</sub> and inc<sub>tc</sub> are site mean declination and inclination in tilt-corrected coordinates. k represents the Fisher concentration parameter of the site level mean directions. α<sub>95</sub> represents the Fisher 95% angular uncertainty of the site level mean directions. vgp lat and vgp lon represent the latitude and longitude of the site-level virtual geomagnetic poles calculated from tilt-corrected directional data. \* marks sites that have paired high-precision zircon U-Pb ages developed by Mohr et al. (2024). CS1 is dated to be 1097.91 ± 0.29 Ma; CS7 is dated to be 1098.09 ± 0.91 Ma; UI4 is dated to be 1098.16 ± 0.59 Ma; UI5 is dated to be 1098.09 ± 0.34 Ma. All ages are presented with 95% confidence.

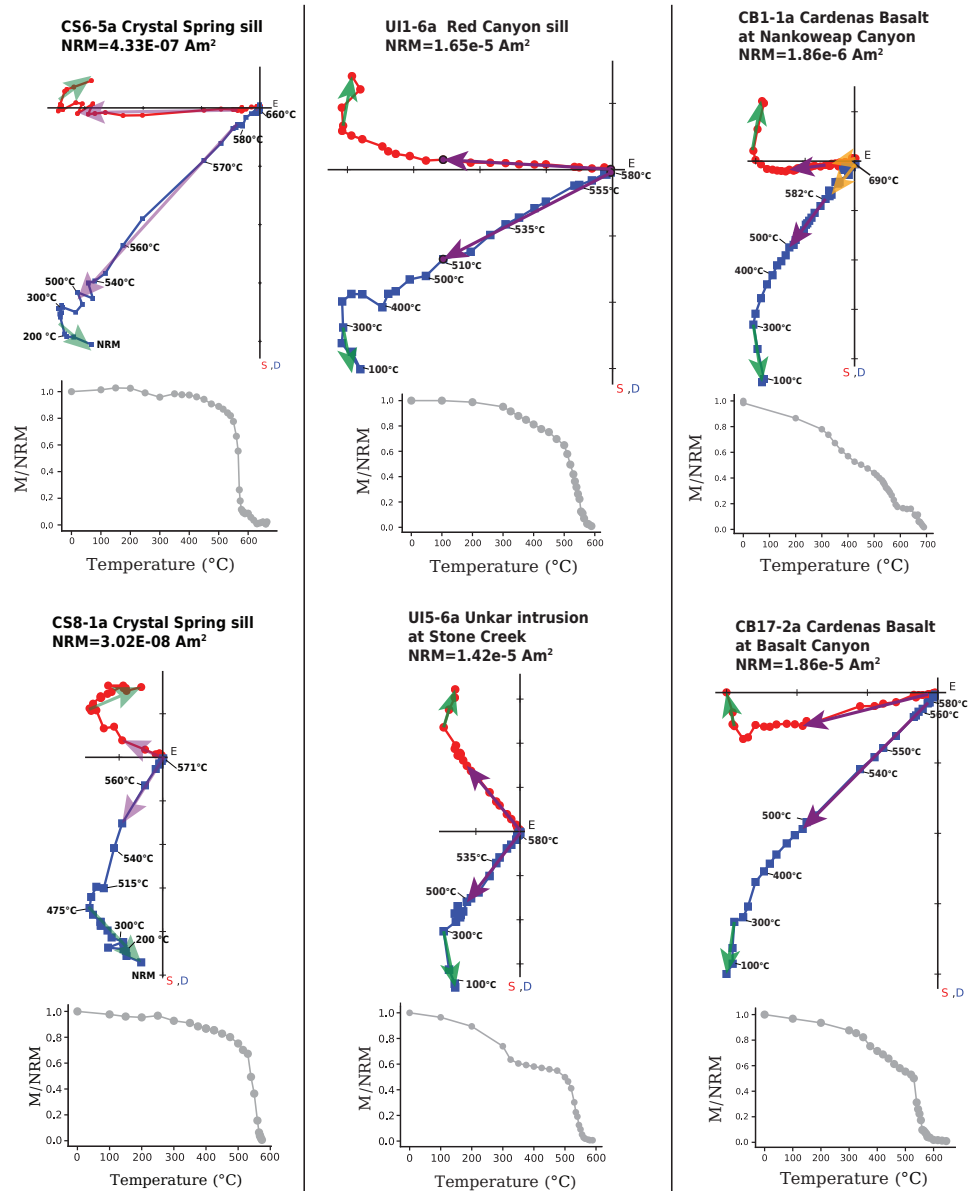


**Figure 4.6:** Example orthogonal vector diagrams of specimen thermal demagnetization results from mafic sills that intruded the Crystal Spring Formation, mafic sills that intruded the Unkar Group, and the Cardenas Basalt. Total specimen magnetic moments ( $M$ ) normalized by the natural remanent magnetizations (NRM) are plotted against temperature steps. The secondary overprint component (green) in the rocks can be removed by heating typically to  $\sim 300^\circ\text{C}$ , but can be up to  $\sim 500^\circ\text{C}$ , or efficiently removed by liquid nitrogen demagnetization. The interpreted primary component (purple) is origin-trending and typically unblocks sharply through  $\sim 500\text{--}580^\circ\text{C}$ . In some Cardenas lava flows such as CB1, a third component that unblocks up to  $\sim 690^\circ\text{C}$  exists, and is interpreted to be carried by hematite that formed during early oxidation. All orthogonal plots are shown in tilt-corrected coordinates.

consistent within-site thermal demagnetization results and have similar thermal demagnetization behaviors between sites (Figure 4.6, 4.7). Typically, an origin-trending characteristic remanence component unblocks between 500°C and 585°C after a secondary overprint component that overlaps with the present local field direction is removed at lower temperatures (Figure 4.6). This thermal demagnetization behavior indicates that the characteristic remanence components in these mafic intrusions are held by low-titanium titanomagnetite. Despite their similar demagnetization behaviors, the mafic intrusions record two distinct groups of remanence directions (Figure 4.7). The ca. 1098 Ma mafic sills in Hotauta Canyon (UI4) and Stone Creek Canyon (UI5) record paleomagnetic directions to the northwest with steep inclinations, whereas the other three undated intrusions in eastern Grand Canyon have westerly directions and much shallower inclinations (Figure 4.6, 4.7).

Thermal demagnetization of the 18 Cardenas Basalt lava flows yielded consistent site-level results (Figure 4.7). After an overprint component that overlaps with the present local field direction was removed by heating up to 300°C (Figure 4.6), the specimens typically demagnetized along an origin-trending path approaching the Curie temperature of magnetite. Some specimens continued to demagnetize up to the Néel temperature of hematite ( $\sim$ 690°C; Özdemir and Dunlop (2006); Figure 4.6). The unblocking temperature ranges indicate that (titano)magnetite and hematite are the dominant remanence-carrying minerals in the lava flows. Least-squares line fits made for the magnetite and hematite components have very similar directions in the same specimens (Figure 4.6; CB1-1a). This result is consistent with the hematite having formed due to early oxidation of the lava flows indicating that it acquired remanent magnetization soon after the eruption of the lavas.

Site-level characteristic directions for all of the intrusions in Death Valley and Grand Canyon as well as Cardenas Basalt flows except for CB4 were calculated using the (titano)magnetite-bearing components. This component isolated through magnetite unblocking temperatures is referred to as the “mid-temperature direction” in Figure 4.7. For site CB4, all except for one specimen have antipodal components, both of which we interpret to be carried by hematite. The antipodal directions recorded within the same specimens may be the result of magnetic self-reversal associated with the oxidation of magnetite into maghemite which subsequently inverted into hematite (Swanson-Hysell et al., 2011). A detailed description of the specimen results for site CB4 is presented in Figure C.2. We combine the normal-polarity (i.e. directions pointing southwest and down) directions held by hematite in six samples together with a normal polarity direction carried by titanomagnetite in one sample for calculating a site mean direction for this flow. Seven samples collected from a baked interflow red sandstone layer (site CBS1) within 0.2 m of the base of lava flow CB11 yielded overlapping paleomagnetic directions with those from the overlying lava flow (Figure C.3). We group the samples from the lava flow and the baked sediments as one site when calculating the mean direction and virtual geomagnetic pole (VGP). Figure 4.8B shows the VGPs of the two dated ca. 1098 Ma sills in eastern Grand Canyon (UI4 and UI5), VGPs of the Cardenas Basalt sites, the mean pole position calculated for the Cardenas Basalt (pole longitude=183.9°, pole latitude=15.9°, N=18, A<sub>95</sub>=7.4°, K=22.7; no rotation correction) and the VGPs of the intrusions near Hance Rapids and Red Canyon (UI1, UI2, and UI3).

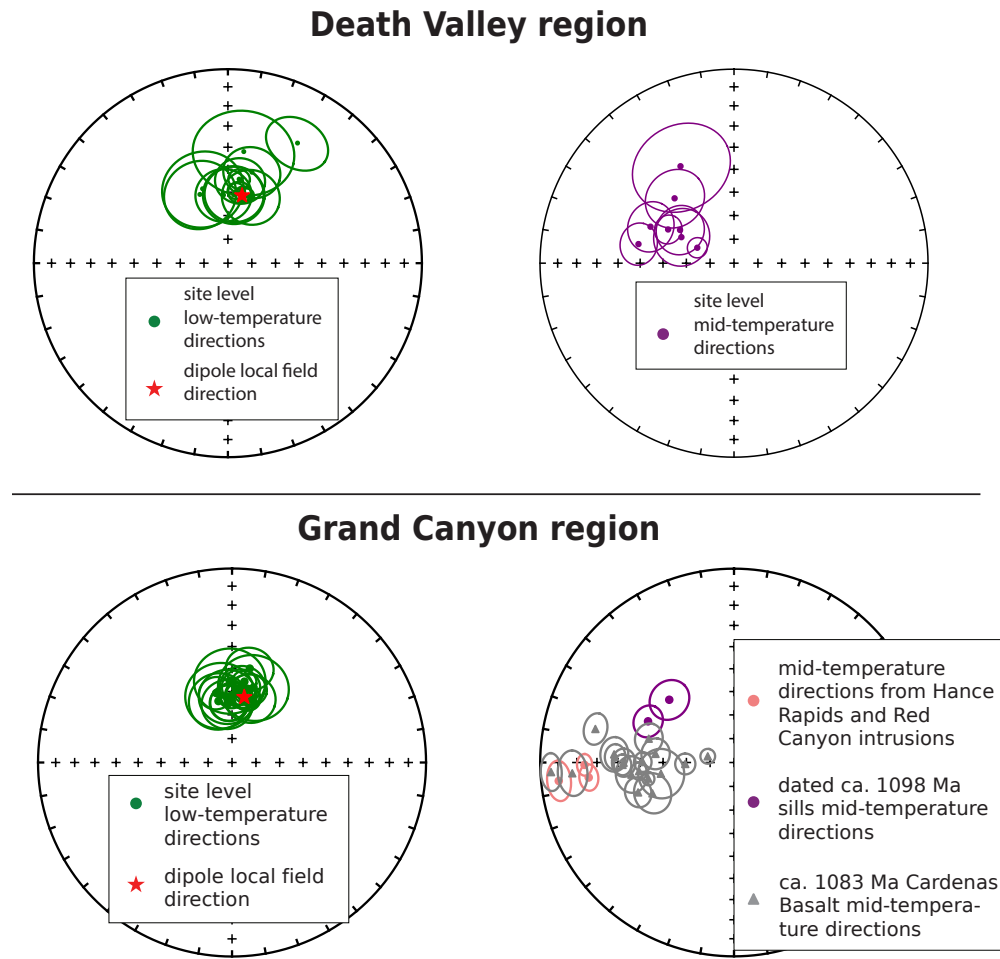


**Figure 4.7:** Summary equal area diagrams for the site level directional results from the Death Valley region and the Grand Canyon region. The site level low-temperature components (green) in geographic coordinates are shown in context of present-day local field directions (red star) at the study localities. The mid-temperature directions (i.e. those that unblock over a temperature range consistent with magnetite) are shown in tilt-corrected coordinates. Note that the specimen directions from the mafic sills at Hotauta Canyon (UI4) and Stone Creek (UI5) (directions shown in purple) are more northerly and steeper than the specimen directions of Cardenas Basalt and the intrusions near Hance Rapids (shown in grey and pink).

## 4.6 Discussion

### Timing of mafic magmatism in the SWLLIP

Statistically indistinguishable high-precision U-Pb zircon ages from three sills in Death Valley, two sills in the Grand Canyon, and a sill in central Arizona were interpreted in Mohr et al. (2024) to be consistent with decompression melting of an upwelling mantle plume ca.

1098 Ma. This hypothesis predicts that other thick sills in the region associated with the SWLLIP were also emplaced ca. 1098 Ma. Paleomagnetic directional data can provide another avenue to gain chronological insight on mafic units for which geochronology data have not been or cannot be developed. Rapid changes in Laurentia's pole position between ca. 1110 and 1070 Ma (Fig. 4.8D; Swanson-Hysell et al., 2019b) enable such data to provide more informative temporal constraints than at many other time intervals.

The new paleomagnetic data from the dated sills in the Death Valley region and in the Grand Canyon are consistent with their high-precision U-Pb zircon ages. The  $1097.91 \pm 0.29$  Ma CS1 sill and the  $1098.09 \pm 0.91$  Ma CS7 sill in Death Valley and the  $1098.16 \pm 0.59$  Ma UI4 sill and  $1098.09 \pm 0.34$  Ma UI5 sill in Grand Canyon have similar VGP positions at high latitudes in present-day coordinates (Figure 4.8A, B). The new paleomagnetic data further show that six additional undated sills in the Death Valley region have directions that are similar to those from the ca. 1098 Ma dated sills (Figs. 4.7 and 4.8). These data are consistent with all of the preserved Death Valley sills being associated with the ca. 1098 Ma pulse of mafic magmatism. Figure 4.8A shows the mean pole position calculated for all the Death Valley region sills. The pole overlaps within uncertainty with the pole position of the ca. 1096 Ma North Shore Volcanic Group upper southwest sequence of the Midcontinent Rift (Figure 4.8A; Swanson-Hysell et al., 2019b). Although the paleomagnetic data of the Death Valley sills have directional uncertainties associated with potential vertical axis block rotations as detailed in the following section, these structural complexities do not take away the interpretation that the steep downward inclinations (Figure 4.6) are compatible with a ca. 1098 Ma age. Additionally, the normal polarity of the magnetizations is consistent with the sills being emplaced during the earliest portion of the ca. 1099 to  $<1075$  Ma Portage Lake normal polarity zone (Swanson-Hysell et al., 2019b)—a late Mesoproterozoic superchron (Driscoll and Evans, 2016).

The paleomagnetic pole position of the ca. 1082 Ma Cardenas Basalt plots at a lower latitude distinct from that of the ca. 1098 Ma mafic sills in Death Valley and the western Grand Canyon (Figure. 4.8A, C). Instead, the Cardenas Basalt pole is close to the paleomagnetic pole of the Michipicoten Island Formation of the Midcontinent Rift whose age is tightly bracketed to be between  $1084.35 \pm 0.20$  Ma and  $1083.52 \pm 0.23$  Ma (Fairchild et al., 2017). In addition, the Cardenas Basalt pole is close to the ca. 1075 Ma paleomagnetic poles of the Nonesuch and Freda Formations (Henry et al., 1977; Slotznick et al., 2023) of the Midcontinent Rift Oronto Group. That these localities  $\sim 2,500$  km apart yield overlapping pole positions when their poles are calculated under the assumption of a time-averaged dipolar field supports interpretations that the field was a stable dipole ca. 1080 Ma. Note that there is uncertainty in the Cardenas pole position associated with hypothesized rotation of the Colorado Plateau in the Mesozoic/Cenozoic (Fig. 4.8D; e.g. Bryan and Gordon, 1990). However, this uncertainty does not take away from the main conclusion as it does not affect interpretations of paleolatitude.

Overall, the large arc distance between the ca. 1098 Ma and the ca. 1082 Ma poles from southwestern Laurentia supports the interpretation based on Midcontinent Rift data that Laurentia experienced rapid plate motion from high latitudes toward the equator in

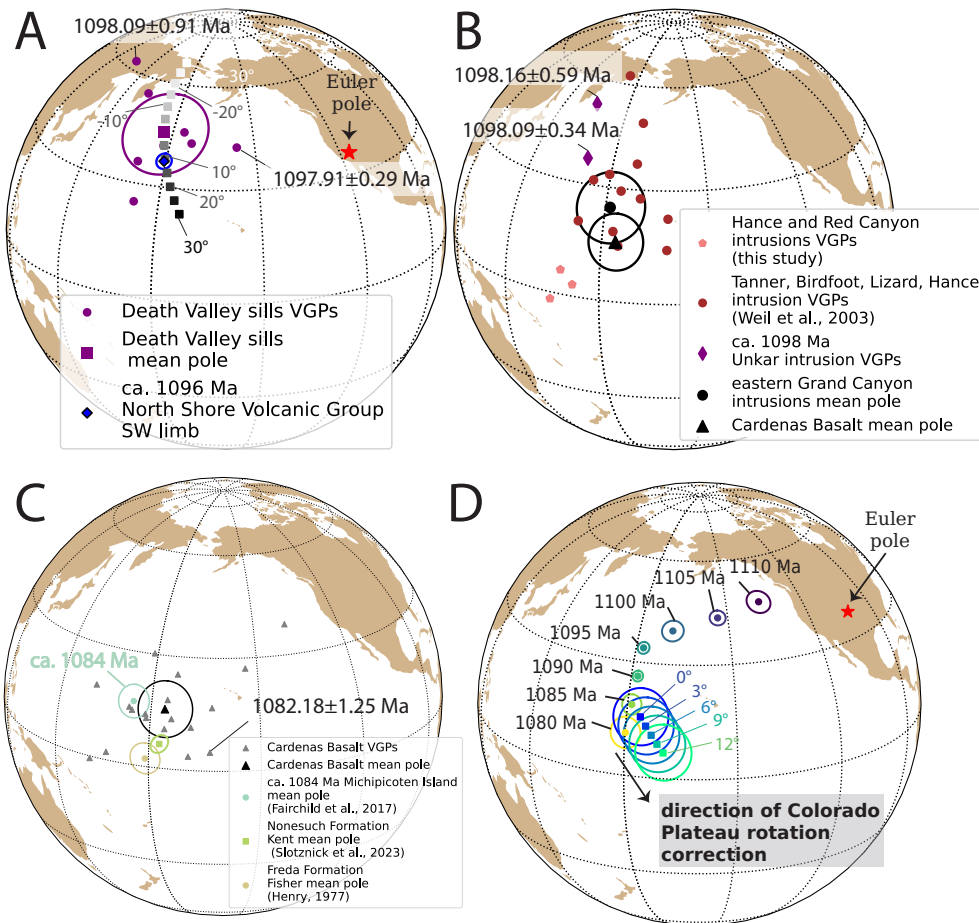


**Figure 4.8:** (A) Virtual geomagnetic poles (VGP) from the Death Valley mafic sills and the associated mean paleomagnetic pole plotted in context of the paleomagnetic pole position of the ca. 1096 Ma North Shore Volcanic Group southwest sequence pole from Swanson-Hysell et al. (2019b). Variable vertical axis rotations of the mean Death Valley sills pole about an Euler pole located at 35.8°N, -116.4°E are shown. Positive (negative) values represent counterclockwise (clockwise) rotations about the Euler pole. (B) VGPs from the Cardenas Basalt and mafic sills within the Unkar Group are plotted together with the mean Cardenas Basalt pole and the mean pole calculated for intrusions that are hypothesized to be coeval with the Cardenas Basalt. VGPs of intrusions include those developed in this study as well as those from Weil et al. (2003). (C) The mean ca. 1082 Ma Cardenas Basalt paleomagnetic pole is plotted together with the ca. 1084 Ma Michipicoten Island Formation paleomagnetic pole (Fairchild et al., 2017) as well as the ca. 1075 Ma Nonesuch Formation pole (Slotznick et al., 2023) and lower Freda Formation pole (Henry et al., 1977). (D) The Cardenas Basalt mean pole position is corrected for the hypothesized Colorado Plateau rotation with progressively larger rotations about an Euler pole position of -107°E, 37°N (Bryan and Gordon, 1990). The resultant pole positions are plotted in context of the synthesized Keweenawan Track (2 stage pole rotations and true polar wander scenario; Swanson-Hysell et al., 2019b). Larger rotations result in less agreement between the Cardenas pole and the pole path based on Midcontinent Rift data. In plots (A) and (C) the VGPs from dated sills and the dated lava flow are labeled with their ages.

the late Mesoproterozoic (Davis and Green, 1997; Swanson-Hysell et al., 2009). This rapid motion is associated with the closure of the Unimos Ocean which culminating in the onset of Grenvillian collisional orogenesis (Swanson-Hysell et al., 2023).

## Comparison to Mesoproterozoic paleomagnetic data from central Arizona

Paleomagnetic data have been developed from mafic sills in central Arizona that intrude the Apache Group sedimentary rocks (Helsley and Spall, 1972; Harlan, 1993; Donadini et al., 2011). Both Harlan (1993) and Donadini et al. (2011) identified sills in the same region that record normal directions and reversed directions with the reversed directions having steeper inclinations. We compiled paleomagnetic data from these two studies with the goal of having each site be a distinct cooling unit. The resultant compilation is provided in Table C.1. The individual site-level directions, corresponding virtual geomagnetic pole positions, and overall mean directions and poles are recalculated by polarity and plotted in Figure 4.9.

The compiled mean pole position of the normal-polarity mafic sills in central Arizona plots near the expected pole position of Laurentia ca. 1095 Ma based on data from the Midcontinent Rift rocks (Figure 4.9; Swanson-Hysell et al., 2019b). However, the distribution of the normal-polarity virtual geomagnetic pole positions is distinct from a Fisher distribution (Fisher, 1953). Given that these VGPs show an elongate distribution along the Keweenawan Track (Figure 4.9), we hypothesize that not all sills were emplaced during the same magmatic episode. However, that the sills record a normal polarity and one sill yielded a U-Pb baddeleyite age of  $1088 \pm 11$  Ma (Bright et al., 2014) which has an uncertainty that overlaps with an CA-ID-TIMS zircon U-Pb age of  $1097.97 \pm 0.12$  Ma from a subhorizontal diabase sill in Salt River Canyon (Mohr et al., 2024) indicate that some of the sills could be coeval with the ca. 1098 Ma mafic sills in Death Valley and Grand Canyon. More precise radiometric dates that is paired with paleomagnetic data are needed from these sills.

Despite the few records, the central Arizona sills with steep negative inclinations have a mean pole position distinct from that of the normal-polarity sills (Figure 4.9). The mean pole plots near the older end of the Keweenawan Track, indicating a high paleolatitude for Laurentia at the time (Figure 4.9). This configuration corresponds with the stable high-latitude position of Laurentia between ca. 1140 and 1105 Ma (Ernst and Buchan, 1993; Piispa et al., 2018; Swanson-Hysell, 2021). That reversed polarity is also consistent with the Alona Bay reversed polarity zone which has been identified during the onset of magmatism in the Midcontinent Rift (Swanson-Hysell et al., 2019b). The potential exists that in addition to there being a linkage between a SWLLIP plume that spread to the Midcontinent Rift ca. 1098 to 1096 Ma as hypothesized in Mohr et al. (2024), a plume upwelling under Laurentia at the onset of Midcontinent Rift development led to magmatism in both regions. To assess such temporal and dynamic connections, more precise ages of these reversed-polarity sills need to be determined.

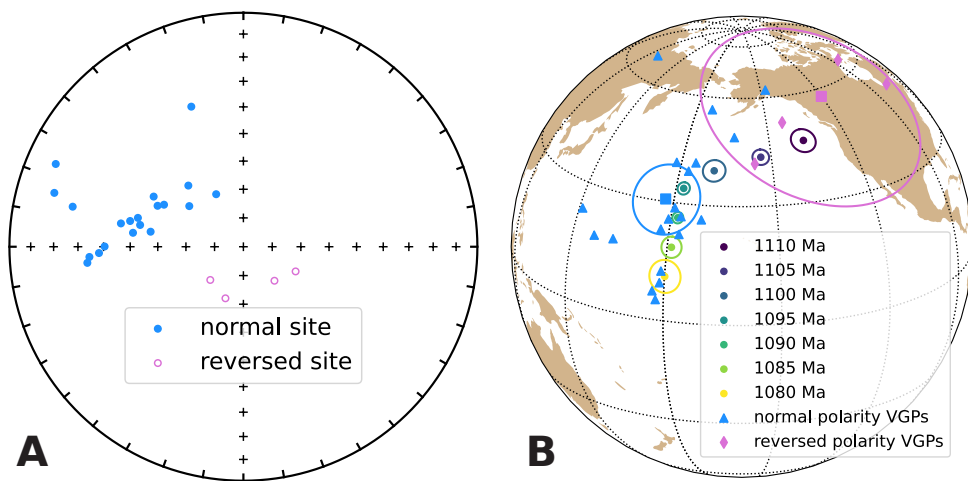


**Figure 4.9:** (A) Compiled paleomagnetic directional data developed by Harlan (1993) and Donadini et al. (2011) from mafic sills in central Arizona. The original data are selected with some recalculated such that each site included in this compilation is an individual cooling unit. Some sills record a reversed polarity with steep inclinations (orchid), while the other sills record a normal polarity with shallower inclinations (blue). The compiled data are in Table C.1. (B) Virtual geomagnetic poles (VGP) of individual cooling units and mean paleomagnetic poles of the central Arizona mafic sills are plotted in context of the synthesized Keweenawan Track of Swanson-Hysell et al. (2019b) (two stage pole with true polar wander scenario). The mean pole position of sills with reversed polarity is close to the older end of the Keweenawan Track while the mean normal-polarity pole plots close to the expected pole position ca. 1095 Ma.

## Death Valley region sills

### Structural complexity associated with Neogene extension

The Death Valley region experienced complex deformation associated with extension and shearing during Neogene extensional tectonism (e.g. Wernicke et al., 1988). It has been suggested that tilting associated with generally west-dipping normal faults, as well as vertical axis rotations of crustal blocks associated with conjugate strike-slip fault systems principally accommodated the deformation (e.g. Serpa and Pavlis, 1996). Geologic mapping and associated structural analyses suggest that strike-slip faults are coeval with normal faulting and have a left-lateral sense when they strike eastward or northeastward (e.g., Garlock fault; Figure 4.2A) and a right-lateral sense when they strike northwestward (e.g., south Death Valley fault; Figure 4.2A); Wright, 1976; Serpa and Pavlis, 1996; Pavlis et al., 2014). However, the extent to which extension is partitioned between the normal faulting and strike-slip faulting have long been debated (e.g. Burchfiel, 1965; Guth, 1981; Snow and Wernicke, 1989; Holm et al., 1993; Petronis et al., 2002; Renik and Christie-Blick, 2013).

The Death Valley region mafic sills that we sampled belong to different range-scale crustal blocks, including the Panamint Mountains, the Black Mountains, and the Nopah Range (Figure 4.2A). Sedimentary strata in the Crystal Spring Formation in these ranges dip variably

to the east (Figure 4.2A). The mafic sills intruded parallel to the bedding of the Crystal Spring Formation, often taking advantage of contacts between different lithologies such as the contact between the argillite facies and the cherty dolomite facies. The dips of the sills vary between  $\sim 23^\circ$  to  $\sim 86^\circ$ . The paleomagnetic directions for the sills are much better grouped when corrected for this tilt ( $\text{dec}=302.8^\circ$ ,  $\text{inc}=58.0^\circ$ ,  $n=8$ ,  $a_{95}=9.5^\circ$ ,  $k=34.8$ ) than when considered in geographic coordinates without tilt correction ( $\text{dec}=295.1^\circ$ ,  $\text{inc}=8.9^\circ$ ,  $a_{95}=21.6^\circ$ ,  $k=7.5$ ) (Figure C.4). This result is consistent with the interpretation that the characteristic remanence component carried by (titano)magnetite in the sills is a primary remanence acquired during initial cooling prior to tilting of the Crystal Spring Formation.

It is more challenging to correct for vertical axis rotations in the Death Valley region as the degrees of rotations are poorly constrained. Sills CS1, CS2, and CS6 are from Warm Spring Canyon of the Panamint Mountains, which is an east-tilting block now bounded by the right-lateral Panamint Valley fault to the west and the left-lateral Garlock fault to the south (Figure 4.2; Snow and Wernicke, 1989; Snow, 2000). Stewart (1983) interpreted that the Panamint Range was detached from above the crystalline core of the Black Mountains and translated some 80 km northwest along west dipping low-angle detachment faults. Petronis et al. (2002) developed paleomagnetic data from Miocene intrusive rocks in the central Panamint Range and Miocene volcanic rocks in the eastern part of the range. Their data from the central range show a pole position that overlaps with that expected for no rotation, which they interpreted to indicate minimal amount of vertical axis rotation. They did find a discordance between paleomagnetic declinations developed from Miocene volcanic rocks in the eastern Panamint Range which appear to show substantial clockwise vertical axis rotations since the Miocene ( $27.6^\circ \pm 15.2^\circ$ , calculated based on nine paleomagnetic sites). However, Petronis et al. (2002) cautioned against interpreting there to have been a large vertical axis rotation in the eastern range as their data may undersample paleosecular variation. In the northwest Black Mountains, paleomagnetic data developed from Miocene intrusive rocks and Proterozoic basement rocks have been interpreted to indicate large vertical axis rotations as a result of oroclinal bending associated with right-lateral shear along the Death Valley fault zone (up to  $\sim 80^\circ$ ; Holm et al., 1993). However, paleomagnetic data developed from late Miocene igneous rocks in the eastern Panamint Mountains indicate minimal rotations in the region (Petronis et al., 2002). These data led Petronis et al. (2002) to hypothesize that the significant vertical axis rotation observed by Holm et al. (1993) could be restricted to the western range where the basement block is sheared along the Death Valley fault zone (Figure 4.2). In this case, the more southeastern parts of the Black Mountains fault block, where sills CS7, CS8, and CS9 were collected, and distal from the fault zone, may have experienced relatively insignificant vertical axis rotation (Figure 4.2). In the Nopah Range, where site CS13 was sampled within the crystalline basement (Figure 4.2), no quantitative constraints exist on the amount of vertical axis rotation. Models that involve no rotation to those with up to  $30^\circ$  of clockwise rotation since the Neogene have all been proposed and interpreted to broadly fit the structural evidence in the region (e.g. Serpa and Pavlis, 1996; Pavlis et al., 2014). Rotation in the Alexander Hills (site CS12) is similarly poorly constrained.

The limited number of paleomagnetic sites from mafic sills in the different range blocks

preclude the assessment of vertical axis rotation at each sampling locality (Figure 4.2A). This limitation is due to the secular variation of the geomagnetic field, which makes it such that single VGPs or low numbers of VGPs do not give accurate or precise estimate of the mean paleomagnetic pole position to be compared to a reference path. However, the tilt-corrected VGPs from the eight mafic sills with well-resolved magnetizations can provide insights into the structural history of the study region when viewed in context of Laurentia's apparent polar wander path in the late Mesoproterozoic. The tilt-corrected virtual geomagnetic poles from all sills are grouped at northern high latitudes, and the mean pole position plots close to the inverted pole position for ca. 1100 Ma and 1095 Ma (Figure 4.8A; Swanson-Hysell et al., 2019b). This position is consistent with the ca. 1098 Ma age given by the indistinguishable zircon U-Pb ages from the three dated sills (Figure 4.1B; Mohr et al., 2024). The overlapping pole positions between the Death Valley sills mean pole and poles from rocks of similar age in the Midcontinent Rift of the continental interior indicate that any vertical axis rotations were not large enough to have displaced the pole from the path ( $<30^\circ$ ; Figure 4.8A).

Until more detailed and quantitative spatial and temporal constraints are developed for the different range blocks of the Death Valley region, it remains inconclusive as to the amount of Neogene vertical axis rotation correction to apply to these Mesoproterozoic sill directions. Given these vertical axis rotation uncertainties, we believe it is the best to not include the Death Valley mafic sills paleomagnetic pole into curated paleogeography databases. Nevertheless, the pole with no vertical axis rotation corrections to the sites is consistent with the expected ca. 1098 position of Laurentia.

## Grand Canyon region intrusions and Cardenas Basalt

Weil et al. (2003) developed paleomagnetic data from 13 mafic intrusions (in the eastern Grand Canyon between RM68 and RM78; Fig. 4.2) as well as three Cardenas Basalt flows at Basalt Canyon. Using the framework that the intrusions were time-equivalent with one another and with the lavas, Weil et al. (2003) grouped all paleomagnetic directions from the intrusive and extrusive rocks to calculate a mean paleomagnetic pole position. There is an overall consistency in the directions of those studied units which is consistent with this interpretation. The pole was assigned an age of  $1090.6 \pm 4.5$  Ma based on an  $^{40}\text{Ar}/^{39}\text{Ar}$  age developed from biotite collected within Unkar sedimentary rocks baked by a sill in the western Grand Canyon at RM131 (outside their paleomagnetic study region; Weil et al., 2003). This mean pole position has been included in pole compilations (e.g. Evans et al., 2021) and used to constrain Laurentia's apparent polar wander path in the late Mesoproterozoic.

The recent high-precision zircon U-Pb ages from the two sills in western Grand Canyon and the thick Cardenas Basalt flow at Nankoweap Canyon indicate that some of the sills in the Unkar Group are not feeders to the Cardenas Basalt given that their ca. 1098 Ma ages are  $\sim 16$  Myr older than the lavas which erupted ca. 1082 Ma (Figure 4.1B; Mohr et al., 2024). Improvements in the paleomagnetic and geochronological records from the Midcontinent Rift (e.g. Tauxe and Kodama, 2009; Kulakov et al., 2013b; Fairchild et al., 2017; Swanson-Hysell et al., 2019b) and advances in synthesizing apparent polar wander paths that incorporate

both positional and temporal uncertainty, have led to the development of an updated ca. 1110 and 1070 Ma Keweenawan Track pole path (Figure 4.8; Swanson-Hysell et al., 2019b; Rose et al., 2022). In context of this updated pole path, the new geochronology data from Mohr et al. (2024) would predict that the ca. 1098 sills and the ca. 1082 Ma Cardenas Basalt would have recorded distinct pole positions with a large ( $\sim 23^\circ$ ) angular distance between them (Swanson-Hysell et al., 2019b; Rose et al., 2022).

The new paleomagnetic data from the Grand Canyon are consistent with the updated geochronology. Although there are not enough dated ca. 1098 Ma mafic sills from the Grand Canyon that paleosecular variation can be averaged out and a mean paleomagnetic pole position can be calculated, the VGPs from the two dated mafic sills both plot at high latitudes, close to the ca. 1100 Ma pole path position based on Midcontinent Rift data (Figure 4.8). On the other hand, the VGPs of the 18 Cardenas Basalt lava flows are consistent with being Fisher distributed (Figure C.5), with a mean pole position at a low latitude. This pole position overlaps with Laurentia's pole path at ca. 1085 Ma and ca. 1080 Ma (Figure 4.8B).

Despite a lack of direct field evidence for feeder dikes, and that the two dated sills in western Grand Canyon cannot be feeders to the lava flows given their older age (Figure 4.1, 4.2B), there would have been feeder dikes to the Cardenas Basalt that crosscut older Unkar sedimentary rocks. While high-precision geochronology on individual intrusions would be needed to unambiguously distinguish potential Cardenas feeders from older intrusions, paleomagnetic data have the potential to provide insight given the rapid apparent polar wander of Laurentia at the time. The VGPs of the Hance sill (UI3), Hance dike (UI2), and the Red Canyon sill (UI1) are well-grouped at equatorial latitudes (Figure 4.8B). These poles are close to the inverted ca. 1080 Ma pole position of the Keweenawan Track. Geographically, these intrusions are close to the Cardenas Basalt near Basalt Canyon and far from the dated ca. 1098 Ma sills (Fig. 4.2B). Geochemical data developed by Larson et al. (1994) also show that the Hance sill and Cardenas Basalt have similar rare earth element patterns (Figure C.6). These data are consistent with the interpretation of the Hance intrusions (UI1, UI2, and UI3) as feeders to the Cardenas Basalt. The Birdfoot dikes, Lizard dikes, and Tanner dikes studied by Weil et al. (2003) are also close to Basalt Canyon (Fig. 4.2). A mean paleomagnetic pole based on VGPs from these intrusions (i.e. dike data from Weil et al. (2003)) and from the Hance intrusions of this study is calculated and shown in Figure 4.8B. This pole position is similar to that from the Cardenas Basalt. The VGPs from these eastern Grand Canyon intrusions pass a common mean test with the Cardenas Basalts VGPs (Fig. 4.8). While some of the individual VGPs plot at higher latitudes which could be consistent with the ca. 1098 Ma pulse of magmatism, the overall similarity of directions is consistent with interpretation of some of these eastern Grand Canyon intrusions being ca. 1082 Ma feeders to the Cardenas Basalt. In contrast, the geochronology and paleomagnetic directions of the western sills show them to be associated with the older ca. 1098 Ma magmatism.

### Complexity associated with hypothesized Colorado Plateau rotation

The Grand Canyon is located at the southwestern edge of the Colorado Plateau which was uplifted, folded, and tilted as a result of compression associated with the subduction of the Farallon plate underneath the North American plate during the late Cretaceous to Paleogene Laramide orogeny (Yonkee and Weil, 2015; Karlstrom and Timmons, 2012; Timmons et al., 2012; Karlstrom et al., 2022). Structural analyses have suggested that the plateau rotated clockwise as a rigid block with respect to cratonic North America due to shear during the orogeny (e.g. Hamilton, 1981, 1988). Efforts to quantitatively constrain the amount of rotation using paleomagnetic data have given different results albeit with agreement that the sense of rotation is clockwise. Kent and Witte (1993) and Steiner (2003) took the approach of developing Mesozoic paleomagnetic poles from the Colorado Plateau and comparing them with reference poles developed from cratonic North America to estimate the amount of rotation. Those studies gave relatively large estimates of interpreted rotations of  $13.5 \pm 3.5^\circ$  and  $9.0 \pm 3.3^\circ$ , respectively. Challenges exist with the approach of estimating the amount of rotation based on single paleomagnetic pole positions such as issues with age uncertainty between poles and reference pole positions. Garza et al. (1998) and Bryan and Gordon (1990) used approaches based on comparing multiple paleomagnetic poles through the Paleozoic to Mesozoic from on and off the plateau simultaneously and interpreted that the amount of rotation is  $\sim 5^\circ$ . These smaller estimated rotations are more consistent with the structural evidence of a small magnitude of strike-slip translation along the boundary of the Colorado Plateau (e.g. Woodward et al., 1997).

The Cardenas Basalt paleomagnetic pole presents an opportunity of using Mesoproterozoic data to gain insights into Colorado Plateau rotation. Figure 4.8D shows the paleomagnetic pole of the Cardenas Basalt in context of the synthesized Keweenawan Track (two Euler scenario; Swanson-Hysell et al., 2019b). As a progressively larger correction for Colorado Plateau rotation (using an Euler pole at  $-107^\circ\text{E}$ ,  $37^\circ\text{N}$ ; Bryan and Gordon, 1990) is applied, the Cardenas Basalt pole moves farther away from the Keweenawan Track and no longer overlaps with the inverted pole positions at ca. 1080 Ma after a  $6^\circ$  correction (Figure 4.8D). While this result is consistent with the interpretation that the Colorado Plateau experienced a relatively small amount of rotation ( $<6^\circ$ ), it is not feasible to use a single Cardenas Basalt pole to constrain the amount of Colorado Plateau rotation more precisely than previous estimates, as the Fisher 95% angular uncertainty associated with the pole position itself is  $11.8^\circ$  (Figure 4.8). Future efforts to constrain Colorado Plateau rotation can incorporate both Mesoproterozoic and Mesozoic poles.

### Outlook for future work in the southwestern Laurentia

The high-precision geochronology data developed by Mohr et al. (2024) revise the southwestern Laurentia large igneous province to feature the emplacement of ca. 1098 Ma thick mafic intrusions (often  $>100$  m in thickness; Wright and Troxel, 1967) from eastern California to central Arizona. The indistinguishable ages from these thick mafic intrusions across a large

areal extent reveal the voluminous and rapid nature of emplacement of the magmatic pulse of the SWLLIP. This large igneous province could include more undated mafic intrusions that could be constrained with paleomagnetic data. Bright et al. (2014) suggested that some mafic sills in New Mexico could also be a part of the SWLLIP, but the available geochronology data does not have the resolution to robustly test the hypothesis. In Figure 4.1, we present an updated version of the areal extent of the SWLLIP as being defined by the ca. 1098 Ma geochronologically constrained mafic magmatism.

Both geochronology and paleomagnetic data indicate that the Cardenas Basalt in the Grand Canyon was emplaced during a distinct episode of magmatism younger than the SWLLIP mafic sills. However, whether the emplacement of the lava flows is associated with a localized regional event or another period of large igneous province style magmatism remains to be tested. One mafic sill in the Dead Mountains of eastern California yielded a weighted mean zircon U-Pb age of  $1082.60 \pm 0.30$  (Mohr et al., 2024), which is indistinguishable with the  $1082.18 \pm 1.25$  Ma age of the Cardenas Basalt (Figure 4.1B). These ages indicate that the ca. 1082 Ma mafic magmatism could have stretched over at least 300 km. Over how large of a region did this ca. 1082 Ma magmatism occur?

The paleomagnetic pole of the Cardenas Basalt can help further constrain the Keweenawan Track given that it is younger than any pole developed from Midcontinent Rift volcanics. Currently, the younger end of the Keweenawan Track is constrained by the ca. 1084 Ma lava flows of the Michipicoten Island Formation and the ca. 1080-1050 Ma Nonesuch Formation and Freda Formation of the Oronto Group (Swanson-Hysell et al., 2019b). Uncertainties associated with correcting for inclination shallowing in sedimentary records and constraining the age of detrital remanence magnetization have led to the post-1085 Ma portion of the path to be less constrained than that from ca. 1110 to 1085 (Figure 4.8). The new temporally constrained Cardenas Basalt pole adds a valuable new constraint to Laurentia's database of paleomagnetic poles given as it is younger than the Michipicoten Island Formation. Additionally, as a pole from volcanics no correction for inclination shallowing is necessary. Once the amount of Colorado Plateau rotation and the associated uncertainty is better constrained, an updated Keweenawan Track can be developed using the new site-based resampling approach of Gallo et al. (2023). This method has the machinery to incorporate uncertainties in pole position, geochronology, as well as the magnitude of Colorado Plateau rotation correction into a synthesized path.

## 4.7 Acknowledgments

Project research was funded by NSF CAREER grant EAR-1847277 to N.L.S.-H. Additional research support came from an H2H8 research grant to Y.Z. as well as a UC Berkeley summer undergraduate research fellowship and a UC Berkeley Department of Earth Science Ramsden grant to N.A. We thank participants in the 2021 Grand Canyon Supergroup field forum for stimulating interactions in the canyon. National Park Service Permits for sampling within Grand Canyon National Park and Death Valley National Park are gratefully acknowledged.

# Chapter 5

## Tracking Rodinia into the Neoproterozoic: new paleomagnetic constraints from the Jacobsville Formation

### 5.1 Abstract

The paleogeography of Laurentia throughout the Neoproterozoic is critical for reconstructing global paleogeography due to its central position in the supercontinent Rodinia. We develop a new paleomagnetic pole from red siltstones and fine-grained sandstones of the early Neoproterozoic Jacobsville Formation which is now constrained to be ca. 990 Ma in age. High-resolution thermal demagnetization experiments resolve detrital remanent magnetizations held by hematite. These directions were reoriented within siltstone intraclasts and pass intraformational conglomerate tests—giving confidence that the magnetization is detrital and primary. An inclination-corrected mean paleomagnetic pole position for the Jacobsville Formation indicates that Laurentia’s motion slowed down significantly following the onset of the Grenvillian orogeny. Prior rapid plate motion associated with closure of the Unimos Ocean between 1110 and 1090 Ma transitioned to slow drift of Laurentia across the equator in the late Mesoproterozoic to early Neoproterozoic. We interpret the distinct position of this well-dated pole from those in the Grenville orogen that have been assigned

---

This chapter is published as a peer-reviewed manuscript: Zhang, Y., Hodgin, E.B., Mohr, M.T., Alemu, T.B., Pierce, J., Fuentes, A.J., Swanson-Hysell, N.L. (2024). Tracking Rodinia into the Neoproterozoic: new paleomagnetic constraints from the Jacobsville Formation. *Tectonics*. doi: <https://doi.org/10.1029/2023TC007866>.

a similar age to indicate that the ages of the poles associated with the Grenville Loop likely need to be revised to be younger due to prolonged exhumation.

## 5.2 Introduction

The extensively studied paleomagnetic records of ca. 1109 to 1084 Ma volcanics and intrusions associated with the North American Midcontinent Rift provide crucial constraints on the paleogeography of Laurentia in the late Mesoproterozoic Era (Halls and Pesonen, 1982; Fairchild et al., 2017; Swanson-Hysell et al., 2019b). The resulting sequence of poles known as the Keweenawan Track is a central record for reconstructing the assembly of the ancient supercontinent Rodinia (Evans, 2021). An advantage of intracratonic magmatic events, such as those preserved in the Midcontinent Rift, is that they lead to emplacement of igneous rocks that can readily retain primary thermal remanent magnetization (TRM) that can be confidently associated with the emplacement age of the unit. However, following the development of the Midcontinent Rift, there was a  $\sim$ 300 Myr quiescence in known intracratonic magmatic activity in Laurentia that lasted until the emplacement of the ca. 775 Ma Gunbarrel large igneous province (Harlan et al., 2003; Mackinder et al., 2019; Swanson-Hysell, 2021). The lack of Laurentian rocks with primary TRM in the early Neoproterozoic has led paleogeographic reconstructions to be reliant on magnetizations acquired by rocks that were metamorphosed during the ca. 1090 to 980 Ma Grenvillian orogeny (Rivers, 2008; Rivers et al., 2012; Swanson-Hysell et al., 2023). However, rocks within the orogen acquired their magnetizations during exhumation after peak metamorphic conditions (McWilliams and Dunlop, 1975). As a result, the timing of remanence acquisition needs to be constrained through the more difficult task of dating cooling associated with exhumation. This gap in well-dated paleomagnetic poles for Laurentia in the late Mesoproterozoic to mid-Neoproterozoic contributes to uncertainty in paleogeography at that time including the configuration of the supercontinent Rodinia.

Paleomagnetic poles can also be developed from sedimentary rocks deposited in basins. Sedimentary rocks of the Oronto Group deposited during post-rift thermal subsidence following the bulk of Midcontinent Rift magmatic activity provide paleomagnetic poles that extend the Keweenawan Track to ca. 1070 Ma (Henry et al., 1977; Slotnick et al., 2023). While there are some contemporaneous basins in northern Laurentia (Greenman et al., 2021), there is minimal basin development within Laurentia following the Grenvillian orogeny until the Rodinia supercontinent began to rift apart ca. 770 Ma (Macdonald et al., 2023).

One rare preservation of an early Neoproterozoic sedimentary succession in Laurentia's interior is the Jacobsville Formation (Fig. 5.1; Hamblin, 1958; Hodgin et al., 2022; DeGraff and Carter, 2022). U-Pb detrital zircon dates developed through chemical abrasion–isotope dilution–thermal ionization mass spectrometry (CA-ID-TIMS) of  $1003.21 \pm 2.23$  Ma and  $992.51 \pm 0.64$  Ma ( $2\sigma$  analytical uncertainty) constrain the maximum deposition age of the Jacobsville Formation (Hodgin et al., 2022). A  $985.5 \pm 35.8$  Ma ( $2\sigma$  analytical uncertainty) U-Pb date from calcite veins within the Keweenaw fault provides a minimum age constraint on Jacobsville deposition, as the Jacobsville Formation is folded in the footwall against Mid-

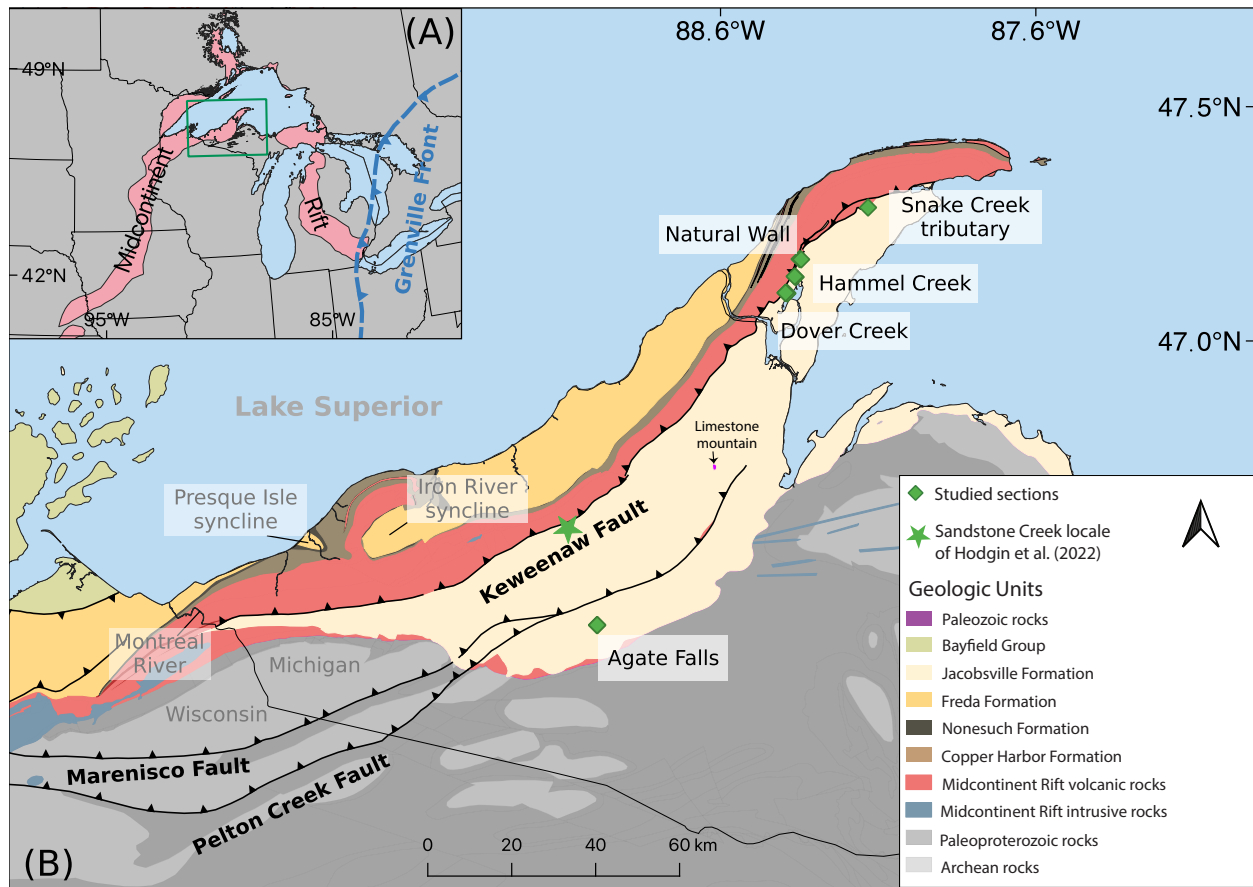


**Figure 5.1:** (A) Regional map showing the extent of the Midcontinent Rift and the location of the Grenville Front relative to the study area. The inset green box shows the extent of panel B. (B) Geologic map of northern Michigan and Wisconsin showing Midcontinent Rift igneous and sedimentary rocks, sedimentary rocks of the Jacobsville Formation and Bayfield Group, other older Paleoproterozoic and Archean rocks, and major post-rift thrust faults. The location of the Jacobsville stratigraphic sections in this study are shown with green diamonds. Map modified from Nicholson et al. (2004).

continent rift volcanics in the hanging wall. Together, these dates bracket the depositional age of the Jacobsville Formation and constrain it to be ca. 990 Ma (Hodgin et al., 2022). These results support the interpretation that the formation was deposited within a synorogenic basin during the Rigolet phase of the Grenvillian orogen and was then deformed during the same orogenic phase.

The Jacobsville Formation contains abundant hematite-bearing sandstone and siltstone which have the potential to record a key pole in Laurentia's apparent polar wander path (APWP) (Dubois, 1962; Roy and Robertson, 1978). Roy and Robertson (1978) conducted a paleomagnetic study that developed a pole which has been used in paleogeographic syntheses where it has been assigned variable ages including an age of ca. 1020 Ma based on APWP extrapolation (e.g. Li et al., 2008). However, the uncertainty in the age of the magnetiza-

tion combined with a lack of field tests, and no application of inclination correction have resulted in the pole not being included in recent curated compilations (e.g. Evans et al., 2021). Obtaining high-quality paleomagnetic data, including robust field tests, motivates the development of new data from the Jacobsville Formation.

In this study, we investigate five stratigraphic sections of the Jacobsville Formation on and near the Keweenaw Peninsula, Michigan, USA (Figs. 5.1 and 5.2). These sections were chosen given the abundance of fine-grained siliciclastic lithologies where magnetization can be constrained through intraclast conglomerate field tests. Additionally, they are within the continuous bedrock belt from which chronostratigraphic constraints have been developed. In contrast to fluvial sandstones in other exposures such as in the eastern Lake Superior region near Sault Ste. Marie, the maximum and minimum depositional ages of these sections can be more confidently constrained.

Within sampled lithologies, high-resolution thermal demagnetization isolates primary detrital remanent magnetization (DRM) from secondary chemical remanent magnetization (CRM). This interpretation is supported by the DRM directions passing intraformational conglomerate tests on siltstone intraclasts that were ripped-up and remobilized within the fluvial depositional environment. A paleomagnetic fold test further constrains the timing of DRM acquisition to predate the folding of the Jacobsville Formation in the footwall of the Keweenaw fault soon after deposition. With these data, we develop a new inclination-corrected paleomagnetic pole for the Jacobsville Formation based on a large number of samples that gives new constraints on the paleogeographic position of Laurentia in the earliest Neoproterozoic.

### 5.3 Geologic setting

The ca. 1109 Ma to 1084 Ma North American Midcontinent Rift is a major intracontinental rift system that extends over 2000 km through the Laurentia craton (Fig. 5.1). Following the end of active extension in the rift, thermal subsidence resulted in the accumulation of >4 km of ca. 1085-1050 Ma Oronto Group strata that are both intercalated with the youngest volcanics and deposited atop them (Fig. 5.1; Daniels, 1982; Cannon, 1989). Subsequently, the rift was inverted as contraction associated with the ca. 1090-980 Ma Grenvillian Orogeny on the eastern margin of Laurentia (Fig. 5.1) propagated into Laurentia's interior (Cannon et al., 1993; Cannon, 1994; Hodgin et al., 2022; Swanson-Hysell et al., 2023).

During rift inversion, Midcontinent Rift volcanic and sedimentary rocks were uplifted along with Paleoproterozoic and Archean lithologies via thrust faults such as the Marenisco fault, forming the crustal-scale Montreal River monocline (Fig. 5.1; Cannon et al., 1993). Rb-Sr biotite thermochronology data of Cannon et al. (1993) show Archean lithologies within the Montreal River monocline to have been exhumed to mid to shallow crustal temperatures ( $\sim 270^{\circ}\text{C}$ ) by ca. 1050 Ma. The Jacobsville Formation overlies an angular unconformity that developed on lithologies that were exhumed through this earlier episode of contractional deformation associated with Grenvillian orogenesis (Fig. 5.1; Hamblin, 1958; Cannon et al.,

1993; Kalliokoski, 1982). Conglomeratic facies occur in the basal Jacobsville Formation, with clasts derived from locally uplifted basement lithologies (Irving and Chamberlin, 1885; Hamblin, 1958; Kalliokoski, 1982).

Bedding planes in the Jacobsville Formation typically have shallow dips. The exception to these near-horizontal orientations is proximal to reverse faults such as the Keweenaw fault (Fig. 5.1) where the Jacobsville Formation was occasionally deformed into monoclinal drag folds resulting in steeply tilted to overturned beds (Fig. 5.1; Irving and Chamberlin, 1885; Cannon and Nicholson, 2001). Recent mapping of the Jacobsville Formation also found that it sometimes onlaps the Midcontinent Rift volcanics within or adjacent to en echelon fault branches of the Keweenaw fault system near the northern end of the Keweenaw Peninsula (Tyrrell, 2019; Mueller, 2021). These observations are consistent with the interpretation that there was deposition of Jacobsville Formation sediments during faulting.

## Overview of Jacobsville sedimentology and stratigraphy

The Jacobsville Formation is a fluvial succession of feldspathic and quartzose conglomerates, sandstones, siltstones, and shales devoid of lava flows or cross-cutting igneous dikes although internal clastic dikes are present (Hamblin, 1958). Sandstones of the Jacobsville Formation are more quartz-rich with generally fewer lithic fragments than sandstones of the Oronto Group such that they can typically be classified as subarkose to quartz arenites (Fig. 5.3; Hamblin, 1958; Ojakangas and Dickas, 2002). While much of the Jacobsville Formation is dominated by sandstone channel deposits, there are clay-rich siltstones that formed in overbank settings that are a major focus of this study.

In southern exposures of the Jacobsville Formation, conglomerate facies typically have provenance sourced from Paleoproterozoic lithologies such as vein quartz and iron formation clasts (Hamblin, 1958; Kalliokoski, 1982). The occurrence of these conglomerates in proximity to the Marenisco fault and Pelton Creek fault and the downsection steepening of stratal dips interpreted as growth strata may represent syn-depositional development of local relief (Fig. 5.1; Kalliokoski, 1982; Hedgman, 1992). Close to the Keweenaw fault in the central Keweenaw Peninsula (Fig. 5.1), the Jacobsville Formation consists dominantly of quartz-rich, trough cross-bedded, medium-grained sandstone, with locally abundant clast-supported pebble to cobble conglomerate, and interbeds of red, hematite-bearing, micaceous siltstone to fine-grained sandstone (Dover Creek, Hammel Creek, Natural Wall; Figs. 5.2 and 5.3). In this region, the conglomerate contains abundant rounded to angular volcanic clasts as large as boulders that are likely derived from uplifted Midcontinent Rift volcanics (Irving and Chamberlin, 1885; Brojanigo, 1984). Thicker intervals of dark red to brick red siltstone and very fine-grained sandstone are interbedded with coarser-grained sandstone and conglomerate at Agate Falls and Dover Creek (Figs. 5.2 and 5.3). Intraclasts of the siltstones are found within some channelized interbeds of sandstone and conglomerate (Fig. 5.4).

The abundance of clasts of rift volcanics in the conglomeratic facies at Dover Creek, Hammel Creek, and Natural Wall indicates the presence of uplifted volcanics in proximity

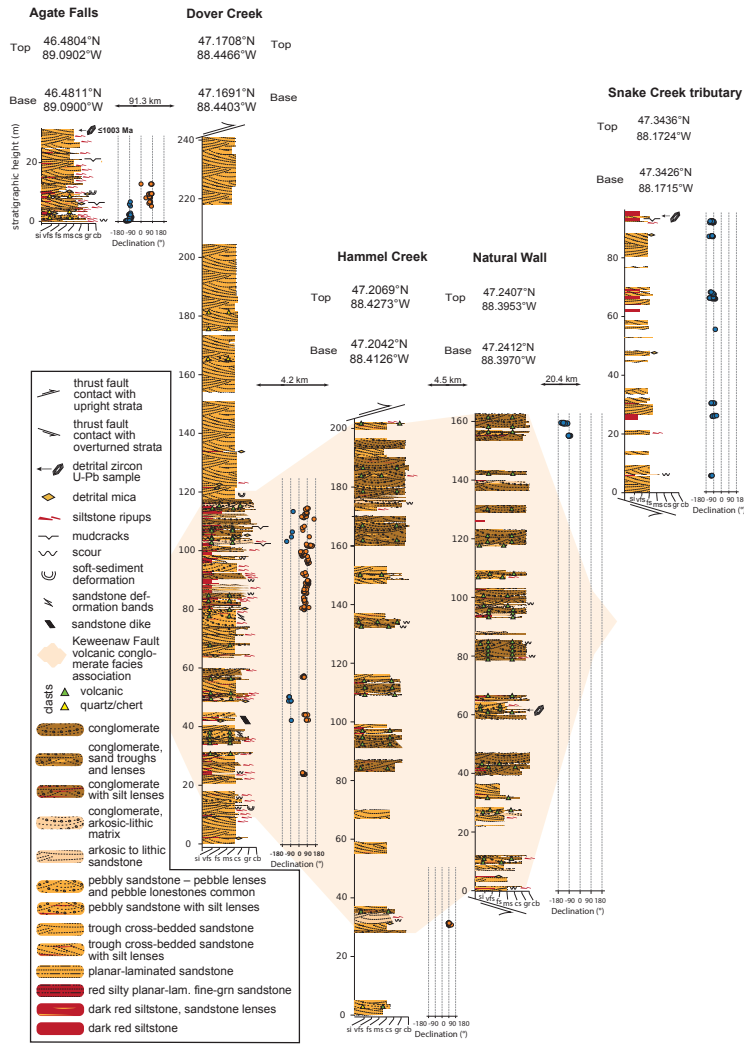


**Figure 5.2:** Lithostratigraphy and magnetostratigraphy for studied sections of the Jacobsville Formation in northern Michigan, USA. GPS locations for the base and top of the sections are noted. Paleomagnetic sampling focused on the dark red siltstone to fine-grained sandstone lithofacies. Paleomagnetic specimen declinations are plotted with blue circles corresponding to normal polarity and orange circles to reverse polarity. The maximum depositional age of the Agate Falls section is constrained by a CA-ID-TIMS detrital zircon U-Pb date of  $1003.2 \pm 2.2$  Ma (sample AF1-29.3 of Hodgin et al. (2022)). In the Snake Creek tributary and Natural Wall sections, the position of the detrital zircon samples BSC1-92.5 and NW1-61.5 from Hodgin et al. (2022) are shown. No U-Pb zircon dates from these samples were younger than the age of Midcontinent Rift volcanics. A correlation of a facies association consisting of volcanic-clast conglomerate, coarse arkosic sandstone, and dark red clay-rich siltstone is inferred between the sections at Dover Creek (along Dover Creek and a tributary falls), Hammel Creek, and Natural Wall (Brojanigo, 1984). The stratigraphic correlation between Jacobsville sections at Agate Falls and Snake Creek tributary with these correlated sections from the central Keweenaw Peninsula is relatively uncertain.



**Figure 5.3:** Field photos of the Jacobsville Formation. (A) The red/white medium-grained sandstone with decimeter-scale trough cross-stratification in this image (taken at the shore near the unincorporated community of Jacobsville  $46.9819^{\circ}\text{N}$ ,  $88.4068^{\circ}\text{W}$ ) is a wide-spread lithofacies in the formation, but was not targeted for paleomagnetic sampling in this study. (B, C, D) At the Snake Creek tributary and the Natural Wall ravine in the northeastern Keweenaw Peninsula, intervals of red fine-grained sandstone to siltstone beds can be found through the steeply dipping to overturned basal strata near the Keweenaw fault and also the nearly horizontal upper strata. At the Dover Creek section (E), thick red siltstone horizons interbedded or interfingering with sandstones and conglomerates are found along a Dover Creek tributary waterfall ( $47.1708^{\circ}\text{N}$ ,  $88.4466^{\circ}\text{W}$ ; this waterfall is distinct, but close to Hungarian Falls). Abundant reoriented siltstone intraclasts can be present within the conglomeratic layers above siltstone beds (Fig. 5.4). (F) At Agate Falls, nearly flat-lying red fissile siltstone beds are exposed. Detrital mica grains deposited parallel to the bedding plane are often present within the siltstone facies. Another set of siltstone intraclasts were sampled from a conglomeratic layer at Agate Falls for a paleomagnetic conglomerate test (Fig. 5.4).

to the Keweenaw fault in the central part of the peninsula during Jacobsville deposition (Figs. 5.1 and 5.2). Coarse-grained arkosic to lithic sandstone is a facies associated with the volcanic-clast conglomerates and likely derived from mechanical weathering of the exhumed volcanics. Chemical weathering of exhumed volcanics from the hanging wall is a likely source of clay within the abundant fine-grained lithologies that are associated with the volcanic-clast conglomeratic facies (Fig. 5.2). Detrital zircon provenance data from Jacobsville samples on the Keweenaw Peninsula developed by Malone et al. (2020) reveal zircon with dates overlapping with Midcontinent Rift volcanism consistent with this provenance interpretation. Detrital mica grains up to ~5 mm in size that are commonly found within siltstone to fine-grained sandstone within the Jacobsville are likely sourced from Paleoproterozoic and Archean lithologies in the region (Fig. 5.1) and preferentially settled in lower energy overbank settings.

The thickness of the Jacobsville strata can vary in northern Michigan (Hamblin, 1958; Kalliokoski, 1982), and complete stratigraphic sections are not exposed at the studied localities (Figs. 5.1 and 5.2). Clay-rich red siltstone is more abundant in conjunction with conglomerates (e.g. 20-120 m in the Dover Creek section; Figs. 5.2 and 5.3) than with the cross-stratified sandstone which dominates much of the formation. Relatively thin lithic to arkosic sandstone beds, which are otherwise uncommon in the Jacobsville Formation, are commonly associated with the volcanic conglomerates and red siltstones near the Keweenaw fault (Fig. 5.2). Together, the volcanic conglomerates, red siltstones, and arkosic sandstones make up a unique facies association. As previously interpreted by Brojanigo (1984), this facies association was likely deposited proximal to actively uplifting volcanic rocks near the Dover Creek, Hammel Creek, and Natural Wall sections (Fig. 5.2). The relative stratigraphic positions of the Agate Falls and Snake Creek tributary sections are less certain (Figs. 5.1 and 5.2).

The Jacobsville Formation has been mapped to have a continuous extent from the Wisconsin and Michigan border northeast to the Keweenaw Peninsula and east to the Marquette region (Fig. 5.1; Hamblin, 1958; Cannon et al., 1995, 1996; Cannon and Nicholson, 2001). In the eastern Lake Superior region near Sault Ste. Marie, Ontario, there are exposures of sedimentary rocks that are also mapped as the Jacobsville Formation (Hamblin, 1958). As observed on the Keweenaw Peninsula, these sandstones are within the footwall of faults where they are overthrust by Midcontinent Rift volcanics near Mamainse Point (Manson and Halls, 1994). To the west, the Jacobsville Formation has been interpreted to be correlative with sedimentary rocks of the Bayfield Group in northern Wisconsin and the Fond du Lac Formation and Hinckley Formation in Minnesota (Thwaites, 1912; Hamblin, 1958; Wallace, 1971; Kalliokoski, 1982; Ojakangas et al., 2001). A challenge associated with these correlations is that the ca. 1075 to 1050 Ma Freda Formation of the Oronto Group and the ca. 990 Ma Jacobsville Formation have quite similar fluvial lithofacies despite being deposited in distinct basinal settings at different times.

## 5.4 Paleomagnetic results and interpretation

Oriented paleomagnetic samples were collected with a portable electric drill from five stratigraphic sections of the Jacobsville Formation in northern Michigan (Figs. 5.1 and 5.2). Additional oriented cores and block samples of siltstone intraclasts within conglomerates and conglomeratic sandstones were sampled within the Dover Creek and Agate Falls sections (Figs. 5.1 and 5.2, and 5.4). To maximize sampling of distinct time snapshots of the geomagnetic field at the time of Jacobsville deposition and average out paleosecular variation, we optimized for vertical stratigraphic coverage (Sapienza et al., 2023). Each sample is a distinct stratigraphic horizon and therefore a paleomagnetic site, representing a unique record of the geomagnetic field. Red fine-grained sandstone to shaly siltstone layers were preferentially sampled as they have lower permeability and are less susceptible to diagenetic alteration through fluid flow than coarser-grained sandstone. These fine-grained lithologies are typically of deep red color in contrast to coarse-grained lithologies that have splotchy tan, red, and light green coloration associated with secondary reduction (Fig. 5.3A). Care was taken to avoid collecting samples with reduction spots. Paleomagnetic cores and blocks were oriented using a magnetic compass and a sun compass when possible. Sun compass data were preferentially used when available. A total of 379 specimens including 30 intraclasts were collected for paleomagnetic study. To minimize the visual impact of sampling, rock containing core holes was knocked out of outcrops following samples—readily done for the friable siltstones and sandstones of the Jacobsville Formation.

Challenges exist in isolating the primary magnetization in sedimentary rocks. Primary detrital remanence acquired during deposition can be masked by secondary remanence acquired through precipitation and growth of diagenetic minerals within sedimentary rocks syn- to post-deposition (e.g. pigmentary hematite formed from precursor phases such as ferrihydrite; Jiang et al., 2018). In red beds, it has been found that formation of pigmentary hematite can post-date the timing of deposition, resulting in a chemical remanent magnetization superimposed upon primary detrital remanent magnetization carried by detrital grains (Collinson, 1974; Tauxe et al., 1980). To isolate the remanence components of sandstones of various grain sizes of the Jacobsville Formation, Roy and Robertson (1978) adopted a method first applied by Collinson (1965) to preferentially remove fine-grained pigmentary hematite through prolonged immersion in concentrated HCl acid. Progressively longer immersion times first dissolve the nanometer-scale pigmentary hematite prior to dissolving the coarser micrometer-scale detrital grains. Studies applying paired acid etching demagnetization and thermal demagnetization show that the pigmentary hematite grains tend to have lower unblocking temperatures than detrital ones (Tauxe et al., 1980; Bilardello and Kodama, 2010b). High-resolution thermal demagnetization experiments with temperature intervals as small as 1-2 °C have also been shown to be effective in isolating detrital remanence from chemical remanence as coarser hematite grains tend to have higher unblocking temperatures closer to the Néel temperature of hematite (Jiang et al., 2015; Swanson-Hysell et al., 2019a).

In the Jacobsville Formation samples that we collected, there are both detrital hematite grains (10s of micrometers) as well as finer grained (sub-micrometer) pigmentary hematite

(Fig. D.1). We adopted a thermal demagnetization protocol with increasingly higher resolution approaching the Néel temperature of hematite ( $5\text{ }^{\circ}\text{C}$  to  $2\text{ }^{\circ}\text{C}$ ; Fig. 5.4, D.2). The specimens underwent step-wise thermal demagnetization at the UC Berkeley Paleomagnetism Lab using an ASC demagnetizer (residual fields  $<10\text{ nT}$ ) with measurements made on a 2G DC-SQUID magnetometer. Due to the thermal gradient in the oven, we keep the specimens at the same location throughout the demagnetization steps. This protocol makes the temperature difference between each step relatively consistent for each specimen compared to if they changed positions within the oven. While the very fine-grained sandstone and siltstone lithologies typically do not have an appreciable present-day local field overprint component, such a component can be present in fine-grained sandstones and is removed by  $\sim 300\text{ }^{\circ}\text{C}$  during thermal demagnetization (Fig. D.2, D.3). A total of 356 specimens yielded detrital remanent magnetizations that can be fit with least-square lines (Kirschvink, 1980). These fits were made using PmagPy (Tauxe et al., 2016) and all paleomagnetic data are available to the measurement level in the MagIC database (<https://doi.org/10.7288/V4/MAGIC/19780>).

## Paleomagnetic field tests

### Fluvial intraclast conglomerate tests

Similar to the thermal demagnetization results of the hematite-bearing fluvial intraclasts of the Freda Formation (Swanson-Hysell et al., 2019a), the siltstone intraclasts of the Jacobsville Formation typically reveal two distinct magnetization components (Fig. 5.4). One component shows similar vector orientations amongst intraclasts and was typically removed up to  $640\text{-}655\text{ }^{\circ}\text{C}$  (Fig. 5.4). The relatively low unblocking temperatures and similarity in directions among the reoriented intraclasts indicate that it is chemical remanent magnetization acquired through crystallization of secondary pigmentary hematite following clast redeposition. After removal of this component, further thermal demagnetization with small step increments at higher temperatures up to  $\sim 689\text{ }^{\circ}\text{C}$  often reveal an origin-trending component (Fig. 5.4). In the data from the clasts, there is typically a significant directional change in specimen magnetization between the mid-temperature component and the high-temperature component. As a result, 27 out of 30 intraclast specimens could be fit with high-temperature least squares lines. Distinct from the well-grouped mid-temperature component directions, the high-temperature directions of the intraclasts are dispersed and the null hypothesis of randomness cannot be rejected at the 95% confidence level ( $n=5$  for intraclasts at Agate Falls and  $n=22$  for intraclasts at Dover Creek; Fig. 5.4; Watson, 1956). This result indicates that the high unblocking temperature remanence is primary and was acquired by detrital hematite grains during initial deposition prior to the clasts being ripped up and reoriented within the depositional environment. This conglomerate test provides strong support for interpreting the high unblocking temperature remanence in the *in situ* beds as a primary DRM.

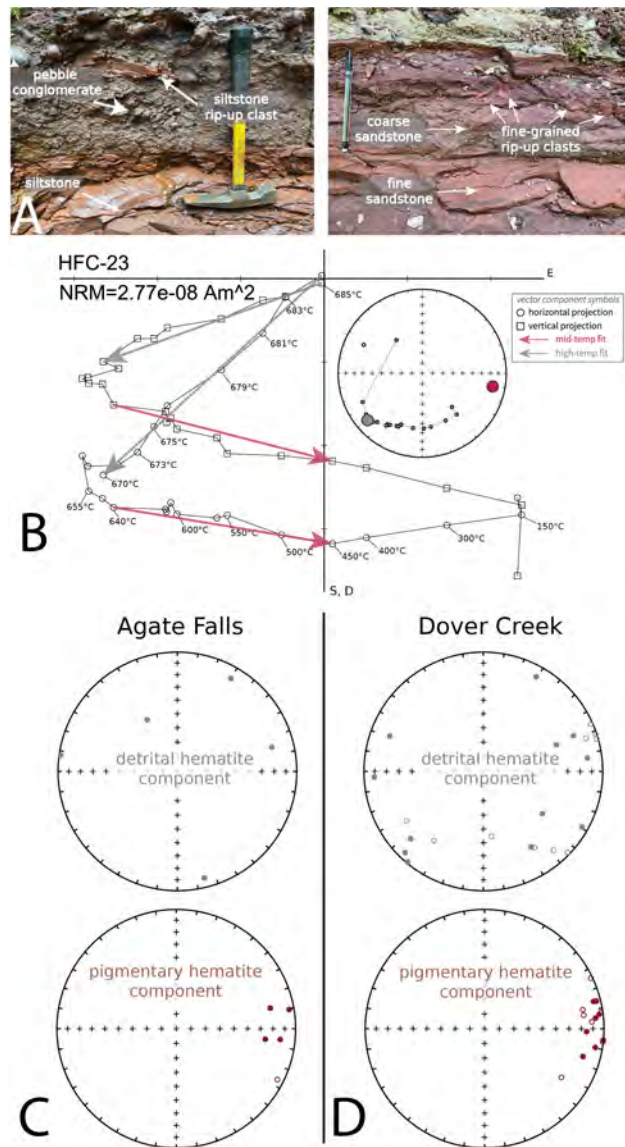


**Figure 5.4:** (A) Field photos of siltstone to fine-grained sandstone fluvial intraclasts within conglomerate and conglomeratic sandstone beds in the Jacobsville Formation. (B) Representative step-wise thermal demagnetization data from an intraclast from Dover Creek (HFC-23) plotted on an orthogonal vector diagram. The plot reveals a mid-temperature component and an origin-trending high-temperature component. The components are present as varying fractions of the overall remanence in different specimens. The direction of the mid-temperature component (interpreted as secondary CRM) is shown as dark red arrows on the orthogonal vector plots and dark red circles on the equal area plots, while the high-temperature component (interpreted as primary DRM) is shown in grey. (C, D) The mid-temperature component has a similar direction among the clasts as can be seen on the summary equal area plots. In contrast, the high-temperature component directions are dispersed and pass the randomness test of Watson (1956). Both the DRM and the CRM directions are shown in geographic coordinates. NRM = natural remanent magnetization.

### Fold test

A total of 71 specimens yielded interpretable DRM directions throughout the stratigraphic section at the Snake Creek tributary (Figs. 5.1 and 5.6). The stratigraphic section is within a large-scale drag fold within the immediate footwall of the Keweenaw fault. As a result, there are exposures of steeply tilted, moderately tilted, as well as nearly horizontal beds along this section that allow us to conduct a paleomagnetic fold test to investigate the timing of magnetization. The chronological constraints on the timing of Keweenaw fault motion indicate that the folding occurred on a timescale of  $\sim$ 10 Myr of deposition—making this fold test a more informative constraint on the age of the remanence than typical for such tests. Given that the more steeply tilted beds accommodated deformation during shortening associated with the Keweenaw fault motion, they could be more prone to non-cylindrical folding and complicate tilt-correction of the paleomagnetic directional data (e.g. Pueyo et al., 2003; Nabavi and Fossen, 2021). Therefore, we conduct a paleomagnetic bootstrap fold test (Tauxe and Watson, 1994) using specimens from the nearly horizontal beds and the moderately tilted beds. The results show that the degrees of untilting that result in the best grouping of the DRM directions have 95% confidence bounds that overlap with 100% unfolding, consistent with the specimens having acquired their magnetization prior to tilting (Fig. 5.5). This positive fold test further supports the interpretation that the Jacobsville red beds acquired a primary detrital remanence during deposition. In contrast, the mid-temperature component directions that typically unblock up to 650 °C from the Snake Creek tributary fails a fold test (Fig. D.4), consistent with them being acquired as chemical remanent magnetizations that postdate the tilting. The positive fold test on the detrital remanence in combination with the similarity of the detrital and chemical remanence directions (Fig. 6B) indicates that the majority of chemical remanence acquisition likely occurred geologically soon after the deformation.

### Paleomagnetic reversals

With the insights gained from the thermal demagnetization results of the Jacobsville fluvial intraclasts and the fold test (Figs. 5.4 and 5.5), we next investigate the detrital remanent magnetizations for all *in situ* specimens from the five stratigraphic sections (Figs. 5.1 and 5.2). The DRM directions are plotted by stratigraphic section location in Figure 5.6. As observed in the sparser data of Roy and Robertson (1978), there are dual polarity magnetizations (Fig. 5.2). The paleomagnetic polarity reversals are shown in stratigraphic context in Figure 5.2 with specimen magnetization declinations plotted against stratigraphic heights. The record of Laurentia’s paleomagnetic poles from the Proterozoic through the Phanerozoic (see compilations in Torsvik et al. (2012) and Swanson-Hysell (2021)) gives a continuity of the orientation of the continent that enables the geomagnetic polarity of the directions to be interpreted. In this framework, the westerly DRM directions are normal geomagnetic polarity and the easterly DRM directions are reversed polarity (Fig. 5.6).

At the Dover Creek section, which goes along Dover Creek and then up the waterfall

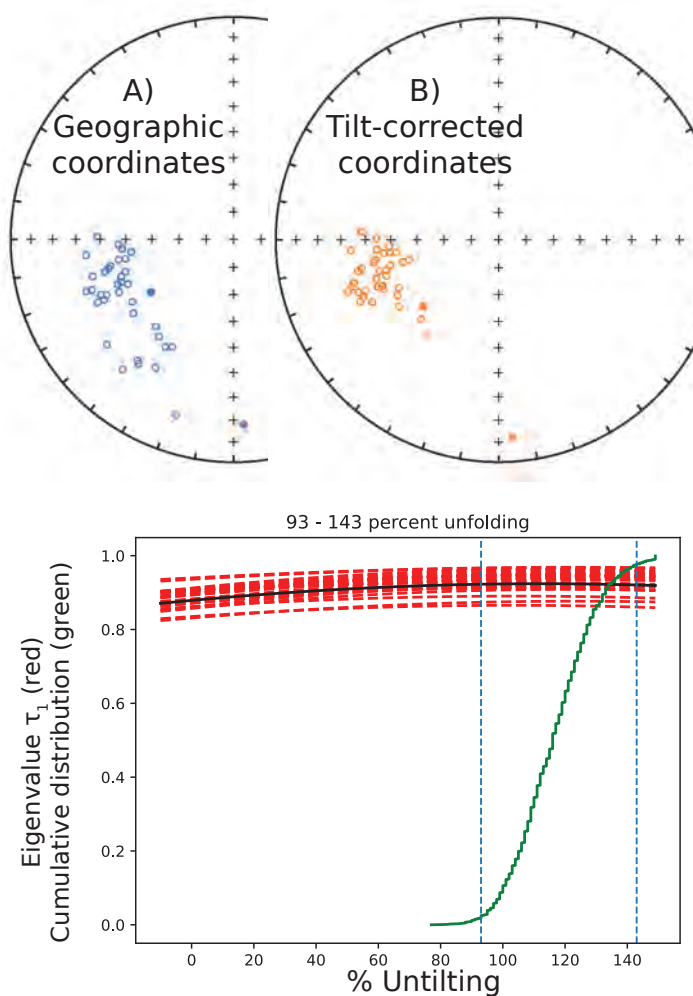


**Figure 5.5:** Bootstrap paleomagnetic fold test (Tauxe and Watson, 1994) of the detrital remanent magnetization directions recorded by specimens from the nearly horizontal beds and moderately tilted beds at the Snake Creek tributary. Complete unfolding lies within the 95% confidence limits of the test, consistent with the magnetization having been acquired prior to tilting.

of a side tributary (the Hungarian Falls side falls), numerous hematite-rich siltstone to fine sandstone layers commonly occur in association with trough cross-bedded sandstone and conglomeratic facies. These lithofacies are particularly well-exposed along a tributary waterfall to Dover Creek such that 158 samples were collected for paleomagnetic study (Fig. 5.1, 5.2), making this section the most densely sampled amongst all the sections. The specimen DRMs show that the geomagnetic field reversed at least nine times during deposition within the section (Fig. 5.2).

The Natural Wall and Hammel Creek sections are in close proximity to the Dover Creek section (Fig. 5.1) and the unique sedimentary facies association of volcanic-clast conglomerate, red siltstone, and coarse arkosic sandstone is similar to the basal ~120 meters of the section at Dover Creek (Fig. 5.2). Our sampling at these two localities is more limited due to there being poorer exposures of siltstone and fine-grained sandstone beds in these sections (Fig. 5.2). At Hammel Creek, 16 samples from two siltstone layers near the base of the section are of reversed polarity (Fig. 5.2). Near the top of the Natural Wall section, consistent normal-polarity directions are recorded by 15 samples (Fig. 5.2).

At the Snake Creek tributary (Fig. 5.1), 71 specimens yielded interpretable DRMs through multiple levels along the ~95-meter-thick section and all show normal-polarity directions (Figs. 5.6 and 5.2). At Agate Falls (Fig. 5.1), clay-rich detrital mica-bearing siltstone layers occur through ~30 meters of strata that are incised by the Middle Branch Ontonagon River (Fig. 5.3). 67 total paleomagnetic samples were collected on both sides of the waterfall (Fig. 5.2). At least three geomagnetic polarity reversals occurred during deposition within the Agate Falls section (Fig. 5.2).

The paleomagnetic reversal test assesses whether two directional data sets share a common mean when one of the polarity directions is flipped to its antipode. Although the occurrence of multiple geomagnetic field reversals during deposition of the Jacobsville Formation is evident (Figs. 5.2 and 5.6), the limited and often discrete records of many polarity chronos are insufficient for pair-wise reversal tests within single sections (Fig. 5.2). Sedimentation within individual siltstone horizons was likely quite rapid given their deposition within fluvial floodplains potentially without sufficient time to average out secular variation within discrete siltstone intervals. We combine all normal and reversed directions from the five sections and perform a reversal test. The McFadden and McElhinny (1990) reversal test results show the angle between the two mean directions ( $15.9^\circ$ ; no inclination shallowing correction) exceeds the critical angle ( $7.5^\circ$ ) (Fig. D.5), thereby failing the test. This difference largely arises due to normal (west directed) directions in the Snake Creek tributary section being slightly steeper in their upward inclination. There are at least four possible explanations for this behavior: 1) the lower number of normal directions which dominantly come from the Snake Creek tributary section may not have averaged out secular variation; 2) there could have been plate motion during Jacobsville deposition with the normal polarity in the Snake Creek tributary section being acquired when Laurentia was at a slightly higher latitude; 3) there could be a bias from the reversed CRM superimposed on the normal DRM in the Snake Creek tributary specimens being incompletely removed during thermal demagnetization; 4) the geomagnetic field in the early Neoproterozoic could have been slightly different than that

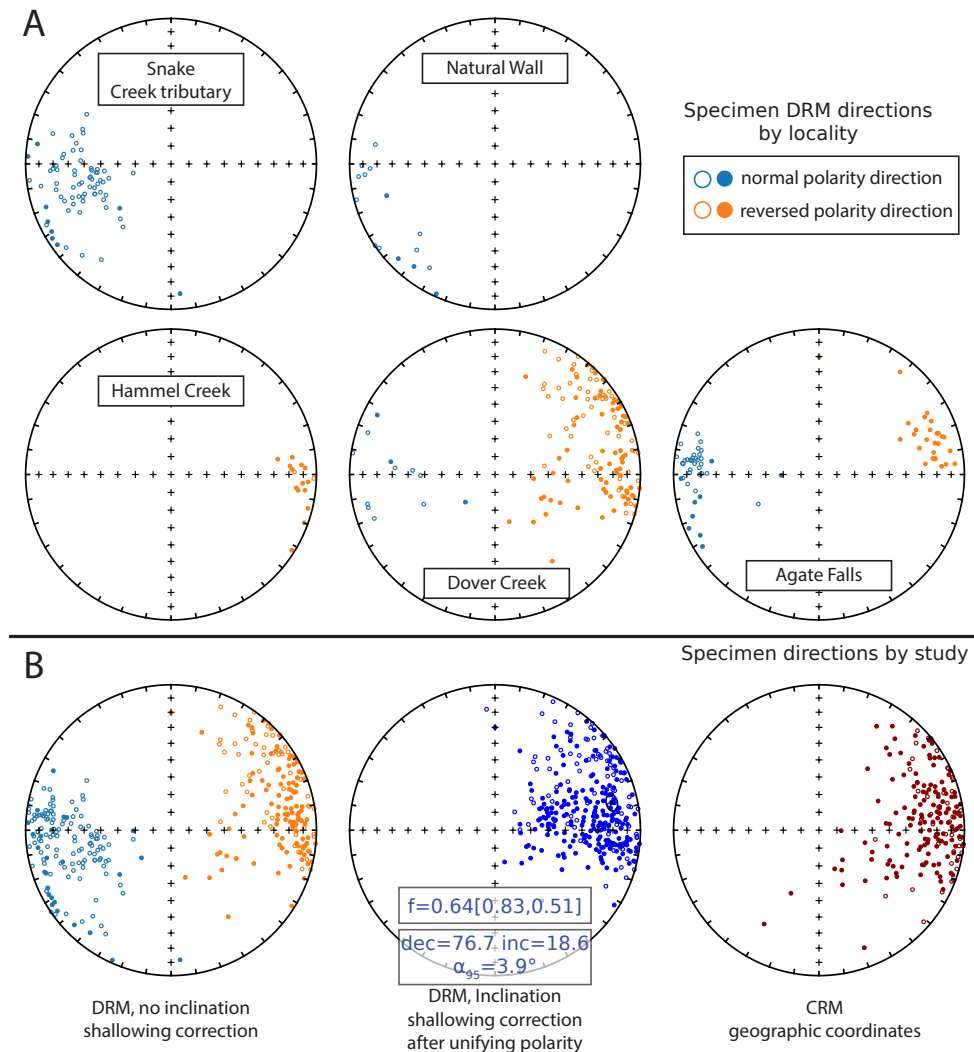


**Figure 5.6:** (A) Specimen detrital remanence directions (DRM) plotted by locality on equal area plots. During sample collection, we optimized for vertical stratigraphic coverage such that each sample constitutes a single horizon and therefore a paleomagnetic site. Specimens from the Snake Creek tributary have a mean direction of  $\text{dec}=256.0^\circ$ ,  $\text{inc}=-30.5^\circ$ ,  $k=9.9$ ,  $\alpha_{95}=5.6^\circ$ ,  $n=71$ ; the Natural Wall section has a mean direction of  $\text{dec}=242.4^\circ$ ,  $\text{inc}=-6.4^\circ$ ,  $k=9.0$ ,  $\alpha_{95}=13.5^\circ$ ,  $n=15$ ; the Hammel Creek section has a mean direction of  $\text{dec}=94.1^\circ$ ,  $\text{inc}=8.7^\circ$ ,  $k=30.7$ ,  $\alpha_{95}=6.8^\circ$ ,  $n=16$ ; the Dover Creek section has a mean direction of  $\text{dec}=73.2^\circ$ ,  $\text{inc}=5.4^\circ$ ,  $k=5.6$ ,  $\alpha_{95}=5.6^\circ$ ,  $n=138$ ; the Agate Falls section has a mean direction of  $\text{dec}=83.4^\circ$ ,  $\text{inc}=13.0^\circ$ ,  $k=13.4$ ,  $\alpha_{95}=4.9^\circ$ ,  $n=67$ . All reported directions are calculated in tilt-corrected coordinates and after unifying polarity. The measurement-level data are available in the MagIC database (<https://doi.org/10.7288/V4/MAGIC/19780>). (B) Summary equal area plots at the study-level combining directions from all localities. The elongation/inclination (E/I) method (Tauxe and Kent, 2004) was used to estimate the amount of inclination shallowing in Jacobsville specimen DRMs after unifying the polarities (flipping the normal [blue] directions to their antipodes). Details on inclination shallowing corrections are shown in Figure 5.7 with the value of  $f=0.64$  used for the directions in the middle panel. All DRM directions are shown in tilt-corrected bedding coordinates. The summary plot of all specimen chemical remanence directions (CRM) are shown in geographic coordinates show well-grouped reversed-polarity directions whose directions are similar to the DRMs.

of more recent times in terms of the dispersion of pole position at distinct time snapshots potentially associated with changes in field intensity. Regardless, the positive intraclast conglomerate test gives confidence that the Jacobsville Formation has a primary detrital remanent magnetization that can be isolated through thermal demagnetization. This result is strengthened through the positive fold test and the broadly antipodal dual polarity data. Additionally, taking the large number of samples together from both polarities to calculate a pole increases the likelihood that the dual polarity pole has averaged out secular variation.

A total of 186 specimens yielded interpretable chemical remanence directions that are of dominantly reversed polarity. These directions are plotted by stratigraphic section location in Figure D.6 and are all shown in Figure 6B. That the CRM directions are a secondary remanence component that postdate the deposition of the Jacobsville Formation is supported by the negative intraformational conglomerate test results and failure in the fold test (Figs. 5.4, S4). However, the similarity of the CRM directions (declination=96.2°, inclination=15.1°,  $\alpha_{95}=4.2^\circ$ , n=186) with the primary DRM directions (declination=76.9°, inclination=13.4°,  $\alpha_{95}=3.3^\circ$ , n=307, no inclination shallowing correction) indicate that growth of the secondary pigmentary hematite which carries the CRM likely occurred soon after deposition when Laurentia was in a similar paleogeographic position.

Overall, the multiple geomagnetic field polarity reversals recorded by the Jacobsville Formation constrain that the end of the Keweenawan normal superchron (Driscoll and Evans, 2016) (which started ca. 1099 Ma; Swanson-Hysell et al., 2019b) had to have ended by the onset of Jacobsville deposition.

## 5.5 Discussion

### Averaging paleosecular variation and correcting for inclination shallowing

Igneous and sedimentary rocks associated with the North American Midcontinent Rift provide a high-resolution record of the ca. 1109 to 1070 Ma Keweenawan Track which tightly constrains the apparent polar wander path for Laurentia in the late Mesoproterozoic (Fig. 5.8; Swanson-Hysell et al., 2019b). However, high-quality paleogeographic constraints thereafter are sparser and more uncertain in their age until the ca. 775 Ma Gunbarrel large igneous province (Harlan et al., 2003) and subsequent ca. 775-719 Ma poles from western Laurentia extensional basins (Weil et al., 2006; Eyster et al., 2019). Developing a new paleomagnetic pole from the Jacobsville Formation presents an opportunity for a well-constrained early Neoproterozoic constraint on Laurentia's paleogeographic position.

Our high-resolution thermal demagnetization successfully isolated detrital magnetization from the secondary chemical magnetization carried by pigmentary hematite that grew after deposition of the Jacobsville Formation. The scatter in the DRM directions can be interpreted to reflect variations in the geomagnetic field during the deposition of the sediments (Steiner, 1983; Tauxe and Kent, 1984). The multiple geomagnetic field reversals captured by

specimens collected from the Dover Creek and Agate Falls sections support that a prolonged period of time is represented by the specimens given that the duration of geomagnetic polarity chron are typically on the order of tens of Kyr to Myr timescales (Fig. 5.2). Therefore, we combine all specimen detrital remanent magnetizations to calculate a paleomagnetic pole for the Jacobsville Formation.

A challenge in interpreting detrital magnetizations is the issue of correcting for inclination shallowing (King, 1955; Tauxe and Kent, 2004; Bilardello, 2016). Scatter of the specimen detrital remanence directions in tilt-corrected coordinates show elongation parallel to the bedding plane, consistent with them being shallowed (Fig. 5.6; Tauxe and Kent, 2004). Such a directional distribution is due to rotation of detrital hematite grains during deposition and subsequent compaction, resulting in inclinations recorded by sedimentary rocks having shallower angles than the local field in which they are deposited. If uncorrected, shallower inclinations obtained from sedimentary rocks can result in erroneously low estimates of paleolatitudes, biasing paleogeographic reconstructions. To estimate the amount of inclination shallowing, we apply the statistical elongation/inclination (E/I) method that evaluates the deviation of the distribution of a large number ( $>100$ ) of observed sedimentary paleomagnetic directional data with the predicted distribution given by a statistical paleosecular variation model (Tauxe and Kent, 2004). Although the TK03 paleosecular variation model is based on data of relatively recent geomagnetic field variations, it has been shown to be compatible with data from the ca. 1.1 Ga lava flows of the Midcontinent Rift (Tauxe and Kodama, 2009). Furthermore, Pierce et al. (2022) showed that applying the E/I method to detrital hematite magnetizations within the ca. 1093 Ma Cut Face Creek Sandstone in the Midcontinent Rift successfully corrects the shallow paleomagnetic inclinations of the sediments to that of the North Shore Volcanic Group lava flows that bracket them. Pierce et al. (2022) also developed a method, that we use here, to represent uncertainties associated with the amount of inclination shallowing into sedimentary paleomagnetic pole positions which can then be summarized with an elliptical Kent distribution (Kent, 1982) rather than a circular Fisher distribution (Fisher, 1953).

Applying the E/I method to the Jacobsville DRM directions results in an estimate for the flattening factor ( $f$  factor) of 0.64 with a 95% uncertainty range of 0.83 to 0.51 (Figs. 5.7). The  $f$  factor of 0.64 is close to the value of 0.58 which is the mean of inclination shallowing factors compiled for hematite-bearing rocks in Pierce et al. (2022) (building on compilations of Bilardello (2016) and Vaes et al. (2021)). The Fisher mean inclination-corrected detrital remanence mean direction is  $\text{dec}=76.7^\circ$ ,  $\text{inc}=18.6^\circ$ ,  $\alpha_{95}=3.9^\circ$ . The Fisher mean inclination-corrected paleomagnetic pole associated with this nominal  $f$  factor is  $\text{Plon}=183.4^\circ\text{E}$ ,  $\text{Plat}=16.9^\circ\text{S}$ ,  $A_{95}=3.1^\circ$ . We apply the method of Pierce et al. (2022) to incorporate the uncertainty in the E/I estimate of the  $f$  factor into the uncertainty of the paleomagnetic pole (Fig. 5.7). This uncertainty results in more uncertainty associated with paleolatitude which for the pole is along the great circle path between the mean pole position and the locality of the Jacobsville sections. Following Pierce et al. (2022), the pole can be represented with a Kent distribution 95% confidence ellipse which is: mean longitude= $183.4^\circ\text{E}$ , mean latitude= $16.9^\circ\text{S}$ , major axis longitude= $255.5^\circ\text{E}$ , major axis latitude= $45.2^\circ\text{N}$ , major

axis magnitude=4.1°, minor axis longitude=108.1°E, minor axis latitude=39.9°N, minor axis magnitude=3.1°(Fig. 5.7; Table 5.1). This pole position is close to the end of the Keweenawan Track (Fig.5.8) and far away from Laurentia's pole positions during the Paleozoic when there was orogenesis along Laurentia's eastern margin (Fig. D.7). This pole position is consistent with the geochronology constraints on the deposition of the Jacobsville Formation and the positive paleomagnetic field tests that the detrital remanence of the Jacobsville Formation was acquired during the earliest Neoproterozoic.

**Table 5.1:** Kent mean paleomagnetic pole for the Jacobsville Formation

pole	mean position	pole (Plon/Plat)	major axis	major 95% confi- dence angle	minor axis	minor 95% confi- dence angle
	$\gamma_1$		$\gamma_2$	$\zeta_{95}$	$\gamma_3$	$\eta_{95}$
Jacobsville <i>E/I</i> cor- rected	183.4°E 16.9°S	/	255.5°E 45.2°N	/ 4.1°	108.1°E 39.9°N	/ 3.1°

Notes: The Fisher mean of the Jacobsville detrital remanence paleomagnetic pole without an inclination shallowing correction is Plon=185.5°E, Plat=14.0°S, A<sub>95</sub>=2.7°; the Fisher mean of the Jacobsville detrital remanence paleomagnetic pole with an inclination shallowing correction of  $f=0.64$  is Plon=183.4°E, Plat=16.9°S, A<sub>95</sub>=3.1°; the Fisher mean of the Jacobsville chemical remanence paleomagnetic pole is Plon=179.6°E, Plat=10.2°S, A<sub>95</sub>=3.6°.

Roy and Robertson (1978) also studied the paleomagnetism of sedimentary rocks grouped as the Jacobsville Formation and isolated a characteristic magnetization component via alternating-field, thermal, and chemical demagnetization on a suite of Jacobsville red beds near the Keweenaw Peninsula (their area A), the town of Marquette (their area B), and Sault Ste Marie (their area C). Although least-squares principal component analyses was not a routine approach in fitting paleomagnetic directions at the time, that study had success in removing the present day local field overprint and was able to resolve dual magnetic polarities at one locality. The mean paleomagnetic pole position calculated from the interpreted primary magnetic remanence from rocks of the Keweenaw Peninsula and Marquette area (J1 A+B pole; pole longitude=183°E, pole latitude=9°S, dp=3°, dm=6°; no inclination correction; Fig. 5.7; Roy and Robertson, 1978) is in the southern hemisphere and lies close to the mean pole from this study (Fig. 5.7). However, their mean pole developed from fine- and medium-grained sandstone near Sault Ste Marie lies in the northern hemisphere with a pole latitude of 12°N (Fig. 5.7). Despite the large uncertainty ellipse associated with this mean pole position, it is distinct from the mean pole position from the Jacobsville Formation in northern Michigan. Instead, it overlaps with the Oronto Group paleomagnetic poles of the ca. 1070 Ma lower Freda Formation and the ca. 1075 Ma Nonesuch Formation (Fig. 5.7; Henry et al., 1977; Slotznick et al., 2023). As suggested by Dubois (1962) and Roy and Robertson (1978), these data suggest that the fluvial red beds in the Sault Ste Marie area that are often taken to be correlative to the Jacobsville Formation (e.g. Malone et al., 2020)

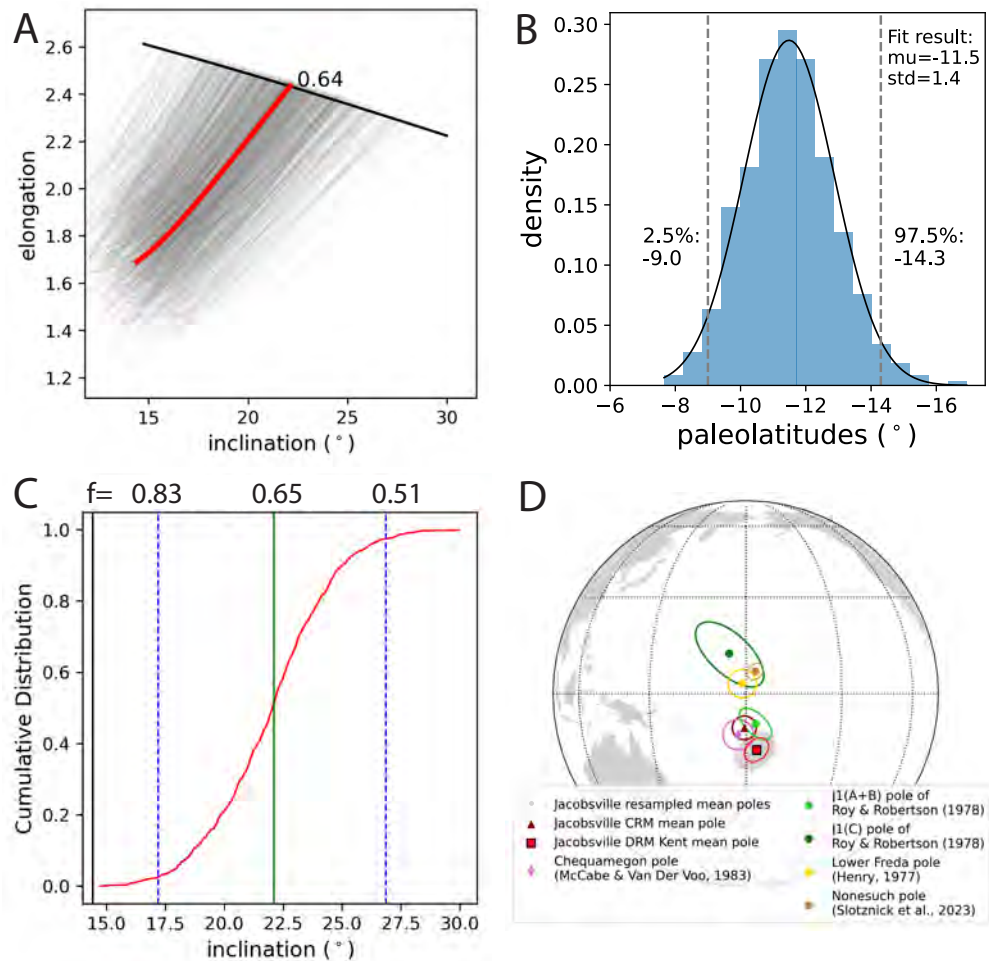


**Figure 5.7:** Results of the estimated amount of inclination shallowing of the detrital remanent magnetization of the Jacobsville Formation using the elongation/inclination (E/I) method (Tauxe and Kent, 2004). (A) The E/I method gives an estimated flattening factor  $f=0.64$  (red curve) based on where the elongation/inclination curve of the dataset intersects that predicted by the TK03 paleosecular variation model (black curve; Tauxe and Kent, 2004). The grey lines show 1,000 bootstrap resamples of the DRM directions which provide an estimate of the uncertainty associated with the  $f$  factor estimate (95% interval from 0.83 to 0.51). (B) The distribution of the paleolatitudes resulting from the corrected inclinations of the E/I bootstrap resamples. That the distribution is drawn from a normal distribution with a mean of  $-11.5^\circ$  and standard deviation of 1.4 cannot be rejected in the Kolmogorov-Smirnov test. The 95% confidence bounds shown by dashed lines span a range of paleolatitudes that need to be incorporated into the uncertainty of the reported paleomagnetic pole. (C) The cumulative distribution of inclinations based on the E/I bootstrap results with the 95% confidence bounds shown in terms of inclination and  $f$  factor. (D) The new Kent mean inclination corrected DRM pole (red square) of the Jacobsville Formation is shown in the context of the pole calculated for the CRM (purple triangle) as well as the Jacobsville pole developed by Roy and Robertson (1978), the Chequamegon Formation pole of McCabe and Van der Voo (1983), and poles from the Oronto Group (Nonesuch Formation, Slotznick et al., 2023; Freda Formation, Henry et al., 1977). The mean pole position of the Kent distribution was calculated following the method of Pierce et al. (2022). The close proximity between Jacobsville poles with the Chequamegon pole is consistent with their deposition being coeval. In contrast, the J1 (C) pole of Roy and Robertson (1978) developed from hematite-bearing sedimentary rocks in the Sault Ste Marie region plots in the northern hemisphere close to the Freda Formation pole.

are likely time equivalent to sedimentary rocks of the Oronto Group and deposited during post-rift thermal subsidence.

Deposition of Bayfield Group sedimentary rocks in northern Wisconsin (west of the studied exposures; Fig. 5.1) has been hypothesized to be coeval with the Jacobsville Formation (Hamblin, 1958; Kalliokoski, 1982; Malone et al., 2016). Published low precision detrital zircon U-Pb dates developed by laser ablation–inductively coupled plasma–mass spectrometry (LA-ICP-MS) dates are consistent with this interpretation with a maximum depositional age of ca. 1035 Ma for the Chequamegon Formation of the Bayfield Group (Craddock et al., 2013). Our updated Jacobsville pole position is close to a pole developed from the Chequamegon Sandstone of the Bayfield Group (Fig. 5.7; pole longitude=177.7°E, pole latitude=12.3°S,  $A_{95}=4.6^\circ$ ; no inclination correction; McCabe and Van der Voo, 1983). These data are consistent with the Bayfield Group being deposited within a contiguous syn-orogenic basin with the Jacobsville Formation during the Rigolet phase of the Grenvillian orogeny. This interpretation can be evaluated with further high-precision geochronology focused on the Bayfield Group.

## Age of the Jacobsville Pole

At the western edge of the Jacobsville bedrock belt in northern Michigan, the formation is in angular unconformity with Midcontinent Rift rocks that were uplifted and tilted prior to Jacobsville deposition (Fig. 5.1; Hedgman, 1992; Cannon et al., 1995). Rb-Sr thermochronologic data developed from Paleoproterozoic to Archean lithologies that were exhumed along the Marenisco Fault along with Midcontinent Rift strata in this region indicate that this uplift occurred ca. 1050 Ma associated with the Ottawan phase of the Grenvillian orogeny (Cannon et al., 1993). Field observations reveal erosional contacts and development of paleosols between the Jacobsville Formation and underlying Midcontinent Rift volcanic rocks at the Sturgeon River within the bedrock belt (Hamblin, 1958; Zbinden et al., 1988). Seismic reflection data beneath Lake Superior have been also been interpreted to indicate that the Jacobsville Formation lies in angular unconformity atop sedimentary rocks of the Oronto Group (Cannon, 1989). This context requires that there was ca. 1050 Ma contractional deformation of Midcontinent Rift strata, erosion of these tilted strata, and renewed subsidence prior to the onset of Jacobsville deposition atop them.

Maximum depositional detrital zircon dates are consistent with this history and provide additional constraints. Hodgin et al. (2022) applied tandem dating where the young population emerging from a large number of low-precision LA-ICP-MS dates are followed by high-precision CA-ID-TIMS analysis. This approach has the advantage of combining the high number of low-precision analyses that can be acquired through LA-ICP-MS with dates developed through CA-ID-TIMS where the deleterious effects of Pb-loss can be mitigated, and more accurate and precise dates can be obtained. These data reveal the youngest zircon at Sandstone Creek near the Keweenaw fault (Figure 5.1) to have a date of  $992.51 \pm 0.64$  Ma ( $2\sigma$  analytical uncertainty) and the youngest zircon at Agate Falls (Figure 5.1) a date of  $1003.21 \pm 2.23$  Ma ( $2\sigma$ ). These dates are consistent with the age of syntectonic magmatism

in the Grenville orogen associated with the Rigolet phase of the orogeny (e.g. Bussy et al., 1995; Turlin et al., 2019; Jannin et al., 2018) which is a potential source for the grains. Overall, these dates constrain a maximum depositional age of the Jacobsville Formation in the earliest Neoproterozoic.

While there has been recent success in applying tandem detrital zircon data to obtain maximum depositional ages that are close to true depositional ages (Karlstrom et al., 2020), the possibility exists that deposition could significantly postdate the youngest dated detrital zircon. A firm minimum depositional age on the age of the Jacobsville is that it is unconformably overlain by the Cambrian Munising Formation whose base was deposited ca. 501 to 497 Ma during the Dresbachian Stage (the Guzhangian Stage in the modern Cambrian time scale) (Hamblin, 1958; Haddox and Dott, 1990). This unconformity is erosional as it truncates Jacobsville strata and intraformational clastic dikes and can have slight angularity (Hamblin, 1958; Haddox and Dott, 1990). That the Jacobsville Formation is older than the Munising Formation lends tighter constraints than the Cambrian age itself given the evidence discussed above that Jacobsville deposition was syn-orogenic. The only candidate for such orogenesis is the ca. 1010-980 Ma Rigolet phase of the Grenvillian orogeny given that subsequent Paleozoic orogenesis (e.g. the Ordovician Taconic and Carboniferous Alleghanian orogenies) post-dates deposition of the Munising Formation.

That the Jacobsville Formation is folded in the footwall of the Keweenaw fault, beneath the older Midcontinent Rift volcanic rocks in the hanging wall, provides another opportunity to develop a minimum depositional age. Seeking to obtain such a constraint, Hodgin et al. (2022) targeted calcite within a Keweenaw fault breccia that cross-cuts a dense network of zeolite veins and slickenslides that yielded a U-Pb date of  $985.5 \pm 35.8$  Ma ( $2\sigma$ ). While this calcite date has large analytical uncertainty, it indicates that the fault breccia developed associated with the Grenvillian orogeny and it overlaps with the ca. 1010-980 Ma ages of metamorphism associated with the Rigolet phase of the orogeny (Swanson-Hysell et al., 2023). It is during this ca. 1010-980 Ma Rigolet phase of the orogeny that the Grenville Front developed (Rivers, 2008) which indicates that this was a time period when contractional deformation associated with the orogeny was propagating into the Superior craton. Together, the detrital zircon, sedimentology, and the fault calcite dates are consistent with the Jacobsville Formation being deposited in a syn-orogenic Grenville backbulge basin and subsequently deformed as contraction associated with the Rigolet phase of the Grenville orogeny propagated into the interior of Laurentia.

Previously, some researchers have interpreted there to have been large-scale regional contractional deformation during the Alleghanian orogeny in the Paleozoic leading to reactivation of reverse faults including the Keweenaw fault (Craddock et al., 2017). While the Keweenaw fault is defined quite broadly in Craddock et al. (2017), the evidence put forward that is relevant to the segment in this study region are: 1) an interpreted post-Grenvillian orogeny age for the Jacobsville Formation which would require that the deformation of the formation was associated with subsequent orogenesis; and 2) deformation within two  $<1.5$  km diameter outliers of Paleozoic sedimentary rocks that overlie the Jacobsville (Limestone Mountain in Figure 5.1). The data used to argue for a post-Grenvillian depositional age of

the Jacobsville Formation were the low-precision LA-ICP-MS detrital zircon dates of Malone et al. (2016) that have now been superseded by the tandem dates of Hodgin et al. (2022). These dates are consistent with syn-Grenvillian deposition. This progress leaves the tilted and/or brecciated Paleozoic strata in the small exposed Paleozoic outliers of the 1.5 x 1 km Limestone Mountain and the neighboring 0.5 x 0.3 km Sherman Hill as evidence of Paleozoic deformation: interpreted to be Paleozoic orogenesis by Hamblin (1958) and Craddock et al. (2017) and suggested to be an impact structure by others (Milstein, 1987). The impact origin interpretation builds on previous interpretations of the structure as being cryptovolcanic (Cannon and Mudrey, 1981)—a common interpretation for structures that have subsequently been recognized as impact related. The tilt and brecciation of these outliers contrasts with widespread flat-laying Paleozoic sedimentary rocks that overlie the reverse faults that underwent contractional deformation associated with rift inversion in Minnesota (Jirsa et al., 2011). These strata constrain Paleozoic deformation to have been relatively minor on the scale of 10s of meters rather than the kilometers of uplift associated with the rift inversion along these reverse faults (Boerboom et al., 2018). Clumped isotope temperatures of ~50°C from the Neoproterozoic fault calcite, also developed by Hodgin et al. (2022), reveal that the Keweenaw fault zone was within a couple kilometers of the surface at the time of late Mesoproterozoic to early Neoproterozoic calcite precipitation. These data are inconsistent with major Paleozoic uplift and support the interpretation that the majority of contractional inversion along the Keweenaw fault occurred during the Rigolet Stage of the orogeny.

Our new paleomagnetic data provide additional insights into the timing of Jacobsville deformation in the early Neoproterozoic. At the Snake Creek tributary section which is folded against the Keweenaw fault (Figure 5.1, 5.2), the chemical remanence directions held by pigmentary hematite fail a fold test (Figure D.4), indicating that the pigmentary hematite holding the remanence grew after deformation of the strata. The mean pole position of the chemical remanent magnetization at the Snake Creek tributary section overlaps with paleomagnetic poles of the Grenville Loop that have been assigned exhumation ages of ca. 970-960 Ma (Figure D.7; Brown and McEnroe, 2012). This chemical remanence pole position and the mean Jacobsville detrital remanence pole position are both far away from Laurentia's pole positions at the times of Paleozoic orogenesis or any younger time in the Phanerozoic (Figure D.7). This result indicates that the majority of the tilting of the Jacobsville in the footwall of the Keweenaw fault could not have occurred during Paleozoic orogenesis such as the Alleghanian orogeny as the chemical remanent magnetization would then be expected to record a direction aligned with the Phanerozoic pole path. Instead, the Rigolet phase of Grenvillian orogeny, which ended by ca. 980 Ma, is the only feasible orogenic interval that could have tilted these strata. This result constrains the Jacobsville Formation in the studied outcrop belt to have been deposited prior to ca. 980 Ma. While Paleozoic reactivation could have occurred, and there could be deformation of that age elsewhere such as at Limestone Mountain, deformation at this time on the Keweenaw fault would have been relatively minor compared to that in the early Neoproterozoic.

In conclusion, our paleomagnetic data and existing chronological data combined with the geological constraints are most consistent with the interpretation that the Jacobsville

Formation within the studied bedrock belt was deposited in a syn-orogenic basin associated with the Rigolet Phase of the Grenvillian orogeny. This syn-orogenic basinal setting, which is consistent with the sedimentology of the formation (Fig. 5.2), provides a mechanism for developing accommodation space. The total duration of deposition of the Jacobsville is uncertain with these constraints alone particularly given the low precision on the  $985.5 \pm 35.8$  Ma calcite date. However, data from the Grenville orogen itself constrain the end of the Rigolet phase to be ca. 980 Ma (Swanson-Hysell et al., 2023). As the studied sections proximal to the Keweenaw fault were deformed in its footwall during this phase of contractional deformation, it is reasonable to interpret deposition as occurring before the ca. 980 Ma cessation of Grenvillian orogenesis. Taken together, we consider the best nominal age constraint for the depositional age of the Jacobsville Formation to pair with the Jacobsville paleomagnetic pole position to be ca. 990 Ma as the Rigolet phase of the orogeny was ongoing. While deposition within peripheral foreland basins typically lasts between 10 and 50 million years (Woodcock, 2004), the backbulge depocenter may not be as stable or long-lived. Given the available chronometric constraints from the Jacobsville Formation, the Keweenaw fault and the Rigolet phase in the Grenville orogen, deposition of the Jacobsville can be considered to have occurred within the 1000 to 980 Ma time interval.

## Slowdown of Laurentia's plate motion due to the Grenvillian orogeny

The ca. 1109-1070 Ma Keweenawan Track constrains rapid motion of Laurentia from high latitudes toward the equator (Fig. 5.9; Davis and Green, 1997; Swanson-Hysell et al., 2019b). Apparent polar wander path inversion results are consistent with the pole path being dominated by plate tectonic motion that could have reached a rate of 30 cm/yr (95% interval of 27-34 cm/yr; one Euler pole scenario; Swanson-Hysell et al., 2019b; Rose et al., 2022); even faster than the rate of Indian plate motion during the closure of the Neotethys Ocean (van Hinsbergen, 2022; Jagoutz et al., 2015). Laurentia's rapid motion preceded and coincided with the onset of the collisional Grenvillian orogeny. In contrast to the rapid changes in pole position associated with the Keweenawan Track, the relatively close proximity between the ca. 990 Ma Jacobsville pole and ca. 1085 to 1070 Ma poles indicate that Laurentia's motion significantly slowed following the onset of the Grenvillian orogeny (Figs. 5.8 and 5.9). Lacking chronostratigraphic constraints, previous treatments have assigned an age to the Jacobsville pole of Roy and Robertson (1978) through extrapolation of the motion of the Keweenawan Track (e.g. Li et al., 2008). With the improved age constraints of Hodgin et al. (2022) and our new paleomagnetic pole, we can instead constrain that Laurentia's motion decreased by an order of magnitude. Incorporating temporal and spatial uncertainty on the poles gives APWP rate of  $\sim 3.2$  cm/yr (95% interval from 2.5 cm/yr to 4.3 cm/yr; Fig. D.8) between ca. 1070 to 990 Ma.

This slowdown in plate motion is geodynamically consistent with the onset of Grenvillian orogenesis. The earliest records of orogenesis on the leading margin of Laurentia occur ca.

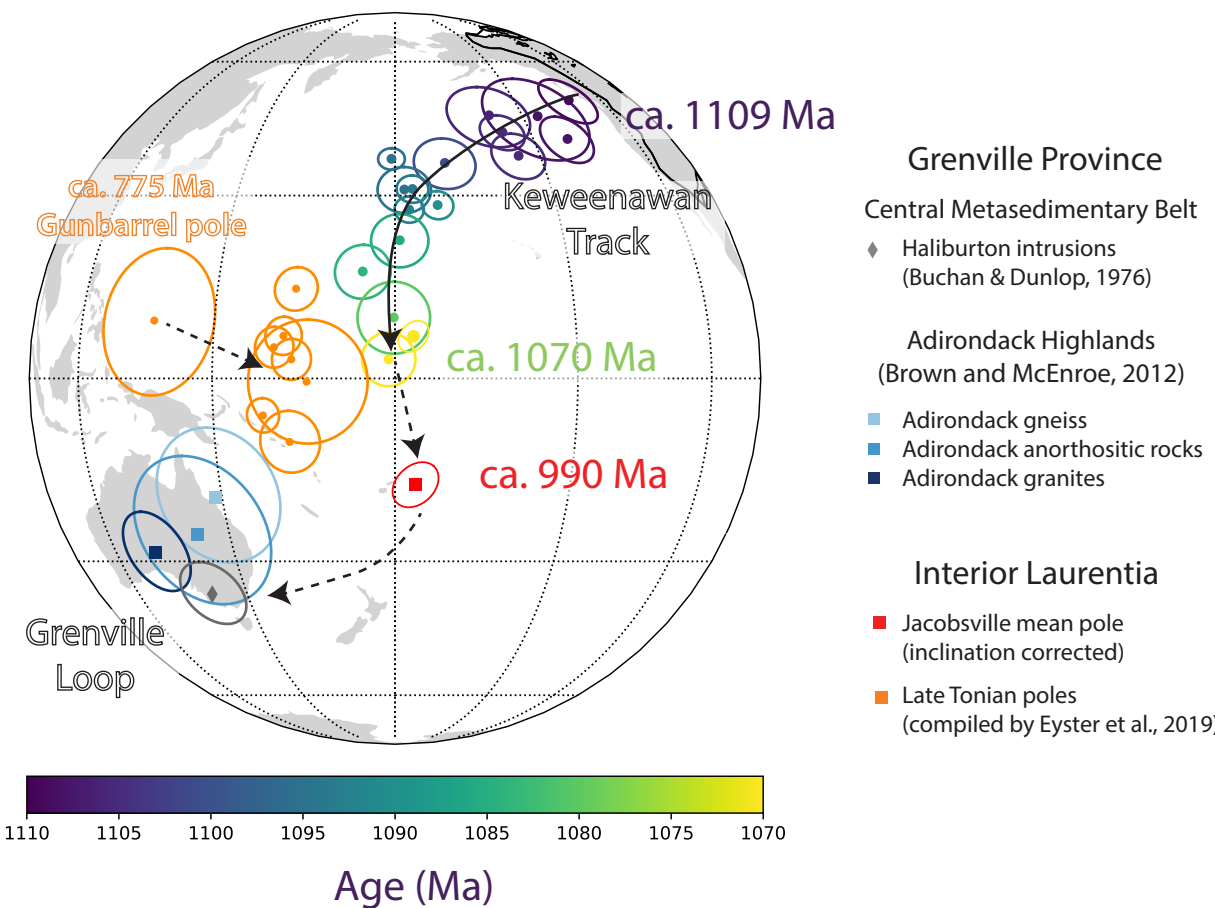


**Figure 5.8:** The inclination-corrected Jacobsville Formation detrital remanent magnetization mean pole position with its Kent uncertainty ellipse is plotted in context of the ca. 1109-1070 Ma Keweenawan Track (poles color-coded by age shown in the colorbar), selected poles from the Grenville Province, and late Tonian poles of Laurentia as compiled by Eyster et al. (2019) (orange colored poles). The southerly pole position of the ca. 990 Ma Jacobsville Formation indicates that the study area was crossing the equator in the late Mesoproterozoic to early Neoproterozoic. Given the large arc distance between the ca. 990 Ma Jacobsville pole and the poles of the Grenville loop, such as those of the the Haliburton intrusions, we suggest that estimates of their age as >1000 Ma (Warnock et al., 2000; Halls, 2015; Evans, 2021) are likely too old. The solid curve with arrow represents a continuous path of the Keweenawan Track, the dashed curves with arrow represent inferred apparent polar wander in the early Neoproterozoic based on data developed and compiled in this study and by Eyster et al. (2019). The pole compilation used in this figure is included as Table S1.

1090 Ma with estimates of peak orogenesis associated with the Ottawan stage of the orogeny occurring ca. 1050 Ma (Rivers et al., 2012; Swanson-Hysell et al., 2023). Inversions of the Keweenawan Track that incorporate multiple tectonic Euler poles indicate a slowdown from rates exceeding 20 cm/yr prior to 1095 Ma to rates below 20 cm/yr after 1095 Ma (Swanson-Hysell et al., 2019b; Rose et al., 2022). This initial slowdown could be associated with soft collision as contractional deformation initiated on the leading edge of Laurentia

(Staal and Zagorevski, 2020). Continued contractional collision led to substantially thickened crust recorded by granulite-facies metamorphic rocks by the time of peak Ottawan phase metamorphism ca. 1050 Ma (Rivers et al., 2012). The large slowdown in plate speed as now constrained by the Jacobsville paleomagnetic pole is associated with this progression to hard continent-continent collision involving increased crustal thickening and progressive transmission of contractional stress that eventually progressed into the interior of Laurentia (Cannon, 1994).

Laurentia's rapid motion was associated with closure of the Unimos Ocean and is consistent with it being on the lower plate that subducted under a conjugate continent (e.g. Amazonia) that collided on its margin (Swanson-Hysell et al., 2023; Fig. 5.9). The Jacobsville paleomagnetic pole constrains this motion to have slowed as orogeny progressed to be a large-scale continent-continent collision. As a result, Laurentia maintained a low-latitude position throughout the duration of the Grenvillian orogeny which sutured continents together into the supercontinent Rodinia (Fig. 5.9).

## Implications for the age of the Grenville Loop

Given that the age and pole position of the Jacobsville Formation had been uncertain and lacking other constraints from sedimentary or volcanic rocks, reconstruction of the paleogeography of Laurentia in the early Neoproterozoic has been reliant on paleomagnetic poles developed from metamorphic rocks within the Grenville Province (e.g. Weil et al., 1998). As is shown in Figure 5.8, paleomagnetic poles of the Grenville Loop plot near Australia in present-day coordinates; forming arc distances ranging from  $\sim 35^\circ$  to more than  $50^\circ$  away from poles at the end of the ca. 1110 to 1070 Ma Keweenawan Track (Fig. 5.8). Determining ages associated with the Grenville Loop poles is crucial for constraining the motion of Laurentia at this time and the configuration between Laurentia and hypothesized conjugate continents such as Baltica within Rodinia (Cawood and Pisarevsky, 2017; Gong et al., 2018; Swanson-Hysell, 2021).

In contrast to rocks of the Midcontinent Rift where magnetizations can be confidently assigned to be the same age as the crystallization ages of the rocks (e.g. Davis and Green, 1997; Fairchild et al., 2017; Swanson-Hysell et al., 2019b), rocks of the Grenville orogen experienced up to granulite facies metamorphism (temperatures  $>900^\circ\text{C}$ ; e.g. Shinevar et al., 2021; Metzger et al., 2021) and acquired magnetic remanence during subsequent exhumation (McWilliams and Dunlop, 1975; Dunlop and Stirling, 1985; Dodson and McClelland-Brown, 1985). During slow post-orogenic exhumation ( $1\text{-}3^\circ\text{C}/\text{Myr}$ ; e.g. Rivers and Volkert, 2023), magnetic minerals acquired remanence by cooling through an extended temperature range over millions to tens of millions of years (Pullaiah et al., 1975; Dodson and McClelland-Brown, 1980) or by crystallizing through exsolution (McEnroe et al., 2007). Determining the age of magnetization in such rocks requires reconstructing cooling histories using isotopic thermochronometers which experience radioisotopic accumulation on mineral-specific closure of elemental diffusion (Dodson, 1973; Dodson and McClelland-Brown, 1985).

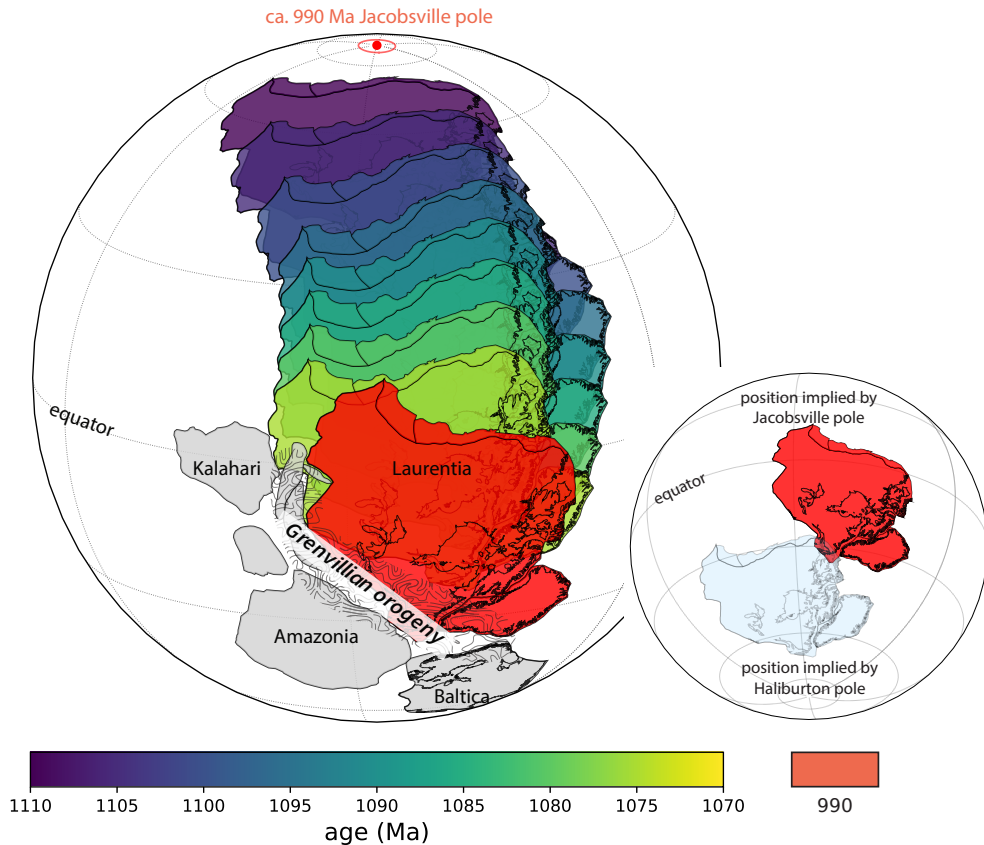


**Figure 5.9:** Paleogeographic position of Laurentia through the late Mesoproterozoic to early Neoproterozoic. The color-coded reconstructions show snapshots of Laurentia's position and orientation at 5 Myr intervals from 1110 to 1075 Ma. These reconstructions implement the two-stage tectonic Euler pole rotation inversion of Swanson-Hysell et al. (2019b). The paleogeographic snapshot colored in red shows the position and orientation of Laurentia ca. 990 Ma as constrained by the Jacobsville paleomagnetic pole developed in this study. Interpreted positions of Laurentia's conjugate continents along its margin are shown in grey. This reconstruction shows that while Laurentia experienced rapid latitudinal changes through the Keweenawan Track that its motion was much slower between ca. 1075 and 990 Ma as the Grenvillian orogeny progressed. The paleogeographic positions of conjugate continents to Laurentia long the Grenville margin in the reconstructions follow the interpretation of Swanson-Hysell et al. (2023). The inset figure compares Laurentia's position predicted by the new Jacobsville paleomagnetic pole (red) and that constrained by the Halibuton intrusions of the Grenvillian orogeny (light blue) which has been assigned an age of 1015 Ma (Warnock et al., 2000). We suggest that this and other Grenville loop poles are younger and that Laurentia traveled from low latitudes toward higher latitudes following ca. 990 Ma while the Grenville orogen was slowly cooling and exhuming.

Based on the interpretation that blocking of magnetic remanence of the magnetite-bearing Halibuton intrusions of the Grenville Central Metamorphic Belt occurred during relatively narrow temperature ranges close to the Curie temperature of magnetite (i.e. 580°C), Warnock et al. (2000) considered that the timing of remanence acquisition during cooling

of the intrusions is bracketed between U-Pb titanite and  $^{40}\text{Ar}/^{39}\text{Ar}$  hornblende dates. As a result, that study interpreted the age associated with the Haliburton paleomagnetic pole to be ca. 1015 Ma. This age has been assigned to the pole in subsequent compilations (e.g. Evans et al., 2021). In the central Adirondack Highlands of the Grenville orogen, magnetite-bearing granitic rocks and anorthositic rocks record pole positions that overlap with the Haliburton pole while their ages have been interpreted by Brown and McEnroe (2012) to be ca. 990-970 Ma, based on U-Pb and  $^{40}\text{Ar}/^{39}\text{Ar}$  thermochronology data developed by Mezger et al. (1991). The ca. 990 Ma Jacobsville pole position is both distinct from the Grenville Loop poles and is consistent with a slowdown of Laurentia's plate motion associated with the Grenvillian orogeny (Fig. 5.8). If ages that have been assigned to Grenville Loop poles are taken at face value, those poles represent the position of Laurentia both before and after the position constrained by the ca. 990 Ma Jacobsville pole. Such an interpretation would imply either rapid plate tectonic motion of Laurentia coeval with the Rigolet phase of the Grenvillian orogeny or rapid oscillatory true polar wander (e.g. Evans, 2003). A more straightforward alternative model that could explain the distinct pole positions between the Jacobsville pole and the Grenville Loop poles is that the poles from the Grenville orogen are younger than currently interpreted. Instead of having acquired remanence during the orogeny, the Grenville rocks could have acquired magnetic remanence during protracted exhumation that followed the ca. 980 Ma cessation of contractional deformation associated with the Rigolet stage of the orogeny. In this scenario, the migration of Rodinia to the higher latitude position represented by the Grenville loop poles would have occurred further into the Neoproterozoic after the Grenvillian orogeny had ceased.

While numerous paleomagnetic data sets have been developed from rocks of the Grenville Province, few are paired with well-calibrated, high-precision thermochronology data. Recent data sets, such as new apatite U-Pb dates of  $923 \pm 14$  Ma ( $2\sigma$  analytical uncertainty) from the Wilberforce pyroxenite (Paul et al., 2021), give tantalizing hints that temperatures that blocked magnetizations in portions of the orogen were achieved later than the ages assigned to paleomagnetic poles would suggest as U-Pb apatite closure temperatures are close to magnetite blocking temperatures (ca. 360-570°C; Cherniak et al., 1991). To test the hypothesis that the Grenville Loop is younger than in previous interpretations, geochronology studies are needed to exploit the resolving power of high-precision whole grain analytical methods (i.e. ID-TIMS) and high-spatial-resolution in-situ methods (e.g. laser ablation depth profiling; Chew and Spikings, 2021) for reconstructing the cooling rate and time-temperature history of the Grenville Province. Testing this hypothesis is critical for reconstructions of the paleogeography of Rodinia in the early Neoproterozoic.

## 5.6 Conclusion

The magnetization of hematite-bearing fine-grained siliciclastic sedimentary rocks from the Jacobsville Formation can be shown to be detrital and primary through positive intraformational conglomerate and fold tests. We use these data to develop a new inclination-corrected

paleomagnetic pole that can be constrained with recently published radiometric age constraints from Hodgin et al. (2022) to be ca. 990 Ma. This high-quality pole is a crucial addition to Laurentia's apparent polar wander path in the earliest Neoproterozoic. Its position indicates that Laurentia's plate motion significantly slowed during Grenvillian collisional orogenesis. The new pole establishes a well-calibrated constraint for the position of the supercontinent Rodinia in early Neoproterozoic with Laurentia being at the center. The Jacobsville pole implies that ages associated with the paleomagnetic poles recorded by metamorphic rocks of the Grenville Province are likely younger than in current interpretations. Further paired studies of high-quality paleomagnetism and high-precision thermochronology are needed to illuminate Rodinia's motion and configuration in the early Neoproterozoic.

## 5.7 Acknowledgments

Project research was funded by NSF CAREER grant EAR-1847277. Jim DeGraff provided helpful guidance in identifying exposures of the Jacobsville Formation. We gratefully acknowledge the Michigan Department of Natural Resources for sampling permitting. We thank Tim Lyons for additional private land access. We thank Madeline Swanson-Hysell for her assistance in the field. We thank David Malone, Douglas Elmore, and two anonymous reviewers for their helpful reviews.

# Bibliography

- Abrajevitch, A. and Van der Voo, R., 2010, Incompatible Ediacaran paleomagnetic directions suggest an equatorial geomagnetic dipole hypothesis: *Earth and Planetary Science Letters*, vol. 293, pp. 164–170, doi: 10.1016/j.epsl.2010.02.038.
- Ageeva, O., Habler, G., Topa, D., Waitz, T., Li, C., Pertsev, A., Griffiths, T., Zhilicheva, O., and Abart, R., 2016, Plagioclase hosted Fe-Ti-oxide micro-inclusions in an oceanic gabbro-plagiogranite association from the Mid Atlantic ridge at 13°34' N: *American Journal of Science*, vol. 316, pp. 85–109, doi: 10.2475/02.2016.01.
- Alken, P., Thébault, E., Beggan, C. D., Amit, H., Aubert, J., Baerenzung, J., Bondar, T. N., Brown, W. J., Califf, S., Chambodut, A., Chulliat, A., Cox, G. A., Finlay, C. C., Fournier, A., Gillet, N., Grayver, A., Hammer, M. D., Holschneider, M., Huder, L., Hulot, G., Jager, T., Kloss, C., Korte, M., Kuang, W., Kuvshinov, A., Langlais, B., Léger, J.-M., Lesur, V., Livermore, P. W., Lowes, F. J., Macmillan, S., Magnes, W., Mandea, M., Marsal, S., Matzka, J., Metman, M. C., Minami, T., Morschhauser, A., Mound, J. E., Nair, M., Nakano, S., Olsen, N., Pavón-Carrasco, F. J., Petrov, V. G., Ropp, G., Rother, M., Sabaka, T. J., Sanchez, S., Saturnino, D., Schnepf, N. R., Shen, X., Stolle, C., Tangborn, A., Tøffner-Clausen, L., Toh, H., Torta, J. M., Varner, J., Vervelidou, F., Vigneron, P., Wardinski, I., Wicht, J., Woods, A., Yang, Y., Zeren, Z., and Zhou, B., 2021, International geomagnetic reference field: the thirteenth generation: *Earth, Planets and Space*, vol. 73, doi: 10.1186/s40623-020-01288-x.
- Arai, Y., 1963, Secular variation in intensity of the past geomagnetic field: M.Sc. thesis, University of Tokyo, Tokyo, Japan.
- Aubert, J., Stéphane, and Poitou, C., 2009, Modelling the palaeo-evolution of the geodynamo: *Geophysical Journal International*, vol. 179, pp. 1414–1428, doi: 10.1111/j.1365-246x.2009.04361.x.
- Badro, J., Siebert, J., and Nimmo, F., 2016, An early geodynamo driven by exsolution of mantle components from Earth's core: *Nature*, vol. 536, pp. 326–328, doi: 10.1038/nature18594.

- Barth, A. P., Wooden, J. L., and Coleman, D. S., 2001, SHRIMP-RG U-Pb zircon geochronology of Mesoproterozoic metamorphism and plutonism in the southwesternmost United States: *The Journal of Geology*, vol. 109, pp. 319–327, doi: 10.1086/319975.
- Barth, A. P., Wooden, J. L., Coleman, D. S., and Fanning, C. M., 2000, Geochronology of the Proterozoic basement of southwesternmost North America, and the origin and evolution of the Mojave crustal province: *Tectonics*, vol. 19, pp. 616–629, doi: 10.1029/1999tc001145.
- Barth, A. P., Wooden, J. L., Coleman, D. S., and Vogel, M. B., 2009, Assembling and disassembling California: A zircon and monazite geochronologic framework for Proterozoic crustal evolution in southern California: *The Journal of Geology*, vol. 117, pp. 221–239, doi: 10.1086/597515.
- Beck, M. E., 1970, Paleomagnetism of Keweenawan intrusive rocks, Minnesota: *Journal of Geophysical Research*, vol. 75, pp. 4985–4996, doi: 10.1029/jb075i026p04985.
- Beck, M. E. and Lindsley, N. C., 1969, Paleomagnetism of the Beaver Bay Complex, Minnesota: *Journal of Geophysical Research*, vol. 74, pp. 2002–2013, doi: 10.1029/jb074i008p02002.
- Berger, G. W., York, D., and Dunlop, D. J., 1979, Calibration of Grenvillian palaeopoles by  $^{40}\text{Ar}/^{39}\text{Ar}$  dating: *Nature*, vol. 277, pp. 46–48, doi: 10.1038/277046a0.
- Besse, J. and Courtillot, V., 2002, Apparent and true polar wander and the geometry of the geomagnetic field over the last 200 Myr: *Journal of Geophysical Research: Solid Earth*, vol. 107, pp. EPM 6–1–EPM 6–31, doi: 10.1029/2000jb000050.
- Beus, S. S., Rawson, R. R., Dalton, R. O., Stevenson, G. M., Reed, S., Daneker, T. M., Karlstrom, T., Swann, G., and Eastwood, R., 1974, Preliminary report on the Unkar Group (Precambrian) in Grand Canyon, Arizona: *In* Karlstrom, T., Swann, G., and Eastwood, R., eds., *Geology of Northern Arizona, Part I, Regional Studies*: Flagstaff, Arizona, Geological Society of America, Rocky Mountain Section Meeting, vol. 1, pp. 34–53.
- Bian, G., Ageeva, O., Rečnik, A., Habler, G., and Abart, R., 2021, Formation pathways of oriented magnetite micro-inclusions in plagioclase from oceanic gabbro: *Contributions to Mineralogy and Petrology*, vol. 176, doi: 10.1007/s00410-021-01864-8.
- Biggin, A. J., Badejo, S., Hodgson, E., Muxworthy, A. R., Shaw, J., and Dekkers, M. J., 2013, The effect of cooling rate on the intensity of thermoremanent magnetization (TRM) acquired by assemblages of pseudo-single domain, multidomain and interacting single-domain grains: *Geophysical Journal International*, vol. 193, pp. 1239–1249, doi: 10.1093/gji/ggt078.

- Biggin, A. J., de Wit, M. J., Langereis, C. G., Zegers, T. E., Voûte, S., Dekkers, M. J., and Drost, K., 2011, Palaeomagnetism of Archaean rocks of the Onverwacht Group, Barberton Greenstone Belt (southern Africa): Evidence for a stable and potentially reversing geomagnetic field at ca. 3.5Ga: *Earth and Planetary Science Letters*, vol. 302, pp. 314–328, doi: 10.1016/j.epsl.2010.12.024.
- Biggin, A. J. and Paterson, G. A., 2014, A new set of qualitative reliability criteria to aid inferences on palaeomagnetic dipole moment variations through geological time: *Frontiers in Earth Science*, vol. 2, doi: 10.3389/feart.2014.00024.
- Biggin, A. J., Piispa, E. J., Pesonen, L. J., Holme, R., Paterson, G. A., Veikkolainen, T., and Tauxe, L., 2015, Palaeomagnetic field intensity variations suggest Mesoproterozoic inner-core nucleation: *Nature*, vol. 526, pp. 245–248, doi: 10.1038/nature15523.
- Biggin, A. J., Steinberger, B., Aubert, J., Suttie, N., Holme, R., Torsvik, T. H., van der Meer, D. G., and van Hinsbergen, D. J. J., 2012, Possible links between long-term geomagnetic variations and whole-mantle convection processes: *Nature Geoscience*, vol. 5, pp. 526–533, doi: 10.1038/ngeo1521.
- Bilardello, D., 2016, The do's and don'ts of inclination shallowing corrections: *Institute for Rock Magnetism Quarterly*, vol. 26, pp. 1–9.
- Bilardello, D. and Kodama, K. P., 2010a, A new inclination shallowing correction of the Mauch Chunk Formation of Pennsylvania, based on high-field AIR results: Implications for the Carboniferous North American APW path and Pangea reconstructions: *Earth and Planetary Science Letters*, vol. 299, pp. 218–227, doi: 10.1016/j.epsl.2010.09.002.
- Bilardello, D. and Kodama, K. P., 2010b, Palaeomagnetism and magnetic anisotropy of Carboniferous red beds from the Maritime Provinces of Canada: evidence for shallow palaeomagnetic inclinations and implications for North American apparent polar wander: *Geophysical Journal International*, vol. 180, pp. 1013–1029, doi: 10.1111/j.1365-246x.2009.04457.x.
- Bilardello, D. and Kodama, K. P., 2010c, Rock magnetic evidence for inclination shallowing in the early Carboniferous Deer Lake Group red beds of western Newfoundland: *Geophysical Journal International*, vol. 181, pp. 275–289, doi: 10.1111/j.1365-246x.2010.04537.x.
- Billingsley, G. H., 2000, Geologic map of the Grand Canyon 30'x 60'quadrangle, Coconino and Mohave Counties, northwestern Arizona: Tech. rep., US Geological Survey.
- Billingsley, G. H. and Wellmeyer, J. L., 2003, Geologic Map of the Mount Trumbull 30'X 60' Quadrangle, Mohave and Coconino Counties, Northwestern Arizona: Tech. rep., US Geological Survey.

- Boerboom, T., Bornhorst, T., Cannon, W., Hinze, W., Jirsa, M., Runkel, A., Schulz, K., Steenberg, J., and Woodruff, L., 2018, Comment on “Paleozoic reactivation structures in the Appalachian-Ouachita-Marathon foreland: Far-field deformation across Pangea, by J. Craddock, D. Malone, R. Porter, J. Compton, J. Luczaj, A. Konstantinou, J. Day, and S. Johnston [Earth Science Reviews 169 (2017), 1–34]: Earth-Science Reviews, vol. 181, pp. 144–152, doi: 10.1016/j.earscirev.2018.02.003.
- Boerboom, T. J., 2004, M-147 Bedrock geology of the Split Rock Point quadrangle, Lake County, Minnesota: Tech. rep., Minnesota Geological Survey.
- Boerboom, T. J., Green, J., and Albers, P., 2007, M-174 Bedrock geology of the Lutsen quadrangle, Cook County, Minnesota: Tech. rep., Minnesota Geological Survey.
- Boerboom, T. J. and Green, J. C., 2006, M-170 Bedrock geology of the Schroeder quadrangle, Cook County, Minnesota: Tech. rep., Minnesota Geological Survey.
- Boerboom, T. J., Green, J. C., Albers, P., and Miller, J., J.D., 2006, M-171 Bedrock geology of the Tofte quadrangle, Cook County, Minnesota: Tech. rep., Minnesota Geological Survey.
- Bono, R. K., Paterson, G. A., and Biggin, A. J., 2022a, MCADAM: A continuous paleomagnetic dipole moment model for at least 3.7 billion years: Geophysical Research Letters, vol. 49, doi: 10.1029/2022gl100898.
- Bono, R. K., Paterson, G. A., van der Boon, A., Engbers, Y. A., Michael Grappone, J., Handford, B., Hawkins, L. M. A., Lloyd, S. J., Sprain, C. J., Thallner, D., and Biggin, A. J., 2022b, The PINT database: a definitive compilation of absolute palaeomagnetic intensity determinations since 4 billion years ago: Geophysical Journal International, vol. 229, pp. 522–545, doi: 10.1093/gji/ggab490.
- Bono, R. K., Tarduno, J. A., Nimmo, F., and Cottrell, R. D., 2019, Young inner core inferred from Ediacaran ultra-low geomagnetic field intensity: Nature Geoscience, vol. 12, pp. 143–147, doi: 10.1038/s41561-018-0288-0.
- Books, K. G., 1968, Magnetization of the lowermost Keweenawan lava flows in the Lake Superior area: US Geological Survey Professional Paper, vol. 600, pp. D248–D254.
- Books, K. G., 1972, Paleomagnetism of some Lake Superior Keweenawan rocks: Professional Paper, doi: 10.3133/pp760.
- Books, K. G., White, W. S., and Beck, M. E., 1966, Magnetization of Keweenawan gabbro in northern Wisconsin and its relation to time of intrusion: Geological Survey Research.
- Brenner, A. R., Fu, R. R., Evans, D. A., Smirnov, A. V., Trubko, R., and Rose, I. R., 2020, Paleomagnetic evidence for modern-like plate motion velocities at 3.2 Ga: Science Advances, vol. 6, p. eaaz8670, doi: 10.1126/sciadv.aaz8670.

- Brenner, A. R., Fu, R. R., Kylander-Clark, A. R. C., Hudak, G. J., and Foley, B. J., 2022, Plate motion and a dipolar geomagnetic field at 3.25 Ga: *Proceedings of the National Academy of Sciences*, vol. 119, doi: 10.1073/pnas.2210258119.
- Bright, R. M., Amato, J. M., Denyszyn, S. W., and Ernst, R. E., 2014, U-Pb geochronology of 1.1 Ga diabase in the southwestern United States: Testing models for the origin of a post-Grenville large igneous province: *Lithosphere*, vol. 6, pp. 135–156, doi: 10.1130/l1335.1.
- Brojanigo, A., 1984, Keweenaw Fault: structures and sedimentology: Master's thesis, Michigan Technological University.
- Brown, L. and McEnroe, S., 2012, Paleomagnetism and magnetic mineralogy of Grenville metamorphic and igneous rocks, Adirondack Highlands, USA: *Precambrian Research*, vol. 212-213, pp. 57–74, doi: 10.1016/j.precamres.2012.04.012.
- Bryan, P. and Gordon, R. G., 1990, Rotation of the Colorado Plateau: An updated analysis of paleomagnetic poles: *Geophysical Research Letters*, vol. 17, pp. 1501–1504, doi: 10.1029/gl017i010p01501.
- Bryan, S. E., Peate, I. U., Peate, D. W., Self, S., Jerram, D. A., Mawby, M. R., Marsh, J. G., and Miller, J. A., 2010, The largest volcanic eruptions on Earth: *Earth-Science Reviews*, vol. 102, pp. 207–229, doi: 10.1016/j.earscirev.2010.07.001.
- Buchan, K. L. and Dunlop, D. J., 1976, Paleomagnetism of the Haliburton Intrusions: Superimposed magnetizations, metamorphism, and tectonics in the Late Precambrian: *Journal of Geophysical Research*, vol. 81, pp. 2951–2967, doi: 10.1029/jb081i017p02951.
- Buffett, B. A., 2000, Earth's core and the geodynamo: *Science*, vol. 288, pp. 2007–2012, doi: 10.1126/science.288.5473.2007.
- Buffett, B. A., 2003, GEOPHYSICS: The thermal state of earth's core: *Science*, vol. 299, pp. 1675–1677, doi: 10.1126/science.1081518.
- Burchfiel, B. C., 1965, Structural geology of the Specter Range quadrangle, Nevada, and its regional significance: *Geological Society of America Bulletin*, vol. 76, p. 175, doi: 10.1130/0016-7606(1965)76[175:sgotsr]2.0.co;2.
- Burchfiel, B. C., Cowan, D. S., and Davis, G. A., 1992, Tectonic overview of the Cordilleran orogen in the western United States: *In* *The Cordilleran Orogen*, Geological Society of America, pp. 407–14, doi: 10.1130/dnag-gna-g3.407.
- Burchfiel, B. C., Pelton, P. J., and Sutter, J., 1970, An early Mesozoic deformation belt in south-central Nevada-southeastern California: *Geological Society of America Bulletin*, vol. 81, p. 211, doi: 10.1130/0016-7606(1970)81[211:aemdbi]2.0.co;2.

- Bussy, F., Krogh, T. E., Klemens, W. P., and Schwerdtner, W. M., 1995, Tectonic and metamorphic events in the westernmost Grenville Province, central Ontario: new results from high-precision U–Pb zircon geochronology: *Canadian Journal of Earth Sciences*, vol. 32, pp. 660–671, doi: 10.1139/e95-055.
- Butler, R., 1992, Paleomagnetism: Magnetic Domains to Geologic Terranes: Blackwell scientific publications, Blackwell Scientific Publications.
- Butler, R. F. and Banerjee, S. K., 1975, Theoretical single-domain grain size range in magnetite and titanomagnetite: *Journal of Geophysical Research*, vol. 80, pp. 4049–4058, doi: 10.1029/jb080i029p04049.
- Calzia, J. and Rämö, O., 2000, Late Cenozoic crustal extension and magmatism, southern Death Valley region, California, Geological Society of America, pp. 135–164: doi: 10.1130/0-8137-0002-7.135.
- Cannon, W. F., 1989, The North American Midcontinent Rift beneath Lake Superior from GLIMPCE seismic reflection profiling: *Tectonics*, vol. 8, pp. 305–332.
- Cannon, W. F., 1992, The Midcontinent rift in the Lake Superior region with emphasis on its geodynamic evolution: *Tectonophysics*, vol. 213, pp. 41–48, doi: 10.1016/0040-1951(92)90250-a.
- Cannon, W. F., 1994, Closing of the Midcontinent Rift-A far-field effect of Grenvillian compression: *Geology*, vol. 22, p. 155, doi: 10.1130/0091-7613(1994)022<0155:cotmra>2.3.co;2.
- Cannon, W. F. and Hinze, W. J., 1992, Speculations on the origin of the North American Midcontinent rift: *Tectonophysics*, vol. 213, pp. 49–55, doi: 10.1016/0040-1951(92)90251-z.
- Cannon, W. F. and Mudrey, M. G., 1981, The potential for diamond-bearing kimberlite in northern Michigan and Wisconsin: Report, U.S. Geological Survey, doi: 10.3133/cir842.
- Cannon, W. F., Nicholson, S., Woodruff, L., Hedgman, C., and Schulz, K., 1995, Geologic map of the Ontonagon and part of the Wakefield 30'x60'quadrangles: Michigan: US Geological Survey Miscellaneous Investigations Series Map, pp. 1–2499.
- Cannon, W. F. and Nicholson, S. W., 2001, Geologic map of the Keweenaw Peninsula and adjacent area, Michigan: USGS Numbered Series, vol. 2696.
- Cannon, W. F., Peterman, Z. E., and Sims, P. K., 1993, Crustal-scale thrusting and origin of the Montreal River monocline-A 35-km-thick cross section of the Midcontinent Rift in northern Michigan and Wisconsin: *Tectonics*, vol. 12, pp. 728–744, doi: 10.1029/93tc00204.

- Cannon, W. F., Woodruff, L., Nicholson, S., and Hedgman, C., 1996, Bedrock geologic map of the Ashland and the northern part of the Ironwood 30- x 60-minute quadrangles, Wisconsin and Michigan: Tech. rep., U.S. Geological Survey, doi: 10.3133/i2566.
- Carter-Stiglitz, B., Moskowitz, B., Solheid, P., Berquó, T. S., Jackson, M., and Kosterov, A., 2006, Low-temperature magnetic behavior of multidomain titanomagnetites: TM0, TM16, and TM35: *Journal of Geophysical Research: Solid Earth*, vol. 111, doi: 10.1029/2006jb004561.
- Cawood, P. A. and Pisarevsky, S. A., 2017, Laurentia-Baltica-Amazonia relations during Rodinia assembly: *Precambrian Research*, vol. 292, pp. 386–397, doi: 10.1016/j.precamres.2017.01.031.
- Cherniak, D., Hanchar, J., and Watson, E., 1997, Rare-earth diffusion in zircon: *Chemical Geology*, vol. 134, pp. 289–301, doi: 10.1016/s0009-2541(96)00098-8.
- Cherniak, D., Lanford, W., and Ryerson, F., 1991, Lead diffusion in apatite and zircon using ion implantation and Rutherford Backscattering techniques: *Geochimica et Cosmochimica Acta*, vol. 55, pp. 1663–1673, doi: 10.1016/0016-7037(91)90137-t.
- Cherniak, D. and Watson, E., 2001, Pb diffusion in zircon: *Chemical Geology*, vol. 172, pp. 5–24, doi: 10.1016/s0009-2541(00)00233-3.
- Chew, D. M. and Spikings, R. A., 2021, Apatite U-Pb Thermochronology: A Review: *Minerals*, vol. 11, p. 1095, doi: 10.3390/min11101095.
- Coe, R. S., 1967, The determination of paleo-intensities of the Earth's magnetic field with emphasis on mechanisms which could cause non-ideal behavior in Thellier's method: *Journal of geomagnetism and geoelectricity*, vol. 19, pp. 157–179, doi: 10.5636/jgg.19.157.
- Coe, R. S., Grommé, S., and Mankinen, E. A., 1978, Geomagnetic paleointensities from radiocarbon-dated lava flows on Hawaii and the question of the Pacific nondipole low: *Journal of Geophysical Research: Solid Earth*, vol. 83, pp. 1740–1756, doi: 10.1029/jb083ib04p01740.
- Collinson, D. W., 1965, Origin of remanent magnetization and initial susceptibility of certain red sandstones: *Geophysical Journal International*, vol. 9, pp. 203–217, doi: 10.1111/j.1365-246x.1965.tb02071.x.
- Collinson, D. W., 1974, The role of pigment and specularite in the remanent magnetism of red sandstones: *Geophysical Journal International*, vol. 38, pp. 253–264, doi: 10.1111/j.1365-246x.1974.tb04119.x.
- Condon, D. J., Schoene, B., McLean, N. M., Bowring, S. A., and Parrish, R. R., 2015, Metrology and traceability of U-Pb isotope dilution geochronology (EARTHTIME tracer

- calibration part I): *Geochimica et Cosmochimica Acta*, vol. 164, pp. 464–480, doi: 10.1016/j.gca.2015.05.026.
- Cornwall, H. R., 1951, Differentiation in lavas of the Keweenawan Series and the origin of the copper deposits of Michigan: *Geological Society of America Bulletin*, vol. 62, p. 159, doi: 10.1130/0016-7606(1951)62[159:dilotk]2.0.co;2.
- Cortés-Ortuño, D., Fabian, K., and de Groot, L. V., 2022, Mapping magnetic signals of individual magnetite grains to their internal magnetic configurations using micromagnetic models: *Journal of Geophysical Research: Solid Earth*, vol. 127, doi: 10.1029/2022jb024234.
- Cottrell, R. D. and Tarduno, J. A., 1999, Geomagnetic paleointensity derived from single plagioclase crystals: *Earth and Planetary Science Letters*, vol. 169, pp. 1–5, doi: 10.1016/s0012-821x(99)00068-0.
- Cottrell, R. D. and Tarduno, J. A., 2000, In search of high-fidelity geomagnetic paleointensities: A comparison of single plagioclase crystal and whole rock Thellier-Thellier analyses: *Journal of Geophysical Research: Solid Earth*, vol. 105, pp. 23,579–23,594, doi: 10.1029/2000jb900219.
- Cottrell, R. D., Tarduno, J. A., and Roberts, J., 2008, The Kiama Reversed Polarity Superchron at Kiama: Toward a field strength estimate based on single silicate crystals: *Physics of the Earth and Planetary Interiors*, vol. 169, pp. 49–58, doi: 10.1016/j.pepi.2008.07.041.
- Courtillot, V. and Olson, P., 2007, Mantle plumes link magnetic superchrons to Phanerozoic mass depletion events: *Earth and Planetary Science Letters*, vol. 260, pp. 495–504, doi: 10.1016/j.epsl.2007.06.003.
- Craddock, J. P., Konstantinou, A., Vervoort, J. D., Wirth, K. R., Davidson, C., Finley-Blasi, L., Juda, N. A., and Walker, E., 2013, Detrital zircon provenance of the Mesoproterozoic Midcontinent Rift, Lake Superior region, U.S.A.: *The Journal of Geology*, vol. 121, pp. 57–73, doi: 10.1086/668635.
- Craddock, J. P., Malone, D. H., Porter, R., Compton, J., Luczaj, J., Konstantinou, A., Day, J. E., and Johnston, S. T., 2017, Paleozoic reactivation structures in the Appalachian-Ouachita-Marathon foreland: Far-field deformation across Pangea: *Earth-Science Reviews*, vol. 169, pp. 1–34, doi: 10.1016/j.earscirev.2017.04.002.
- Creer, K. M., Irving, E., and Runcorn, S. K., 1954, The direction of the geomagnetic field in remote epochs in Great Britain: *Journal of geomagnetism and geoelectricity*, vol. 6, pp. 163–168, doi: 10.5636/jgg.6.163.

- Cych, B., Morfeld, M., and Tauxe, L., 2021, Bias corrected estimation of paleointensity (BiCEP): An improved methodology for obtaining paleointensity estimates: *Geochemistry, Geophysics, Geosystems*, vol. 22, doi: 10.1029/2021gc009755.
- Daniels, P. A., 1982, 7C: Upper Precambrian sedimentary rocks: Oronto Group, Michigan-Wisconsin: *In Geological Society of America Memoirs*, Geological Society of America, pp. 107–134, doi: 10.1130/mem156-p107.
- Davies, C. J., Bono, R. K., Meduri, D. G., Aubert, J., Greenwood, S., and Biggin, A. J., 2021, Dynamo constraints on the long-term evolution of Earth's magnetic field strength: *Geophysical Journal International*, doi: 10.1093/gji/ggab342.
- Davies, C. J., Pozzo, M., Gubbins, D., and Alfè, D., 2015, Constraints from material properties on the dynamics and evolution of Earth's core: *Nature Geoscience*, vol. 8, pp. 678–685, doi: 10.1038/ngeo2492.
- Davis, D. W. and Green, J. C., 1997, Geochronology of the North American Midcontinent Rift in western Lake Superior and implications for its geodynamic evolution: *Canadian Journal of Earth Sciences*, vol. 34, pp. 476–488, doi: 10.1139/e17-039.
- Davis, D. W. and Paces, J. B., 1990, Time resolution of geologic events on the Keweenaw Peninsula and implications for development of the Midcontinent Rift system: *Earth and Planetary Science Letters*, vol. 97, pp. 54–64, doi: 10.1016/0012-821x(90)90098-i.
- Davis, D. W. and Sutcliffe, R. H., 1985, U-Pb ages from the Nipigon plate and northern Lake Superior: *Geological Society of America Bulletin*, vol. 96, p. 1572, doi: 10.1130/0016-7606(1985)96<1572:uaftnp>2.0.co;2.
- de Koker, N., Steinle-Neumann, G., and Vlcek, V., 2012, Electrical resistivity and thermal conductivity of liquid Fe alloys at high P and T, and heat flux in Earth's core: *Proceedings of the National Academy of Sciences*, vol. 109, pp. 4070–4073, doi: 10.1073/pnas.1111841109.
- DeGraff, J. M. and Carter, B. T., 2022, Detached structural model of the Keweenaw fault system, Lake Superior region, North America: Implications for its origin and relationship to the Midcontinent Rift System: *GSA Bulletin*, doi: 10.1130/b36186.1.
- Dehler, C., Gehrels, G., Porter, S., Heizler, M., Karlstrom, K., Cox, G., Crossey, L., and Timmons, M., 2017, Synthesis of the 780–740 Ma Chuar, Uinta Mountain, and Pahrump (ChUMP) groups, western USA: Implications for Laurentia-wide cratonic marine basins: *Geological Society of America Bulletin*, vol. 129, pp. 607–624, doi: 10.1130/b31532.1.
- Dehler, C., Schmitz, M., Bullard, A., Porter, S., Timmons, M., Karlstrom, K., and Cothren, H., 2023, Precise U-Pb age models refine Neoproterozoic western Laurentian rift initiation, correlation, and Earth system changes: *Precambrian Research*, vol. 396, p. 107,156, doi: 10.1016/j.precamres.2023.107156.

- Delaney, P., 1987, Heat transfer during emplacement and cooling of mafic dykes: Geological Association of Canada.
- Denyszyn, S. W., Halls, H. C., Davis, D. W., and Evans, D. A., 2009, Paleomagnetism and U-Pb geochronology of Franklin dykes in High Arctic Canada and Greenland: a revised age and paleomagnetic pole constraining block rotations in the Nares Strait region: Canadian Journal of Earth Sciences, vol. 46, pp. 689–705, doi: 10.1139/e09-042.
- Diehl, J. F. and Haig, T. D., 1994, A paleomagnetic study of the lava flows within the Copper Harbor Conglomerate, Michigan: new results and implications: Canadian Journal of Earth Sciences, vol. 31, pp. 369–380, doi: 10.1139/e94-034.
- Dodson, M. H., 1973, Closure temperature in cooling geochronological and petrological systems: Contributions to Mineralogy and Petrology, vol. 40, pp. 259–274, doi: 10.1007/bf00373790.
- Dodson, M. H. and McClelland-Brown, E., 1980, Magnetic blocking temperatures of single-domain grains during slow cooling: Journal of Geophysical Research, vol. 85, p. 2625, doi: 10.1029/jb085ib05p02625.
- Dodson, M. H. and McClelland-Brown, E., 1985, Isotopic and palaeomagnetic evidence for rates of cooling, uplift and erosion: Geological Society, London, Memoirs, vol. 10, pp. 315–325, doi: 10.1144/gsl.mem.1985.010.01.26.
- Doherty, W., 1989, An internal standardization procedure for the determination of yttrium and the rare earth elements in geological materials by inductively coupled plasma-mass spectrometry: Spectrochimica Acta Part B: Atomic Spectroscopy, vol. 44, pp. 263–280, doi: 10.1016/0584-8547(89)80031-x.
- Domeier, M., der Voo, R. V., and Torsvik, T. H., 2012, Paleomagnetism and Pangea: The road to reconciliation: Tectonophysics, vol. 514-517, pp. 14–43, doi: 10.1016/j.tecto.2011.10.021.
- Domeier, M., Robert, B., Meert, J. G., Kulakov, E. V., McCausland, P. J., Trindade, R. I., and Torsvik, T. H., 2023, The enduring Ediacaran paleomagnetic enigma: Earth-Science Reviews, p. 104444, doi: 10.1016/j.earscirev.2023.104444.
- Donadini, F., Pesonen, L. J., Korhonen, K., Deutsch, A., Harlan, S., Heaman, L., Helsinki, M. S., and Sangchan, P., 2012, Symmetric and asymmetric reversals in the 1.1 Ga central Arizona diabases: The debate continues: In Supercontinent Symposium, pp. 35–36.
- Donadini, F., Pesonen, L. J., Korhonen, K., Deutsch, A., and Harlan, S. S., 2011, Paleomagnetism and paleointensity of the 1.1 Ga old diabase sheets from central Arizona: Geophysica, vol. 47, pp. 3–30.

- Doubrovine, P. V., Steinberger, B., and Torsvik, T. H., 2012, Absolute plate motions in a reference frame defined by moving hot spots in the Pacific, Atlantic, and Indian oceans: *Journal of Geophysical Research: Solid Earth*, vol. 117, doi: 10.1029/2011jb009072.
- Doyle, M., 2016, Geologic and geochemical attributes of the Beaver River Diabase and Greenstone Flow: Testing a possible intrusive-volcanic link in the 1.1 Ga Midcontinent Rift: Master's thesis, University of Minnesota.
- Driscoll, P. E., 2016, Simulating 2 Ga of geodynamo history: *Geophysical Research Letters*, vol. 43, pp. 5680–5687, doi: 10.1002/2016gl068858.
- Driscoll, P. E. and Evans, D. A., 2016, Frequency of Proterozoic geomagnetic superchrons: *Earth and Planetary Science Letters*, vol. 437, pp. 9–14, doi: 10.1016/j.epsl.2015.12.035.
- Dubois, P. M., 1962, Palaeomagnetism and correlation of Keweenawan rocks: Tech. rep., Geological Survey of Canada, doi: 10.4095/100589.
- Dunlop, D. J. and Özdemir, Ö., 2001, Beyond Néel's theories: thermal demagnetization of narrow-band partial thermoremanent magnetizations: *Physics of the Earth and Planetary Interiors*, vol. 126, pp. 43–57, doi: 10.1016/s0031-9201(01)00243-6.
- Dunlop, D. J. and Stirling, J. M., 1985, Post-tectonic magnetizations from the Cordova gabbro, Ontario and Palaeozoic reactivation in the Grenville Province: *Geophysical Journal International*, vol. 81, pp. 521–550, doi: 10.1111/j.1365-246x.1985.tb06420.x.
- Elston, D. P., 1989, Middle and late Proterozoic Grand Canyon Supergroup, Arizona: *In* Geology of Grand Canyon, Northern Arizona (with Colorado River Guides): Lee Ferry to Pierce Ferry, Arizona, American Geophysical Union, pp. 94–105, doi: 10.1029/ft115p0094.
- Elston, D. P. and Scott, G. R., 1973, Paleomagnetism of some Precambrian basaltic flows and red beds, Eastern Grand Canyon, Arizona: *Earth and Planetary Science Letters*, vol. 18, pp. 253–265, doi: 10.1016/0012-821x(73)90064-2.
- Elston, D. P. and Scott, G. R., 1976, Unconformity at the Cardenas-Nankoweap contact (Precambrian), Grand Canyon Supergroup, northern Arizona: *Geological Society of America Bulletin*, vol. 87, p. 1763, doi: 10.1130/0016-7606(1976)87<1763:uatccp>2.0.co;2.
- Ernst, R. E. and Buchan, K. L., 1993, Paleomagnetism of the Abitibi dyke swarm, southern Superior Province, and implications for the Logan Loop: *Canadian Journal of Earth Sciences*, vol. 30, pp. 1886–1897, doi: 10.1139/e93-167.
- Evans, D. A. D., 2003, True polar wander and supercontinents: *Tectonophysics*, vol. 362, pp. 303–320, doi: 10.1016/s0040-1951(02)000642-x.
- Evans, D. A. D., 2021, Meso-Neoproterozoic Rodinia supercycle: *In* Ancient Supercontinents and the Paleogeography of Earth, Elsevier, pp. 549–576, doi: 10.1016/b978-0-12-818533-9.00006-0.

- Evans, D. A. D., Pesonen, L. J., Eglington, B. M., Elming, S.-Å., Gong, Z., Li, Z.-X., Mc-Causland, P. J., Meert, J. G., Mertanen, S., Pisarevsky, S. A., Pivarunas, A. F., Salminen, J., Swanson-Hysell, N. L., Torsvik, T. H., Trindade, R. I., Veikkolainen, T., and Zhang, S., 2021, An expanding list of reliable paleomagnetic poles for Precambrian tectonic reconstructions: *In Ancient Supercontinents and the Paleogeography of Earth*, Elsevier, pp. 605–639, doi: 10.1016/b978-0-12-818533-9.00007-2.
- Evans, D. A. D., Trindade, R. I. F., Catelani, E. L., D'Agrella-Filho, M. S., Heaman, L. M., Oliveira, E. P., Söderlund, U., Ernst, R. E., Smirnov, A. V., and Salminen, J. M., 2015, Return to Rodinia? Moderate to high palaeolatitude of the São Francisco/Congo craton at 920 Ma: Geological Society, London, Special Publications, vol. 424, pp. 167–190, doi: 10.1144/sp424.1.
- Evans, M. E., 1976, Test of the dipolar nature of the geomagnetic field throughout Phanerozoic time: Nature, vol. 262, pp. 676–677, doi: 10.1038/262676a0.
- Eyster, A., Weiss, B. P., Karlstrom, K., and Macdonald, F. A., 2019, Paleomagnetism of the Chuar Group and evaluation of the late Tonian Laurentian apparent polar wander path with implications for the makeup and breakup of Rodinia: GSA Bulletin, doi: 10.1130/b32012.1.
- Fairchild, L. M., Swanson-Hysell, N. L., Ramezani, J., Sprain, C. J., and Bowring, S. A., 2017, The end of Midcontinent Rift magmatism and the paleogeography of Laurentia: Lithosphere, vol. 9, pp. 117–133, doi: 10.1130/l580.1.
- Feinberg, J. M., Scott, G. R., Renne, P. R., and Wenk, H.-R., 2005, Exsolved magnetite inclusions in silicates: Features determining their remanence behavior: Geology, vol. 33, p. 513, doi: 10.1130/g21290.1.
- Feinberg, J. M., Solheid, P. A., Swanson-Hysell, N. L., Jackson, M. J., and Bowles, J. A., 2015, Full vector low-temperature magnetic measurements of geologic materials: Geochemistry, Geophysics, Geosystems, vol. 16, pp. 301–314, doi: 10.1002/2014gc005591.
- Feinberg, J. M., Wenk, H.-R., Scott, G. R., and Renne, P. R., 2006, Preferred orientation and anisotropy of seismic and magnetic properties in gabbronorites from the Bushveld layered intrusion: Tectonophysics, vol. 420, pp. 345–356, doi: 10.1016/j.tecto.2006.03.017.
- Ferry, J. M. and Watson, E. B., 2007, New thermodynamic models and revised calibrations for the Ti-in-zircon and Zr-in-rutile thermometers: Contributions to Mineralogy and Petrology, vol. 154, pp. 429–437, doi: 10.1007/s00410-007-0201-0.
- Fisher, N. I., Lewis, T., and Embleton, B. J., 1987, Statistical analysis of spherical data: Cambridge university press.
- Fisher, R., 1953, Dispersion on a sphere: Proceedings of the Royal Society A: Mathematical, Physical and Engineering Sciences, vol. 217, pp. 295–305, doi: 10.1098/rspa.1953.0064.

- Foucher, M., 2018, Probing the Precambrian geodynamo: analysis of the geomagnetic field behavior and calibration of pseudo-thellier paleointensity method for Mesoproterozoic rocks: Ph.D. thesis, Michigan Technological University.
- Frost, D. A., Avery, M. S., Buffett, B. A., Chidester, B. A., Deng, J., Dorfman, S. M., Li, Z., Liu, L., Lv, M., and Martin, J. F., 2022, Multidisciplinary constraints on the thermal-chemical boundary between Earth's core and mantle: Geochemistry, Geophysics, Geosystems, doi: 10.1029/2021GC009764.
- Gallo, L. C., Domeier, M., Sapienza, F., Swanson-Hysell, N. L., Vaes, B., Zhang, Y., Arnould, M., Eyster, A., Gürer, D., Király, Á., Robert, B., Rolf, T., Shephard, G., and van der Boon, A., 2023, Embracing uncertainty to resolve polar wander: A case study of Cenozoic North America: *Geophysical Research Letters*, vol. 50, p. e2023GL103,436, doi: 10.1029/2023GL103436.
- Garza, R. S. M., Acton, G. D., and Geissman, J. W., 1998, Carboniferous through Jurassic paleomagnetic data and their bearing on rotation of the Colorado plateau: *Journal of Geophysical Research: Solid Earth*, vol. 103, pp. 24,179–24,188, doi: 10.1029/98jb02053.
- Gerstenberger, H. and Haase, G., 1997, A highly effective emitter substance for mass spectrometric Pb isotope ratio determinations: *Chemical Geology*, vol. 136, pp. 309–312, doi: 10.1016/S0009-2541(96)00033-2.
- Glenn, D. R., Fu, R. R., Kehayias, P., Le Sage, D., Lima, E. A., Weiss, B. P., and Walsworth, R. L., 2017, Micrometer-scale magnetic imaging of geological samples using a quantum diamond microscope: *Geochemistry, Geophysics, Geosystems*, vol. 18, pp. 3254–3267, doi: 10.1002/2017gc006946.
- Gomi, H., Ohta, K., Hirose, K., Labrosse, S., Caracas, R., Verstraete, M. J., and Hernlund, J. W., 2013, The high conductivity of iron and thermal evolution of the Earth's core: *Physics of the Earth and Planetary Interiors*, vol. 224, pp. 88–103, doi: 10.1016/j.pepi.2013.07.010.
- Gong, Z., Evans, D. A., Elming, S.-Å., Söderlund, U., and Salminen, J. M., 2018, Paleomagnetism, magnetic anisotropy and U-Pb baddeleyite geochronology of the early Neoproterozoic Blekinge-Dalarna dolerite dykes, Sweden: *Precambrian Research*, vol. 317, pp. 14–32, doi: 10.1016/j.precamres.2018.08.019.
- Gong, Z., Evans, D. A., Zhang, Z., and Yan, C., 2023, Mid-Proterozoic geomagnetic field was more consistent with a dipole than a quadrupole: *Geology*, doi: 10.1130/G50941.1.
- Green, G. N., 1992, The digital geologic map of Colorado in ARC/INFO format: Tech. rep., U.S. Geological Survey.
- Green, J. C., 1982, 5: Geology of Keweenawan extrusive rocks: *Geological Society of America Memoirs*, vol. 156, pp. 47–56.

- Greenman, J. W., Rooney, A. D., Patzke, M., Ielpi, A., and Halverson, G. P., 2021, Re-Os geochronology highlights widespread latest Mesoproterozoic (ca. 1090–1050 Ma) cratonic basin development on northern Laurentia: *Geology*, doi: 10.1130/g48521.1.
- Grout, F. F. and Schwartz, G. M., 1939, The geology of the anorthosites of the Minnesota coast of Lake Superior: Tech. Rep. 28, Minnesota Geological Survey.
- Gubbins, D., Alfè, D., Masters, G., Price, G. D., and Gillan, M., 2004, Gross thermodynamics of two-component core convection: *Geophysical Journal International*, vol. 157, pp. 1407–1414, doi: 10.1111/j.1365-246x.2004.02219.x.
- Gundy, C. E. V., 1951, Nankoweap Group of the Grand Canyon Algonkian of Arizona: *Geological Society of America Bulletin*, vol. 62, p. 953, doi: 10.1130/0016-7606(1951)62[953:ngotgc]2.0.co;2.
- Guth, P. L., 1981, Tertiary extension north of the Las Vegas Valley shear zone, Sheep and Desert Ranges, Clark County, Nevada: *Geological Society of America Bulletin*, vol. 92, p. 763, doi: 10.1130/0016-7606(1981)92<763:tenotl>2.0.co;2.
- Haddox, C. A. and Dott, R. H., 1990, Cambrian shoreline deposits in northern Michigan: *Journal of Sedimentary Research*, vol. 60, pp. 697–716, doi: 10.1306/212F9250-2B24-11D7-8648000102C1865D.
- Haggerty, S. E. and Baker, I., 1967, The alteration of olivine in basaltic and associated lavas: *Contributions to Mineralogy and Petrology*, vol. 16, pp. 233–257, doi: 10.1007/bf00371094.
- Halgedahl, S. L., Day, R., and Fuller, M., 1980, The effect of cooling rate on the intensity of weak-field TRM in single-domain magnetite: *Journal of Geophysical Research: Solid Earth*, vol. 85, pp. 3690–3698, doi: 10.1029/jb085ib07p03690.
- Halls, H. C., 1974, A paleomagnetic reversal in the Osler Volcanic Group, northern Lake Superior: *Canadian Journal of Earth Sciences*, vol. 11, pp. 1200–1207, doi: 10.1139/e74-113.
- Halls, H. C., 2015, Paleomagnetic evidence for ~4000 km of crustal shortening across the 1 Ga Grenville orogen of North America: *Geology*, p. G37188.1, doi: 10.1130/g37188.1.
- Halls, H. C., Lovette, A., Hamilton, M., and Söderlund, U., 2015, A paleomagnetic and U–Pb geochronology study of the western end of the Grenville dyke swarm: Rapid changes in paleomagnetic field direction at ca. 585 Ma related to polarity reversals?: *Precambrian Research*, vol. 257, pp. 137–166, doi: 10.1016/j.precamres.2014.11.029.
- Halls, H. C. and Pesonen, L. J., 1982, 9: Paleomagnetism of Keweenawan rocks: *Geology and Tectonics of the Lake Superior Basin*, pp. 173–202, doi: 10.1130/mem156-p173.

- Hamblin, W. K., 1958, Cambrian sandstones of northern Michigan: Michigan Geological Survey Publication.
- Hamilton, W., 1981, Plate-tectonic mechanism of Laramide deformation.: Contributions to Geology - University of Wyoming, Laramie, vol. 19, pp. 87–92.
- Hamilton, W. B., 1988, Laramide crustal shortening, Geological Society of America, pp. 27–40: doi: 10.1130/mem171-p27.
- Hammond, J. G., 1983, Late Precambrian diabase intrusions in the southern Death Valley region, California: Their petrology, geochemistry, and tectonic significance: Ph.d., University of Southern California, United States – California.
- Hammond, J. G., 1986, Geochemistry and petrogenesis of Proterozoic diabase in the southern Death Valley region of California: Contributions to Mineralogy and Petrology, vol. 93, pp. 312–321, doi: 10.1007/bf00389390.
- Hammond, J. G. and Wooden, J., 1990, Isotopic constraints on the petrogenesis of Proterozoic diabase in southwestern USA: *In* International dyke conference. 2, pp. 145–156.
- Harlan, S. S., 1993, Paleomagnetism of Middle Proterozoic diabase sheets from central Arizona: Canadian Journal of Earth Sciences, vol. 30, pp. 1415–1426, doi: 10.1139/e93-122.
- Harlan, S. S., Heaman, L., LeCheminant, A. N., and Premo, W. R., 2003, Gunbarrel mafic magmatic event: A key 780 Ma time marker for Rodinia plate reconstructions: Geology, vol. 31, p. 1053, doi: 10.1130/g19944.1.
- Härtel, B., Matthews, W. A., and Enkelmann, E., 2023, Duluth Complex FC1 apatite and zircon: reference materials for (U-Th)/He dating?: Geostandards and Geoanalytical Research, doi: 10.1111/ggr.12492.
- Hawkins, L., Anwar, T., Shcherbakova, V., Biggin, A., Kravchinsky, V., Shatsillo, A., and Pavlov, V., 2019, An exceptionally weak Devonian geomagnetic field recorded by the Viluy Traps, Siberia: Earth and Planetary Science Letters, vol. 506, pp. 134–145, doi: 10.1016/j.epsl.2018.10.035.
- Hawkins, L. M. A., Grappone, J. M., Sprain, C. J., Saengduean, P., Sage, E. J., Thomas-Cunningham, S., Kugabalan, B., and Biggin, A. J., 2021, Intensity of the Earth's magnetic field: Evidence for a Mid-Paleozoic dipole low: Proceedings of the National Academy of Sciences, vol. 118, p. e2017342,118, doi: 10.1073/pnas.2017342118.
- Heaman, L. M., Easton, R. M., Hart, T. R., Hollings, P., MacDonald, C. A., and Smyk, M., 2007, Further refinement to the timing of Mesoproterozoic magmatism, Lake Nipigon region, Ontario: Canadian Journal of Earth Sciences, vol. 44, pp. 1055–1086, doi: 10.1139/e06-117.

- Heaman, L. M. and Grotzinger, J. P., 1992, 1.08 Ga diabase sills in the Pahrump Group, California: Implications for development of the Cordilleran miogeocline: *Geology*, vol. 20, p. 637, doi: 10.1130/0091-7613(1992)020<0637:gdsitp>2.3.co;2.
- Hedman, C., 1992, Provenance and tectonic setting of the Jacobsville Sandstone, from Ironwood to Keweenaw Bay, Michigan: Master's thesis, University of Cincinnati. Department of Geology.
- Hedley, I., 1968, Chemical remanent magnetization of the FeOOH, Fe<sub>2</sub>O<sub>3</sub> system: *Physics of the Earth and Planetary Interiors*, vol. 1, pp. 103–121, doi: 10.1016/0031-9201(68)90055-1.
- Helsley, C. E. and Spall, H., 1972, Paleomagnetism of 1140 to 1150 million-year diabase sills from Gila County, Arizona: *Journal of Geophysical Research*, vol. 77, pp. 2115–2128, doi: 10.1029/jb077i011p02115.
- Hendricks, J. D., 1972, Younger Precambrian basaltic rocks of the Grand Canyon, Arizona: Ph.D. thesis, Northern Arizona University.
- Hendricks, J. D., 1989, Petrology and chemistry of igneous rocks of Middle Proterozoic Unkar Group, Grand Canyon Supergroup, northern Arizona: *In* *Geology of Grand Canyon, Northern Arizona (with Colorado River Guides)*: Lee Ferry to Pierce Ferry, Arizona, American Geophysical Union, pp. 106–116, doi: 10.1029/ft115p0106.
- Hendricks, J. D., Lucchitta, I., Karlstrom, T., Swann, G., and Eastwood, R., 1974, Upper Precambrian igneous rocks of the Grand Canyon, Arizona: *In* *Geology of northern Arizona*, pp. 65–86.
- Henry, S. G., Mauk, F. J., and der Voo, R. V., 1977, Paleomagnetism of the upper Keweenawan sediments: the Nonesuch Shale and Freda Sandstone: *Canadian Journal of Earth Sciences*, vol. 14, pp. 1128–1138, doi: 10.1139/e77-103.
- Heslop, D., Scealy, J. L., Wood, A. T. A., Tauxe, L., and Roberts, A. P., 2023, A bootstrap common mean direction test: *Journal of Geophysical Research: Solid Earth*, vol. 128, doi: 10.1029/2023jb026983.
- Hinze, W. J. and Chandler, V. W., 2020, Reviewing the configuration and extent of the Midcontinent Rift system: *Precambrian Research*, vol. 342, p. 105,688, doi: 10.1016/j.precamres.2020.105688.
- Hnat, J. S., van der Pluijm, B. A., and van der Voo, R., 2006, Primary curvature in the Mid-Continent Rift: Paleomagnetism of the Portage Lake Volcanics (northern Michigan, USA): *Tectonophysics*, vol. 425, pp. 71–82, doi: 10.1016/j.tecto.2006.07.006.
- Hodgin, E. B., Swanson-Hysell, N. L., DeGraff, J. M., Kylander-Clark, A. R., Schmitz, M. D., Turner, A. C., Zhang, Y., and Stolper, D. A., 2022, Final inversion of the Midcontinent Rift during the Rigolet Phase of the Grenvillian Orogeny: *Geology*, doi: 10.1130/g49439.1.

- Hoffman, P. F., 1988, United plates of America, the birth of a craton: early Proterozoic assembly and growth of Laurentia: *Annual Review of Earth and Planetary Sciences*, vol. 16, pp. 543–603, doi: 10.1146/annurev.ea.16.050188.002551.
- Holm, D. K., Geissman, J. W., and Wernicke, B., 1993, Tilt and rotation of the footwall of a major normal fault system: Paleomagnetism of the Black Mountains, Death Valley extended terrane, California: *Geological Society of America Bulletin*, vol. 105, pp. 1373–1387, doi: 10.1130/0016-7606(1993)105<1373:tarotf>2.3.co;2.
- Hounslow, M. W., Domeier, M., and Biggin, A. J., 2018, Subduction flux modulates the geomagnetic polarity reversal rate: *Tectonophysics*, vol. 742–743, pp. 34–49, doi: 10.1016/j.tecto.2018.05.018.
- Howard, K. A., 1991, Intrusion of horizontal dikes: Tectonic significance of Middle Proterozoic diabase sheets widespread in the upper crust of the southwestern United States: *Journal of Geophysical Research*, vol. 96, p. 12,461, doi: 10.1029/91jb00112.
- Hsieh, W.-P., Goncharov, A. F., Labrosse, S., Holtgrewe, N., Lobanov, S. S., Chuvashova, I., Deschamps, F., and Lin, J.-F., 2020, Low thermal conductivity of iron-silicon alloys at Earth's core conditions with implications for the geodynamo: *Nature Communications*, vol. 11, doi: 10.1038/s41467-020-17106-7.
- Huber, N., 1973, The Portage Lake Volcanics (Middle Keweenawan) on Isle Royale, Michigan: Tech. rep., United States Geological Survey.
- Huntoon, P., Billingsley, G., Sears, J., Ilg, B., Karlstrom, K., Williams, M., and Hawkins, D., 1996, Geologic map of the Eastern Grand Canyon National Park: Tech. rep., Grand Canyon Association and Museum of Northern Arizona.
- Irving, E., 1977, Drift of the major continental blocks since the Devonian: *Nature*, vol. 270, pp. 304–309, doi: 10.1038/270304a0.
- Irving, R. D. and Chamberlin, T. C., 1885, Observations on the junction between the Eastern sandstone and the Keweenaw series on Keweenaw Point, Lake Superior: Tech. rep., U.S. Geological Survey, doi: 10.3133/b23.
- Jaffe, H. W., Robinson, P., Tracy, R. J., and Ross, M., 1975, Orientation of pigeonite exsolution lamellae in metamorphic augite: correlation with composition and calculated optimal phase boundaries: *American Mineralogist: Journal of Earth and Planetary Materials*, vol. 60, pp. 9–28.
- Jagoutz, O., Royden, L., Holt, A. F., and Becker, T. W., 2015, Anomalously fast convergence of India and Eurasia caused by double subduction: *Nature Geoscience*, vol. 8, pp. 475–478, doi: 10.1038/ngeo2418.

- Jannin, S., Gervais, F., Moukhsil, A., and Augland, L. E., 2018, Late-Grenvillian channel flow in the central Grenville Province (Manicouagan Reservoir area): New constraints from a structural and geochronological study of the Allochthon Boundary Thrust: *Journal of Structural Geology*, vol. 115, pp. 132–151, doi: 10.1016/j.jsg.2018.07.019.
- Jiang, Z., Liu, Q., Dekkers, M. J., Tauxe, L., Qin, H., Barrón, V., and Torrent, J., 2015, Acquisition of chemical remanent magnetization during experimental ferrihydrite–hematite conversion in Earth-like magnetic field—implications for paleomagnetic studies of red beds: *Earth and Planetary Science Letters*, vol. 428, pp. 1–10, doi: 10.1016/j.epsl.2015.07.024.
- Jiang, Z., Liu, Q., Roberts, A. P., Barrón, V., Torrent, J., and Zhang, Q., 2018, A new model for transformation of ferrihydrite to hematite in soils and sediments: *Geology*, doi: 10.1130/g45386.1.
- Jirsa, M. A., Boerboom, T., Chandler, V., Mossler, J., Runkel, A., and Setterholm, D., 2011, S-21 Geologic map of Minnesota-bedrock geology: Tech. rep., Minnesota Geological Survey.
- Kalliokoski, J., 1982, 7E: Jacobsville Sandstone: Geology and Tectonics of the Lake Superior Basin, pp. 147–156, doi: 10.1130/mem156-p147.
- Karlstrom, K., Mohr, M., Schmitz, M., Sundberg, F., Rowland, S., Blakey, R., Foster, J., Crossey, L., Dehler, C., and Hagadorn, J., 2020, Redefining the Tonto Group of Grand Canyon and recalibrating the Cambrian time scale: *Geology*, vol. 48, pp. 425–430, doi: 10.1130/g46755.1.
- Karlstrom, K. E. and Humphreys, E. D., 1998, Persistent influence of Proterozoic accretionary boundaries in the tectonic evolution of southwestern North America: Interaction of cratonic grain and mantle modification events: *Rocky Mountain Geology*, vol. 33, pp. 161–179, doi: 10.2113/33.2.161.
- Karlstrom, K. E. and Timmons, J. M., 2012, Faulting and uplift in the Grand Canyon region: *In Grand Canyon Geology: Two Billion Years of Earth's History*, Geological Society of America, doi: 10.1130/2012.2489(06).
- Karlstrom, K. E., Wilgus, J., Thacker, J. O., Schmandt, B., Coblenz, D., and Albonico, M., 2022, Tectonics of the Colorado Plateau and its margins: *Annual Review of Earth and Planetary Sciences*, vol. 50, pp. 295–322, doi: 10.1146/annurev-earth-032320-111432.
- Kasbohm, J., Schoene, B., and Burgess, S., 2021, Radiometric constraints on the timing, tempo, and effects of large igneous province emplacement: doi: 10.1002/9781119507444.ch2.
- Kent, D. V. and Witte, W. K., 1993, Slow apparent polar wander for North America in the Late Triassic and large Colorado Plateau rotation: *Tectonics*, vol. 12, pp. 291–300, doi: 10.1029/92tc01966.

- Kent, J. T., 1982, The Fisher-Bingham distribution on the sphere: *Journal of the Royal Statistical Society: Series B (Methodological)*, vol. 44, pp. 71–80, doi: 10.1111/j.2517-6161.1982.tb01189.x.
- King, R. F., 1955, The remanent magnetism of artificially deposited sediments: *Geophysical Journal International*, vol. 7, pp. 115–134, doi: 10.1111/j.1365-246x.1955.tb06558.x.
- Kirschvink, J. L., 1980, The least-squares line and plane and the analysis of palaeomagnetic data: *Geophysical Journal International*, vol. 62, pp. 699–718, doi: 10.1111/j.1365-246x.1980.tb02601.x.
- Kodama, K. P., 2012, *Paleomagnetism of Sedimentary Rocks*: Wiley, doi: 10.1002/9781118384138.
- Kodama, K. P., 2021, Combined magnetostratigraphy from three localities of the Rainstorm Member of the Johnnie Formation in California and Nevada, United States Calibrated by Cyclostratigraphy: A 13 R/Ma Reversal Frequency for the Ediacaran: *Frontiers in Earth Science*, vol. 9, doi: 10.3389/feart.2021.764714.
- Kodama, K. P., Carnes, L. K., Tarduno, J. A., and Berti, C., 2019, Palaeointensity of the 1.3 billion-yr-old Gardar basalts, southern Greenland revisited: no evidence for onset of inner core growth: *Geophysical Journal International*, vol. 217, pp. 1974–1987, doi: 10.1093/gji/ggz126.
- Kodama, K. P. and Davi, J. M., 1995, A compaction correction for the paleomagnetism of the Cretaceous Pigeon Point Formation of California: *Tectonics*, vol. 14, pp. 1153–1164, doi: 10.1029/95tc01648.
- Konôpková, Z., McWilliams, R. S., Gómez-Pérez, N., and Goncharov, A. F., 2016, Direct measurement of thermal conductivity in solid iron at planetary core conditions: *Nature*, vol. 534, pp. 99–101, doi: 10.1038/nature18009.
- Krogh, T., 1973, A low contamination method for the hydrothermal decomposition of zircon and extraction of U and Pb for isotopic age determinations: *Geochimica Cosmochimica Acta*, vol. 37, pp. 485–494, doi: 10.1016/0016-7037(73)90213-5.
- Kulakov, E. V., Smirnov, A. V., and Diehl, J. F., 2013a, Absolute geomagnetic paleointensity as recorded by ~1.09 Ga Lake Shore Traps (Keweenaw Peninsula, Michigan): *Studia Geophysica et Geodaetica*, vol. 57, pp. 565–584, doi: 10.1007/s11200-013-0606-3.
- Kulakov, E. V., Smirnov, A. V., and Diehl, J. F., 2013b, Paleomagnetism of ~1.09 Ga Lake Shore Traps (Keweenaw Peninsula, Michigan): new results and implications: *Canadian Journal of Earth Sciences*, vol. 50, pp. 1085–1096, doi: 10.1139/cjes-2013-0003.
- Kushiro, I., 1980, Viscosity, density, and structure of silicate melts at high pressures, and their petrological applications: *Physics of magmatic processes*, pp. 93–120.

- Labotka, T. C., Albee, A. L., Lanphere, M. A., and McDowell, S. D., 1980, Stratigraphy, structure, and metamorphism in the central Panamint Mountains (Telescope Peak quadrangle), Death Valley area, California: GSA Bulletin, vol. 91, pp. 843–933, doi: 10.1130/gsab-p2-91-843.
- Labotka, T. C., Warasila, R. L., and Spangler, R. R., 1985, Polymetamorphism in the Panamint Mountains, California: A  $^{39}\text{Ar}$ - $^{40}\text{Ar}$  study: Journal of Geophysical Research: Solid Earth, vol. 90, pp. 10,359–10,371, doi: 10.1029/jb090ib12p10359.
- Labrosse, S., 2003, Thermal and magnetic evolution of the Earth's core: Physics of the Earth and Planetary Interiors, vol. 140, pp. 127–143, doi: 10.1016/j.pepi.2003.07.006.
- Labrosse, S., 2015, Thermal evolution of the core with a high thermal conductivity: Physics of the Earth and Planetary Interiors, vol. 247, pp. 36–55, doi: 10.1016/j.pepi.2015.02.002.
- Landau, M., Aubert, J., and Olson, P., 2017, The signature of inner-core nucleation on the geodynamo: Earth and Planetary Science Letters, vol. 465, pp. 193–204, doi: 10.1016/j.epsl.2017.02.004.
- Landau, M., Fournier, A., Nataf, H.-C., Cébron, D., and Schaeffer, N., 2022, Sustaining earth's magnetic dynamo: Nature Reviews Earth & Environment, doi: 10.1038/s43017-022-00264-1.
- Lane, A. C., 1911, The Keweenaw series of Michigan: Michigan Geological and Biological Survey Publication 6, vol. 2, p. 983.
- Lanphere, M. A., 1964, Geochronologic Studies in the Eastern Mojave Desert, California: The Journal of Geology, vol. 72, pp. 381–399, doi: 10.1086/626997.
- Larson, E., Patterson, P., and Mutschler, F., 1994, Lithology, chemistry, age, and origin of the Proterozoic Cardenas Basalt, Grand Canyon, Arizona: Precambrian Research, vol. 65, pp. 255–276, doi: 10.1016/0301-9268(94)90108-2.
- Larson, R. L. and Olson, P., 1991, Mantle plumes control magnetic reversal frequency: Earth and Planetary Science Letters, vol. 107, pp. 437–447, doi: 10.1016/0012-821x(91)90091-u.
- Lawson, A. C., 1893, The anorthosites of the Minnesota Coast of Lake Superior: Geological and Natural History Survey of Minnesota: Bulletin, vol. 8, pp. 1–23.
- Lhuillier, F., Shcherbakov, V. P., and Sycheva, N. K., 2023, Detecting dipolarity of the geomagnetic field in the paleomagnetic record: Proceedings of the National Academy of Sciences, vol. 120, doi: 10.1073/pnas.2220887120.
- Li, Z., Bogdanova, S., Collins, A., Davidson, A., Waele, B. D., Ernst, R., Fitzsimons, I., Fuck, R., Gladkochub, D., Jacobs, J., Karlstrom, K., Lu, S., Natapov, L., Pease, V.,

- Pisarevsky, S., Thrane, K., and Vernikovsky, V., 2008, Assembly, configuration, and break-up history of Rodinia: A synthesis: *Precambrian Research*, vol. 160, pp. 179–210, doi: 10.1016/j.precamres.2007.04.021.
- Lima, E. A. and Weiss, B. P., 2016, Ultra-high sensitivity moment magnetometry of geological samples using magnetic microscopy: *Geochemistry, Geophysics, Geosystems*, vol. 17, pp. 3754–3774, doi: 10.1002/2016gc006487.
- Lloyd, S. J., Biggin, A. J., Halls, H., and Hill, M. J., 2021a, First palaeointensity data from the Cryogenian and their potential implications for inner core nucleation age: *Geophysical Journal International*, doi: 10.1093/gji/ggab090.
- Lloyd, S. J., Biggin, A. J., and Li, Z.-X., 2021b, New paleointensity data suggest possible Phanerozoic-type paleomagnetic variations in the Precambrian: *Geochemistry, Geophysics, Geosystems*, doi: <https://doi.org/10.1029/2021GC009990>.
- Lloyd, S. J., Biggin, A. J., Paterson, G. A., and McCausland, P. J., 2022, Extremely weak early Cambrian dipole moment similar to Ediacaran: Evidence for long-term trends in geomagnetic field behaviour?: *Earth and Planetary Science Letters*, vol. 595, p. 117,757, doi: 10.1016/j.epsl.2022.117757.
- Longo, A. A., 1984, A correlation for a middle Keweenawan flood basalt: the Greenstone flow, Isle Royale and Keweenaw Peninsula, Michigan: Master's thesis, Michigan Technological University.
- Lucchitta, I., 1979, Late Cenozoic uplift of the southwestern Colorado Plateau and adjacent lower Colorado River region: *Tectonophysics*, vol. 61, pp. 63–95, doi: 10.1016/0040-1951(79)90292-0.
- Lucchitta, I. and Hendricks, J. D., 1983, Characteristics, depositional environment, and tectonic interpretations of the Proterozoic Cardenas Lavas, eastern Grand Canyon, Arizona: *Geology*, vol. 11, p. 177, doi: 10.1130/0091-7613(1983)11<177:cdeati>2.0.co;2.
- Macdonald, F. A., Prave, A. R., Petterson, R., Smith, E. F., Pruss, S. B., Oates, K., Waechter, F., Trotzuk, D., and Fallick, A. E., 2013, The Laurentian record of Neoproterozoic glaciation, tectonism, and eukaryotic evolution in Death Valley, California: *Geological Society of America Bulletin*, vol. 125, pp. 1203–1223, doi: 10.1130/b30789.1.
- Macdonald, F. A., Yonkee, W. A., Flowers, R. M., and Swanson-Hysell, N. L., 2023, Neo-proterozoic of Laurentia: *In Laurentia: Turning Points in the Evolution of a Continent*, Geological Society of America, pp. 331–380, doi: 10.1130/2022.1220(19).
- Mackinder, A., Cousens, B. L., Ernst, R. E., and Chamberlain, K. R., 2019, Geochemical, isotopic, and U-Pb zircon study of the central and southern portions of the 780 Ma Gunbarrel Large Igneous Province in western Laurentia: *Canadian Journal of Earth Sciences*, vol. 56, pp. 738–755, doi: 10.1139/cjes-2018-0083.

- Macouin, M., Valet, J., Besse, J., Buchan, K., Ernst, R., LeGoff, M., and Scharer, U., 2003, Low paleointensities recorded in 1 to 2.4 Ga Proterozoic dykes, Superior Province, Canada: *Earth and Planetary Science Letters*, vol. 213, pp. 79–95, doi: 10.1016/s0012-821x(03)00243-7.
- Mahon, R. C., Dehler, C. M., Link, P. K., Karlstrom, K. E., and Gehrels, G. E., 2014a, Detrital zircon provenance and paleogeography of the Pahrump Group and overlying strata, Death Valley, California: *Precambrian Research*, vol. 251, pp. 102–117, doi: 10.1016/j.precamres.2014.06.005.
- Mahon, R. C., Dehler, C. M., Link, P. K., Karlstrom, K. E., and Gehrels, G. E., 2014b, Geochronologic and stratigraphic constraints on the Mesoproterozoic and Neoproterozoic Pahrump Group, Death Valley, California: A record of the assembly, stability, and breakup of Rodinia: *Geological Society of America Bulletin*, vol. 126, pp. 652–664, doi: 10.1130/b30956.1.
- Malone, D. H., Stein, C. A., Craddock, J. P., Kley, J., Stein, S., and Malone, J. E., 2016, Maximum depositional age of the Neoproterozoic Jacobsville Sandstone, Michigan: Implications for the evolution of the Midcontinent Rift: *Geosphere*, vol. 12, pp. 1271–1282, doi: 10.1130/ges01302.1.
- Malone, D. H., Stein, C. A., Craddock, J. P., Stein, S., and Malone, J. E., 2020, Neoproterozoic sedimentation and tectonics of the Laurentian midcontinent: Detrital zircon provenance of the Jacobsville Sandstone, Lake Superior Basin, USA and Canada: *Terra Nova*, doi: 10.1111/ter.12481.
- Manson, M. L. and Halls, H. C., 1994, Post-Keweenawan compressional faults in the eastern Lake Superior region and their tectonic significance: *Canadian Journal of Earth Sciences*, vol. 31, pp. 640–651, doi: 10.1139/e94-057.
- Mattinson, J. M., 2005, Zircon U–Pb chemical abrasion (“CA-TIMS”) method: Combined annealing and multi-step partial dissolution analysis for improved precision and accuracy of zircon ages: *Chemical Geology*, vol. 220, pp. 47–66, doi: 10.1016/j.chemgeo.2005.03.011.
- Maxbauer, D. P., Feinberg, J. M., and Fox, D. L., 2016, MAX UnMix: A web application for unmixing magnetic coercivity distributions: *Computers & Geosciences*, vol. 95, pp. 140–145, doi: 10.1016/j.cageo.2016.07.009.
- McCabe, C. and Van der Voo, R., 1983, Paleomagnetic results from the upper Keweenawan Chequamegon Sandstone: implications for red bed diagenesis and Late Precambrian apparent polar wander of North America: *Canadian Journal of Earth Sciences*, vol. 20, pp. 105–112, doi: 10.1139/e83-010.
- McClelland, E., 1987, Self-reversal of chemical remanent magnetization: a palaeomagnetic example: *Geophysical Journal International*, vol. 90, pp. 615–625, doi: 10.1111/j.1365-246x.1987.tb00744.x.

- McClelland, E. and Goss, C., 1993, Self reversal of chemical remanent magnetization on the transformation of maghemite to haematite: *Geophysical Journal International*, vol. 112, pp. 517–532, doi: 10.1111/j.1365-246x.1993.tb01185.x.
- McElhinny, M. W., 1973, Palaeomagnetism and plate tectonics: Cambridge Earth Science Series, Cambridge University Press.
- McElhinny, M. W., McFadden, P. L., and Merrill, R. T., 1996, The time-averaged paleomagnetic field 0–5 Ma: *Journal of Geophysical Research: Solid Earth*, vol. 101, pp. 25,007–25,027, doi: 10.1029/96jb01911.
- McEnroe, S. A., Robinson, P., Langenhorst, F., Frandsen, C., Terry, M. P., and Ballaran, T. B., 2007, Magnetization of exsolution intergrowths of hematite and ilmenite: Mineral chemistry, phase relations, and magnetic properties of hemo-ilmenite ores with micron- to nanometer-scale lamellae from Allard Lake, Quebec: *Journal of Geophysical Research*, vol. 112, doi: 10.1029/2007jb004973.
- McFadden, P. and McElhinny, M., 1990, Classification of the reversal test in palaeomagnetism: *Geophysical Journal International*, vol. 103, pp. 725–729, doi: 10.1111/j.1365-246X.1990.tb05683.x.
- McWilliams, M. O. and Dunlop, D. J., 1975, Precambrian paleomagnetism: magnetizations reset by the Grenville Orogeny: *Science*, vol. 190, pp. 269–272, doi: 10.1126/science.190.4211.269.
- Meert, J. G., 2014, Ediacaran–Early Ordovician paleomagnetism of Baltica: A review: *Gondwana Research*, vol. 25, pp. 159–169, doi: 10.1016/j.gr.2013.02.003.
- Metzger, E. P., Leech, M. L., Davis, M. W., Reeder, J. V., Swanson, B. A., and Waring, H. V., 2021, Ultrahigh-temperature granulite-facies metamorphism and exhumation of deep crust in a migmatite dome during late- to post- orogenic collapse and extension in the central Adirondack Highlands (New York, USA): *Geosphere*, doi: 10.1130/ges02318.1.
- Mezger, K., Rawnsley, C. M., Bohlen, S. R., and Hanson, G. N., 1991, U-Pb garnet, sphene, monazite, and rutile ages: Implications for the duration of high-grade metamorphism and cooling histories, Adirondack Mts., New York: *The Journal of Geology*, vol. 99, pp. 415–428, doi: 10.1086/629503.
- Miller, J., J.D., 1988, M-065 Geologic map of the Silver Bay and Split Rock Point NE quadrangles, Lake County, Minnesota: Tech. rep., Minnesota Geological Survey.
- Miller, J., J.D. and Boerboom, T. J., 1989, M-066 geologic map of the Illgen City quadrangle, Lake County, Minnesota: Tech. rep., Minnesota Geological Survey.

- Miller, J., J.D., Boerboom, T. J., and Jerde, E., 1994, M-082 Bedrock geologic map of the Cabin Lake and Cramer quadrangles, Lake and Cook Counties, Minnesota: Tech. rep., Minnesota Geological Survey.
- Miller, J., J.D. and Chandler, V. W., 1997, Geology, petrology, and tectonic significance of the Beaver Bay Complex, northeastern Minnesota: *In* Middle Proterozoic to Cambrian rifting, central North America, Geological Society of America, doi: 10.1130/0-8137-2312-4. 73.
- Miller, J., J.D. and Nicholson, S. W., 2013, Geology and Mineral Deposits of the 1.1 Ga Midcontinent Rift in the Lake Superior Region – An Overview: *In* Field guide to the copper-nickel-platinum group element deposits of the Lake Superior Region, Precambrian Research Center.
- Miller, J., J.D., Severson, M. J., Chandler, V. W., and Peterson, D. M., 2001, M-119 Geologic map of the Duluth Complex and related rocks, northeastern Minnesota: Tech. rep., Minnesota Geological Survey.
- Miller, J., J.D. and Weiblen, P. W., 1990, Anorthositic rocks of the Duluth Complex: Examples of rocks formed from plagioclase crystal mush: *Journal of Petrology*, vol. 31, pp. 295–339, doi: 10.1093/petrology/31.2.295.
- Milstein, R. L., 1987, Anomalous Paleozoic outliers near Limestone Mountain, Michigan: *In* North-Central Section of the Geological Society of America, Geological Society of America, pp. 263–268, doi: 10.1130/0-8137-5403-8.263.
- Mitchell, R. N., Bleeker, W., van Breemen, O., Lecheminant, T. N., Peng, P., Nilsson, M. K. M., and Evans, D. A. D., 2014, Plate tectonics before 2.0 Ga: Evidence from paleomagnetism of cratons within supercontinent Nuna: *American Journal of Science*, vol. 314, pp. 878–894, doi: 10.2475/04.2014.03.
- Mittal, T., Knezek, N., Arveson, S. M., McGuire, C. P., Williams, C. D., Jones, T. D., and Li, J., 2020, Precipitation of multiple light elements to power Earth's early dynamo: *Earth and Planetary Science Letters*, vol. 532, p. 116,030, doi: 10.1016/j.epsl.2019.116030.
- Mohr, M., Schmitz, M., Swanson-Hysell, N., Karlstrom, K., Macdonald, F., Holland, M., Zhang, Y., and Anderson, N., 2024, High-precision U-Pb geochronology links magmatism in the southwestern Laurentia large igneous province and Midcontinent Rift: *Geology*, doi: 10.1130/g51786.1.
- Morrison, D. A., Ashwal, L. D., Phinney, W. C., Shih, C.-Y., and Wooden, J. L., 1983, Pre-Keweenawan anorthosite inclusions in the Keweenawan Beaver Bay and Duluth Complexes, northeastern Minnesota: *Geological Society of America Bulletin*, vol. 94, p. 206, doi: 10.1130/0016-7606(1983)94<206:paiitk>2.0.co;2.

- Moskowitz, B. M., Jackson, M., and Kissel, C., 1998, Low-temperature magnetic behavior of titanomagnetites: *Earth and Planetary Science Letters*, vol. 157, pp. 141–149, doi: 10.1016/s0012-821x(98)00033-8.
- Mueller, S. A., 2021, Structural analysis and interpretation of deformation along the Keweenaw fault system west of Lake Gratiot, Keweenaw County, Michigan: Master's thesis, Michigan Technological University, doi: 10.37099/mtu.dc.etdr/1167.
- Mulder, J. A., Karlstrom, K. E., Fletcher, K., Heizler, M. T., Timmons, J. M., Crossey, L. J., Gehrels, G. E., and Pecha, M., 2017, The syn-orogenic sedimentary record of the Grenville Orogeny in southwest Laurentia: *Precambrian Research*, vol. 294, pp. 33–52, doi: 10.1016/j.precamres.2017.03.006.
- Müller, R. D., Royer, J.-Y., and Lawver, L. A., 1993, Revised plate motions relative to the hotspots from combined Atlantic and Indian Ocean hotspot tracks: *Geology*, vol. 21, p. 275, doi: 10.1130/0091-7613(1993)021<0275:rpmrtt>2.3.co;2.
- Muxworthy, A. R. and McClelland, E., 2000, The causes of low-temperature demagnetization of remanence in multidomain magnetite: *Geophysical Journal International*, vol. 140, pp. 115–131, doi: 10.1046/j.1365-246x.2000.00000.x.
- Nabavi, S. T. and Fossen, H., 2021, Fold geometry and folding – a review: *Earth-Science Reviews*, vol. 222, p. 103,812, doi: 10.1016/j.earscirev.2021.103812.
- Nagy, L., Williams, W., Muxworthy, A. R., Fabian, K., Almeida, T. P., Conbhui, P. Ó., and Shcherbakov, V. P., 2017, Stability of equidimensional pseudo-single-domain magnetite over billion-year timescales: *Proceedings of the National Academy of Sciences*, vol. 114, pp. 10,356–10,360, doi: 10.1073/pnas.1708344114.
- Nagy, L., Williams, W., and Tauxe, L., 2021, Estimating the effect of cooling rate on the acquisition of magnetic remanence: *Geophysical Research Letters*, vol. 48, doi: 10.1029/2021gl095284.
- Néel, L., 1955, Some theoretical aspects of rock-magnetism: *Advances in Physics*, vol. 4, pp. 191–243, doi: 10.1080/00018735500101204.
- Nicholson, S. W., Dicken, C. L., Foose, M. P., and Mueller, J., 2004, Integrated geologic map databases for the United States; the upper midwest states: Minnesota, Wisconsin, Michigan, Illinois, and Indiana: Tech. rep., US Geological Survey.
- Nimmo, F. and Schubert, G., 2015, Thermal and compositional evolution of the core: *Core Dynamics, Treatise on Geophysics*, pp. 217–241.
- Ohta, K. and Hirose, K., 2021, The thermal conductivity of the Earth's core and implications for its thermal and compositional evolution: *National Science Review*, vol. 8, doi: 10.1093/nsr/nwaa303.

- Ohta, K., Kuwayama, Y., Hirose, K., Shimizu, K., and Ohishi, Y., 2016, Experimental determination of the electrical resistivity of iron at Earth's core conditions: *Nature*, vol. 534, pp. 95–98, doi: 10.1038/nature17957.
- Ojakangas, R. W. and Dickas, A. B., 2002, The 1.1-Ga Midcontinent Rift System, central North America: sedimentology of two deep boreholes, Lake Superior region: *Sedimentary Geology*, vol. 147, pp. 13–36, doi: 10.1016/s0037-0738(01)00185-3.
- Ojakangas, R. W., Morey, G., and Green, J., 2001, The Mesoproterozoic Midcontinent Rift System, Lake Superior Region, USA: *Sedimentary Geology*, vol. 141-142, pp. 421–442, doi: 10.1016/s0037-0738(01)00085-9.
- Oliveira, A., Schmitz, M., Wall, C., and Hollanda, M., 2022, A bulk annealing and dissolution-based zircon concentration method for mafic rocks: *Chemical Geology*, p. 120817, doi: 10.1016/j.chemgeo.2022.120817.
- Olson, P., 2007, Gravitational dynamos and the low-frequency geomagnetic secular variation: *Proceedings of the National Academy of Sciences*, vol. 104, pp. 20,159–20,166, doi: 10.1073/pnas.0709081104.
- Olson, P. L., Coe, R. S., Driscoll, P. E., Glatzmaier, G. A., and Roberts, P. H., 2010, Geodynamo reversal frequency and heterogeneous core–mantle boundary heat flow: *Physics of the Earth and Planetary Interiors*, vol. 180, pp. 66–79, doi: 10.1016/j.pepi.2010.02.010.
- O'Rourke, J. G., Korenaga, J., and Stevenson, D. J., 2016, Thermal evolution of Earth with magnesium precipitation in the core: *Earth and Planetary Science Letters*, vol. 458, pp. 263–272, doi: 10.1016/j.epsl.2016.10.057.
- O'Rourke, J. G. and Stevenson, D. J., 2016, Powering Earth's dynamo with magnesium precipitation from the core: *Nature*, vol. 529, pp. 387–389, doi: 10.1038/nature16495.
- Özdemir, Ö. and Dunlop, D. J., 2006, Magnetic memory and coupling between spin-canted and defect magnetism in hematite: *Journal of Geophysical Research: Solid Earth*, vol. 111, doi: 10.1029/2006jb004555.
- Özdemir, Ö., Dunlop, D. J., and Moskowitz, B. M., 1993, The effect of oxidation on the Verwey transition in magnetite: *Geophysical Research Letters*, vol. 20, pp. 1671–1674, doi: 10.1029/93gl01483.
- Paces, J. B. and Miller, J., J.D., 1993, Precise U-Pb ages of Duluth Complex and related mafic intrusions, northeastern Minnesota: Geochronological insights to physical, petrogenetic, paleomagnetic, and tectonomagmatic processes associated with the 1.1 Ga Midcontinent Rift System: *Journal of Geophysical Research: Solid Earth*, vol. 98, pp. 13,997–14,013, doi: 10.1029/93jb01159.

- Palmer, H. and Davis, D., 1987, Paleomagnetism and U-Pb geochronology of volcanic rocks from Michipicoten Island, Lake Superior, Canada: precise calibration of the Keweenawan polar wander track: *Precambrian Research*, vol. 37, pp. 157–171, doi: 10.1016/0301-9268(87)90077-5.
- Palmer, H. C. and Halls, H. C., 1986, Paleomagnetism of the Powder Mill Group, Michigan and Wisconsin: A reassessment of the Logan Loop: *Journal of Geophysical Research*, vol. 91, p. 11,571, doi: 10.1029/jb091ib11p11571.
- Paterson, G. A., 2011, A simple test for the presence of multidomain behavior during paleointensity experiments: *Journal of Geophysical Research*, vol. 116, doi: 10.1029/2011jb008369.
- Paterson, G. A., Tauxe, L., Biggin, A. J., Shaar, R., and Jonestrask, L. C., 2014, On improving the selection of Thellier-type paleointensity data: *Geochemistry, Geophysics, Geosystems*, vol. 15, pp. 1180–1192, doi: 10.1002/2013gc005135.
- Paul, A. N., Spikings, R. A., and Gaynor, S. P., 2021, U-Pb ID-TIMS reference ages and initial Pb isotope compositions for Durango and Wilberforce apatites: *Chemical Geology*, vol. 586, p. 120,604, doi: 10.1016/j.chemgeo.2021.120604.
- Pavlis, T. L., Rutkofske, J., Guerrero, F., and Serpa, L. F., 2014, Structural overprinting of Mesozoic thrust systems in eastern California and its importance to reconstruction of Neogene extension in the southern Basin and Range: *Geosphere*, vol. 10, pp. 732–756, doi: 10.1130/ges00993.1.
- Pesonen, L. J. and Halls, H. C., 1983, Geomagnetic field intensity and reversal asymmetry in late Precambrian Keweenawan rocks: *Geophysical Journal International*, vol. 73, pp. 241–270, doi: 10.1111/j.1365-246x.1983.tb03816.x.
- Pesonen, L. J. and Nevanlinna, H., 1981, Late Precambrian Keweenawan asymmetric reversals: *Nature*, vol. 294, pp. 436–439, doi: 10.1038/294436a0.
- Petronis, M. S., Geissman, J. W., Holm, D. K., Wernicke, B., and Schauble, E., 2002, Assessing vertical axis rotations in large-magnitude extensional settings: A transect across the Death Valley extended terrane, California: *Journal of Geophysical Research: Solid Earth*, vol. 107, doi: 10.1029/2001jb000239.
- Pierce, J., Zhang, Y., Hodgin, E. B., and Swanson-Hysell, N. L., 2022, Quantifying inclination shallowing and representing flattening uncertainty in sedimentary paleomagnetic poles: *Geochemistry, Geophysics, Geosystems*, vol. 23, doi: 10.1029/2022gc010682.
- Piispa, E. J., Smirnov, A. V., Pesonen, L. J., and Mitchell, R. H., 2018, Paleomagnetism and geochemistry of ~1144-Ma lamprophyre dikes, northwestern Ontario: Implications for the North American polar wander and plate velocities: *Journal of Geophysical Research: Solid Earth*, doi: 10.1029/2018jb015992.

- Pozzo, M., Davies, C., Gubbins, D., and Alfè, D., 2012, Thermal and electrical conductivity of iron at Earth's core conditions: *Nature*, vol. 485, pp. 355–358, doi: 10.1038/nature11031.
- Pozzo, M., Davies, C. J., and Alfè, D., 2022, Towards reconciling experimental and computational determinations of Earth's core thermal conductivity: *Earth and Planetary Science Letters*, vol. 584, p. 117,466, doi: 10.1016/j.epsl.2022.117466.
- Pueyo, E., Parés, J., Millán, H., and Pocovi, A., 2003, Conical folds and apparent rotations in paleomagnetism (a case study in the Southern Pyrenees): *Tectonophysics*, vol. 362, pp. 345–366, doi: 10.1016/s0040-1951(02)00645-5.
- Pullaiah, G. and Irving, E., 1975, Paleomagnetism of the contact aureole and late dikes of the Otto Stock, Ontario, and its application to early Proterozoic apparent polar wandering: *Canadian Journal of Earth Sciences*, vol. 12, pp. 1609–1618, doi: 10.1139/e75-143.
- Pullaiah, G., Irving, E., Buchan, K., and Dunlop, D., 1975, Magnetization changes caused by burial and uplift: *Earth and Planetary Science Letters*, vol. 28, pp. 133–143, doi: 10.1016/0012-821x(75)90221-6.
- Reidel, S. P., Camp, V. E., Tolan, T. L., and Martin, B. S., 2013, The Columbia River flood basalt province: Stratigraphy, areal extent, volume, and physical volcanology: *In The Columbia River Flood Basalt Province*, Geological Society of America, doi: 10.1130/2013.2497(01).
- Remond, G., Cesbron, F., Chapoulie, R., Ohnenstetter, D., Roques-Carmes, C., and Schvoerer, M., 1992, Cathodoluminescence applied to the microcharacterization of mineral materials: a present status in experimentation and interpretation: *Scanning microscopy*, vol. 6, p. 2.
- Renik, B. and Christie-Blick, N., 2013, A new hypothesis for the amount and distribution of dextral displacement along the Fish Lake Valley-northern Death Valley-Furnace Creek fault zone, California-Nevada: *Tectonics*, vol. 32, pp. 123–145, doi: 10.1029/2012tc003170.
- Riisager, P. and Riisager, J., 2001, Detecting multidomain magnetic grains in Thellier palaeointensity experiments: *Physics of the Earth and Planetary Interiors*, vol. 125, pp. 111–117, doi: 10.1016/s0031-9201(01)00236-9.
- Rivers, T., 2008, Assembly and preservation of lower, mid, and upper orogenic crust in the Grenville Province—Implications for the evolution of large hot long-duration orogens: *Precambrian Research*, vol. 167, pp. 237–259, doi: 10.1016/j.precamres.2008.08.005.
- Rivers, T., 2012, Upper-crustal orogenic lid and mid-crustal core complexes: signature of a collapsed orogenic plateau in the hinterland of the Grenville Province: *Canadian Journal of Earth Sciences*, vol. 49, pp. 1–42, doi: 10.1139/e11-014.

- Rivers, T., 2015, Tectonic setting and evolution of the Grenville orogen: An assessment of progress over the last 40 years: *Geoscience Canada*, vol. 42, pp. 77–124, doi: 10.12789/geocanj.2014.41.057.
- Rivers, T., Culshaw, N., Hynes, A., Indares, A., Jamieson, R., Martignole, J., Percival, J., Cook, F., and Clowes, R., 2012, The Grenville Orogen—a post-LITHOPROBE perspective: tectonic styles in Canada: The lithoprobe perspective, vol. 49, pp. 97–236.
- Rivers, T. and Volkert, R. A., 2023, Slow cooling in the metamorphic cores of Grenvillian large metamorphic core complexes and the thermal signature of the Ottawan orogenic lid: *In Laurentia: Turning Points in the Evolution of a Continent*, Geological Society of America, doi: 10.1130/2022.1220(16).
- Rose, I. R., Zhang, Y., and Swanson-Hysell, N. L., 2022, Bayesian paleomagnetic Euler pole inversion for paleogeographic reconstruction and analysis: *Journal of Geophysical Research: Solid Earth*, doi: 10.1029/2021jb023890.
- Roy, J. L. and Robertson, W. A., 1978, Paleomagnetism of the Jacobsville Formation and the apparent polar path for the interval -1100 to -670 m.y. for North America: *Journal of Geophysical Research*, vol. 83, p. 1289, doi: 10.1029/jb083ib03p01289.
- Rubatto, D., 2002, Zircon trace element geochemistry: partitioning with garnet and the link between U–Pb ages and metamorphism: *Chemical Geology*, vol. 184, pp. 123–138, doi: 10.1016/s0009-2541(01)00355-2.
- Salminen, J., Klein, R., Veikkolainen, T., Mertanen, S., and Mänttäri, I., 2017, Mesoproterozoic geomagnetic reversal asymmetry in light of new paleomagnetic and geochronological data for the Häme dyke swarm, Finland: Implications for the Nuna supercontinent: *Precambrian Research*, vol. 288, pp. 1–22, doi: 10.1016/j.precamres.2016.11.003.
- Sapienza, F., Gallo, L. C., Zhang, Y., Vaes, B., Domeier, M., and Swanson-Hysell, N. L., 2023, Quantitative analysis of paleomagnetic sampling strategies: *Journal of Geophysical Research: Solid Earth*, doi: 10.1029/2023jb027211.
- Schaltegger, U., Fanning, C. M., Günther, D., Maurin, J. C., Schulmann, K., and Gebauer, D., 1999, Growth, annealing and recrystallization of zircon and preservation of monazite in high-grade metamorphism: conventional and in-situ U–Pb isotope, cathodoluminescence and microchemical evidence: *Contributions to Mineralogy and Petrology*, vol. 134, pp. 186–201, doi: 10.1007/s004100050478.
- Schmitz, M. D., Bowring, S. A., and Ireland, T. R., 2003, Evaluation of Duluth Complex anorthositic series (AS3) zircon as a U–Pb geochronological standard: new high-precision isotope dilution thermal ionization mass spectrometry results: *Geochimica et Cosmochimica Acta*, vol. 67, pp. 3665–3672, doi: 10.1016/s0016-7037(03)00200-x.

- Schmitz, M. D. and Schoene, B., 2007, Derivation of isotope ratios, errors, and error correlations for U-Pb geochronology using  $^{205}\text{Pb}$ - $^{235}\text{U}$ - $(^{233}\text{U})$ -spiked isotope dilution thermal ionization mass spectrometric data: *Geochem. Geophys. Geosyst.*, vol. 8, p. Q08,006, doi: 10.1029/2006GC001492.
- Schoene, B., Crowley, J. L., Condon, D. J., Schmitz, M. D., and Bowring, S. A., 2006, Reassessing the uranium decay constants for geochronology using ID-TIMS U-Pb data: *Geochimica et Cosmochimica Acta*, vol. 70, pp. 426–445, doi: 10.1016/j.gca.2005.09.007.
- Sears, J. W., 1973, Structural geology of the Precambrian Grand Canyon series, Arizona: Ph.D. thesis, University of Wyoming.
- Sears, J. W., 1990, Geologic structure of the the Grand Canyon Supergroup: In Beus, S. and Morales, M., eds., *Grand Canyon Geology*, Oxford University Press.
- Sears, J. W., 2022, Challenging the dipolar paradigm for Proterozoic Earth, Geological Society of America, pp. 201–211: doi: 10.1130/2021.2553(17).
- Self, S., Jay, A., Widdowson, M., and Keszthelyi, L., 2008, Correlation of the Deccan and Rajahmundry Trap lavas: Are these the longest and largest lava flows on Earth?: *Journal of Volcanology and Geothermal Research*, vol. 172, pp. 3–19, doi: 10.1016/j.jvolgeores.2006.11.012.
- Selkin, P., Gee, J., Meurer, W., and Hemming, S., 2008, Paleointensity record from the 2.7 Ga Stillwater Complex, Montana: *Geochemistry, Geophysics, Geosystems*, vol. 9, doi: 10.1029/2008gc001950.
- Selkin, P., Gee, J., and Tauxe, L., 2007, Nonlinear thermoremanence acquisition and implications for paleointensity data: *Earth and Planetary Science Letters*, vol. 256, pp. 81–89, doi: 10.1016/j.epsl.2007.01.017.
- Selkin, P., Gee, J., Tauxe, L., Meurer, W., and Newell, A., 2000, The effect of remanence anisotropy on paleointensity estimates: a case study from the Archean Stillwater Complex: *Earth and Planetary Science Letters*, vol. 183, pp. 403–416, doi: 10.1016/s0012-821x(00)00292-2.
- Serpa, L. and Pavlis, T. L., 1996, Three-dimensional model of the late Cenozoic history of the Death Valley region, southeastern California: *Tectonics*, vol. 15, pp. 1113–1128, doi: 10.1029/96tc01633.
- Shaar, R. and Tauxe, L., 2013, Thellier GUI: An integrated tool for analyzing paleointensity data from Thellier-type experiments: *Geochemistry, Geophysics, Geosystems*, vol. 14, pp. 677–692, doi: 10.1002/ggge.20062.
- Shank, S. G., 1989, The petrology of the Beaver Bay Complex near Silver Bay, northeastern Minnesota: Master's thesis, University of Minnesota.

- Shcherbakova, V. V., Bakhmutov, V. G., Thallner, D., Shcherbakov, V. P., Zhidkov, G. V., and Biggin, A. J., 2019, Ultra-low palaeointensities from East European Craton, Ukraine support a globally anomalous palaeomagnetic field in the Ediacaran: *Geophysical Journal International*, vol. 220, pp. 1928–1946, doi: 10.1093/gji/ggz566.
- Shcherbakova, V. V., Biggin, A. J., Veselovskiy, R. V., Shatsillo, A. V., Hawkins, L. M. A., Shcherbakov, V. P., and Zhidkov, G. V., 2017, Was the Devonian geomagnetic field dipolar or multipolar? Palaeointensity studies of Devonian igneous rocks from the Minusa Basin (Siberia) and the Kola Peninsula dykes, Russia: *Geophysical Journal International*, vol. 209, pp. 1265–1286, doi: 10.1093/gji/ggx085.
- Shcherbakova, V. V., Pasenko, A. M., Zhidkov, G. V., Shcherbakov, V. P., and Aphnogenova, N. A., 2023, An ultralow geomagnetic field intensity in the Mesoproterozoic based on studies of 1380 Ma old intrusive bodies from the Udzha aulacogen of the Siberian Platform: *Izvestiya, Physics of the Solid Earth*, vol. 59, pp. 682–703, doi: 10.1134/s1069351323050105.
- Shcherbakova, V. V., Vodovozov, V. Y., Zhidkov, G. V., Aphnogenova, N. A., Sal'naya, N. V., and Leichenkov, G. L., 2022, Ultra-low geomagnetic field intensity in the Mesoproterozoic based on the dike complex rocks of the Bunger Oasis (1133 Ma, east Antarctica): *Izvestiya, Physics of the Solid Earth*, vol. 58, pp. 859–881, doi: 10.1134/s106935132206012x.
- Shcherbakova, V. V., Zhidkov, G. V., Shcherbakov, V. P., Golovanova, I. V., Danukalov, K. N., and Salmanova, R. Y., 2021, Ultra-low geomagnetic field intensity in the Devonian obtained from the southern Ural rock studies: *Izvestiya, Physics of the Solid Earth*, vol. 57, pp. 900–912, doi: 10.1134/s1069351321060070.
- Shinevar, W. J., Jagoutz, O., and VanTongeren, J. A., 2021, Gore Mountain garnet amphibolite records UHT conditions: implications for the rheology of the lower continental crust during orogenesis: *Journal of Petrology*, vol. 62, doi: 10.1093/petrology/egab007.
- Shride, A. F., 1967, Younger Precambrian geology in southern Arizona: doi: 10.3133/pp566.
- Slotznick, S. P., Swanson-Hysell, N. L., Zhang, Y., Clayton, K. E., Wellman, C. H., Tosca, N. J., and Strother, P. K., 2023, Reconstructing the paleoenvironment of an oxygenated Mesoproterozoic shoreline and its record of life: *GSA Bulletin*, doi: 10.1130/B36634.1.
- Snow, J. K., 2000, Cenozoic tectonism in the central Basin and Range: magnitude, rate, and distribution of upper crustal strain: *American Journal of Science*, vol. 300, pp. 659–719, doi: 10.2475/ajs.300.9.659.
- Snow, J. K., Asmerom, Y., and Lux, D. R., 1991, Permian-Triassic plutonism and tectonics, Death Valley region, California and Nevada: *Geology*, vol. 19, p. 629, doi: 10.1130/0091-7613(1991)019<0629:ptpatd>2.3.co;2.

- Snow, J. K. and Wernicke, B., 1989, Uniqueness of geological correlations: An example from the Death Valley extended terrain: Geological Society of America Bulletin, vol. 101, pp. 1351–1362, doi: 10.1130/0016-7606(1989)101<1351:uogcae>2.3.co;2.
- Sprain, C. J., Swanson-Hysell, N. L., Fairchild, L. M., and Gaastra, K., 2018, A field like today's? The strength of the geomagnetic field 1.1 billion years ago: Geophysical Journal International, vol. 213, pp. 1969–1983, doi: 10.1093/gji/ggy074.
- Staal, C. V. and Zagorevski, A., 2020, Accretion, soft and hard collision: similarities, differences and an application from the Newfoundland Appalachian orogen: Geoscience Canada, vol. 47, pp. 103–118, doi: 10.12789/geocanj.2020.47.161.
- Stacey, F. and Loper, D., 2007, A revised estimate of the conductivity of iron alloy at high pressure and implications for the core energy balance: Physics of the Earth and Planetary Interiors, vol. 161, pp. 13–18, doi: 10.1016/j.pepi.2006.12.001.
- Steiner, M. B., 1983, Detrital remanent magnetization in hematite: Journal of Geophysical Research, vol. 88, p. 6523, doi: 10.1029/jb088ib08p06523.
- Steiner, M. B., 2003, A cratonic Middle Jurassic paleopole: Callovian-Oxfordian stillstand (J-2 cusp), rotation of the Colorado Plateau, and Jurassic North American apparent polar wander: Tectonics, vol. 22, doi: 10.1029/2001tc001284.
- Stevens, C. H., Stone, P., Dunne, G. C., Greene, D. C., Walker, J. D., and Swanson, B. J., 1997, Paleozoic and Mesozoic evolution of east-central California: International Geology Review, vol. 39, pp. 788–829, doi: 10.1080/00206819709465303.
- Stevenson, G. M. and Beus, S. S., 1982, Stratigraphy and depositional setting of the upper Precambrian Dox Formation in Grand Canyon: Geological Society of America Bulletin, vol. 93, p. 163, doi: 10.1130/0016-7606(1982)93<163:sadsot>2.0.co;2.
- Stewart, E. K., Grauch, V., Woodruff, L., and Heller, S., 2018, Seismic stratigraphy of the 1.1 Ga Midcontinent Rift beneath western Lake Superior Part II: Evolution of rift-fill through time: *In* GSA Annual Meeting in Indianapolis, Indiana, USA-2018, GSA.
- Stewart, J. H., 1983, Extensional tectonics in the Death Valley area, California: Transport of the Panamint Range structural block 80 km northwestward: Geology, vol. 11, p. 153, doi: 10.1130/0091-7613(1983)11<153:etitdv>2.0.co;2.
- Strickland, A., Wooden, J. L., Mattinson, C. G., Ushikubo, T., Miller, D. M., and Valley, J. W., 2013, Proterozoic evolution of the Mojave crustal province as preserved in the Ivanpah Mountains, southeastern California: Precambrian Research, vol. 224, pp. 222–241, doi: 10.1016/j.precamres.2012.09.006.

- Sun, S.-S. and McDonough, W. F., 1989, Chemical and isotopic systematics of oceanic basalts: implications for mantle composition and processes: Geological Society, London, Special Publications, vol. 42, pp. 313–345, doi: 10.1144/gsl.sp.1989.042.01.19.
- Swanson-Hysell, N. L., 2021, The Precambrian paleogeography of Laurentia: *In* Ancient Supercontinents and the Paleogeography of Earth, Elsevier, pp. 109–153, doi: 10.1016/b978-0-12-818533-9.00009-6.
- Swanson-Hysell, N. L., Avery, M. S., Zhang, Y., Hodgin, E. B., Sherwood, R. J., Apen, F. E., Boerboom, T. J., Keller, B. C., and Cottle, J. M., 2021a, The paleogeography of Laurentia in its early years: new constraints from the Paleoproterozoic East-Central Minnesota batholith: *Tectonics*, doi: 10.1029/2021tc006751.
- Swanson-Hysell, N. L., Burgess, S. D., Maloof, A. C., and Bowring, S. A., 2014a, Magmatic activity and plate motion during the latent stage of Midcontinent Rift development: *Geology*, vol. 42, pp. 475–478, doi: 10.1130/g35271.1.
- Swanson-Hysell, N. L., Fairchild, L. M., and Slotznick, S. P., 2019a, Primary and secondary red bed magnetization constrained by fluvial intraclasts: *Journal of Geophysical Research: Solid Earth*, vol. 124, pp. 4276–4289, doi: 10.1029/2018jb017067.
- Swanson-Hysell, N. L., Feinberg, J. M., Berquó, T. S., and Maloof, A. C., 2011, Self-reversed magnetization held by martite in basalt flows from the 1.1-billion-year-old Keweenawan rift, Canada: *Earth and Planetary Science Letters*, vol. 305, pp. 171–184, doi: 10.1016/j.epsl.2011.02.053.
- Swanson-Hysell, N. L., Hoaglund, S. A., Crowley, J. L., Schmitz, M. D., Zhang, Y., and Miller, J. D., 2021b, Rapid emplacement of massive Duluth Complex intrusions within the North American Midcontinent Rift: *Geology*, doi: 10.1130/g47873.1.
- Swanson-Hysell, N. L., Maloof, A. C., Weiss, B. P., and Evans, D. A. D., 2009, No asymmetry in geomagnetic reversals recorded by 1.1-billion-year-old Keweenawan basalts: *Nature Geoscience*, vol. 2, pp. 713–717, doi: 10.1038/ngeo622.
- Swanson-Hysell, N. L., Ramezani, J., Fairchild, L. M., and Rose, I. R., 2019b, Failed rifting and fast drifting: Midcontinent Rift development, Laurentia's rapid motion and the driver of Grenvillian orogenesis: *GSA Bulletin*, vol. 131, pp. 913–940, doi: 10.1130/b31944.1.
- Swanson-Hysell, N. L., Rivers, T., and van der Lee, S., 2023, The late Mesoproterozoic to early Neoproterozoic Grenvillian orogeny and the assembly of Rodinia: Turning point in the tectonic evolution of Laurentia: *In* Laurentia: Turning Points in the Evolution of a Continent, Geological Society of America, doi: 10.1130/2022.1220(14).
- Swanson-Hysell, N. L., Vaughan, A. A., Mustain, M. R., and Asp, K. E., 2014b, Confirmation of progressive plate motion during the Midcontinent Rift's early magmatic stage from the

- Osler Volcanic Group, Ontario, Canada: Geochemistry, Geophysics, Geosystems, vol. 15, pp. 2039–2047, doi: 10.1002/2013gc005180.
- Tan, E., Gurnis, M., and Han, L., 2002, Slabs in the lower mantle and their modulation of plume formation: *Geochemistry, Geophysics, Geosystems*, vol. 3, pp. 1–24, doi: 10.1029/2001gc000238.
- Tapani Rämö, O. and Calzia, J. P., 1998, Nd isotopic composition of cratonic rocks in the southern Death Valley region: Evidence for a substantial Archean source component in Mojavia: *Geology*, vol. 26, p. 891, doi: 10.1130/0091-7613(1998)026<0891:nicocr>2.3.co;2.
- Tarduno, J. A., Blackman, E. G., and Mamajek, E. E., 2014, Detecting the oldest geodynamo and attendant shielding from the solar wind: Implications for habitability: *Physics of the Earth and Planetary Interiors*, vol. 233, pp. 68–87, doi: 10.1016/j.pepi.2014.05.007.
- Tarduno, J. A. and Cottrell, R. D., 2005, Dipole strength and variation of the time-averaged reversing and nonreversing geodynamo based on Thellier analyses of single plagioclase crystals: *Journal of Geophysical Research: Solid Earth*, doi: 10.1029/2005jb003970.
- Tarduno, J. A., Cottrell, R. D., Davis, W. J., Nimmo, F., and Bono, R. K., 2015, A Hadean to Paleoarchean geodynamo recorded by single zircon crystals: *Science*, vol. 349, pp. 521–524, doi: 10.1126/science.aaa9114.
- Tarduno, J. A., Cottrell, R. D., and Smirnov, A. V., 2006, The paleomagnetism of single silicate crystals: Recording geomagnetic field strength during mixed polarity intervals, superchrons, and inner core growth: *Reviews of Geophysics*, vol. 44, doi: 10.1029/2005rg000189.
- Tauxe, L., 1993, Sedimentary records of relative paleointensity of the geomagnetic field: Theory and practice: *Reviews of Geophysics*, vol. 31, pp. 319–354, doi: 10.1029/93rg01771.
- Tauxe, L., 2005, Inclination flattening and the geocentric axial dipole hypothesis: *Earth and Planetary Science Letters*, vol. 233, pp. 247–261, doi: 10.1016/j.epsl.2005.01.027.
- Tauxe, L. and Kent, D. V., 1984, Properties of a detrital remanence carried by haematite from study of modern river deposits and laboratory redeposition experiments: *Geophysical Journal International*, vol. 76, pp. 543–561, doi: 10.1111/j.1365-246x.1984.tb01909.x.
- Tauxe, L. and Kent, D. V., 2004, A simplified statistical model for the geomagnetic field and the detection of shallow bias in paleomagnetic inclinations: was the ancient magnetic field dipolar?: *Geophysical Monograph Series*, pp. 101–115, doi: 10.1029/145gm08.
- Tauxe, L., Kent, D. V., and Opdyke, N. D., 1980, Magnetic components contributing to the NRM of Middle Siwalik red beds: *Earth and Planetary Science Letters*, vol. 47, pp. 279–284, doi: 10.1016/0012-821x(80)90044-8.

- Tauxe, L. and Kodama, K. P., 2009, Paleosecular variation models for ancient times: Clues from Keweenawan lava flows: *Physics of the Earth and Planetary Interiors*, vol. 177, pp. 31–45, doi: 10.1016/j.pepi.2009.07.006.
- Tauxe, L., Kylstra, N., and Constable, C., 1991, Bootstrap statistics for paleomagnetic data: *Journal of Geophysical Research*, vol. 96, p. 11,723, doi: 10.1029/91jb00572.
- Tauxe, L., Santos, C., Cych, B., Zhao, X., Roberts, A., Nagy, L., and Williams, W., 2020, Understanding nonideal paleointensity recording in igneous rocks: insights from aging experiments on lava samples and the causes and consequences of “fragile” curvature in Arai plots: *Geochemistry, Geophysics, Geosystems*, vol. 22, doi: 10.1029/2020gc009423.
- Tauxe, L., Shaar, R., Jonestrask, L., Swanson-Hysell, N. L., Minnett, R., Koppers, A. A. P., Constable, C. G., Jarboe, N., Gaastra, K., and Fairchild, L., 2016, PmagPy: Software package for paleomagnetic data analysis and a bridge to the Magnetics Information Consortium (MagIC) Database: *Geochemistry, Geophysics, Geosystems*, vol. 17, pp. 2450–2463, doi: 10.1002/2016gc006307.
- Tauxe, L. and Staudigel, H., 2004, Strength of the geomagnetic field in the Cretaceous Normal Superchron: New data from submarine basaltic glass of the Troodos Ophiolite: *Geochemistry, Geophysics, Geosystems*, vol. 5, doi: 10.1029/2003gc000635.
- Tauxe, L. and Watson, G., 1994, The fold test: an eigen analysis approach: *Earth and Planetary Science Letters*, vol. 122, pp. 331–341, doi: 10.1016/0012-821x(94)90006-x.
- Thallner, D., Biggin, A. J., and Halls, H. C., 2021a, An extended period of extremely weak geomagnetic field suggested by palaeointensities from the Ediacaran Grenville dykes (SE Canada): *Earth and Planetary Science Letters*, vol. 568, p. 117,025, doi: 10.1016/j.epsl.2021.117025.
- Thallner, D., Biggin, A. J., McCausland, P. J. A., and Fu, R. R., 2021b, New paleointensities from the Skinner Cove Formation, Newfoundland, suggest a changing state of the geomagnetic field at the Ediacaran-Cambrian transition: *Journal of Geophysical Research: Solid Earth*, doi: 10.1029/2021jb022292.
- Thellier, O., E.; Thellier, 1959, Sur l’intensité du champ magnétique terrestre dans le passé historique et géologique: *Annales de Geophysique*, vol. 15, pp. 285–378.
- Thwaites, F. T., 1912, Sandstones of the Wisconsin coast of Lake Superior, vol. 8: Wisconsin Geological and Natural History Survey.
- Timmons, J. M., Bloch, J., Fletcher, K., Karlstrom, K. E., Heizler, M., and Crossey, L. J., 2012, The Grand Canyon Unkar Group: Mesoproterozoic basin formation in the continental interior during supercontinent assembly: *In Grand Canyon Geology: Two Billion Years of Earth's History*, Geological Society of America, doi: 10.1130/2012.2489(02).

- Timmons, J. M., Karlstrom, K. E., Dehler, C. M., Geissman, J. W., and Heizler, M. T., 2001, Proterozoic multistage (ca. 1.1 and 0.8 Ga) extension recorded in the Grand Canyon Supergroup and establishment of northwest- and north-trending tectonic grains in the southwestern United States: Geological Society of America Bulletin, vol. 113, p. 0163, doi: 10.1130/0016-7606(2001)113<0163:pmcage>2.0.co;2.
- Timmons, J. M., Karlstrom, K. E., Heizler, M. T., Bowring, S. A., Gehrels, G. E., and Crossey, L. J., 2005, Tectonic inferences from the ca. 1255–1100 Ma Unkar Group and Nankoweap Formation, Grand Canyon: Intracratonic deformation and basin formation during protracted Grenville orogenesis: Geological Society of America Bulletin, vol. 117, p. 1573, doi: 10.1130/b25538.1.
- Torsvik, T. H., Van der Voo, R., Preeden, U., Mac Niocaill, C., Steinberger, B., Doubrovine, P. V., van Hinsbergen, D. J., Domeier, M., Gaina, C., Tohver, E., and et al., 2012, Phanerozoic polar wander, palaeogeography and dynamics: Earth-Science Reviews, vol. 114, pp. 325–368, doi: 10.1016/j.earscirev.2012.06.007.
- Turlin, F., Vanderhaeghe, O., Gervais, F., André-Mayer, A.-S., Moukhsil, A., Zeh, A., Soldadi, F., and I.P.T.N., 2019, Petrogenesis of LREE-rich pegmatitic granite dykes in the central Grenville Province by partial melting of Paleoproterozoic-Archean metasedimentary rocks: Evidence from zircon U-Pb-Hf-O isotope and trace element analyses: Precambrian Research, vol. 327, pp. 327–360, doi: 10.1016/j.precamres.2019.02.009.
- Tyrrell, C., 2019, Keweenaw fault geometry and slip kinematics-Bête Grise Bay, Keweenaw Peninsula, Michigan: Master's thesis, Michigan Technological University, doi: 10.37099/mtu.dc.etdr/947.
- Ullman, D. J., Carlson, A. E., LeGrande, A. N., Anslow, F. S., Moore, A. K., Caffee, M., Syverson, K. M., and Licciardi, J. M., 2015, Southern Laurentide ice-sheet retreat synchronous with rising boreal summer insolation: Geology, vol. 43, pp. 23–26, doi: 10.1130/g36179.1.
- Unsworth, J. and Duarte, F. J., 1979, Heat diffusion in a solid sphere and Fourier theory: An elementary practical example: American Journal of Physics, vol. 47, pp. 981–983, doi: 10.1119/1.11601.
- Vaes, B., Li, S., Langereis, C. G., and van Hinsbergen, D. J. J., 2021, Reliability of palaeomagnetic poles from sedimentary rocks: Geophysical Journal International, vol. 225, pp. 1281–1303, doi: 10.1093/gji/ggab016.
- Vaes, B., van Hinsbergen, D. J., van de Lagemaat, S. H., van der Wiel, E., Lom, N., Advokaat, E. L., Boschman, L. M., Gallo, L. C., Greve, A., Guilmette, C., Li, S., Lippert, P. C., Montheil, L., Qayyum, A., and Langereis, C. G., 2023, A global apparent polar wander path for the last 320 Ma calculated from site-level paleomagnetic data: Earth-Science Reviews, p. 104547, doi: 10.1016/j.earscirev.2023.104547.

- Valet, J.-P. and Herrero-Bervera, E., 2011, Time-averaged and mean axial dipole field, Springer Netherlands, pp. 131–137: doi: 10.1007/978-94-007-0323-0\_9.
- Van Andel, S. I. and Hospers, J., 1966, Systematic errors in the palaeomagnetic inclination of sedimentary rocks: *Nature*, vol. 212, pp. 891–893, doi: 10.1038/212891a0.
- van Hinsbergen, D. J. J., 2022, Indian plate paleogeography, subduction and horizontal underthrusting below Tibet: paradoxes, controversies and opportunities: *National Science Review*, vol. 9, doi: 10.1093/nsr/nwac074.
- van Hinsbergen, D. J. J., Steinberger, B., Doubrovine, P. V., and Gassmöller, R., 2011, Acceleration and deceleration of India-Asia convergence since the Cretaceous: Roles of mantle plumes and continental collision: *Journal of Geophysical Research*, vol. 116, doi: 10.1029/2010jb008051.
- Veikkolainen, T., Pesonen, L., and Korhonen, K., 2014a, An analysis of geomagnetic field reversals supports the validity of the Geocentric Axial Dipole (GAD) hypothesis in the Precambrian: *Precambrian Research*, vol. 244, pp. 33–41, doi: 10.1016/j.precamres.2013.10.009.
- Veikkolainen, T. and Pesonen, L. J., 2021, Precambrian geomagnetic field—an overview, Elsevier, pp. 81–108: doi: 10.1016/b978-0-12-818533-9.00008-4.
- Veikkolainen, T., Pesonen, L. J., and Evans, D. A. D., 2014b, PALEOMAGIA: A PHP/MYSQL database of the Precambrian paleomagnetic data: *Studia Geophysica et Geodaetica*, vol. 58, pp. 425–441, doi: 10.1007/s11200-013-0382-0.
- Vervoort, J. D., Wirth, K., Kennedy, B., Sandland, T., and Harpp, K. S., 2007, The magmatic evolution of the Midcontinent rift: New geochronologic and geochemical evidence from felsic magmatism: *Precambrian Research*, vol. 157, pp. 235–268, doi: 10.1016/j.precamres.2007.02.019.
- Verwey, E. J. W., 1939, Electronic conduction of magnetite ( $\text{Fe}_3\text{O}_4$ ) and its transition point at low temperatures: *Nature*, vol. 144, pp. 327–328, doi: 10.1038/144327b0.
- Walcott, C. D., 1883, Pre-Carboniferous strata in the Grand Canyon of the Colorado, Arizona: *American Journal of Science*, vol. s3-26, pp. 437–442, doi: 10.2475/ajs.s3-26.156.437.
- Wallace, D. M. I., 1971, The sedimentology and tectonic significance of the Bayfield Group (Upper Keweenawan?), Wisconsin and Minnesota: Ph.D. thesis, The University of Wisconsin-Madison.
- Warnock, A. C., Kodama, K. P., and Zeitler, P. K., 2000, Using thermochronometry and low-temperature demagnetization to accurately date Precambrian paleomagnetic poles: *Journal of Geophysical Research: Solid Earth*, vol. 105, pp. 19,435–19,453, doi: 10.1029/2000jb900114.

- Wasserburg, G. J., Albee, A. L., and Lanphere, M. A., 1964, Migration of radiogenic strontium during metamorphism: *Journal of Geophysical Research*, vol. 69, pp. 4395–4401, doi: 10.1029/jz069i020p04395.
- Wasserburg, G. J., Wetherill, G. W., and Wright, L. A., 1959, Ages in the Precambrian terrane of Death Valley, California: *The Journal of Geology*, vol. 67, pp. 702–708, doi: 10.1086/626628.
- Watson, E. B., Wark, D. A., and Thomas, J. B., 2006, Crystallization thermometers for zircon and rutile: *Contributions to Mineralogy and Petrology*, vol. 151, pp. 413–433, doi: 10.1007/s00410-006-0068-5.
- Watson, G. S., 1956, A test for randomness of directions: *Geophysical Journal International*, vol. 7, pp. 160–161, doi: 10.1111/j.1365-246x.1956.tb05561.x.
- Weil, A. B., der Voo, R. V., Niocaill, C. M., and Meert, J. G., 1998, The Proterozoic supercontinent Rodinia: paleomagnetically derived reconstructions for 1100 to 800 Ma: *Earth and Planetary Science Letters*, vol. 154, pp. 13–24, doi: 10.1016/s0012-821x(97)00127-1.
- Weil, A. B., Geissman, J. W., and Ashby, J. M., 2006, A new paleomagnetic pole for the Neoproterozoic Uinta Mountain supergroup, Central Rocky Mountain States, USA: *Precambrian Research*, vol. 147, pp. 234–259, doi: 10.1016/j.precamres.2006.01.017.
- Weil, A. B., Geissman, J. W., Heizler, M., and Van der Voo, R., 2003, Paleomagnetism of Middle Proterozoic mafic intrusions and Upper Proterozoic (Nankoweap) red beds from the Lower Grand Canyon Supergroup, Arizona: *Tectonophysics*, vol. 375, pp. 199–220, doi: 10.1016/s0040-1951(03)00339-1.
- Wenk, H.-R., Chen, K., and Smith, R., 2011, Morphology and microstructure of magnetite and ilmenite inclusions in plagioclase from Adirondack anorthositic gneiss: *American Mineralogist*, vol. 96, pp. 1316–1324, doi: 10.2138/am.2011.3760.
- Wernicke, B., Axen, G. J., and Snow, J. K., 1988, Basin and Range extensional tectonics at the latitude of Las Vegas, Nevada: *Geological Society of America Bulletin*, vol. 100, pp. 1738–1757, doi: 10.1130/0016-7606(1988)100<1738:bareta>2.3.co;2.
- White, W., 1960, The Keweenawan lavas of Lake Superior, an example of flood basalts: *American Journal of Science*, vol. 258, pp. 367–374.
- Whitmeyer, S., 2007, Tectonic model for the Proterozoic growth of North America: *Geosphere*, vol. 3, p. 220, doi: 10.1130/ges00055.1.
- Williams, Q., 2018, The thermal conductivity of Earth's core: a key geophysical parameter's constraints and uncertainties: *Annual Review of Earth and Planetary Sciences*, vol. 46, pp. 47–66, doi: 10.1146/annurev-earth-082517-010154.

- Williams, W., Evans, M. E., and Krása, D., 2010, Micromagnetics of paleomagnetically significant mineral grains with complex morphology: *Geochemistry, Geophysics, Geosystems*, vol. 11, doi: 10.1029/2009gc002828.
- Woodcock, N. H., 2004, Life span and fate of basins: *Geology*, vol. 32, p. 685, doi: 10.1130/g20598.1.
- Woodward, L. A., Anderson, O. J., and Lucas, S. G., 1997, Mesozoic stratigraphic constraints on Laramide right slip on the east side of the Colorado Plateau: *Geology*, vol. 25, p. 843, doi: 10.1130/0091-7613(1997)025<0843:mscolr>2.3.co;2.
- Workman, J. B., Menges, C. M., Page, W. R., Taylor, E. M., Eken, E. B., Rowley, P. D., Dixon, G. L., Thompson, R. A., and Wright, L. A., 2003, Geologic map of the Death Valley ground-water model area, Nevada and California: Tech. rep., United States Geological Survey-Nevada, doi: 10.2172/809981.
- Wright, L., 1976, Late Cenozoic fault patterns and stress fields in the Great Basin and westward displacement of the Sierra Nevada block: *Geology*, vol. 4, p. 489, doi: 10.1130/0091-7613(1976)4<489:lcfpas>2.0.co;2.
- Wright, L. and Troxel, B., 1967, Limitations on right-lateral, strike-slip displacement, Death Valley and Furnace Creek fault zones, California: *Geological Society of America Bulletin*, vol. 78, p. 933, doi: 10.1130/0016-7606(1967)78[933:lorsdd]2.0.co;2.
- Wright, L. and Troxel, B., 1968, Talc deposits of the Southern Death Valley-Kingston Range Region, California: Division of Mines and Geology.
- Wright, L., Troxel, B., Williams, E., Roberts, M., and Diehl, P., 1974, Precambrian sedimentary environments of the Death Valley region, eastern California: Geologic features of Death Valley, California: California Division of Mines and Geology Special Report, vol. 106, pp. 7–15.
- Wrucke, C., 1966, Precambrian and Permian rocks in the vicinity of Warm Spring Canyon, Panamint Range, California.: Ph.D. thesis, Stanford University.
- Wrucke, C. and Shride, A., 1972, Correlation of Precambrian diabase in Arizona and southern California: *In Geological Society of America Abstracts with Programs*, vol. 4, pp. 265–266.
- Wrucke, C., Stone, P., and Stevens, C., 2007, Geologic Map of the Warm Spring Canyon Area, Death Valley National Park, Inyo County, California, with a discussion of the regional significance of the stratigraphy and structure: Tech. rep., Geological Survey (US).
- Xu, S. and Dunlop, D. J., 2004, Thellier paleointensity theory and experiments for multidomain grains: *Journal of Geophysical Research: Solid Earth*, vol. 109, doi: 10.1029/2004jb003024.

- Yonkee, W. A. and Weil, A. B., 2015, Tectonic evolution of the Sevier and Laramide belts within the North American Cordillera orogenic system: *Earth-Science Reviews*, vol. 150, pp. 531–593, doi: 10.1016/j.earscirev.2015.08.001.
- Yu, Y., 2003, On partial thermoremanent magnetization tail checks in Thellier paleointensity determination: *Journal of Geophysical Research*, vol. 108, doi: 10.1029/2003jb002420.
- Yu, Y. and Tauxe, L., 2006, Effect of multi-cycle heat treatment and pre-history dependence on partial thermoremanence (pTRM) and pTRM tails: *Physics of the Earth and Planetary Interiors*, vol. 157, pp. 196–207, doi: 10.1016/j.pepi.2006.04.006.
- Yu, Y., Tauxe, L., and Genevey, A., 2004, Toward an optimal geomagnetic field intensity determination technique: *Geochemistry, Geophysics, Geosystems*, vol. 5, doi: 10.1029/2003gc000630.
- Zbinden, E., Holland, H., Feakes, C., and Dobos, S., 1988, The Sturgeon Falls paleosol and the composition of the atmosphere 1.1 Ga BP: *Precambrian Research*, vol. 42, pp. 141–163, doi: 10.1016/0301-9268(88)90014-9.
- Zhang, Y., Anderson, N. S., Mohr, M. T., Nelson, L. L., Macdonald, F. A., Schmitz, M. D., Thurston, O. G., Guenthner, W. R., Karlstrom, K. E., and Swanson-Hysell, N. L., 2024, Paleomagnetism of the southwest Laurentia large igneous province and Cardenas Basalt: pulsed magmatism during rapid late Mesoproterozoic plate motion [code repository]: doi: 10.5281/ZENODO.10625968.
- Zhang, Y., Hou, M., Liu, G., Zhang, C., Prakapenka, V., Greenberg, E., Fei, Y., Cohen, R., and Lin, J.-F., 2020, Reconciliation of experiments and theory on transport properties of iron and the geodynamo: *Physical review letters*, vol. 125, doi: 10.1103/physrevlett.125.078501.
- Zhang, Y., Swanson-Hysell, N. L., Schmitz, M. D., Miller, J. D., and Avery, M. S., 2021, Synchronous emplacement of the anorthosite xenolith-bearing Beaver River diabase and one of the largest lava flows on Earth: *Geochemistry, Geophysics, Geosystems*, doi: 10.1029/2021gc009909.
- Ziegler, L. B., Constable, C. G., Johnson, C. L., and Tauxe, L., 2011, PADM2M: a penalized maximum likelihood model of the 0–2 Ma palaeomagnetic axial dipole moment: *Geophysical Journal International*, vol. 184, pp. 1069–1089, doi: 10.1111/j.1365-246x.2010.04905.x.

## Appendix A

# Supporting Information for “Synchronous emplacement of the anorthosite xenolith-bearing Beaver River diabase and one of the largest lava flows on Earth”

## Field observations on sampled Beaver River diabase and anorthosite xenoliths

The measured dimensions of each anorthosite xenolith sampled for paleomagnetism study during the fieldwork of this study are summarized in Table A.1. The estimated distance from each anorthosite site to the closest diabase site are also shown in the table.

## CA-ID-TIMS U-Pb zircon geochronology methods

U-Pb dates were obtained by chemical abrasion isotope dilution thermal ionization mass spectrometry (ID-TIMS) in the Boise State University (BSU) Isotope Geology Laboratory (Table S2; Fig. A.1).

Zircons were separated from the bulk rock sample using a sledge, Retsch DM200 disc mill, 500  $\mu\text{m}$  sieve, Wilfley Shaker Table, LB-1 Frantz magnetic separator, and methylene iodide heavy liquid. Heavy separates were annealed at 900°C for 48 to 60 hours in quartz crucibles in a muffle furnace. Individual zircons were chemically abraded. Chemical abrasion was carried out by transferring zircons to 3 ml Teflon Perfluoroalkoxy alkane (PFA) beakers in which they were rinsed in 3.5 M HNO<sub>3</sub> and ultrapure H<sub>2</sub>O prior to loading into 300  $\mu\text{l}$  Teflon PFA microcapsules. Fifteen microcapsules were placed in a large-capacity Parr vessel

**Table A.1:** Summary of anorthosite xenolith dimensions and their approximate distance from the closest diabase site.

Anorthosite site	Xenolith dimension (m)	Closest diabase site	Distance from anorthosite site to closest diabase site (m)
AX1	3.1 × 1.3	BD1	<5
AX2	4 × 15 × 30	BD1	<5
AX3	100 × 30	BD2	200
AX4	20 × 10	BD2	50
AX5	0.5 × 0.45	BD2	20
AX6	0.7 × 0.6	BD2	20
AX7	0.8 × 0.5	BD2	20
AX8	0.4 × 0.25	BD2	20
AX9	0.3 × 0.6	BD2	20
AX10	0.47 × 0.47	BD2	20
AX11	120 × 30	BD3	150
AX12	31 × 5	BD4	32
AX13	36 × 8	BD3	30
AX14	10 × 3	BD4	150
AX15	5.8 × 5.5	BD5	<5
AX16	27.5 × 5	BD5	25
AX17	4.2 × 2	BD5	<5
AX18	15.6 × 3	BD5	<5
AX19	7.5 × 2.9	BD6	9
AX20	8.1 × 6.5	BD7	<5
AX21	3.2 × 1.2	BD7	300
AX22	5 × 12 × 10	BD10	<10

and the zircon partially dissolved in 120  $\mu\text{l}$  of 29 M HF for 12 hours at 190°C. Zircons were returned to 3 ml Teflon PFA beakers, HF was removed, and zircons were immersed in 3.5 M HNO<sub>3</sub>, ultrasonically cleaned for an hour, and fluxed on a hotplate at 80°C for an hour. The HNO<sub>3</sub> was removed and zircon was rinsed twice in ultrapure H<sub>2</sub>O before being reloaded into the 300  $\mu\text{l}$  Teflon PFA microcapsules (rinsed and fluxed in 6 M HCl during sonication and washing of the zircons) and spiked with the <sup>233</sup>U-<sup>235</sup>U-<sup>205</sup>Pb BSU tracer solution (BSU1B). Zircons were dissolved in Parr vessels in 120  $\mu\text{l}$  of 29 M HF at 220°C for 48 hours, dried to fluorides, and re-dissolved in 6 M HCl at 180°C overnight. Pb and U were separated from the zircon matrix using an HCl-based anion-exchange chromatographic procedure (Krogh, 1973), eluted together and dried with 2  $\mu\text{l}$  of 0.05 N H<sub>3</sub>PO<sub>4</sub>.

Pb and U were loaded on a single outgassed Re filament in 5  $\mu\text{l}$  of a silica-gel/phosphoric acid mixture (Gerstenberger and Haase, 1997), and Pb and U isotopic measurements made

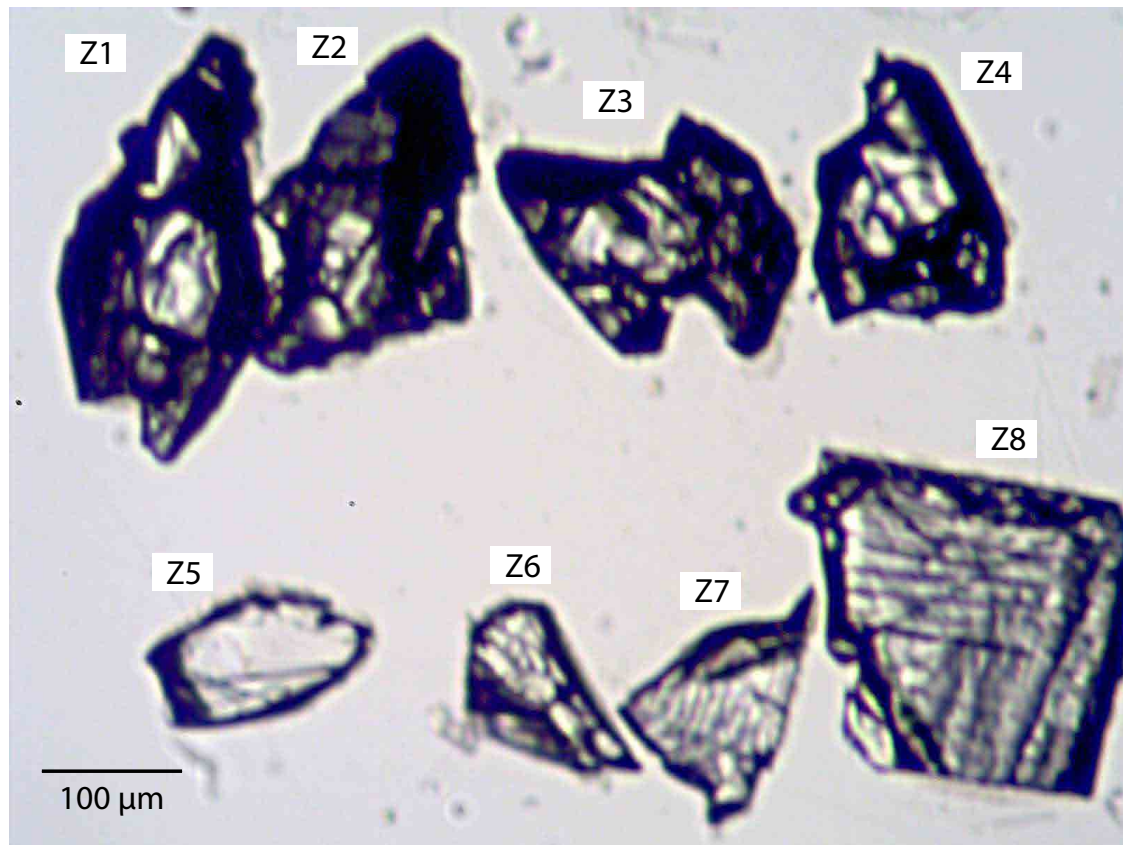


**Figure A.1:** Image of individual zircons used for ID-TIMS U-Pb geochronology from sample MS99033. Zircons (z1-z4) are subhedral to anhedral crystals and (z5-z8) are platy fragments.

on a GV Isoprobe-T multicollector thermal ionization mass spectrometer equipped with an ion-counting Daly detector. Pb isotopes were measured by peak-jumping all isotopes on the Daly detector for 190 cycles with a mass bias correction of  $0.16 \pm 0.03\%/\text{a.m.u.}$  ( $1\sigma$ ). Transitory isobaric interferences due to high-molecular weight organics, particularly on  $^{204}\text{Pb}$  and  $^{207}\text{Pb}$ , disappeared within 30-45 cycles, while ionization efficiency averaged 104 cps/pg of each Pb isotope. Linearity (to  $\geq 1.4 \times 10^6$  cps) and the associated deadtime correction of the Daly detector were determined by analysis of NBS982. Uranium was analyzed as  $\text{UO}_2^+$  ions in static Faraday mode on  $10^{12}$  ohm resistors for up to 300 cycles, and corrected for isobaric interference of  $^{233}\text{U}^{18}\text{O}^{16}\text{O}$  on  $^{235}\text{U}^{16}\text{O}^{16}\text{O}$  with an  $^{18}\text{O}/^{16}\text{O}$  of 0.00206. Ionization efficiency averaged 20 mV/ng of each U isotope. U mass fractionation was corrected using the  $^{233}\text{U}/^{235}\text{U}$  ratio of the BSU1B tracer.

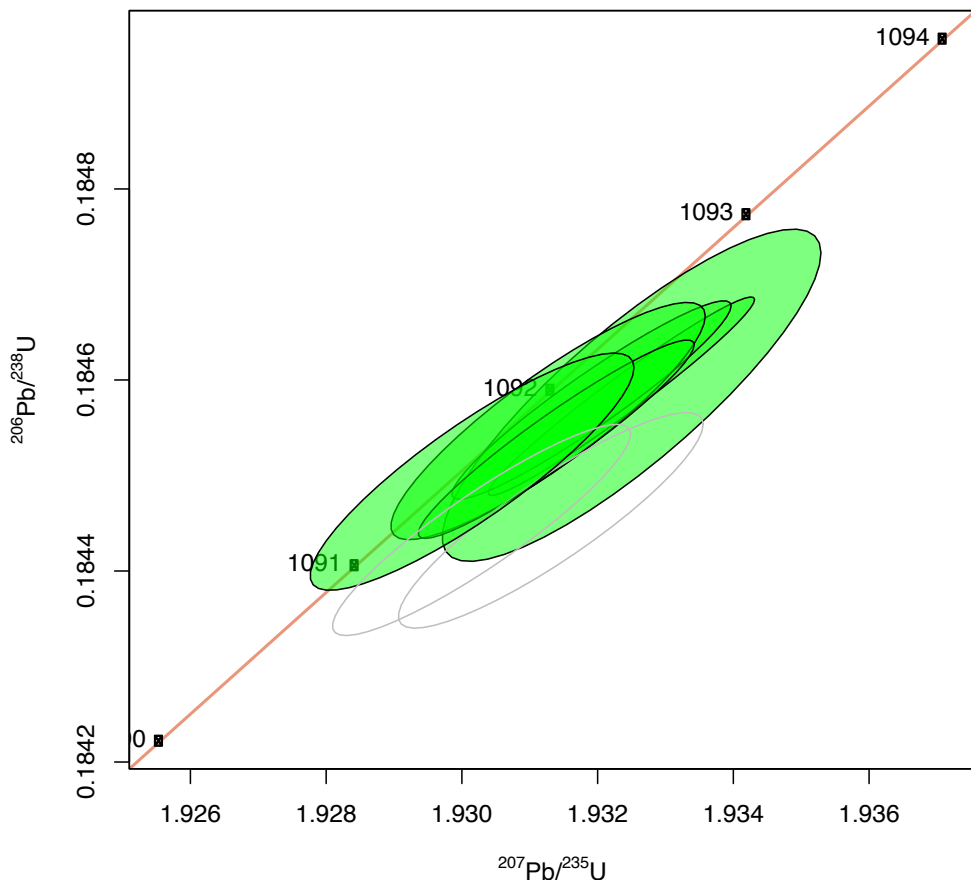


**Figure A.2:** U-Pb concordia plots for the new zircon dates from anorthosite xenoliths AX16, geochronology sample MS99033. The ellipses represent  $2\sigma$  analytical uncertainty on individual zircon dates. Green filled ellipses are analyses included in the  $^{206}\text{Pb}/^{238}\text{U}$  weighted mean dates while the grey ellipses are those that were excluded.

## LA-ICPMS plagioclase geochemistry

Rare earth elements (REE) ICPMS analyses are done by the GeoAnalytical Lab at Washington State University. Four plagioclase crystals with minimal visible other mineral inclusions from anorthosite sample MS99033 were picked for REE analyses (Table S3). The Flux used for the fusion is di-Lithium-tetraborate (Spectromelt<sup>®</sup> A-10, EM Science, Gibbstown, NJ). Reagents are HNO<sub>3</sub> 69-70% (Fisher ACS plus grade), HF 48-52% (Baker ACS reagent grade), HClO<sub>4</sub> 67-71% (Fisher Trace Metal Grade), and H<sub>2</sub>O<sub>2</sub> (Baker ACS Reagent). The HF is further purified before use by sub-boiling distillation in a Teflon still. All water used is >18 M deionized water from a Nanopure analytical grade water system (Barnstead/Thermolyne)

Powdered samples are mixed with an equal amount of lithium tetraborate flux (typically 2g), placed in a carbon crucible and fused at 1000°C in a muffle furnace for 30 minutes.

After cooling, the resultant fusion bead is briefly ground in a carbon-steel ring mill and a 250 mg portion is weighed into a 30 ml, screw-top Teflon PFA vial for dissolution. The acid dissolution consists of a first evaporation with HNO<sub>3</sub> (2ml), HF (6 ml), and HClO<sub>4</sub> (2 ml) at 110°C. After evaporating to dryness, the sample is wetted and the sides of the vial are rinsed with a small amount of water before a second evaporation with HClO<sub>4</sub> (2 ml) at 160°C. After the second evaporation, samples are brought into solution by adding approximately 10 ml of water, 3 ml HNO<sub>3</sub>, 5 drops H<sub>2</sub>O<sub>2</sub>, 2 drops of HF and warmed on a hot plate until a clear solution is obtained. The sample is then transferred to a clean 60 ml HDPE bottle diluted up to a final weight of 60g with deionized water.

Solutions are analyzed on an Agilent model 4500 ICPMS and are diluted an additional 10X at the time of analysis using Agilent's Integrated Sample Introduction System (ISIS). This yields a final dilution factor of 1:4800 relative to the amount of sample fused. Instrumental drift is corrected using Ru, In, and Re as internal standards. Internal standardization for the REEs uses a linear interpolation between In and Re after Doherty (1989) to compensate for mass-dependant differences in the rate and degree of instrumental drift. Isobaric interference of light rare earth oxides on the mid- heavy REEs can be a significant source of error in ICPMS analysis, so tuning is optimized to keep the CeO/Ce ratio below 0.5%. Correction factors used to compensate for the remaining oxide interferences are estimated using two mixed-element solutions. The first contains Ba, Pr, and Nd, and the second Tb, Sm, Eu, and Gd. Standardization is accomplished by processing duplicates of three in-house rock standards interspersed within each batch of 18 unknowns. Concentrations, oxide- and drift corrections are then calculated offline using a spreadsheet. Methods description is provided by: <https://environment.wsu.edu/facilities/geoanalytical-lab/technical-notes/icp-ms-method/>.

## LA-ICPMS zircon geochemistry

15 zircons extracted from sample MS99033 were analyzed by laser ablation inductively coupled plasma mass spectrometry (LA-ICPMS) using a ThermoElectron, iCAP-RQ, single quadrupole ICPMS and a Teledyne (Photon Machines) Analyte Excite+ 193 nm excimer Analyte laser with a HelEx ablation cell at BSU. Analytical protocols, standard materials, and data reduction software developed at BSU were used for acquisition and calibration of U-Pb dates and a suite of high field strength elements (HFSE) and rare earth elements (REE). Zircon were ablated with a 25 µm diameter laser spot using fluence and pulse rates of ~2.5 J/cm<sup>2</sup> and ~5 Hz, respectively, during a 20-second analysis excavating a pit 25 µm deep. Ablated material was carried to the nebulizer flow of the plasma by a 1.2 L/min He gas stream. Total sweep duration is 895 ms, and quadrupole dwell times were 5 ms for Si and Zr, 40 ms for <sup>202</sup>Hg, <sup>204</sup>Pb, <sup>208</sup>Pb, <sup>232</sup>Th, and <sup>238</sup>U, 80 ms for <sup>206</sup>Pb, 200 ms for <sup>49</sup>Ti and <sup>207</sup>Pb, and 10 ms for all other HFSE and REE. Background count rates were obtained prior to each spot analysis and subtracted from the raw count rate for each analyte. Concentrations were calculated using background-subtracted count rates internally normalized to <sup>29</sup>Si and

calibrated with the primary standards NIST SRM-610 and -612 glasses. Ablation pits that intersected mineral inclusions were identified based on Ti and P spikes. The Ti-in-zircon thermometer was calculated using an average  $\text{TiO}_2$  activity value of 0.7 in crustal rocks (Watson et al., 2006) and an average  $\text{SiO}_2$  activity value of 1.0 (Ferry and Watson, 2007).

## Additional zircon photomicrograph

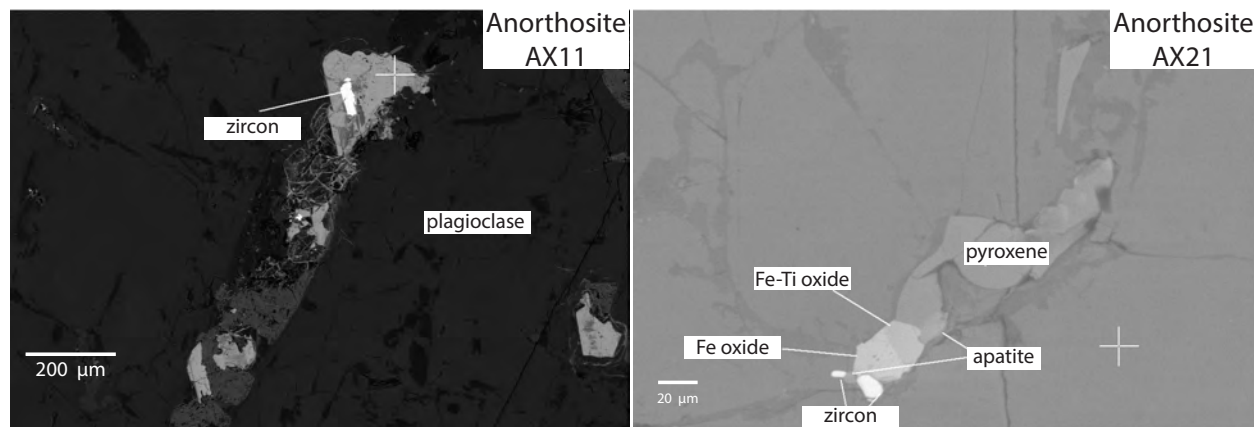


**Figure A.3:** Backscattered electron (BSE) images of anorthosite xenoliths. Subhedral to anhedral zircons form next to mafic melt pockets.

Fig. A.3 shows subhedral and anhedral zircons in anorthosite xenoliths AX11 and AX21 in back scattered electron (BSE) images of anorthosite thin sections. All zircons found are interstitial to the plagioclase. This texture is consistent with the interpretation of a zircon formation from interstitial melt liquids preserved in plagioclase mush.

## Beaver River diabase structural correction

Structural measurements were obtained from the published geologic maps of the study area as well as our field data. We calculated the mean directions from the combined volcanic bedding measurements from the Schroeder-Lutsen basalt and igneous layering measurements from the Beaver River diabase and constructed two sets of tilt correction data for the paleomagnetic sites in the southern and eastern Beaver Bay Complex (Boerboom, 2004; Boerboom and Green, 2006; Boerboom et al., 2006, 2007; Miller et al., 2001). The mean dip angle for the two areas are very similar while the dip trends are different, with the southern Beaver Bay Complex showing a slightly more easterly trend than the eastern Beaver Bay Complex. This difference in dip trend reflects the overall arcuate shape of the Beaver Bay Complex intrusions along the shore of Lake Superior.

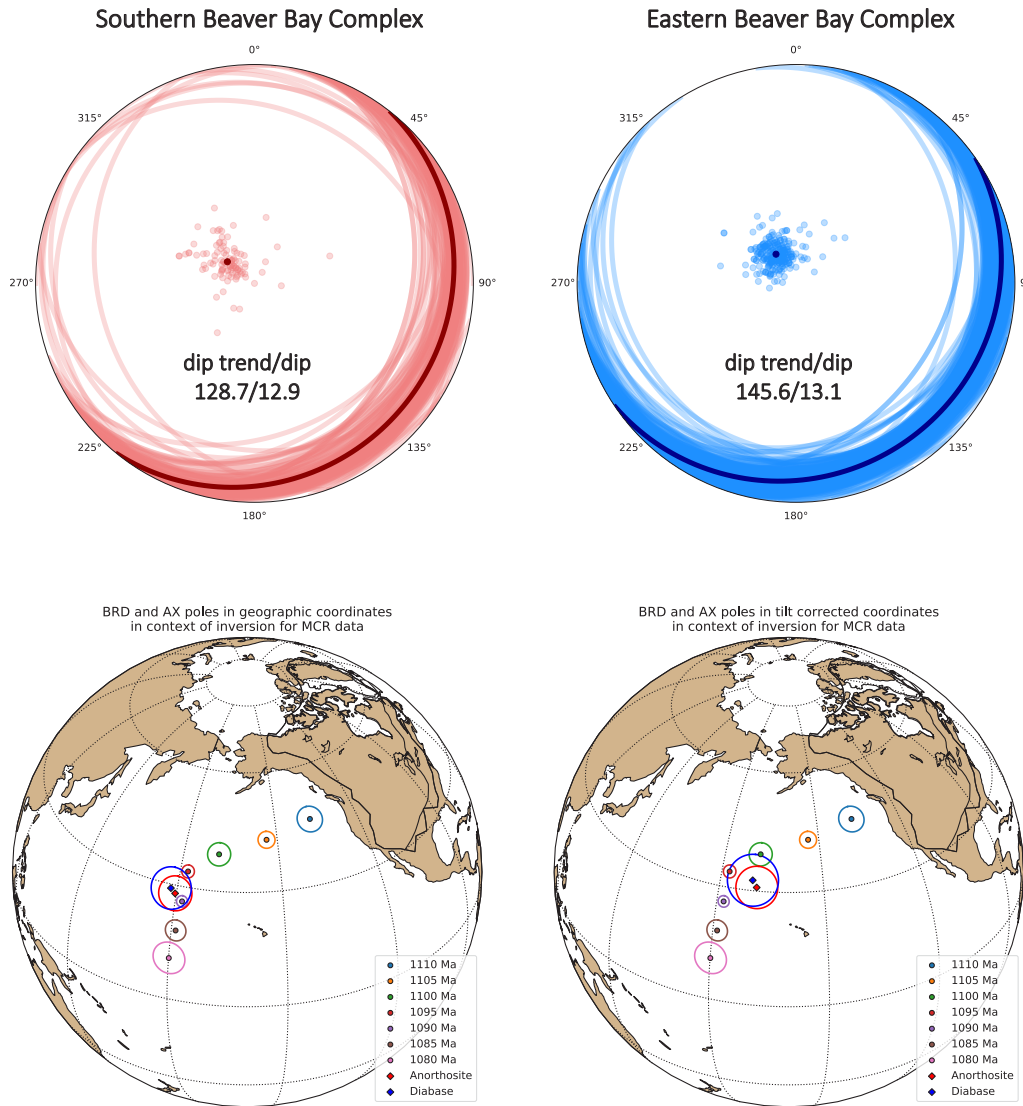


**Figure A.4:** Stereonet plots of the compiled structural orientation data to tilt correct the paleomagnetic directions obtained from the Beaver River diabase and the anorthositic xenoliths therein. The mean pole position of the diabase and anorthositic units before and after the tilt correction are shown in context of the inverted Keweenawan Track developed by Swanson-Hysell et al. (2019b).

To summarize, We use a bedding dip direction - dip of 145.6 - 13.1 for paleomagnetic site AX3, AX4, AX5, AX6, AX7, AX8, AX9, AX10, and BD2, BD14, BD15, BD16 in the Eastern Beaver Bay Complex region. We use a bedding dip direction - dip of 128.7 - 12.9 for site AX1, AX2, AX11, AX12, AX13, AX14, AX15, AX16, AX17, AX18, AX19, AX20, AX21, AX22, BD1, BD3, BD4, BD5, BD6, BD7, BD8, BD9, BD10, BD11, BD12, BD13, BD17 in the Southern Beaver Bay Complex.

Fig. A.4 shows the stereonet plots of the bedding orientations compiled for tilt correcting the paleomagnetic directions of samples collected in the Southern Beaver Bay Complex and the Eastern Beaver Bay Complex. The resultant mean pole position for the diabase changes from  $29.0^{\circ}\text{N}$ ,  $178.2^{\circ}\text{E}$ , N = 15, A95 =  $5.2^{\circ}$ , k = 55.3 before tilt correction to  $32.5^{\circ}\text{N}$ ,  $189.5^{\circ}\text{E}$ , N = 15, A95 =  $6.3^{\circ}$ , k = 37.4 after tilt correction. For the anorthosite, the mean pole position changes from  $28.0^{\circ}\text{N}$ ,  $179.6^{\circ}\text{E}$ , N = 17, A95 =  $4.3^{\circ}$ , k = 70.6 before tilt correction to  $30.9^{\circ}\text{N}$ ,  $190.8^{\circ}\text{E}$ , N = 17, A95:  $5.2^{\circ}$ , k = 48.5 after tilt correction. The uncertainty ellipses for both units are slightly larger after tilt correcting the directions. This may reflect the uncertainties associated with using igneous fabrics as our paleohorizontal references. Nevertheless, the mean pole position of the diabase and anorthosite still overlaps and is consistent with the expected position derived from the inverted Keweenawan Track *ca.* 1092 Ma (Swanson-Hysell et al., 2019b).

**Table S2. Zircon chemical abrasion IDTIMS U-Pb isotopic data**

Sample	Compositional Parameters						Radiogenic Isotope Ratios						Isotopic Ages								
	Th	$^{206}\text{Pb}^*$	mol %	$\text{Pb}^*$	$\text{Pb}_c$	$^{206}\text{Pb}$	$^{208}\text{Pb}$	$^{207}\text{Pb}$	$^{207}\text{Pb}$	$^{235}\text{U}$	$^{238}\text{U}$	$^{206}\text{Pb}$	corr.	$^{207}\text{Pb}$	$^{207}\text{Pb}$	$^{206}\text{Pb}$	$\pm$	$^{235}\text{U}$	$\pm$	$^{238}\text{U}$	$\pm$
	(a)	U	$\times 10^{-13}$ mol	$^{206}\text{Pb}^*$	$\text{Pb}_c$	(pg)	$^{204}\text{Pb}$	$^{206}\text{Pb}$	$^{208}\text{Pb}$	% err	(e)	(f)	(e)	coef.	$^{206}\text{Pb}$	$\pm$	$^{235}\text{U}$	$\pm$	$^{238}\text{U}$	$\pm$	
MS99033 Anorthosite xenolith in Beaver Bay Diabase (Beaver Bay Complex)																					
z4	0.944	0.8673	0.9977	144	0.17	7696	0.286	0.0759659	0.066	1.93250	0.118	0.184584	0.077	0.856	1093.27	1.31	1092.41	0.79	<b>1091.97</b>	<b>0.77</b>	
z8	1.010	6.9857	0.9997	1133	0.18	59449	0.306	0.0759607	0.040	1.93235	0.083	0.184583	0.046	0.974	1093.13	0.81	1092.35	0.56	<b>1091.96</b>	<b>0.46</b>	
z1	2.435	6.7175	0.9985	309	0.81	12367	0.738	0.0759449	0.047	1.93191	0.087	0.184579	0.046	0.948	1092.72	0.93	1092.20	0.59	<b>1091.94</b>	<b>0.46</b>	
z7	1.008	1.4490	0.9986	239	0.17	12587	0.305	0.0759289	0.056	1.93127	0.098	0.184557	0.055	0.886	1092.30	1.11	1091.98	0.66	<b>1091.82</b>	<b>0.55</b>	
z3	1.863	3.3407	0.9992	519	0.22	22932	0.565	0.0759415	0.044	1.93139	0.086	0.184538	0.046	0.950	1092.63	0.89	1092.02	0.58	<b>1091.72</b>	<b>0.47</b>	
z6	0.978	0.8594	0.9978	154	0.16	8164	0.296	0.0759062	0.059	1.93015	0.101	0.184504	0.055	0.878	1091.70	1.19	1091.59	0.68	<b>1091.54</b>	<b>0.55</b>	
z5	0.971	1.3031	0.9983	196	0.19	10381	0.294	0.0759732	0.056	1.93131	0.095	0.184453	0.050	0.891	1093.46	1.12	1091.99	0.64	1091.26	0.50	
z2	0.909	1.7688	0.9985	229	0.22	12318	0.276	0.0759373	0.053	1.93029	0.093	0.184443	0.049	0.910	<u>1092.52</u>	<u>1.06</u>	<u>1091.64</u>	<u>0.62</u>	<u>1091.20</u>	<u>0.49</u>	
weighted mean $^{206}\text{Pb}/^{238}\text{U}$ age = 1091.83 ± 0.21 (0.37) [1.15] Ma (2s); MSWD = 0.41 (n=6)																					

(a) z1, z2 etc. are labels for single zircon fragments annealed and chemically abraded after Mattinson (2005); bold indicates analyses used in weighted mean calculations.

(b) Model Th/U ratio iteratively calculated from the radiogenic  $^{208}\text{Pb}/^{206}\text{Pb}$  ratio and  $^{206}\text{Pb}/^{238}\text{U}$  age.(c)  $\text{Pb}^*$  and  $\text{Pb}_c$  represent radiogenic and common Pb, respectively; mol %  $^{206}\text{Pb}^*$  with respect to radiogenic, blank and initial common Pb.

(d) Measured ratio corrected for spike and fractionation only. Fractionation estimated at 0.18 (Daly) or 0.10 (Faraday) ± 0.02 %/a.m.u. based on analysis of NBS-981 &amp; 982.

(e) Corrected for fractionation, spike, and common Pb; all common Pb was assumed to be procedural blank:  $^{206}\text{Pb}/^{204}\text{Pb}$  = 18.60 ± 0.72%;  $^{207}\text{Pb}/^{204}\text{Pb}$  = 15.69 ± 0.62%;  $^{208}\text{Pb}/^{204}\text{Pb}$  = 38.51 ± 0.74% (all uncertainties 1-sigma). Isotope dilution measurements made with the ET535 spike (Condon et al., 2015).

(f) Errors are 2-sigma, propagated using the algorithms of Schmitz and Schoene (2007).

(g) Calculations are based on the decay constants of Jaffey et al. (1971). All ratios and ages corrected for initial  $^{230}\text{Th}/^{238}\text{U}$  disequilibrium with Th/U [magma] = 3.

Sample ID	La	Ce	Pr	Nd	Sm	Eu	Gd	Tb	Dy	Ho	Er	Tm	Yb	Lu	Ba	Th	Nb	Y	Hf	Ta	U	Pb	Rb	Cs	Sr	Sc	Zr
MS99033-1	1.36	2.38	0.27	1.07	0.19	0.39	0.18	0.03	0.16	0.03	0.08	0.01	0.07	0.01	57	0.01	0.06	0.95	0.01	0.00	0.00	0.37	1.7	0.10	512	0.3	1
MS99033-2	1.48	2.60	0.31	1.17	0.23	0.37	0.21	0.03	0.19	0.03	0.09	0.01	0.07	0.01	56	0.01	0.07	1.18	0.02	0.00	0.01	0.50	2.3	0.13	500	0.3	1
MS99033-3	1.46	2.59	0.30	1.18	0.24	0.37	0.23	0.04	0.22	0.05	0.12	0.02	0.10	0.01	61	0.01	0.04	1.49	0.02	0.00	0.02	1.28	3.8	0.29	493	0.4	1
MS99033-4	1.46	2.52	0.29	1.19	0.21	0.38	0.21	0.03	0.17	0.03	0.09	0.01	0.07	0.01	58	0.01	0.04	1.09	0.02	0.00	0.01	0.42	2.8	0.20	506	0.3	1

The units of all analyses are in parts per million (ppm).

## Appendix B

**Supporting Information for “High  
geomagnetic field intensity recorded  
by anorthosite xenoliths requires a  
strongly powered late  
Mesoproterozoic geodynamo”**

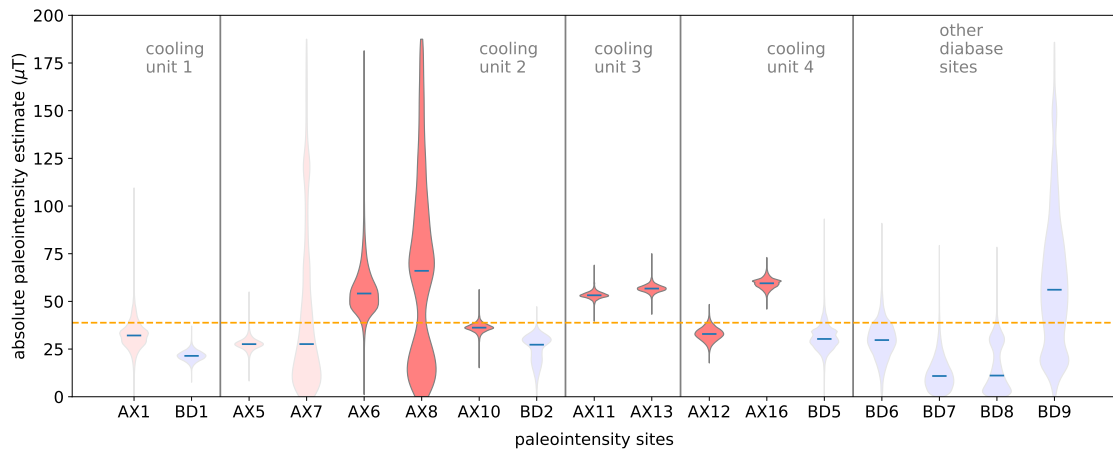


**Figure B.1:** Violin plots of site-level posterior paleointensity distributions estimated using the bias corrected estimation of paleointensity (BiCEP) method developed by ref. Cych et al. (2021). Blue bars of each violin plot represent the median of the distributions. The yellow dashed line is the mean paleointensity of the posterior estimates across all sites estimated using BiCEP ( $38.82 \pm 4.60$  mT). Assuming that paleointensity estimates from specimens that come from a same cooling unit are distributed around a true paleointensity value with the various deflections being expressed as the curvature parameter of the NRM/TRM plot (Arai, 1963; Paterson, 2011), the method uses all paleointensity measurement-level data without applying selection criteria. For comparison of results from this independent method with those based on our selection (as shown in Fig. 4 in manuscript), we highlight the anorthosite sites that pass our paleointensity selection and make other anorthosite and diabase more transparent. The results from the BiCEP method address the uncertainties associated with anorthosite AX6 and AX8. This is associated with the relatively variable specimen behaviors within these two sites. For sites AX10, AX11, AX13, AX12, and AX16, the posterior probability distributions have very narrow bounds, consistent with the interpretation that these anorthosites are faithful paleointensity recorders that have high-quality paleointensity behaviors. AX—anorthosite xenolith site; BD—Beaver River diabase site. The grouping of cooling units is based on the spatial proximity between site locations and the inclusion relationship of host diabase and anorthosite xenoliths reported by ref. Zhang et al. (2021).

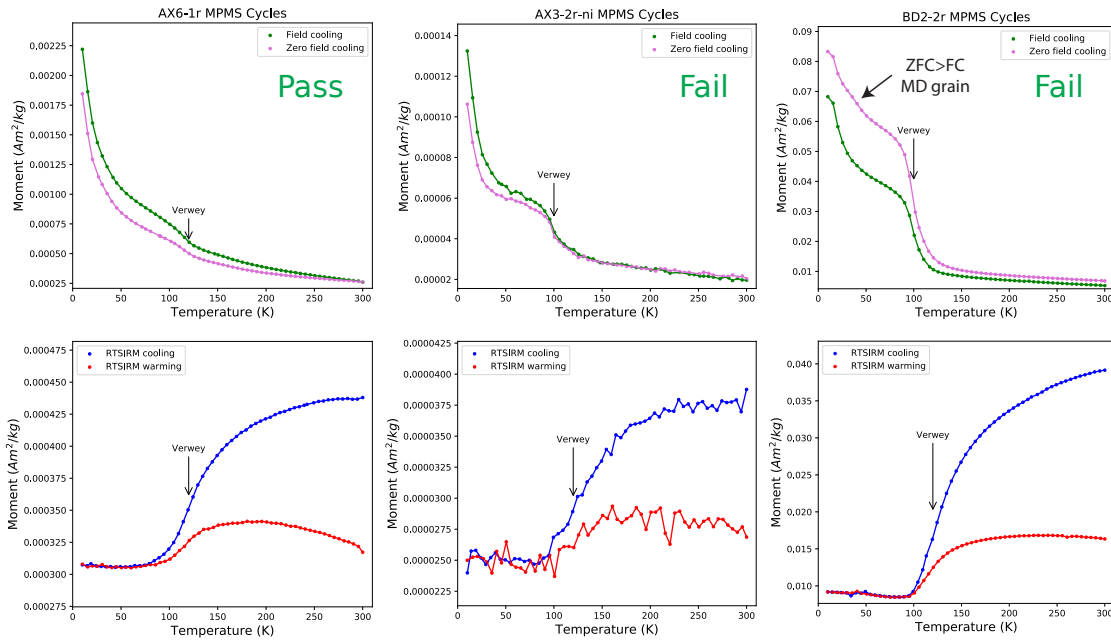


**Figure B.2:** Low-temperature magnetic property measurement system (MPMS) experiment results. “Pass” or “Fail” represents whether their sister specimens passed our paleointensity selection or not. In the field-cooled (FC) experiments, the magnetization was measured upon warming following the specimen having cooled in an applied field of 2.5 T from 300 to 10 K. In the zero-field-cooled (ZFC) experiment, a low-temperature saturation isothermal remanence (LTSIRM) of 2.5 T was applied at 10 K after the specimen cooled in a (near-)zero field. In the room-temperature saturation isothermal remanence (RTSIRM) experiment, the sample was pulsed with a 2.5 T field at room temperature ( $\sim 300$  K) and then cooled to 10 K and warmed back to room temperature in a (near-) zero field. Specimen AX6-1r is from anorthosite AX6 which passed our paleointensity selection. It has a well-defined Verwey transition  $\sim 120$  K (Verwey, 1939). Specimens AX3-2r-ni and BD2-2r show Verwey transition but the transition temperatures are suppressed below  $\sim 120$  K. Specimen BD2-2r has a consistently higher moment during the zero-field-cooled step than during the field-cooled step. This is consistent with the interpretation that multidomain (MD) magnetic carriers exist in significant quantity in this specimen (Carter-Stiglitz et al., 2006).

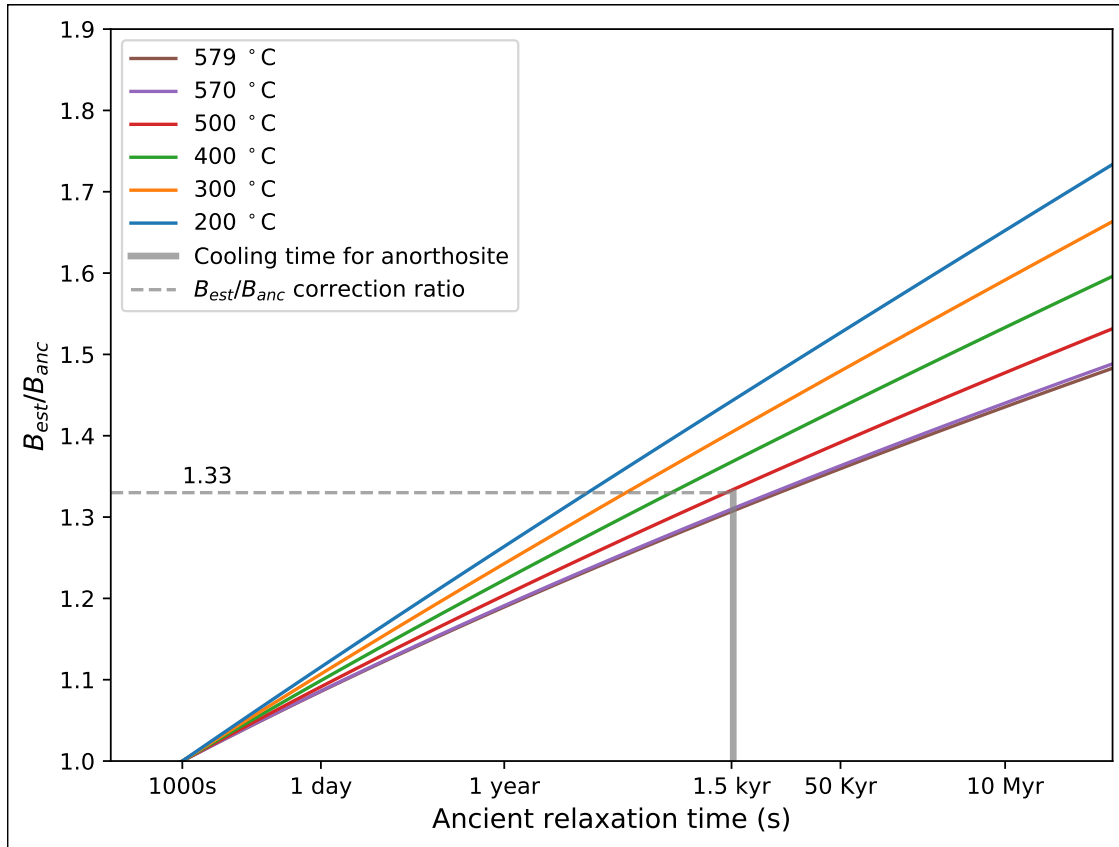


**Figure B.3:** Graph of predicted paleointensity overestimate due to slow cooling of the intrusive Beaver River diabase and anorthositic xenoliths relative to the cooling rate in laboratory following the model of ref. Halgedahl et al. (1980). Because the majority of the anorthosites have unblocking temperatures between 500°C and 580°C, we estimate that the slow cooling during natural remanence acquisition could have resulted in a 33% overestimate. Thus, a correction factor of 0.75 is applied at specimen level for the paleointensity summary plot.

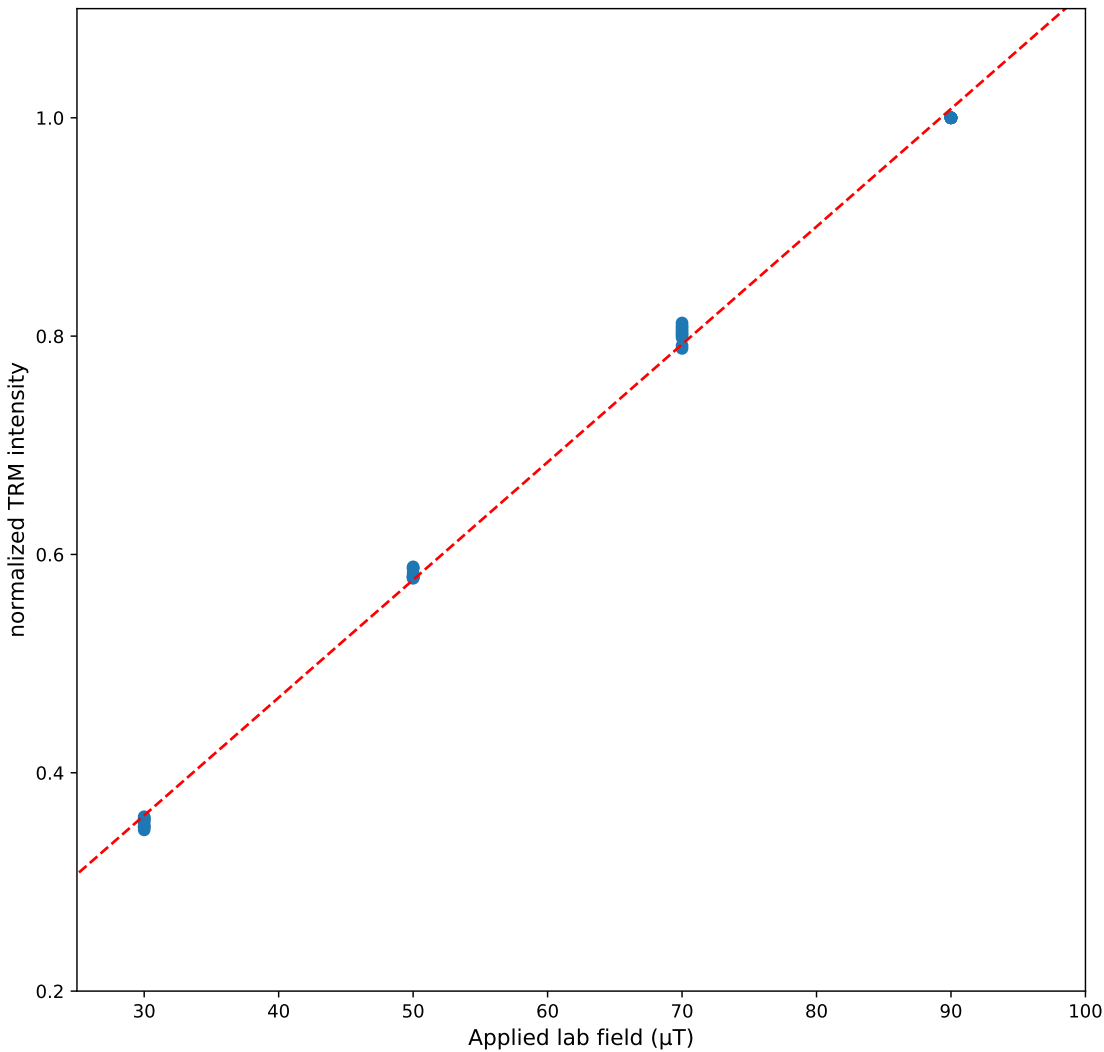


**Figure B.4:** Plot of thermal remanent magnetization acquisition experiment results. After IZZI-type Thellier paleointensity experiments, full TRMs were imparted on the same specimens in known lab fields of 30, 50, 70, and 90  $\mu\text{T}$ . The red dashed line shows a linear fit through the data points. The results show that the anorthosite xenoliths do not acquire saturation remanence or display non-linear remanence acquisition under fields relevant to this study. Therefore, non-linear acquisition correction is not needed for our paleointensity results.

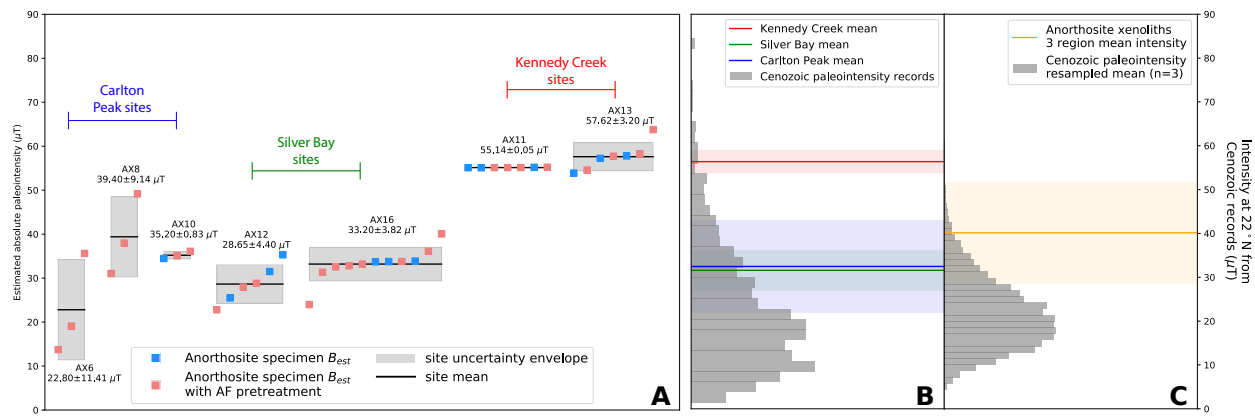


**Figure B.5:** Data from this study as in Figure 4 of the main text, but compared to the Cenozoic paleointensity database rather than the PADM2M model. A) Summary plot of individual specimen absolute paleointensity results (square symbols) and their averages and standard deviations at site level (black bars with grey uncertainty boxes) from this study. All results are corrected for cooling rate with a factor of 0.75. Each 'AX' site is an individual anorthosite xenolith within the Beaver River diabase. The sites with successful experiments come from 3 regions which would have cooled at distinct times yielding similar estimates within the each region with differences between regions. B) Specimen level means calculated for these regions are compared to the distribution of intensities calculated from the existing paleointensity data in the Cenozoic (past 66 Myr) in the PINT database (PINT v8.0.0; <http://www.pintdb.org/>; Bono et al., 2022a) at the latitude corresponding to the paleolatitude of study region (22°N). C) The mean of the 3 regional means is compared to means calculated from 3 random values drawn from the Cenozoic data. The paleointensity records used for resampling are filtered for  $Q_{PI} \geq 3$  (Biggin and Paterson, 2014). The distribution represents a total of 10,000 iterations of taking 3 random draws and calculating the mean.

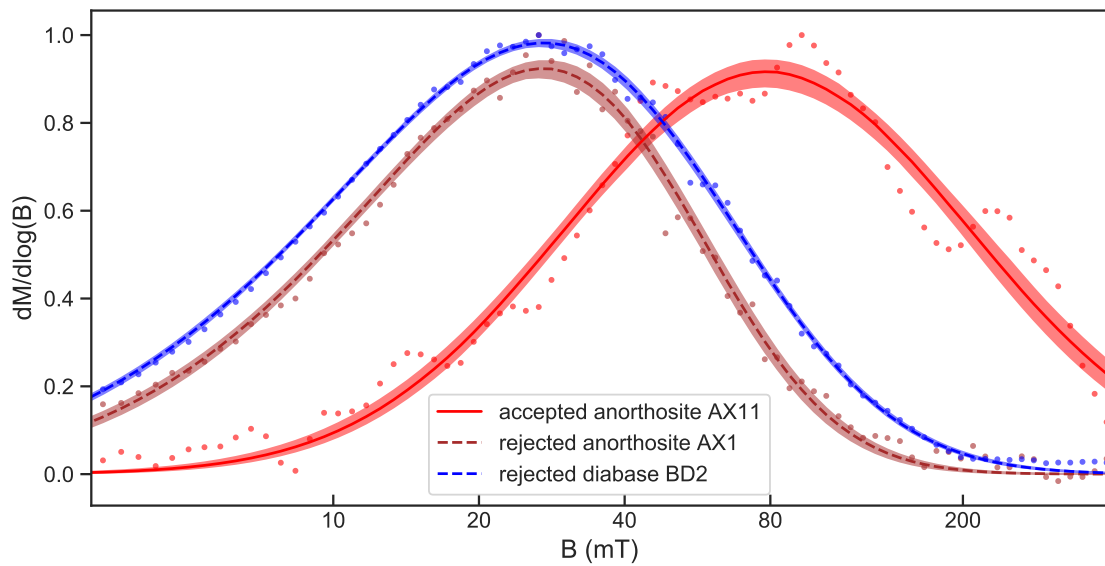


**Figure B.6:** Example coercivity spectra of anorthosite and diabase specimens from sites that pass or fail our paleointensity selection criteria. The specimens and fits are the same as those shown in Figure 5 in the manuscript. Data points used for fitting the coercivity curves are shown in this figure.

**Table B.1:** Specimen paleointensity results that passed our selection.  $B_{anc}$  is the calculated ancient field intensity over the chosen temperature interval in  $\mu\text{T}$ .  $T_{min}$  and  $T_{max}$  indicate the temperature interval over which the best fit for paleointensity was defined. N is the number of steps used within the selected interval for paleointensity determination. FRAC is the fraction of remanence used for fitting. NpTRM shows the number of pTRM checks within the selected interval for paleointensity determination.  $\beta$  is the scatter parameter. GAP-MAX is the maximum magnetization gap between two adjacent steps. MAD is the maximum angle of deviation. DANG is the deviation angle. SCAT is the scatter parameter.  $\text{inc}_t$  is the tilt-corrected inclination. Paleolatitude is calculated from the inclination values reported in Zhang et al. (2021).  $\gamma$  is the gamma statistic that measures the angle between the last pTRM step used for paleointensity determination and the applied field direction.  $V(\text{A})\text{DM}$  is the virtual (axial) dipole moment reported in  $10^{21}\text{Am}^2$  ( $\text{ZAm}^2$ ).  
 10a

Site	Specimen	$B_{anc}$	$T_{min}$	$T_{max}$	N	FRAC	NpTRM	$\beta$	GAP-MAX (°)	DANG (°)	SCAT	$\text{inc}_t$ (°)	Paleolatitude	$\gamma$	$V\text{DM}$ ( $\text{ZAm}^2$ )	
AX6	AX6-2a	137.72	400	585	18	0.70	10	0.04	0.12	3.4	3.4	PASS	38.9	22.0	2.7	29.8
AX6	AX6-3a	19.09	400	585	18	0.76	10	0.04	0.10	4.3	2.9	PASS	38.9	22.0	3.2	41.4
AX6	AX6-1a	35.61	475	585	15	0.60	10	0.02	0.16	2.9	1.7	PASS	38.9	22.0	2.0	77.3
AX8	AX8-3a	31.05	400	580	17	0.75	9	0.03	0.14	4.4	2.2	PASS	40.3	23.0	11.2	66.5
AX8	AX8-2a	37.98	400	580	17	0.63	9	0.04	0.16	3.2	1.3	PASS	40.3	23.0	3.7	81.4
AX8	AX8-1a	49.16	425	566	13	0.60	8	0.07	0.20	5.3	3.0	PASS	40.3	23.0	7.0	105.3
AX10	AX10-1a	34.47	425	585	17	0.78	10	0.06	0.24	5.6	2.6	PASS	36.6	20.4	4.7	76.3
AX10	AX10-2a	35.05	450	585	16	0.62	10	0.04	0.20	5.3	2.2	PASS	36.6	20.4	7.8	77.6
AX10	AX10-3a	36.10	425	585	17	0.69	10	0.04	0.24	4.0	1.6	PASS	36.6	20.4	5.8	79.9
AX11	AX11-1a	55.11	425	560	10	0.67	6	0.08	0.21	5.3	2.5	PASS	35.2	19.4	5.9	123.5
AX11	AX11-2a	55.11	400	560	11	0.65	6	0.07	0.21	3.9	1.5	PASS	35.2	19.4	9.9	123.5
AX11	AX11-4a	55.12	500	570	11	0.66	8	0.09	0.20	1.5	3.3	PASS	35.2	19.4	5.6	123.5
AX11	AX11-6a	55.13	200	562	14	0.69	7	0.07	0.17	4.0	1.3	PASS	35.2	19.4	3.0	123.5
AX11	AX11-9a	55.14	100	562	15	0.67	7	0.06	0.17	5.3	1.1	PASS	35.2	19.4	11.9	123.5
AX11	AX11-3a	55.20	400	560	11	0.66	6	0.08	0.21	4.0	2.1	PASS	35.2	19.4	8.2	123.7
AX11	AX11-5a	55.22	400	566	14	0.73	8	0.05	0.18	2.9	0.9	PASS	35.2	19.4	1.9	123.7
AX12	AX12-1a	22.81	475	585	16	0.75	10	0.06	0.17	1.7	0.6	PASS	35.2	35.7	0.9	41.5
AX12	AX12-1a	25.48	0	580	21	0.97	9	0.03	0.17	5.5	4.7	PASS	55.2	35.7	10.0	46.3
AX12	AX12-6a	27.95	425	564	12	0.69	7	0.08	0.22	3.6	2.1	PASS	55.2	35.7	5.0	50.8
AX12	AX12-8a	28.83	475	565	12	0.75	8	0.06	0.25	1.5	2.3	PASS	55.2	35.7	1.6	52.4
AX12	AX12-4a	31.50	500	585	14	0.66	10	0.05	0.24	3.9	3.2	PASS	55.2	35.7	11.4	57.3
AX12	AX12-2a	35.29	425	570	14	0.70	8	0.05	0.24	3.4	2.4	PASS	55.2	35.7	7.0	64.2
AX13	AX13-3a	53.89	100	550	12	0.71	5	0.08	0.22	5.9	1.9	PASS	35.1	19.4	3.4	120.9
AX13	AX13-7a	54.59	475	585	15	0.61	10	0.03	0.20	3.6	2.1	PASS	35.1	19.4	11.6	122.4
AX13	AX13-4a	57.24	200	550	11	0.65	5	0.04	0.18	8.8	1.1	PASS	35.1	19.4	3.7	128.4
AX13	AX13-6a	57.74	200	555	12	0.70	6	0.06	0.22	3.8	1.5	PASS	35.1	19.4	4.5	129.5
AX13	AX13-2a	57.79	200	555	12	0.71	6	0.05	0.20	8.1	2.2	PASS	35.1	19.4	4.1	129.6
AX13	AX13-9a	58.26	0	564	17	0.94	7	0.03	0.16	6.0	1.1	PASS	35.1	19.4	2.6	130.7
AX13	AX13-8a	63.78	450	570	13	0.81	8	0.02	0.24	3.7	1.8	PASS	35.1	19.4	5.1	143.0
AX16	AX16-15a	23.99	475	570	13	0.61	8	0.07	0.17	3.1	1.4	PASS	49.2	30.1	2.6	46.8
AX16	AX16-13a	31.34	400	570	15	0.72	8	0.07	0.20	3.5	1.9	PASS	49.2	30.1	1.1	61.2
AX16	AX16-16a	32.56	400	562	13	0.65	7	0.09	0.18	5.1	2.9	PASS	49.2	30.1	2.0	63.6
AX16	AX16-14a	32.81	400	565	14	0.63	8	0.08	0.14	3.8	2.1	PASS	49.2	30.1	6.0	64.1
AX16	AX16-11a	33.21	450	570	14	0.70	8	0.06	0.15	2.9	2.1	PASS	49.2	30.1	4.6	64.9
AX16	AX16-4a	33.70	425	575	15	0.76	9	0.05	0.21	4.8	1.1	PASS	49.2	30.1	4.2	65.8
AX16	AX16-1a	33.76	200	564	15	0.87	7	0.06	0.22	5.6	2.4	PASS	49.2	30.1	4.5	65.9
AX16	AX16-5a	33.77	425	560	10	0.65	6	0.10	0.24	7.4	3.9	PASS	49.2	30.1	4.0	65.9
AX16	AX16-2a	33.87	425	564	12	0.65	7	0.07	0.22	4.3	1.4	PASS	49.2	30.1	4.9	66.1
AX16	AX16-9a	36.12	500	585	15	0.61	10	0.04	0.17	3.0	1.2	PASS	49.2	30.1	4.3	70.5
AX16	AX16-10a	40.05	510	585	14	0.62	10	0.04	0.20	2.8	1.1	PASS	49.2	30.1	5.5	78.2

**Table B.2:** Summary statistics for the Q<sub>P1</sub> quality criteria of Biggin and Paterson (2014).

Site	N	Age (Ma)	Method	AGE	STAT	TRM	ALT	MD	ACN	TECH	LITH	QPI
AX6	3	1091.8	T+	1	0	1	1	1	1	0	0	5
AX8	2	1091.8	T+	1	0	1	1	1	1	0	0	5
AX10	3	1091.8	T+	1	0	1	1	1	1	0	0	5
AX11	7	1091.8	T+	1	1	1	1	1	1	0	0	6
AX12	6	1091.8	T+	1	1	1	1	1	1	0	0	6
AX13	7	1091.8	T+	1	1	1	1	1	1	0	0	6
AX16	11	1091.8	T+	1	1	1	1	1	1	0	0	6

**Table B.3:** Summary paleointensity result statistics at site-level, region-level, and overall arithmetic means. The statistics names are the same as in Table B.1. n represents the total number of specimen- or site- or region-level results used for calculating mean values.  $\text{inc}_{tc}$  is the tilt-corrected mean inclination. Site-level means for AX6, AX8, AX10, AX11, AX12, AX13, AX16 are calculated based on specimen results. Regional means for Carlton Peak, Kennedy Creek, and Silver Bay are calculated by grouping specimen results from AX6 and AX8 and AX10, AX11 and AX13, AX12 and AX16, respectively. Overall site mean values are calculated using all site-level results in this table. Overall region-mean values are calculated using all regional mean results in this table. All paleointensity values and corresponding virtual dipole moments are corrected for cooling rate by a factor of 0.75. Taking a threshold p value of 0.01, the independent two-sample t-test results show that specimen paleointensity distributions of site AX12 and AX16, and those of site AX11 and AX13 are indistinguishable; region Kennedy Creek have distinguishable distributions from the other two regions; Silver Bay region and Carlton Peak region values are indistinguishable.

	B <sub>anc</sub>	n	FRAC	GAP-MAX	MAD (°)	DANG (°)	inc <sub>tc</sub>	Paleolatitude	γ	VDM (ZAm <sup>2</sup> )
specimen mean for sites	AX6	22.8	3	0.69	0.13	3.6	2.7	38.9	22.0	2.6
	AX8	39.4	3	0.66	0.17	4.3	2.2	40.3	23.0	49.5
	AX10	35.2	3	0.70	0.23	5.0	2.1	36.6	20.4	7.3
	AX11	55.2	7	0.68	0.19	3.8	1.8	35.2	19.4	84.4
	AX12	28.6	6	0.75	0.22	3.3	2.5	55.2	35.7	6.1
	AX13	57.6	7	0.73	0.2	5.7	1.7	35.1	19.4	123.6
	AX16	33.2	11	0.68	0.19	4.2	2.0	49.2	30.1	52.1
specimen mean for regions	Carlton Peak	32.5	9	0.68	0.17	4.3	2.3	38.6	21.8	64.8
	Kennedy Creek	56.4	14	0.70	0.20	4.8	1.7	35.2	19.4	5.3
	Silver Bay	31.6	17	0.71	0.20	3.9	2.2	51.3	32.1	126.4
overall site mean		38.9	7							83.1
overall region mean		40.2	3							85.8

## Appendix C

**Supporting Information for  
“Paleomagnetism of the southwestern  
Laurentia large igneous province and  
Cardenas Basalt: pulsed magmatism  
during rapid late Mesoproterozoic  
plate motion”**

**Table C.1:** Compilation of paleomagnetic data collected from mafic sills in central Arizona by Harlan (1993) and Donadini et al. (2011). The study of Donadini et al. (2011) revisited some field areas of Harlan (1993) and resampled some diabase sills in the earlier study. However, the determination of individual cooling units was not clear in Donadini et al. (2011). We compiled data from both studies with a focus on distinguishing individual paleomagnetic sites as distinct cooling units based on geographic and paleomagnetic information provided in the original publications. Data rejected by the original authors are not included. Original “site” level data with better Fisher statistics (higher concentration parameter k values) are preferentially used in cases where repeat sampling of the same cooling unit is interpreted to have happened. We interpret site GD12 and GD13 of Harlan (1993) are the same as site OD in Donadini et al. (2011) and thus recalculated mean statistics. dir\_inc—inclination; dir\_dec—declination; n—number of samples used in calculating the mean direction; a95—95% confidence angle of site mean direction; plat/Plat—pole latitude; plon/Plon—pole longitude. The site level pole locations are recalculating using the directions and site location information provided in the original studies.

site	dir_dec	dir_inc	k	a95	n	slon	slat	pole reference	plon	plat	polarity
GD01-02	279.2	57				249.5	33.7	Harlan (1993)	188.7	26.4	N
GD03	285.3	51.4	165	3.6	11	249.5	33.8	Harlan (1993)	180.7	28.8	N
GD04	295.5	56.6	81.9	7.7	7	249.5	33.8	Harlan (1993)	182.9	38.4	N
GD05	283.2	26	108.5	5.8	7	249.5	33.8	Harlan (1993)	163.9	18.4	N
GD06-07	282.8	48.9				249.3	33.5	Harlan (1993)	179.3	25.8	N
GD08	318	61.2	56.1	5.6	13	249.3	33.5	Harlan (1993)	186.8	56.1	N
GD09	299.2	53.8	21.1	11.5	9	249.3	33.5	Harlan (1993)	178.3	40.3	N
GD10	267.5	38.2	421.5	3.3	6	249.3	33.5	Harlan (1993)	178.7	9.7	N
GD17	285.9	17.1	34.5	8.3	10	249.1	33.6	Harlan (1993)	157.7	18	N
GD18-20	339.6	36.3				249.2	33.5	Harlan (1993)	128	67.5	N
GD22	270.1	40.4	120.3	5.1	8	249.5	33.8	Harlan (1993)	178.9	12.7	N
GD24	297.9	58.5	168	4	9	249.5	33.8	Harlan (1993)	184.8	40.8	N
GD29	306.9	66.4	678.5	2	9	249.4	33.6	Harlan (1993)	197.2	48.2	N
GD30	264.1	33.4	157.6	5.4	6	249.4	33.6	Harlan (1993)	177.8	5.3	N
DF	332.6	69.4	145.1	3.5	13	249.3	33.5	Donadini et al. (2011)	212.7	62.5	N
DG	266.2	34.4	58.7	8	7	249.4	33.6	Donadini et al. (2011)	176.9	7.4	N
DJ	281.9	52.8	325.5	2.9	9	-110.48	33.65	Donadini et al. (2011)	182.8	26.7	N
KD	293.8	13.4	142.3	3.3	14	-110.97	33.89	Donadini et al. (2011)	151.2	23.5	N
MD	277.2	50.7	110.4	4.2	12	-110.98	33.87	Donadini et al. (2011)	182.9	22.2	N
GD12_GD13_OD	280.8	45.7	313.7	7		-110.98	33.81	Harlan (1993); Donadini et al. (2011)	177.6	23	N
GD11	115.3	-69.9	173.7	4.2	8	-110.96	33.75	Harlan (1993)	24.3	-41	R
GD15-27	224.9	-73.7				-110.5	33.8	Harlan (1993)	103.8	-50.9	R
BD	137.6	-74	66.1	8.2	7	-110.61	33.61	Donadini et al. (2011)	36.5	-52	R
WD	199.2	-71	92.1	3.1	24	-110.69	33.55	Donadini et al. (2011)	95	-64.4	R
normal polarity mean	287.6	47.4	14.4	8.5	N	177.4	30.6		8.9		
reversed polarity mean	167.4	-77	31.8	16.6	4	239.9	57.5		30.6		

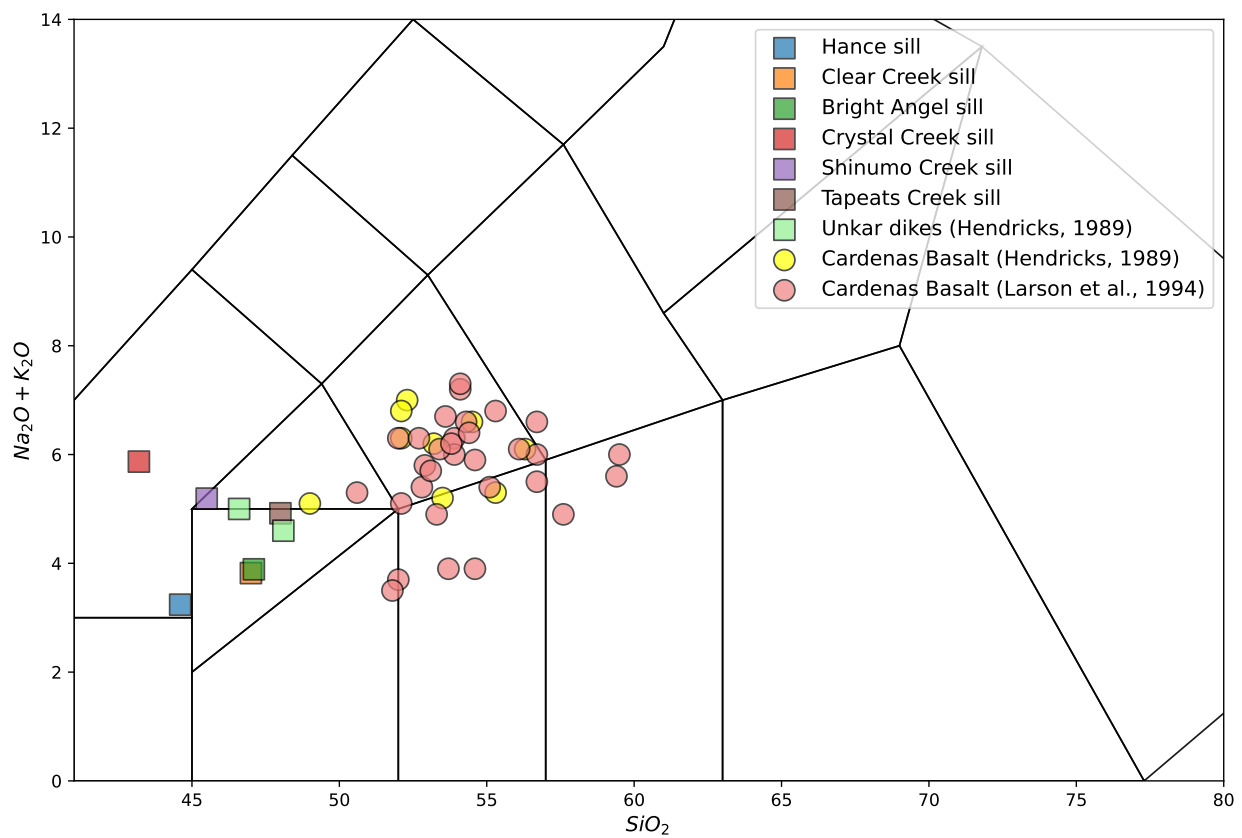


**Figure C.1:** Total alkali-silica diagram of the Cardenas Basalt and mafic intrusions within the Unkar Group. The sills and dikes typically have lower silica content (basalt) than the Cardenas Basalt (basaltic trachy-andesite). Data for the Cardenas Basalt are from Hendricks (1989) and Larson et al. (1994). Data for the intrusions are from Hendricks (1989).

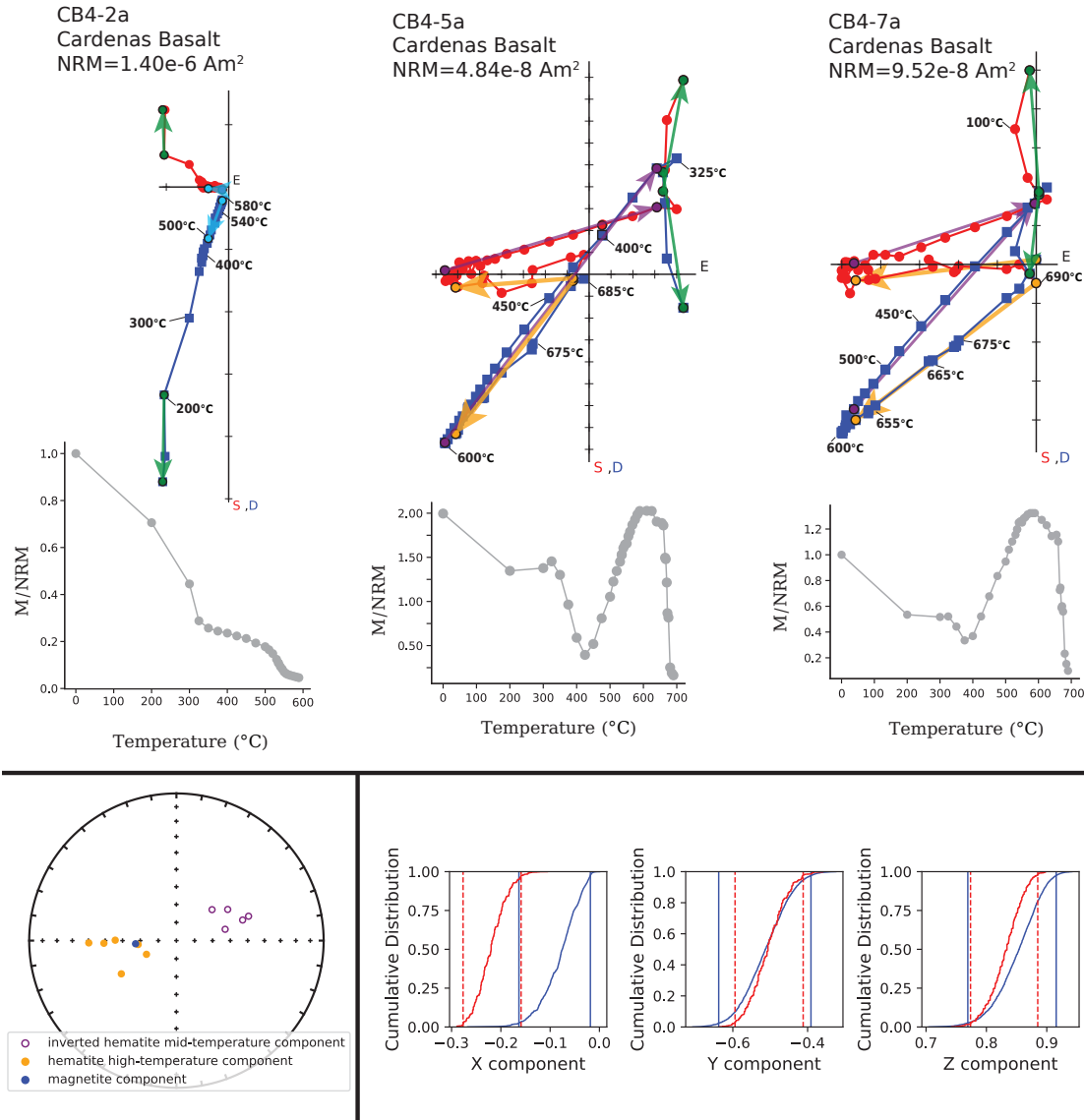


**Figure C.2:** Top panel: Thermal demagnetization data of paleomagnetic specimens collected near the bottom of lava flow CB4. Specimen CB4-2a has a demagnetization behavior similar to other lava flows—after the removal of the present day local field overprint, an origin-trending magnetite-carrying characteristic component unblocks up to 580°C. However, for all other specimens, after the removal of the present day local field overprint by ~300°C (green vector), their total magnetic moments typically increase as the thermal demagnetization approaches ~600°C. This mid-temperature component is followed by an origin-trending decay approaching the Néel temperature of hematite. Bottom panel: Bootstrap reversal test (Tauxe et al., 1991) of the mid-temperature and high-temperature remanence component of CB4. The directions pass the bootstrap reversal test and McFadden and McElhinny (1990) reversal test with a ‘C’ classification. The high-temperature component that unblocks sharply near the hematite Néel temperature has the same polarity with titanomagnetite carried directions in other Cardenas Basalt flows. This similarity is consistent with the hematite forming from oxidation soon after eruption (Haggerty and Baker, 1967). A likely origin of the antipodal component is that it is a self-reversed chemical remanent magnetization held by fine-grained hematite that formed as a result of inversion of maghemite precursors (Hedley, 1968; McClelland, 1987; McClelland and Goss, 1993; Swanson-Hysell et al., 2011). This self-reversal behavior is more likely than one that involves the reversal of the geomagnetic field after the emplacement of the CB4 lava flow. No reversed direction is observed in the adjacent lava flows and previous compilations of paleomagnetic data during this time suggest that the Cardenas lava flows were emplaced during a normal-polarity superchron (Swanson-Hysell et al., 2019b; Driscoll and Evans, 2016).

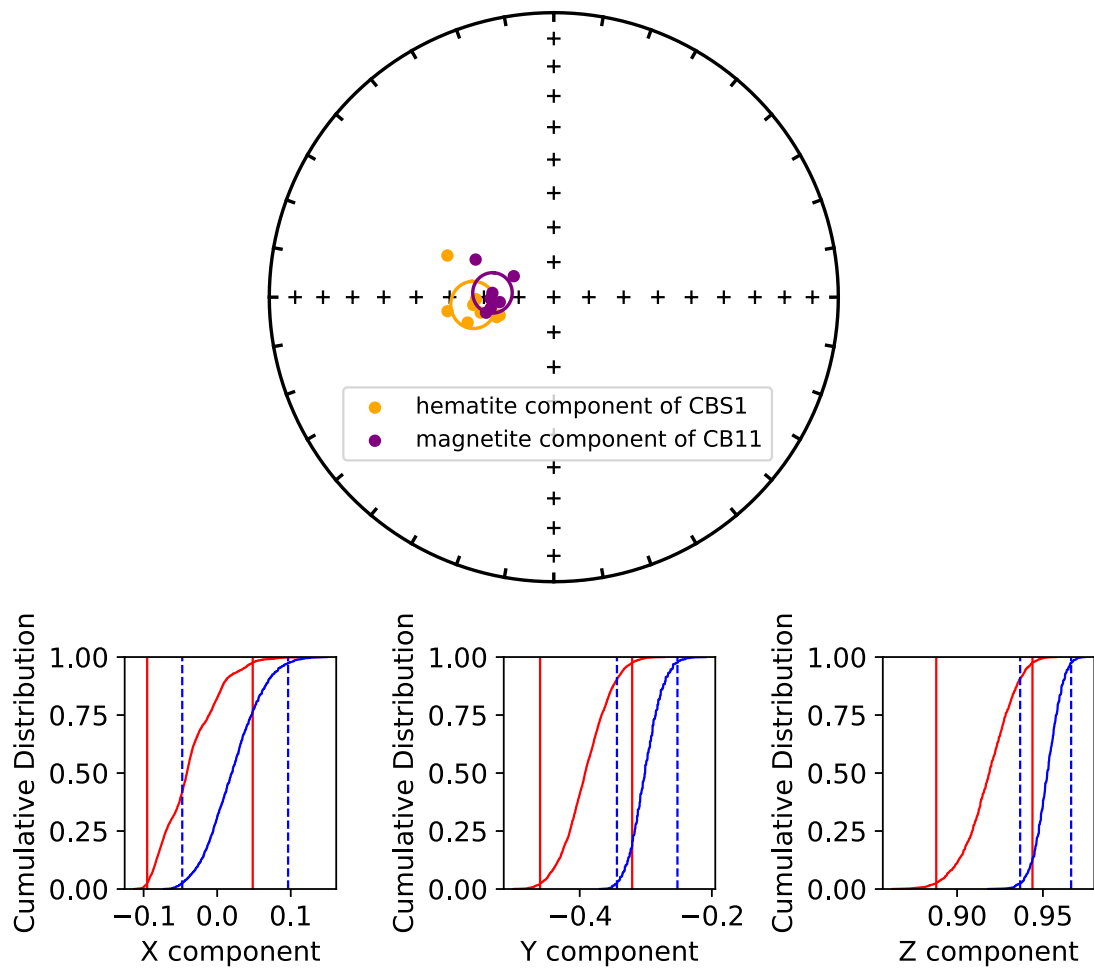


**Figure C.3:** Top: Equal area plot showing the hematite magnetization specimen directions (orange) of the interflow sandstone CBS1 which is stratigraphically below the CB11 lava flow, whose magnetite magnetization directions are shown in purple. Bottom: Bootstrap common mean test of Tauxe et al. (1991) between the specimens directions of the sandstone and the lava flow show a positive result. The specimen directions also passes a common mean test of McFadden and McElhinny (1990) with a ‘B’ classification and have a positive support for sharing a common mean based on the Bayesian approach of Heslop et al. (2023).

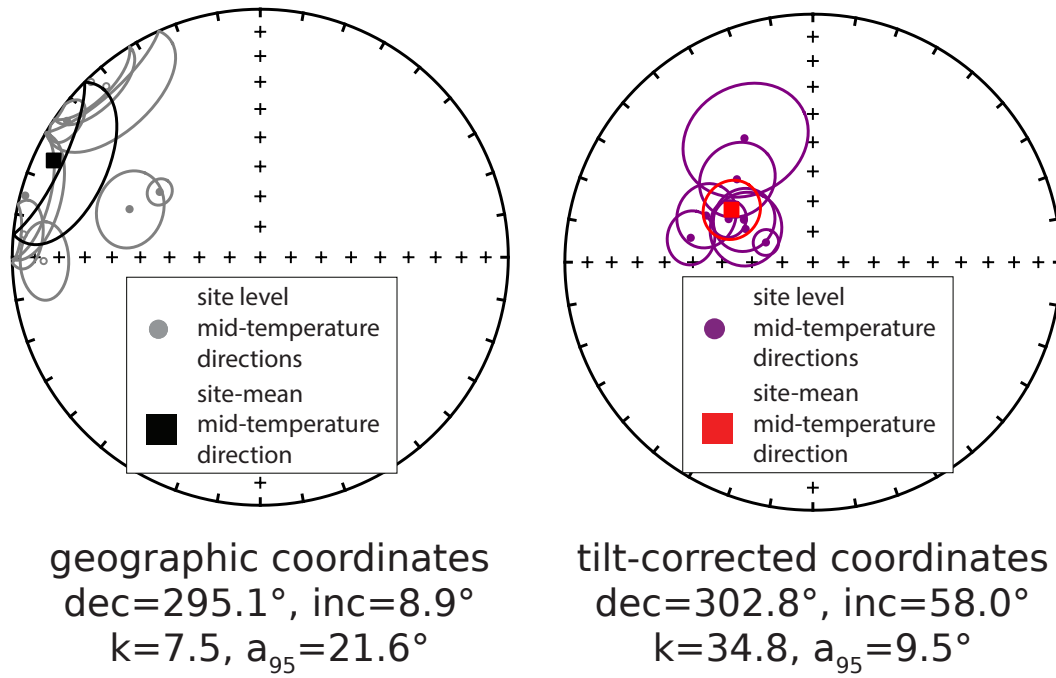


**Figure C.4:** Equal area plots showing the site-level directions and site-mean directions of the Death Valley diabase sills that yielded coherent within-site thermal demagnetization results in both geographic coordinates (left) and tilt-corrected coordinates (right). The site-mean direction in geographic coordinates is dec=295.1°, inc=8.9°, n=8, k=7.5,  $a_{95}=21.6^\circ$ . The site-mean direction in tilt-corrected coordinates is dec=302.8°, inc=58.0°, k=34.8,  $a_{95}=9.5^\circ$ . Applying tilt correction to the sills significantly improves the grouping of the site level directions.

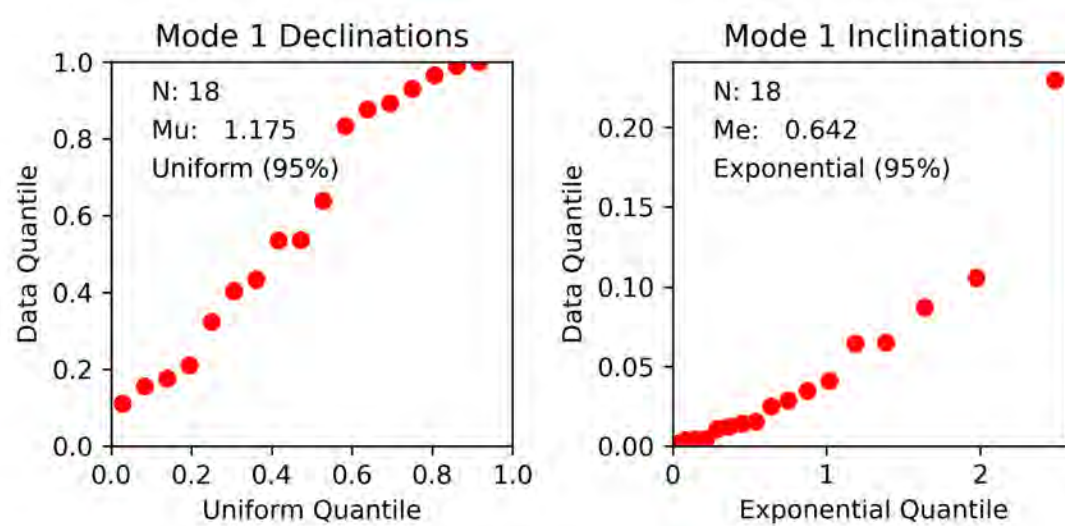


**Figure C.5:** Fisher quantile-quantile (Fisher et al., 1987) test of the distribution of the site level virtual geomagnetic poles of the Cardenas Basalt lava flows. The results show that the null hypothesis that the VGPs are Fisher-distributed cannot be rejected.

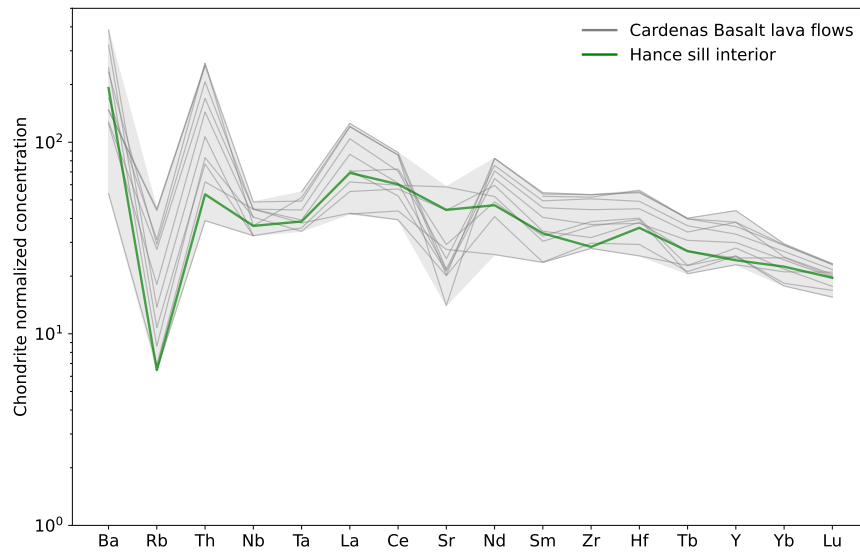


**Figure C.6:** Trace element geochemistry data from Larson et al. (1994). The elemental abundance of the interior of the Hance sill is similar to that of the Cardenas Basalt lavas. Virtual geomagnetic poles developed from the Hance sill, Hance dike, and another undated sill in Red Canyon adjacent to Hance rapids plot closer to those of the Cardenas Basalt than the dated ca. 1098 Ma poles as shown in the main text. These data are consistent with the interpretation that the intrusions near Hance rapids are feeders to the Cardenas Basalt.

## Appendix D

# Supporting Information for “Tracking Rodinia into the Neoproterozoic: new paleomagnetic constraints from the Jacobsville Formation”

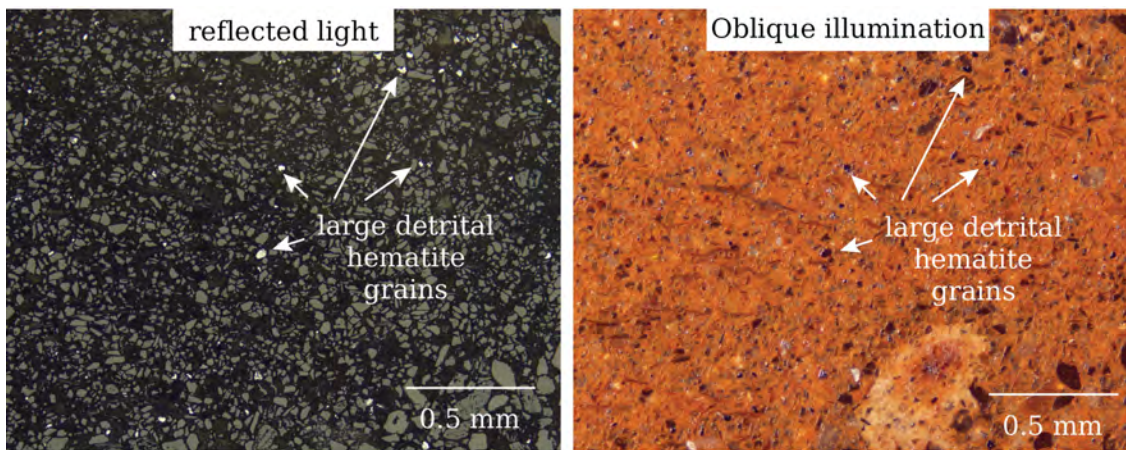


**Figure D.1:** Side-by-side reflected light and oblique illumination images of a thin section of the same field of view of sample NW2-7 collected from Natural Wall ravine. The white arrows point towards examples of large sub-millimeter-scale detrital hematite grains that have bright reflectance under reflected light. Almost all subangular grains in grey color in the reflected image are quartz grains. The red color in the oblique illumination image is a result of diffuse reflectance of pigmentary hematite grains that often coat the boundaries of detrital grains.

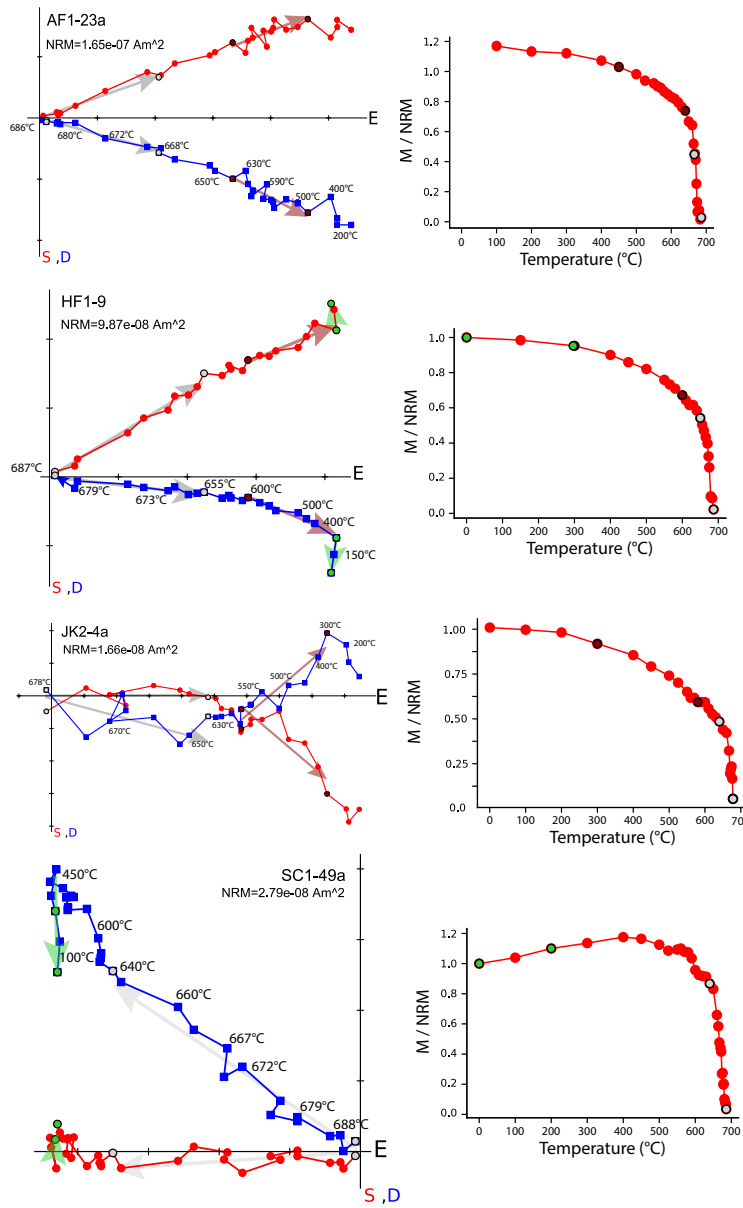


**Figure D.2:** Representative orthogonal vector diagrams of demagnetization experiments for specimens from different stratigraphic sections of this study. An overprint component subparallel to the present day field direction in the study area is typically minimally present in siltstone to very fine-grained sandstone facies. This component shown in light green can be fit with a least-squares line in fine-grained facies. After the removal of the low-temperature component, a mid-temperature component typically unblocks through a wide range of temperature steps by up to  $\sim 650^\circ\text{C}$ . Finally, an origin-trending component with typically a shallower inclination than that of the mid-temperature component sharply unblocks through heating with smaller temperature intervals up toward the Néel temperature of hematite ( $\sim 690^\circ\text{C}$ ). AF-Agate Falls section; HF-Hungarian side falls section near Dover Creek; JK-Hammel Creek section; SC-Snake Creek tributary section. M-magnetic moment; NRM-natural remanent magnetic moment. All diagrams are shown in tilt-corrected coordinates.

**Table D.1:** Compilation of up-to-date Keweenawan Track paleomagnetic poles and ca. 780-720 Ma Laurentian paleomagnetic poles.

## APPENDIX D. SUPPORTING INFORMATION—JACOBSSVILLE FORMATION

Pole	Pole lat	Pole lon	A95	Compilation of Fisher mean paleomagnetic poles				Age reference
				Age	Nominal Age	Lower	Upper	
Osler reverse (lower)	40.9	218.6	4.8	Swanson-Hysell et al. (2014b)	1108	1105.15	1110	Davis and Sutcliffe (1985); Swanson-Hysell et al. (2019b)
Osler reverse (upper)	42.3	203.4	3.7	Halls (1974); Davis and Sutcliffe (1985); Swanson-Hysell et al. (2014b)	1105.15	1104.82	1105.48	As discussed in Swanson-Hysell et al. (2019b)
Mamaïnse lower reversed 1	49.5	227	5.3	Swanson-Hysell et al. (2014a)	1109	1106	1112	As discussed in Swanson-Hysell et al. (2014a)
Mamaïnse lower reversed 2	37.5	205.2	4.5	Swanson-Hysell et al. (2014a)	1105	1100.4	1109	As discussed in Swanson-Hysell et al. (2014a)
Mamaïnse lower normal and upper reversed	36.1	189.7	4.9	Swanson-Hysell et al. (2014a)	1100.36	1100.1	1100.61	As discussed in Swanson-Hysell et al. (2014a)
Mamaïnse upper normal	31.2	183.2	2.5	Swanson-Hysell et al. (2014a)	1094	1090	1100	As discussed in Swanson-Hysell et al. (2014a)
Grand Portage Basalts	46	201.7	6.8	Books (1968); Tauxe and Kodama (2009); Books (1972); Tauxe and Kodama (2009); Tauxe and Kodama (2009); Books (1972); Tauxe and Kodama (2009); Books (1972); Tauxe and Kodama (2009); Fairchild et al. (2017)	1106	1105.28	1108	As discussed in Swanson-Hysell et al. (2019b)
North Shore Volcanic Group (upper NE sequence)	31.1	181.7	4.2	Books (1972); Tauxe and Kodama (2009); Tauxe and Kodama (2009); Books (1972); Tauxe and Kodama (2009); Books (1972); Tauxe and Kodama (2009); Fairchild et al. (2017)	1095	1092	1098	Davis and Green (1997); Fairchild et al. (2017)
North Shore Volcanic Group (upper SW sequence)	36.9	179.3	2.1	Swanson-Hysell et al. (2019b)	1096.18	1093.94	1096.75	As discussed in Swanson-Hysell et al. (2019b)
Schroeder Lutsen Basalts	28.3	187.6	2.5	Fairchild et al. (2017)	1090	1085	1091.5	Fairchild et al. (2017)
Portage Lake Volcanics	27.5	182.5	2.3	Books (1972); Hnat et al. (2006)	1092.51	1091.59	1093.37	As discussed in Swanson-Hysell et al. (2019b)
Lake Shore Traps	22.2	180.8	4.5	Diehl and Haig (1994)	1085.47	1084	1091	Fairchild et al. (2017); As discussed in Swanson-Hysell et al. (2019b)
Siemens Creek Volcanics Michipicoten Island Formation	45.8	214	9.2	Palmer and Halls (1986)	1108	1105	1111	Davis and Green (1997); Fairchild et al. (2017)
Freda Formation	17	174.7	4.4	Palmer and Davis (1987); Fairchild et al. (2017)	1083.95	1083.52	1084.39	As discussed in Swanson-Hysell et al. (2019b)
Haliburton Intrusions Adirondack Highlands anorthositic rocks	2.2	179	4.2	Henry et al. (1977)	1070	1060	1083.5	As discussed in Swanson-Hysell et al. (2019b)
Adirondack Highlands gneiss	-36.2	141.7	6.0	Buchan and Dunlop (1976)	1015	1000	1030	Warnock et al. (2000)
Adirondack Highlands	-19	148.7	11.2	Brown and McEnroe (2012)				
anorthositic rocks	-25.2	143.4	12.9	Brown and McEnroe (2012)				
Franklin large igneous province Victoria/Mainland/Baffin	6.7	131.7	7.1	Brown and McEnroe (2012)	716.33	715.79	716.87	As discussed in Eyster et al. (2019)
Combo Carbon	14.2	163.8	3.5	Eyster et al. (2019)	751	743.4	758.6	As discussed in Eyster et al. (2020)
Butte-Awatubi Carbon Canyon	-0.5	166	9.7	compilation by Eyster et al. (2019)	757	750.2	763.8	As discussed in Eyster et al. (2021)
Nankoweap	-10	163	4.9	compilation by Eyster et al. (2019)	755	782	782	As discussed in Eyster et al. (2021)
UMG Group 3	4.9	160.6	3.2	compilation by Eyster et al. (2019)	760	766	766	As discussed in Eyster et al. (2022)
UMG Group 2	-5.8	158.7	2.7	compilation by Eyster et al. (2019)	772	774.39	775.47	
UMG Group 1	3	163.5	3.2	compilation by Eyster et al. (2019)	774.93	774.39	775.47	
Gunbarrel mean	9.1	138.2	11.7	Eyster et al. (2019)				

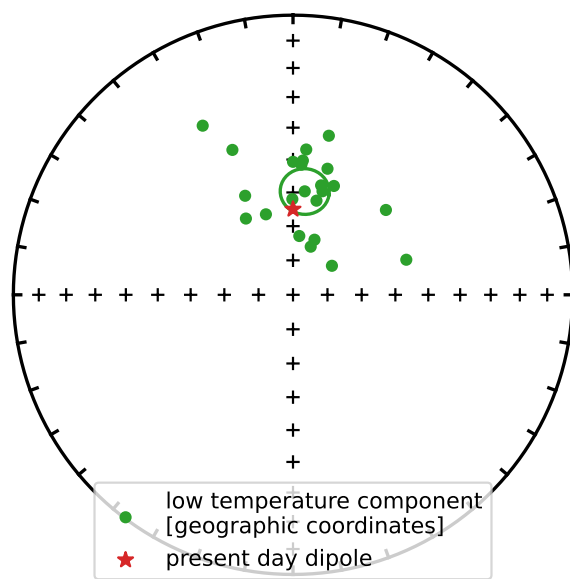


**Figure D.3:** Jacobsville present day local field directions. This present day overprint component is typically removed by  $\sim 300^{\circ}\text{C}$ .

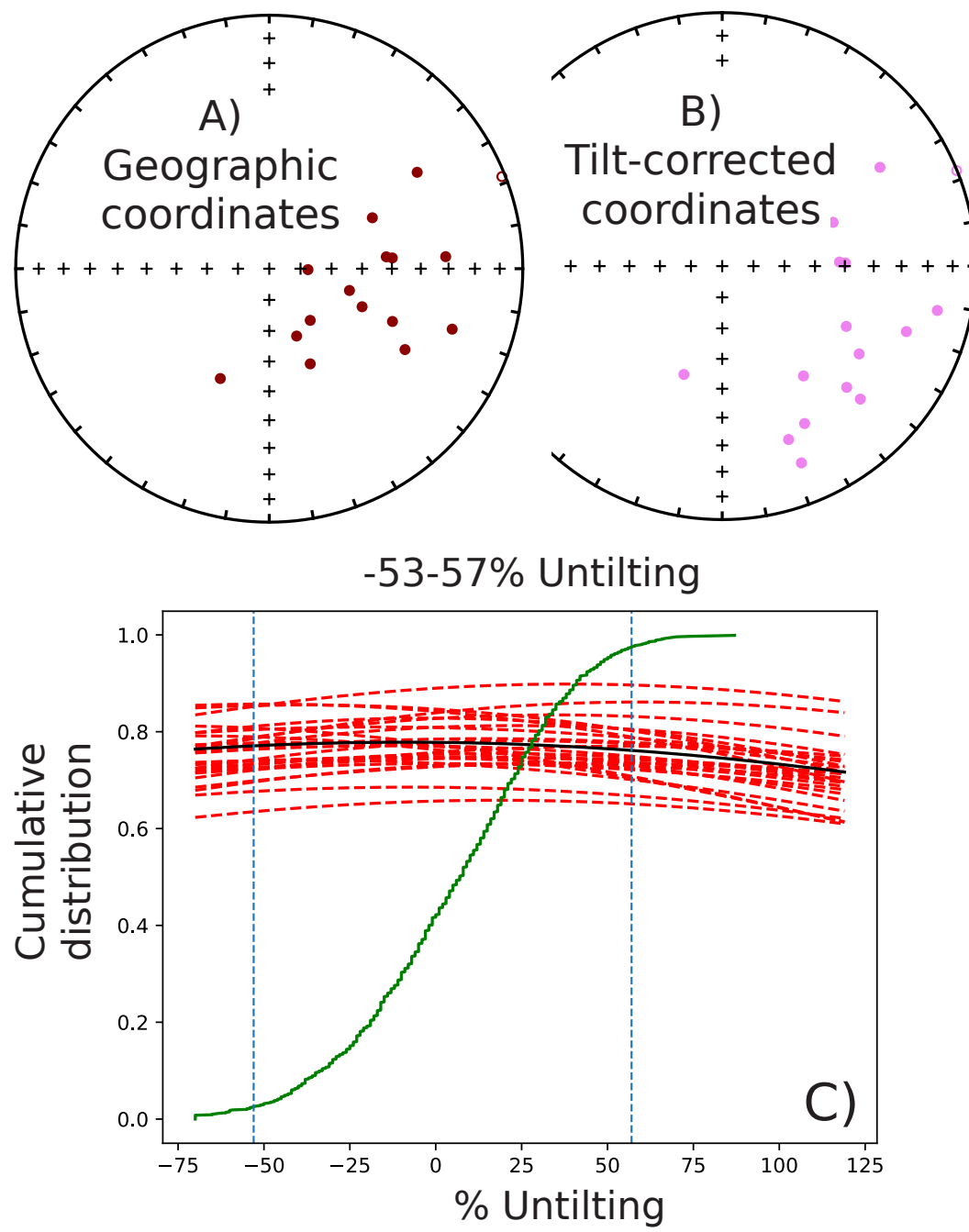


**Figure D.4:** Bootstrap paleomagnetic fold test (Tauxe and Watson, 1994) of the chemical remanent magnetization directions recorded by specimens from the nearly horizontal beds and moderately tilted beds at the Snake Creek tributary. Complete unfolding does not lie within the 95% confidence limits of the test, consistent with the magnetization having been acquired syn- to post-folding.

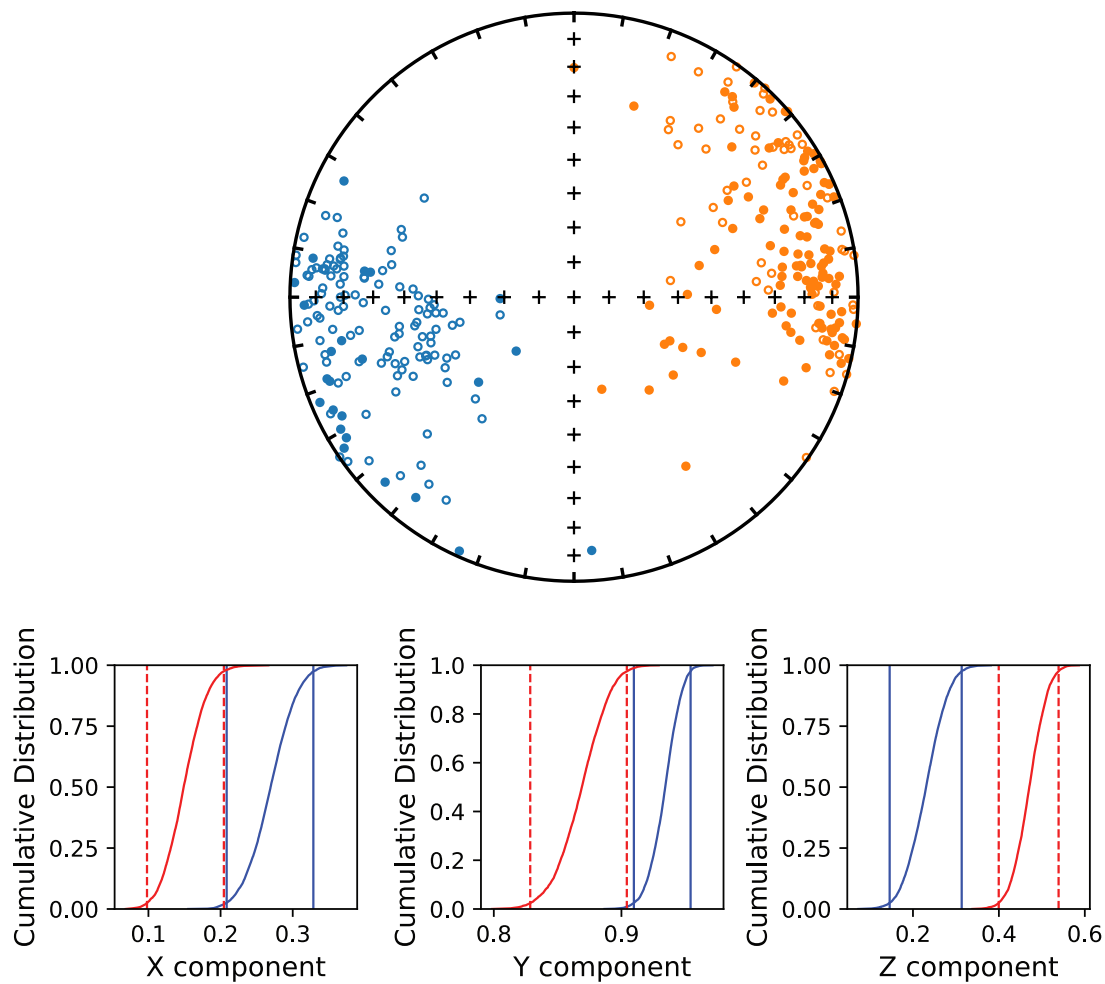


**Figure D.5:** Jacobsville detrital remanence directions showing dual polarities plotted on an equal area stereonet plot. The directions do not pass a reversal test of McFadden and McElhinny (1990) as the angle between the mean directions is  $15.9^\circ$  larger than the critical angle of  $7.5^\circ$ . The directions also do not pass the bootstrap reversal test of Tauxe et al. (1991).

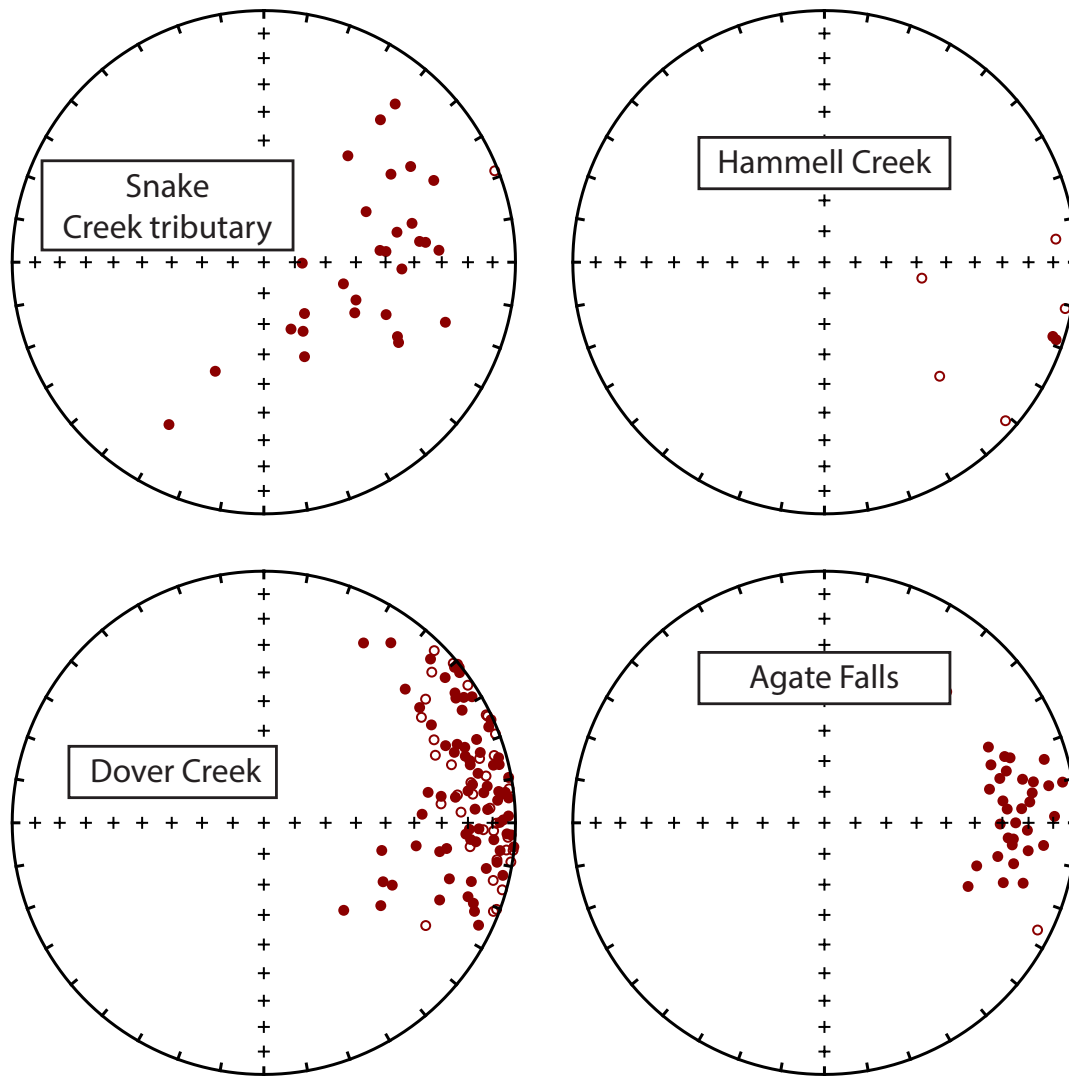


**Figure D.6:** Jacobsville chemical remanence magnetization directions plotted by section. Samples collected from the Natural Wall section do not have interpretable chemical remanence component that can be fit with least-squares lines. All directions are plotted in geographic coordinates.

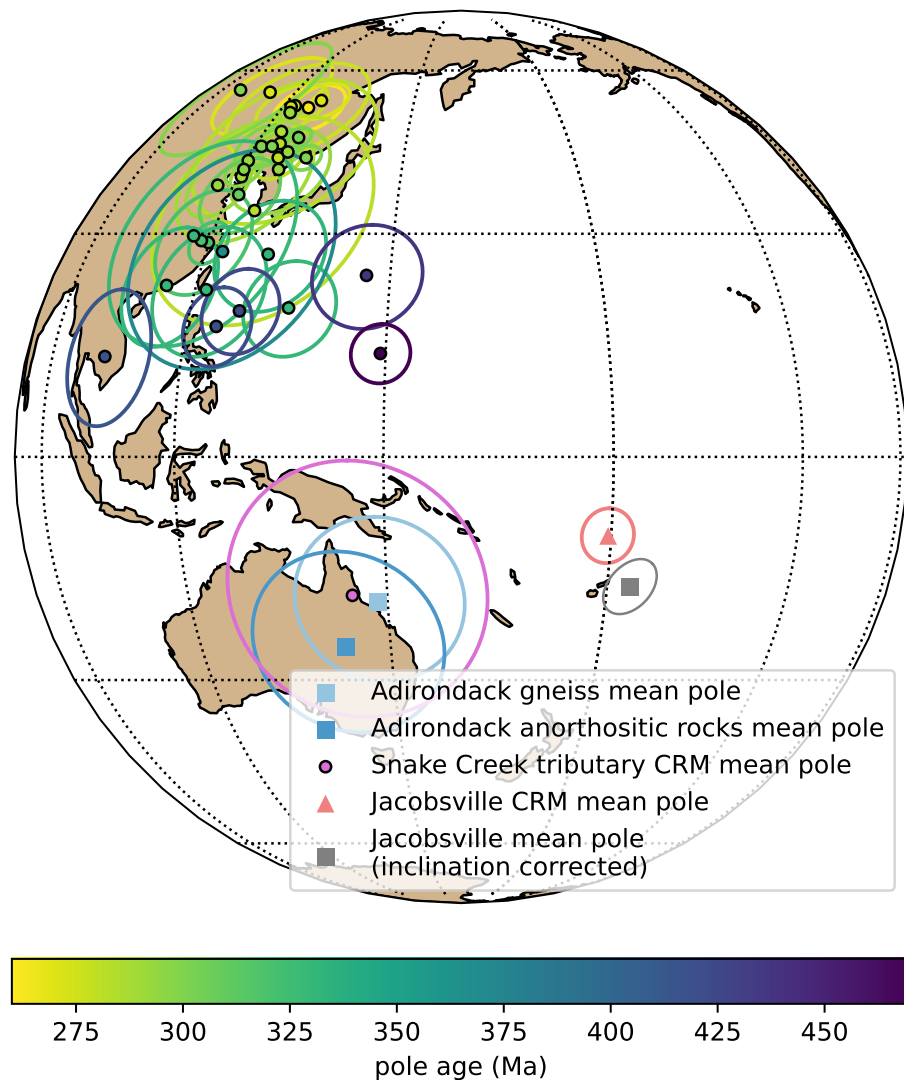


**Figure D.7:** Jacobsville detrital remanence Kent mean pole position and chemical remanence Fisher mean pole position (in geographic coordinates) plotted in context of Laurentia's paleomagnetic poles during Appalachian orogeny (ca. 460-260 Ma) as compiled in Torsvik et al. (2012). The mean chemical remanence pole position from the Snake Creek tributary section is plotted in context of the ca. 970-960 Ma poles developed by Brown and McEnroe (2012) from the Adirondack Highlands of the Grenville orogen. That this chemical remanence component failed a fold test (Figure D.4) and yields a pole position that overlaps with the Grenville poles are consistent with the interpretation that the chemical remanence of the Jacobsville Formation at this locality was acquired during the early Neoproterozoic, soon after Jacobsville deposition and deformation. That the Jacobsville DRM and CRM mean poles are distinct and far away from any of Laurentia's mid- to late-Paleozoic poles supports the interpretation that the Jacobsville detrital remanence magnetization was acquired during the Rigolet phase of the Grenvillian orogeny and the chemical remanence overprint was likely acquired soon after deposition as discussed in detail in the manuscript.

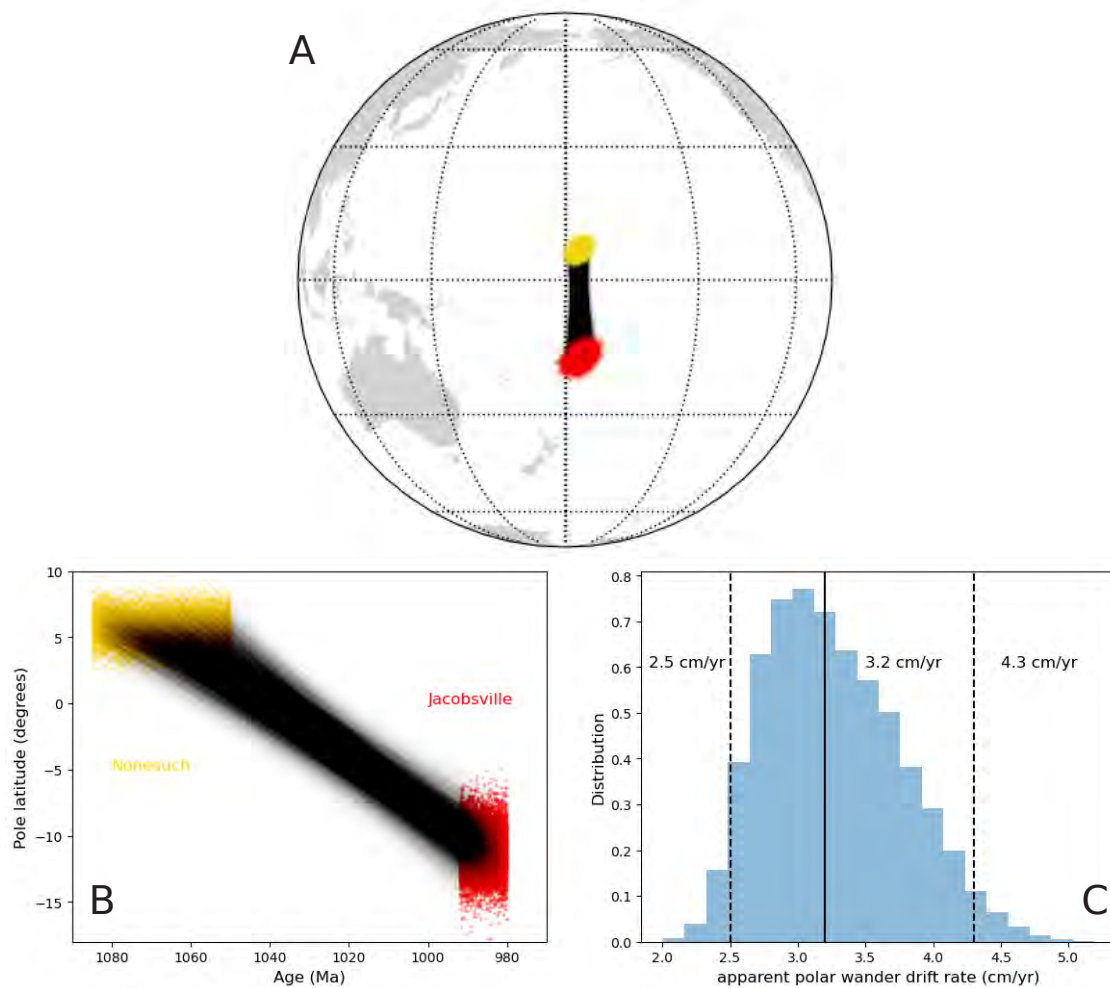


**Figure D.8:** Monte Carlo simulations of apparent polar wander rates implied by paleomagnetic and geochronologic data between the Nonesuch Formation and the Jacobsville Formation. (A) The gold and red points are 10,000 simulated Kent distribution mean paleomagnetic poles for the Nonesuch Formation and Jacobsville Formation, respectively. The simulated poles are connected by gray lines which represent the apparent polar wander great circle paths. (B) The points color-coded in the same way as in (A) show the simulated paleomagnetic pole latitudes plotted against their simulated pole ages using uniform distributions. The points are connected by gray lines which represent the simulated pole latitudinal motion. The histogram on the right shows all 10,000 of the simulated rates that yield the labeled 2.5 percentile value of 2.5 cm/yr, median value of 3.2 cm/yr and 97.5 percentile value of 4.3 cm/yr.

Compilation of Kent mean paleomagnetic poles									
Pole	Pole lat	Pole lon	Major axis lat	Major axis lon	Major axis magnitude	Minor axis lat	Minor axis lon	Age reference	Age reference
								Lower	Upper
Nonesuch Formation	6.6	182.9	27.6	280.2	2.8	41.6	87	2	Slotznick et al. (2023)
Jacobsville Formation	16.9	183.4	45.2	255.5	4.1	39.9	108.1	3.1	this study
								990	985
								992	992
									As discussed in Swanson-Hysell et al. (2019b)
									Hodgin et al. (2022); as discussed in the manuscript